

Département de Géomatique appliquée

Faculté des lettres et sciences humaines

Université de Sherbrooke

Development of high-precision snow mapping tools for Arctic environments

Daniel Kramer

A thesis submitted to the Département de géomatique appliquée of the Université de
Sherbrooke in fulfilment of the requirements of the degree of

DOCTOR OF PHILOSOPHY

Spring 2023

© Daniel Kramer, 2023

Supervisor: Prof. Alexandre Langlois, University of Sherbrooke

Co-supervisor: Dr. Donald McLennan, Arctic Research Foundation

Co-supervisor: Prof. Alain Royer, University of Sherbrooke

External jury member: Assoc. Prof. Eero Rinne, University Centre in Svalbard

Internal jury member: Frédéric Bouchard, University of Sherbrooke

Internal jury member: Samuel Foucher, University of Sherbrooke.

IN MEMORY OF JOSHUA KING

ABSTRACT

Snow is highly variable in time and space and thus many observation points are needed to describe the present state of the snowpack accurately. This description of the state of the snowpack is necessary to validate and improve snow modeling efforts and remote sensing applications.

The traditional snowpit analysis delivers a highly detailed picture of the present state of the snow in a particular location but lacks the distribution in space and time as it is a time-consuming method. On the opposite end of the spatial scale are orbital solutions covering the surface of the Earth in regular intervals, but at the cost of a much lower resolution.

To improve the ability to collect spatial snow data efficiently during a field campaign, we developed a custom-made, remotely piloted aircraft system (RPAS) to deliver snow depth maps over a few hundred square meters by using Structure-from-Motion (SfM). The RPAS is capable of flying in extremely low temperatures where no commercial solutions are available. The system achieves a horizontal resolution of 6 cm with snow depth RMSE of 39% without vegetation (48.5% with vegetation)

As the SfM method does not distinguish between different snow layers, I developed an algorithm for a frequency modulated continuous wave (FMCW) radar that distinguishes between the two main snow layers that are found regularly in the Arctic: “Depth Hoar” and “Wind Slab”. The distinction is important as these characteristics allow to determine the amount of water stored in the snow that will be available for the ecosystem during the melt season. Depending on site conditions, the radar estimates the snow depth with an RMSE between 13% and 39%.

Finally, I equipped the radar with a high precision geolocation system. With this setup, the geolocation uncertainty of the radar on average < 5 cm. From the radar measurement, the distance to the top and the bottom of the snowpack can be extracted. In addition to snow depth, it also delivers data points to interpolate an elevation model of the underlying solid surface. I used the Triangular Irregular Network (TIN) method for any interpolation. The system can be mounted on RPAS and snowmobiles and thus delivers a lot of flexibility.

These tools will assist snow modeling as they provide data from an area instead of a single point. The data can be used to force or validate the models. Improved models will help to predict the size, health, and movements of ungulate populations, as their survival depends on it (Langlois et al., 2017). Similar to the validation of snow models, the presented tools allow a comparison and validation of other remote sensing data (e.g. satellite) and improve the understanding limitations. Finally, the resulting maps can be used by ecologist to better assess the state of the ecosystem as they have a more complete picture of the snow cover on a larger scale that it could be achieved with traditional snowpits.

Keywords: snow depth, snow stratigraphy, FMCW, radar, RPAS, dGNSS, mapping

RÉSUMÉ

Le manteau neigeux varie grandement dans le temps et l'espace, il faut donc de nombreux points d'observation pour le décrire précisément et ponctuellement, ce qui permet de valider et d'améliorer la modélisation de la neige et les applications en télédétection.

L'analyse traditionnelle par des coupes de neige dévoile des détails pointus sur l'état de la neige à un endroit et un moment précis, mais est une méthode chronophage à laquelle la distribution dans le temps et l'espace font défaut. À l'opposé sur la fourchette de la précision, on retrouve les solutions orbitales qui couvrent la surface de la Terre à intervalles réguliers, mais à plus faible résolution.

Dans l'optique de recueillir efficacement des données spatiales sur la neige durant les campagnes de terrain, nous avons développé sur mesure un système d'aéronef télépiloté (RPAS) qui fournit des cartes d'épaisseur de neige pour quelques centaines de mètres carrés, selon la méthode Structure from motion (SfM). Notre RPAS peut voler dans des températures extrêmement froides, au contraire des autres systèmes sur le marché. Il atteint une résolution horizontale de 6 cm et un écart-type d'épaisseur de neige de 39 % sans végétation (48,5 % avec végétation).

Comme la méthode SfM ne permet pas de distinguer les différentes couches de neige, j'ai développé un algorithme pour un radar à onde continue à modulation de fréquence (FM-CW) qui permet de distinguer les deux couches principales de neige que l'on retrouve régulièrement en Arctique : le givre de profondeur et la plaque à vent. Les distinguer est crucial puisque les caractéristiques différentes des couches de neige font varier la quantité d'eau disponible pour l'écosystème lors de la fonte. Selon les conditions sur place, le radar arrive à estimer l'épaisseur de neige selon un écart-type entre 13 et 39 %.

Finalement, j'ai équipé le radar d'un système de géolocalisation à haute précision. Ainsi équipé, le radar a une marge d'erreur de géolocalisation d'en moyenne <5 cm. À partir de la mesure radar, on peut déduire la distance entre le haut et le bas du manteau neigeux. En plus de l'épaisseur de neige, on obtient également des points de données qui permettent d'interpoler un modèle d'élévation de la surface solide sous-jacente. J'ai utilisé la méthode de structure triangulaire (TIN) pour toutes les interpolations. Le système offre beaucoup de flexibilité puisqu'il peut être installé sur un RPAS ou une motoneige.

Ces outils épaulent la modélisation du couvert neigeux en fournissant des données sur un secteur, plutôt que sur un seul point. Les données peuvent servir à entraîner et à valider les modèles. Ainsi améliorés, ils peuvent, par exemple, permettre de prédire la taille, le niveau de santé et les déplacements de populations d'ongulés, dont la survie dépend de la qualité de la neige. (Langlois et coll., 2017.) Au même titre que la validation de modèles de neige, les outils présentés permettent de comparer et de valider d'autres données de télédétection (par ex. satellites) et d'élargir notre champ de compréhension. Finalement, les cartes ainsi créées peuvent aider les écologistes à évaluer l'état d'un écosystème en leur donnant accès à une plus grande quantité d'information sur le manteau neigeux qu'avec les coupes de neige traditionnelles.

Mots-clés : épaisseur du couvert neigeux, stratigraphie de la neige, FMCW, radar, RPAS, dGNSS, cartographie

ACKNOWLEDGEMENTS

How did I end up here? Certainly not all on my own.

There are a lot of people that have my thanks, inside and outside of the scientific world.

From the scientific world

First and foremost, I would like to thank Alexandre Langlois for supervising my thesis. Intensely in areas where I have my weaknesses but with all the freedom where I know my stuff. I had a blast writing my PhD and would do it all over again. Looking forward to more years of collaboration, floating Ardbegs and listening to Cypress Hill while cutting down trees.

Marius Jonassen, Stephan Kral, Lukas Frank, Eero Rinne, and in general the University Centre in Svalbard. The single most thing I enjoy in life is being in Longyearbyen, teaching courses at UNIS. Already looking forward to the next visit.

Jean-Benoit Madore. Not only for a close friendship and discussing science, but also for helping navigate a foreign country, always giving me a helping hand with translations and administrative problems.

Donald McLennan. What can I say? Thanks for fantastic field experiences, supervision and helping me with the administrative work at Polar Knowledge Canada.

Alain Royer and Joshua King, for lifting my high-school calculations to research physics by pointing out lots of holes in my work. And for great field campaigns.

Arko, Johann Wagner and Erin Cox for friendship, help and support in Cambridge Bay and generally being awesome.

Julien Meloche for crashing drones with me. And feeding me during fieldwork.

Timo Vihma and Ari-Matti Harri. My time at the Finnish Meteorological Institute is not forgotten and was one of the best episodes in my life.

Also great thanks to Günther Heinemann and David Schröder for getting me interested in polar research and first supervisions.

From outside the scientific world

Thanks to everyone in my family, close and extended. Especially to my parents, Helga and Gerhard, and my grandparents for guidance, funding my studies and being patient while I was deep in techno.

To my brothers, Timm and Christian...thanks for everything.

The other family

Thomas Vormann, Teemu Lantz, Bambi Eskeröd, Katarina Wågberg, Jana Staffel and Vicktoria Dreier for good times and very close friendships. My compact friend Laudel. And, of course: Suzie Mäenpää.

From the rest of the world

Sarah, Alexandra M., Sophie, Judith, Anna, Alexandra K., and so many more from Germany, Finland, the EU and the rest of the world.

Anne Menkhaus and Uwe Baltes for long lasting friendships, support in my studies and Uwe for being the best scuba diving instructor.

The third family

DJ Triton, Jone Kaján and the worldwide rave community.

1 CONTENTS

Abstract.....	iv
RÉSUMÉ.....	vi
Acknowledgements	viii
List of figures	xiii
List of tables	xvi
List of Abbreviations and Symbols	xvii
1 Introduction	- 1 -
1.1 General introduction	- 1 -
1.2 Motivation.....	- 2 -
1.3 Defining the subject.....	- 4 -
1.3.1 Objectives and hypotheses.....	- 9 -
1.4 Thesis overview	- 10 -
2 Background	- 12 -
2.1 Snow	- 12 -
2.1.1 Formation	- 12 -
2.1.2 Accumulation and metamorphism.....	- 14 -
2.1.3 The Arctic snowpack	- 19 -
2.1.4 Seasonal life cycle and spatial variability of the Arctic snowpack	- 20 -
2.2 Relevant electromagnetic concepts.....	- 21 -
2.2.1 Radar.....	- 23 -
2.3 Snow in the microwave region	- 29 -
2.3.1 Properties.....	- 29 -
2.3.2 Absorption and scattering.....	- 30 -
2.3.3 Refractive Index and Snell's law.....	- 31 -
3 Data and Methods.....	- 33 -
3.1 Research sites.....	- 33 -
3.1.1 Greiner Lake Watershed.....	- 34 -
3.1.2 Trail Valley Creek	- 35 -
3.1.3 SIRENE Research station.....	- 36 -
3.2 Data and methods.....	- 38 -
3.2.1 Notes.....	- 38 -
3.2.2 Snow pits and snow depth measurements	- 39 -
3.2.3 Satellite-based geolocation procedures	- 40 -

3.2.4	Ground Control Points (GCP)	- 44 -
3.2.5	Digital representations of the surface	- 45 -
4	Designing a do-it-yourself (DIY) Unmanned Aerial Vehicle (UAV) for Arctic research purposes and proving its capabilities by retrieving snow depth via structure-from-motion. ...	47 -
4.1	Introduction to article.....	- 47 -
4.2	Designing a do-it-yourself (DIY) Unmanned Aerial Vehicle (UAV) for Arctic research purposes and proving its capabilities by retrieving snow depth via structure-from-motion.	- 51 -
4.2.1	Abstract.....	- 52 -
4.2.2	Introduction	- 53 -
4.2.3	UAV development and overview	- 55 -
4.2.4	UAV – Application: Snow Depth Retrieval	- 72 -
4.2.5	Conclusions	- 81 -
4.2.6	Acknowledgements	- 82 -
4.2.7	Appendix	- 83 -
4.3	Commentary.....	- 88 -
4.3.1	Comparison to the literature	- 88 -
4.3.2	Comparison to snowpits	- 90 -
4.3.3	Towards the next chapter.....	- 91 -
5	Assessment of Arctic snow stratigraphy and water equivalent using a portable Frequency Modulated Continuous Wave radar.	- 92 -
5.1	Introduction to article.....	- 92 -
5.2	Assessment of Arctic snow stratigraphy and water equivalent using a portable Frequency Modulated Continuous Wave RADAR	- 95 -
5.2.1	Abstract.....	- 96 -
5.2.2	Introduction	- 97 -
5.2.3	Data and methods	- 99 -
5.2.4	Snow depth retrieval	- 106 -
5.2.5	Results	- 108 -
5.2.6	Discussion.....	- 115 -
5.2.7	Summary and future work	- 118 -
5.2.8	Acknowledgements	- 120 -
5.3	Commentary.....	- 122 -
5.3.1	Footprint, over probing and ecotypes	- 122 -
5.3.2	Towards the next chapter.....	- 123 -
6	High precision mapping of snow depth with the SIRA	- 124 -

6.1	Introduction to the chapter	- 124 -
6.2	High precision mapping of snow depth with the SIRA	- 127 -
6.2.1	Introduction	- 127 -
6.2.2	Methodology.....	- 131 -
6.2.3	Mapping.....	- 133 -
6.3	Results.....	- 137 -
6.3.1	Reference maps.....	- 137 -
6.3.2	Local snow conditions	- 139 -
6.3.3	SIRA measurements and maps	- 140 -
6.3.4	RPAS flights	- 143 -
6.4	Analysis	- 145 -
6.4.1	Snow	- 145 -
6.4.2	Map evaluations.....	- 146 -
6.4.3	Cross-use of methods	- 148 -
6.4.4	Surveying aspects	- 149 -
6.5	Conclusion and future work.....	- 153 -
6.6	Acknowledgement	- 155 -
6.7	Commentary.....	- 155 -
7	Conclusion.....	- 156 -
7.1	Summary	- 156 -
7.2	Limitations	- 158 -
7.2.1	RPAS	- 158 -
7.2.2	SIRA	- 159 -
7.2.3	Surveying.....	- 160 -
7.3	Ongoing contributions and future work.....	- 161 -
7.3.1	Ongoing contributions	- 161 -
7.3.2	Future work	- 163 -
7.4	Closing comments.....	- 164 -
8	References	- 165 -

LIST OF FIGURES

FIGURE 1.1: RELATIONS AND INTERACTIONS BETWEEN IN SITU OBSERVATIONS, RS APPROACHES AND SNOW MODELLING (DONG, 2018).	- 5 -
FIGURE 1.2: ENVIRONMENT AND CLIMATE CHANGE CANADA NETWORK OF AUTOMATIC WEATHER STATIONS (AS OF 2022-11-12).	- 6 -
FIGURE 2.1: THE NAKAYA DIAGRAM DESCRIBES HOW TEMPERATURE AND HUMIDITY INFLUENCE THE SHAPE OF THE SNOW CRYSTAL.	- 13 -
FIGURE 2.2: CRYSTALS OF A DH (LEFT) AND RG (RIGHT). THE LATTER IS A TYPICAL GRAIN FOUND IN WS. PICTURES TAKEN BY SIMON LEVASSEUR.	- 16 -
FIGURE 2.3: CW PRINCIPLE. THE CW TRANSMITTER CONTINUOUSLY EMITS AN EM WAVE F_0. VIA THE DUPLEXER, THE SIGNAL IS SENT BY THE ANTENNA TOWARDS THE OBJECT. THE DUPLEXER SWITCHES THE ANTENNA FROM TRANSMIT TO RECEIVE AND THE ANTENNA WILL RECEIVE THE RETURNING SIGNAL. THE MIXER RECEIVES F_0 AND $F_0 \mp F_b$. THEN IT ISOLATES F_b, WHICH IS SHOWN E.G. ON THE USER INTERFACE (UI). IF THE ANTENNA IS STATIONARY, THIS EQUATES TO THE TARGET'S VELOCITY. ADAPTED FROM ENGINEERING FUNDA (2017).	- 24 -
FIGURE 2.4: FMCW SIGNAL CONSIDERATIONS. ADAPTED FROM (TEXAS INSTRUMENTS, 2018).	- 26 -
FIGURE 2.5: FMCW PRINCIPLE. ADAPTED FROM TEXAS INSTRUMENTS (2022).	- 27 -
FIGURE 2.6: WAVE INTERFERENCE AND ITS RESULTING BEAT FREQUENCY.	- 27 -
FIGURE 2.7: PRINCIPLE OF ZERO PADDING. PICTURE TAKEN FROM WWW.EDUCBA.COM.	- 28 -
FIGURE 2.8: SNELL'S LAW. IN PURPLE IS THE INCIDENT PROCESS AND ITS MATERIAL IN BLACK. IN TURQUOISE, THE REFRACTIVE PROCESS, AND ITS MATERIAL IN BLUE.	- 31 -
FIGURE 2.9: THE FIGURE SHOWS THE SEPARATION OF THE SNOWPACK IN TWO LAYERS AND HOW SNELL'S LAW HAS BEEN APPLIED. H_s IS THE TOTAL SNOW DEPTH AND THE TWO GRAY LAYERS DISTINGUISH DEPTH HOAR (BOTTOM) AND WIND SLAB (TOP). THE RED AND BLUE ARROWS ARE THE INCIDENT AND REFLECTED ANGLE WITH THE DOTTED GREEN LINE MARKING THE INTERFACES.	- 32 -
FIGURE 3.1: OVERVIEW OF THE THREE RESEARCH SITES AND AREAS FOR THE PROJECT. BACKGROUND MAP: GOOGLE HYBRID.	- 33 -
FIGURE 3.2: GREINER LAKE WATERSHED AND CAMBRIDGE BAY. IN GREY, THE RELIEF OF THE AREA; IN BLUE LAKES AND RIVERS. WITH THE EXCEPTIONS OF A FEW SMALL MOUNTAINS, THE AREA IS RELATIVELY FLAT. DATA TAKEN FROM WWW.OPENSTREETMAP.ORG AND HTTPS://GEOGRATIS.GC.CA.	- 34 -
FIGURE 3.3: ECOTYPES OF THE IMA, FROM PONOMARENKO ET AL. (2019).	- 35 -
FIGURE 3.4: 3D MODEL OF THE TVC CAMPSITE AND IMMEDIATE SURROUNDINGS. X- AND Y-SCALES TO SCALE, BUT Z-SCALE ALTERED FOR A BETTER PRESENTATION. UNDERLYING HEIGHT DATA HAS BEEN PROVIDED BY BRANDEN WALKER.	- 36 -
FIGURE 3.5: OVERVIEW OF THE SIRENE STATION AND SURROUNDING AREA AS A COMBINATION OF RPAS DATA AND MODELLING. PATRICK MENARD PRODUCED PICTURE MATERIAL OF THE STATION, WITH BACKGROUND INFORMATION RETRIEVED FROM GOOGLE HYBRID. THE STATION IS AREA ELEVATED. THIS MODEL ONLY SERVES PRESENTATION PURPOSES AND IS THUS NOT TO SCALE.	- 37 -
FIGURE 3.6: CONCEPT FOR SNOW PIT MEASUREMENTS. BLUE DOTS SHOW THE SPOTS FOR TEMPERATURE MEASUREMENTS AND YELLOW DOTS, SPOTS FOR SNOW GRAIN SAMPLES. AS THIS GRAPHIC IS A CONCEPT, VARIATIONS MAY OCCUR DURING FIELDWORK.	- 40 -
FIGURE 3.7: dGNSS PRINCIPLE: RED LINES REPRESENT THE TIME SIGNAL SENT BY THE NAVIGATION SATELLITE AND RECEIVED BY THE ROVER AND THE BASE STATION. THE GREEN LINE IS THE CORRECTION SIGNAL SENT FROM THE BASE STATION TO THE ROVER VIA THE LoRa RADIO. THE BLUE SPHERE IS THE EFFECTIVE RADIUS OF LoRa AS GIVEN FROM THE MANUFACTURER.	- 45 -
FIGURE 4.1: FOOTPRINT OF A SNOW PROBE AND THE WALL OF A SNOW PIT.	- 48 -
FIGURE 4.2: SCHEMATIC OF THE WORKFLOW TO DEVELOP A DIY UAV.	- 50 -
FIGURE 4.3: EXPERIMENTAL SET-UP.	- 58 -
FIGURE 4.4: COMPARISON OF THREE DIFFERENT BATTERIES AT THREE DIFFERENT TEMPERATURES.	- 61 -
FIGURE 4.5: RESULTS FOR THREE DIFFERENT BATTERY TYPES AT THREE DIFFERENT TEMPERATURES.	- 62 -
FIGURE 4.6: LONG-TERM EXPOSURE OF A BATTERY TO DIFFERENT TEMPERATURES. NOTE THE DISTINCT DROP OF DISCHARGE CAPACITY AT AROUND 50 MIN FOR TEMPERATURES $< -30^{\circ}\text{C}$.	- 63 -

FIGURE 4.7: FROM LEFT TO RIGHT: SKYSURFER, PENGUIN, INTERIOR OF THE PENGUIN, DJI PHANTOM 3 PRO.	- 67 -
FIGURE 4.8: WIRING DIAGRAM OF THE ELECTRONICS.	- 68 -
FIGURE 4.9: ORTHOPHOTO AND DSM IMAGES OF THE STUDY SITE NEAR CAMBRIDGE BAY (69°13'19.66" N, 104°53'54.91"W). THE UPPER LEFT (A) SHOWS THE ORTHOPHOTO FROM THE SUMMER FLIGHT WITH MORE VEGETATION ON THE LEFT AND MORE ROCKS ON THE RIGHT. THE LOWER LEFT (B) SHOWS THE RESULTING DSM FROM THE SUMMER FLIGHT. ON THE RIGHT SIDE (C) AND (D) SHOW THE ORTHOPHOTO AND DSM RESULTS FOR THE WINTER FLIGHTS.	- 78 -
FIGURE 4.10: SNOW DEPTH MAP RESULTING FROM THE SfM APPROACH. THE DELIMITED AREA IN BLACK SHOWS NEGATIVE RESULTS AND IS DUE TO THE INFLUENCE OF THE VEGETATION.	- 79 -
FIGURE 4.11: REGRESSION BETWEEN THE VALIDATION POINTS AND THE UAV POINTS.	- 80 -
FIGURE 4.12: MAP OF STUDY SITE AT GREINER LAKE WATERSHED.	- 84 -
FIGURE 4.13: ORTHOPHOTOS FROM APRIL-FLIGHTS.	- 85 -
FIGURE 4.14: DETAILED GCP-INFO FROM SUMMER DSM.	- 86 -
FIGURE 4.15: DETAILED GCP-INFO FROM WINTER DSM.	- 86 -
FIGURE 4.16: DIY-COMPONENTS (LEFT) VS. COMMERCIAL COMPONENTS (RIGHT).	- 87 -
FIGURE 4.17: RESULTS FROM WALKER ET AL. (2020). PLEASE NOTE THE SNOW DEPTH COLORING. COMPARABLE TO CAMBRIDGE BAY ARE ONLY THE BLUEST PARTS.	- 89 -
FIGURE 5.1: WORKFLOW OF THE ALGORITHM-DEVELOPMENT FOR SIRA.	- 94 -
FIGURE 5.2: LOCATION OF MAIN RESEARCH SITES AND LOCATIONS OF SNOW PITS/FMCW RADAR MEASUREMENTS. THE COORDINATES OF THE TVC STATION ARE 68°44'31.29" N; 133°29'57.02" W, AND FOR THE NORTHERN SHORE OF GREINER LAKE 69°13'12.19" N; 104°54'2.12" W. DATA TAKEN FROM WWW.OPENSTREETMAP.ORG AND HTTPS://GEOGRATIS.GC.CA.	- 100 -
FIGURE 5.3: THE FIGURE SHOWS R_{avg} FROM ONE OF THE SNOW PITS DURING A CAMPAIGN IN CAMBRIDGE BAY. THE BLUE LINE SHOWS THE RETURN SIGNAL IN DECIBELS [dB] (X-AXIS) AND THE DISTANCE [CM] ON THE Y-AXIS. THE RED LINES MARK THE DETECTED PEAK AND THE RED POINTS, THE VERTICAL DISTANCE IN CM. THESE ARE RAW VALUES THAT ARE NOT CORRECTED FOR THE RI. THE GREEN LINES/POINTS SHOW THE ADJUSTMENT FOR AN OFFSET CAUSE BY THE RADAR PLASTIC COVER. THESE ALSO ARE NOT CORRECTED FOR THE RI. THE LAYER/INFO PART SHOWS THE SECTIONING OF THE DATA AFTER OUR METHODOLOGY. THE BLACK PART IS AFOREMENTIONED PLASTIC COVER AND IS USED AS THE 0-POINT. THE LIGHT BLUE PART IS THE LAYER OF AIR AND IS NOT CORRECTED FOR RI (RI OF AIR IS CLOSE TO 1), FOLLOWED BY THE WIND SLAB LAYER, WHICH CONSISTS IN THIS CASE OF THREE PEAKS. THE LOWEST TWO PEAKS ENCLOSE THE DEPTH HOAR AND EVERYTHING BELOW THE LOWEST PEAK IS CONSIDERED GROUND. THE PEAKS ARE IDENTIFIED BY CALCULATING THE DIFFERENCE BETWEEN TWO CONSECUTIVE POINTS ALONG THE PROFILE TWICE ENABLING INFLEXION POINTS TO BE IDENTIFIED.	- 106 -
FIGURE 5.4: THE FIGURES SHOW RADAR-RETRIEVED D_s AGAINST THE MANUALLY RETRIEVED D_s. THE CAMPAIGNS ARE SEPARATED BY SYMBOLS AND FOR CB2, ECOTYPES ARE PRESENTED IN DIFFERENT COLOURS. A REGRESSION LINE HAS BEEN ADDED FOR TOTAL D_s AND D_{ws}, WHICH HAVE SHOWN TO BE STATISTICALLY SIGNIFICANT.	- 115 -
FIGURE 5.5: FOOTPRINT OF SIRA (NOT TO SCALE).	- 122 -
FIGURE 6.1: THE FIGURE SHOWS THE DIFFERENT SURFACES AND LAYERS THAT THE SIRA CAN MAP.	- 125 -
FIGURE 6.2: SCHEMATIC FOR THIS CHAPTER INCLUDING THE SPECIFIC OBJECTIVES.	- 126 -
FIGURE 6.3: THE RESEARCH STATION SIRENE AND THE LOCATION OF THE GROUND CONTROL POINT (GCP).	- 131 -
FIGURE 6.4: BASE STATION AND GROUND CONDITIONS (LEFT), SIRA SETUP (RIGHT).	- 133 -
FIGURE 6.5: MAP OF THE DSM_{REF}. THE RED-BORDERED SQUARE DELINEATES THE STATION BUILDING. CONTOUR LINES ARE SHOWN IN RED AT 50 CM INTERVALS (THICK RED LINES). HEIGHT GIVEN IN METRE A.S.L.	- 138 -
FIGURE 6.6: TSD MAP_{REF} MEASURED WITH A METRE STICK AND A dGNSS MODULE.	- 139 -
FIGURE 6.7: DSM_{SIRA} WITH THE ELEVATION GIVEN A.S.L. AND CONTOUR LINES WITH 50 CM INTERVALS (RED LINES).	- 141 -
FIGURE 6.8: SNOW DISTRIBUTION BASED ON THE SIRA RETRIEVALS.	- 142 -
FIGURE 6.9: DERIVED DSM FROM THE RPAS FLIGHT DURING SNOW-OFF CONDITIONS. UNITS ARE IN METRES AND A.S.L. AND THE CONTOUR LINE INTERVAL (RED) IS 50 CM.	- 144 -
FIGURE 6.10: TSD MAP_{RPAS}. TSD IS GIVEN IN METRES.	- 145 -

FIGURE 6.11: DIFFERENCES IN TSD BETWEEN THE SIRA AND THE REFERENCE MEASUREMENTS.	- 147 -
FIGURE 6.12: DIFFERENCE BETWEEN TSD_{RPAS} AND TSD_{SIRA}.	- 148 -
FIGURE 6.13: DIFFERENCES BETWEEN THE D_s MAP_{REF} AND THE CALCULATED DS MAP COMBINING THE DSM_{REF} WITH THE DSSM_{RPAS}.	- 149 -
FIGURE 6.14: THE MAPS SHOW THE IMPORTANCE OF A DATA QUALITY CHECK. AT THE RED POINT, A LOW FIX-QUALITY OF 1 HAS BEEN USED DURING THE TIN CALCULATION. IN B), THE POINT HAS BEEN REMOVED.	- 150 -
FIGURE 6.15: DIFFERENCE IN TSD-ESTIMATION WITH LOW FIX-QUALITY (A) AND HIGH FIX-QUALITY (B). .	- 151 -
FIGURE 6.16: DSM COMPARISON BETWEEN THE DIFFERENT METHODS. THE UNITS ARE GIVEN IN M...	- 152 -

LIST OF TABLES

TABLE 3.1: SNOW PITS: PROS AND CONS.....	- 41 -
TABLE 3.2: GNSS SYSTEMS AND THEIR FREQUENCIES. ADAPTED FROM HEXAGON (2021).....	- 43 -
TABLE 4.1: BATTERIES USED IN EXPERIMENTS. ALL BATTERIES HAVE 4 CELLS.	- 57 -
TABLE 4.2: TIME IN SECONDS UNTIL THE BATTERY REACHES 14.50 V. SHORTLY AFTER THIS VALUE, VOLTAGES FOR ALL BATTERIES DROP SHARPLY UNTIL REACHING THE CUT-OFF LIMIT OF 12.5 V. THE DISPLAYED VALUE IS THE MEAN OF 3 TESTS.	- 64 -
TABLE 4.3: AS THE SKYSURFER STOPPED OPERATING AT -5°C, TESTS WERE NOT CONTINUED BELOW THIS LIMIT. SIMILARLY, TESTS FOR THE PENGUIN AND TALON WERE NOT CONDUCTED ABOVE -15°C, AS THEY HAD ALREADY BEEN SHOWN TO BE OPERATIONAL DOWN TO -40°C AND WITH LIMITATIONS TO - 50°C. THE 'X' MEANS THAT THE ELECTRONIC DEVICE FAILED THE TEST, THE CHECK MARK THAT THE TEST WAS SUCCESSFUL AND A CHECK MARK IN BRACKETS THAT THE ELECTRONIC DEVICE STILL WORKED, BUT AT A REDUCED CAPACITY.....	- 70 -
TABLE 4.4: DSM DESCRIPTION FOR SUMMER AND WINTER FLIGHTS. BOTH FLIGHTS WERE IN MANUAL MODE.	- 77 -
TABLE 4.5: LINEAR REGRESSION PARAMETERS AND RMSE FROM SNOW DEPTH VALIDATION POINTS. .	- 80 -
TABLE 4.6: CAMERA PARAMETERS USED IN BOTH DSM.....	- 83 -
TABLE 4.7: ADVANTAGEOUS AND DISADVANTAGEOUS OF SFM.	- 91 -
TABLE 5.1: BRIEF DESCRIPTION OF ECOTYPES OCCURRING IN THIS STUDY. DATA FROM PONOMARENKO ET AL. (2019).	- 102 -
TABLE 5.2: SIRA CHARACTERISTICS.	- 105 -
TABLE 5.3: YEARLY AND CAMPAIGN AVERAGES OF TOTAL SNOW DEPTH, DEPTH HOAR AND WIND SLAB THICKNESSES. RESULTS ARE PRESENTED YEARLY FOR EACH CB CAMPAIGN BETWEEN 2015 AND 2019 (2019: 2 CAMPAIGNS) AND ARE AVERAGED FOR THAT PERIOD. TVC DATA FROM A SINGLE CAMPAIGN IS SHOWN IN THE SECOND LAST COLUMN. THE LAST COLUMN SHOWS THE OVERALL AVERAGE OF ALL SITES TOGETHER. Σ IS THE STANDARD DEVIATION, SNOW DEPTH IS GIVEN IN CM, ρ_s IN KG·M ³ . THE RI IS UNIT LESS. D _{DH} IS THE MEASURED DEPTH OF THE DEPTH HOAR AND D _{WS} THE MEASURED DEPTH OF THE WIND SLAB.	- 109 -
TABLE 5.4: THE TABLE SHOWS DATA FOR ALL PITS THAT HAVE A CORRESPONDING RADAR MEASUREMENT. THE LEFT COLUMN PRESENTS THE DATA FROM THE MANUAL MEASUREMENTS, WHEREAS THE MIDDLE (INDIVIDUAL RI, IRI) AND THE RIGHT COLUMN (GRI) SHOWS THE RADAR RESULTS. RESULTS IN THE RIGHT COLUMN (GRI) ARE BASED ON A GENERALIZED RI FROM THE PREVIOUS SECTION. THE LAST ROW SHOWS THE TOTAL SWE [MM].	- 111 -
TABLE 5.5: THE TABLE SHOWS THE RESULTS FOR THE DIFFERENT SNOW PARAMETERS AND ROUGHNESS FOR EACH ET.	- 113 -
TABLE 5.6: ADVANTAGES AND DISADVANTAGES OF THE FMCW MEASUREMENTS.	- 123 -
TABLE 6.1: IMPORTANT ACRONYMS FOR THIS CHAPTER.....	- 126 -
TABLE 6.2: RTK DSM ERROR, EXPRESSED AS RMS (ROOT MEAN SQUARED ERROR). FIRST THREE COLUMNS STAND FOR THE BASE STATION, AND THE LAST COLUMN FOR THE ROVER. ERRORS MUST BE SUMMED UP. THE VALUES ARE IN M.	- 134 -
TABLE 6.3: REFERENCE AND SIRA MEASUREMENTS FOR THE VALIDATION SNOW PIT.....	- 140 -
TABLE 6.4: THIS TABLE SHOWS THE RESULTS OF TSD MEASUREMENTS TAKEN OVER THE AREA OF SIRENE.	- 141 -
TABLE 6.5: COORDINATES OF THE GCPs.....	- 143 -

LIST OF ABBREVIATIONS AND SYMBOLS

A	= Ampere
ABS	= Acrylonitrile Butadiene Styrene
a.s.l.	= Above Sea Level
AUW	= All-up weight
AWS	= Automatic Weather Station
ASI	= Air-Surface-Interface
B	= Bandwidth
c	= Speed of light
CB	= Cambridge Bay
CHARS	= Canadian High Arctic Research Station
CW	= Continuous Wave
ϵ	= Dielectric Permittivity
ϵ_0	= Dielectric permittivity of a vacuum
ϵ'	= Capacity to store electric energy
ϵ''	= Dielectric loss
EF	= Electric Field
EM	= Electromagnetic
ET	= Ecotype
Δd	= Range resolution
DEM	= Digital Elevation Model
DF	= Decomposing and Fragmented precipitation particles
DFbk	= Decomp. and Frag. Precip. Particles, Wind-broken
DFdc	= Decomp. and Frag. Precip. Particles, Partly decomposed precip. particles
dGNSS	= differential GNSS
dGPS	= differential GPS
DH	= Depth Hoar
DHch	= Depth Hoar, Chained
DHcp	= Depth Hoar, Cups
DHla	= Depth Hoar, Large striated crystals
DHpr	= Depth Hoar, Prisms
DHxr	= Depth Hoar, Rounding Depth Hoar
DIY	= Do it yourself
d_s	= Snow depth
DSM	= Digital Surface Model
DSSM	= Digital Snow Surface Model
DTM	= Digital Terrain Model
f	= Frequency
f_0	= Initial frequency
f_d	= Doppler frequency
FBW	= Fly-By-Wire
FRQ-NT	= Fonds québécois de la recherche sur la nature et les technologies
IF _f	= Intermediate Frequency
IF	= Ice Formation
IFbi	= Ice Formation, Basal ice
IFil	= Ice Formation, Ice layer
IFic	= Ice Formation, Ice column

IFrc	= Ice Formation, Rain crust
IFsc	= Ice Formation, Sun crust
IGSO	= Inclined Geostationary Earth Orbit
IMA	= Intensive Monitoring Area
iRI	= Individual RI
FC	= Faceted Crystals
FCsf	= Faceted Crystals, Near surface faceted particles
FCso	= Faceted Crystals, Solid faceted particles
FCxr	= Faceted Crystals, Rounding faceted particles
GCP	= Ground Control Point
GEO	= Geostationary Earth Orbit
GLNOASS	= Globalnaya Navigazionnaya Sputnikovaya Sistema
GLW	= Greiner Lake Watershed
GNSS	= Global Navigation Satellite System
GPS	= Global Positioning System
gRI	= Generalized RI
GRIMP	= Groupe de Recherche Interdisciplinaire sur les Milieux Polaires
κ	= Dielectric constant
λ	= Wavelength
LIDAR	= LIght Detection and Ranging
LWC	= Liquid Water Content
FMCW	= Frequency modulates Continuous Wave
M	= Magnetic field
MEO	= Medium Earth Orbit
MF	= Melt Form
MFcr	= Melt Form, Melt-freeze crusts
MFcl	= Melt Form, clustered rounded grains
MFpc	= Melt Forms, Rounded polycrystals
MFsl	= Melt Forms, Slush
NE	= Net evaporation
NDVI	= Normalized Difference Vegetation Index
NSERC	= National Science and Engineering Research Council for Canada
P	= Precipitation rate
PLA	= Polylactic acid
PMW	= Passive MicroWave
PP	= Precipitation particle
PPco	= Precipitation particle, column
PPip	= Precipitation particle, ice pallets
PPir	= Precipitation particle, irregular crystals
PKC	= Polar Knowledge Canada
PPgp	= Precipitation particle, graupel
PPhl	= Precipitation particle, hail
PPnd	= Precipitation particle, needle
PPpl	= Precipitation particle, plate
PPrm	= Precipitation particle, rime
PPsd	= Precipitation particle, stellars and dendrites
MM	= Machine-Made snow
ρ_s	= Density of snow

PPK	= Post-Processing-Kinematic
PPP	= Precise Point Positioning
QZSS	= Quasi-Zenith Satellite System
R	= Resistance
Ro	= Run-off
RADAR	= RADio Detection And Ranging
R _x	= Receiving antenna
RT	= Ramp Time
RTK	= Real-Time-Kinematic
RG	= Rounded Grains
RGlr	= Rounded Grains, large
RGsr	= Rounded Grains, small
RGwp	= Rounded Grains, wind packed
RGxf	= Rounded Grains, Faceted rounded particles
RMSE	= Root Mean Square Error
ROI	= Region Of Interest
ROS	= Rain-on-Snow
RI	= Refractive Index
RPAS	= Remotely Piloted Aircraft System
RS	= Remote Sensing
S	= Slope of chirp
S _a	= Snow accumulation rate
SCE	= Snow Cover Extend
SfM	= Structure from Motion
SFOC	= Special Flight Operations Certificates
SHsu	= Surface hoar crystal
SHcv	= Surface Hoar, Cavity or crevasse hoar
SHxr	= Surface Hoar, Rounding surface hoar
SIRA	= Snow-and-Ice-radar
SIFT	= Scale Invariant Feature Transform
SIRENE	= Site Interdisciplinaire de Recherche en ENvironnement Extérieur
SO	= Specific Objective
SSI	= Snow-Surface-Interface
SWE	= Snow Water Equivalent
τ	= Time delay
T _{air}	= Air temperature
TIN	= Triangulated Irregular Network
TC	= Transport Canada
T _x	= Transmitting antenna
TG	= Temperature Gradient
TSD	= Total Snow Depth
TVC	= Trail Valley Creek
UAV	= Unmanned Aerial Vehicle
VIS	= Visible part of the electromagnetic spectrum
W	= Horizontal flux of drifting snow
WS	= Wind Slab

“Even if everyone agrees, everyone can be wrong.”

Bertrand Russel

1 INTRODUCTION

1.1 GENERAL INTRODUCTION

The cryosphere brings together all the regions with frozen water on planet Earth. It is part of the global climate system and is directly linked to the atmosphere. The cryosphere ranges from seasonal snow patches in low- and mid-latitudes, alpine regions with their glaciers, permafrost in the Arctic, to the giant ice sheets of Greenland and Antarctica with their surrounding sea ice.

A recent study by Rantanen et al. (2022) has shown that since 1979 the Arctic has warmed up up to four times as fast as the rest of the globe. This strongly affects ecosystems and society due to the interconnection between wildlife, vegetation, and snow (Tsang et al., 2022; Pörtner et al. (2022)). The two large ice sheets hold about 77% of Earth's freshwater (Barry and Gan, 2011), and their melting could have a significant impact on sea level rise (Golledge, 2020). The decline of sea ice opens new shipping routes (Wei et al., 2020) and areas to exploit resources (Morgunova, 2020). In regions with more human presence, changes are noticed as well and communities are confronted with cryosphere-related issues (transportation, health, economic, etc.).

Permafrost is thawing in many areas (Lyon et al., 2009) and a decrease of snow cover extent (SCE) and duration has been observed (Connolly et al., 2019; Mudryk et al., 2020). The seasonal variability of SCE and duration are at the core of many cryospheric processes modulating the surface energy balance of Arctic ecosystems. In the Northern hemisphere alone, snow can cover an area of 46.5 million km² in late January, but only 3.9 million km² in late August (Barry and Gan, 2011). These great seasonal changes, influenced by the underlying new climatic patterns, motivates research on monitoring the spatiotemporal distribution of snow.

1.2 MOTIVATION

In recent years, changes in the cryosphere have been observed globally, including in the three main cryospheric locations: the Arctic, Antarctica and Alpine regions. In the polar regions, an accelerated warming has been repeatedly reported over the last decades (e.g., IPCC 2019). According to Yamanouchi and Takata (2020), the rate of warming happens twice as fast in the Arctic compared to lower latitudes, a phenomenon referred to as the “Arctic amplification” (Serreze and Barry, 2011). Larger atmospheric circulation patterns like the North Atlantic Oscillation (Wanner et al. 2001), the Arctic Oscillation (Thomsen and Wallace, 1998; Baldwin and Dunkerton, 1999) and the Pacific Decadal Oscillation (Mantua and Hare, 2002) are affected as well. Changes in these large atmospheric circulation patterns have local consequences - for example, an increased occurrence of winter extreme events such as rain-on-snow (ROS) (Liston and Hiemsta, 2001; Rennert et al., 2009; Dolant et al., 2017; Langlois et al., 2017). Over the last 40 to 50 years, the Arctic amplification, caused by a series of climate-related feedbacks (Serreze and Barry, 2011; IPCC, 2019), was robustly linked to anomalies in SCE (Bormann et al., 2018; Mudryk et al. 2018; Thackeray et al. 2019) and to an increase in ROS events in the maritime regions of the Arctic (Callaghan et al., 2011; Langlois et al., 2017; Dolant et al., 2017).

Facing this accelerated warming, large ice caps are losing mass, with a prominent example being Greenland (Yamanouchi and Takata, 2020). Smaller ice caps and glaciers are also retreating in multiple locations such as in Svalbard (Van Pelt et al., 2021), in Canada (Kendall and Giles, 2019) and in South America (Meier, 2021). There is also a notable reduction of sea ice cover, especially in the northern hemisphere. For example, Stroeve and Notz (2018) reported an ongoing loss of arctic sea ice across all seasons. This was reported as well by Kwok (2018), based on a variety of retrieval methods including satellites and submarine-based measurements. The summer sea ice has declined by 45% for the last three

decades (Vincent, 2020) and the increase in air temperatures impacts polynya occurrence and duration (Couture et al., 2021). In turn this can influence ROS occurrence.

In addition to the decline of glaciers and sea ice, negative anomalies of terrestrial snow cover have been observed over the past few decades, which drastically impacts the cryospheric response to the Arctic amplification. Snow is a highly variable material (Rutter et al. (2014) and during winter, snow covers up to 80% of the land masses (Shi et al., 2016). This is of particular relevance to the surface energy balance given that snow has a high albedo (new snow reflects 80-90% of incoming radiation; Brown and Goodison, 2005) and low thermal conductivity (Sturm et al., 1997; Giese and Hawley, 2015; O'Neil and Burn, 2017) affecting soil, vegetation and the ecosystem at large. Slayter et al. (2022) describe snow as one of the most important factors governing the ecology of many terrestrial ecosystems. For example, snow moulds depend on snow cover for their survival to avoid freezing (Matsumoto, 2009) and bacteria living in the snow cover are considered one of the most important parts in the microbial diversity in the biosphere (Miteva, 2008). Snow beds play a key role as a later melt cause leaching of basic compounds from the upper soil horizon (Gargano et al., 2010). Also from a hydrological perspective, snow plays an important role. Levasseur et al. (2021) reported that in Northern Canada, snowmelt dominates the annual peak river discharge. Further, changes in melt onset, intensity and duration affect the hydrological systems. Studying Havikpak Creek, Northwest Territories (Canada), Krogh and Pomeroy (2019) suggest a 70% increase in peak Snow Water Equivalent (SWE) with a 9% shortening of the snow-on season and a 31% increase in snowfall by the end of the century.

The insulating effect of snow affects the freeze-thaw cycles (e.g., Park et al., 2014). A shorter snow cover duration exposes the bare ground earlier in spring, which results in a longer thaw-season for the permafrost (Woo et al., 2007). Thawing Permafrost has been observed worldwide (Romanovsky et al., 2010), and the impacts are significant for vegetation

growth (Ponomarenko et al., 2019). For example, Zhang et al. (2018) highlighted that shrubs in the Arctic tundra are increasing their relative dominance in tundra ecosystems and are spreading laterally on suitable sites. In succession, vegetation affects snow cover dynamics because different vegetation types among ecotypes (Ponomarenko et al., 2019) influence snow depth (d_s) and snow stratigraphy (Gacitua et al., 2013; Busseau et al., 2017; Park et al., 2018; Royer et al., 2021; Kramer et al., 2021).

The snow-related multilevel impacts of climate change will affect social, economic, and environmental drivers, which has gained more and more attention from policymakers. Reliable and permanent snow monitoring is needed to improve our understanding of how climate change shapes the cryosphere. Of special interest are the development of remote sensing retrievals and snow models, which simulate key snow state variables affecting surface energy balance, ground thermal regime, melt dynamics and hydrological processes. Snow plays a crucial role at numerous scales, its complexity stems from its high spatiotemporal variability and it evolves along with ongoing changes in vegetative and atmospheric patterns. But herein also lies the problem: how can we measure snow variability across scales over long periods of time? This question defines the core motivation of this thesis.

1.3 DEFINING THE SUBJECT

The direct *in situ* monitoring of snow in the Arctic provides the baseline for more advanced approaches in the development of snow models and remote sensing techniques that provide information on snow state variables. Dong (2018) reflects on strengths and weaknesses of three approaches and describes how they complement each other (Fig. 1.1). *In situ* measurements are robust and offer a high flexibility to implement new techniques, ideas, and sensors. Matching individual observations from different observers into a fully objective approach remains difficult; most techniques have been homogenized to some extent

(e.g., Pirazzini et al., 2018) with publications like the “International Snow Classification for Seasonal Snow on the Ground” (ICSSG, 2009). It standardized terms and descriptions by providing guidelines based on the work and practices of many researchers around the World.

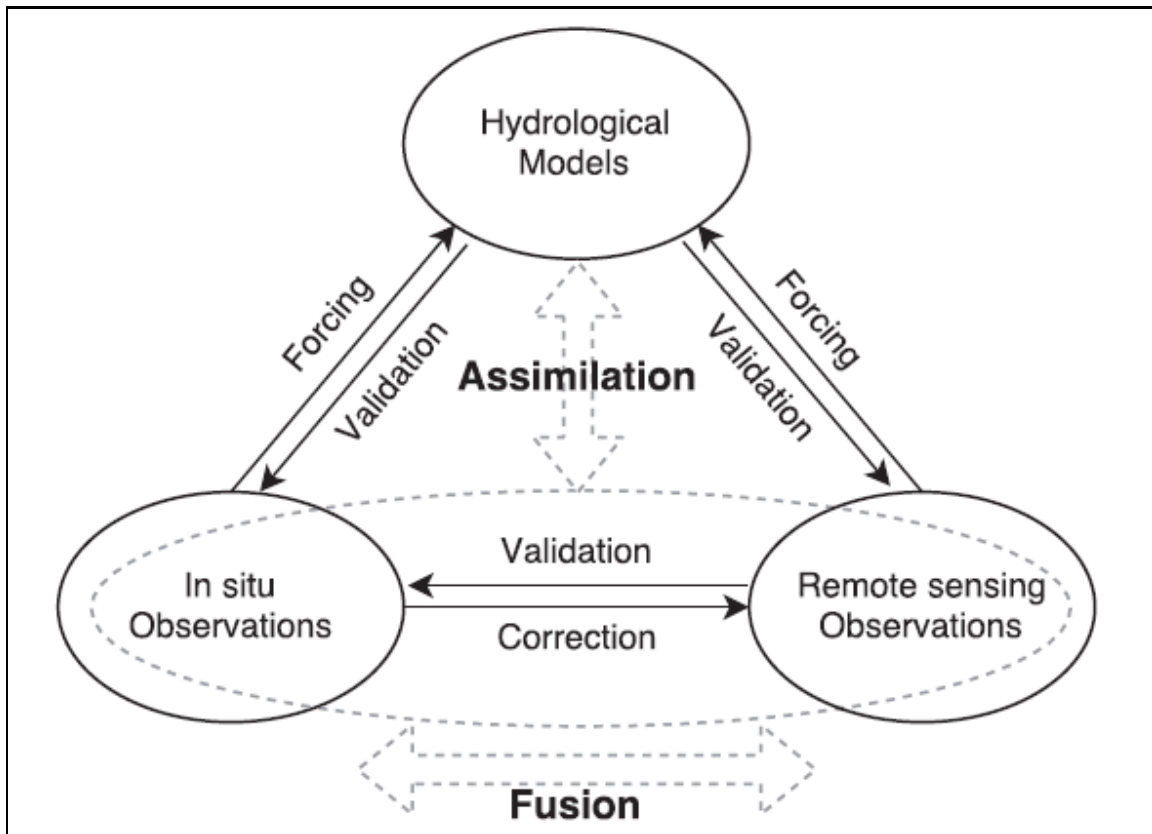


Figure 1.1: Relations and interactions between in situ observations, RS approaches and snow modelling (Dong, 2018).

Despite their importance, *in situ* measurements in the Arctic are scarce. The problem arises from the logistical and financial constraints of conducting fieldwork, further amplified for operations in the Arctic (e.g., Zweng et al. 2018; Bergstedt et al. 2018). The distribution of weather stations in Canada (Fig. 1.2) demonstrates this par example. The network of stations in the South, with a high population density and near the US-border, is dense. This network thins out towards the North where often a single station has to represent a large, sparsely inhabited regions.

Data scarcity restrains both snow model and satellite retrieval development given that numerous processes (e.g., metamorphism, compaction) are empirically driven. To date, no snow model specifically developed for the Arctic exists (Domine et al., 2019) and it is necessary to utilise models developed for alpine applications. In a similar fashion, the lack of data inhibits the improvement of remote sensing algorithms (Tsang et al., 2022) as it is difficult to define in one parameter the complexity of Arctic snow (Meloche, 2022). Maps of snow depth would greatly improve the certainty for both approaches (Meloche, 2022; Langlois, 2022).

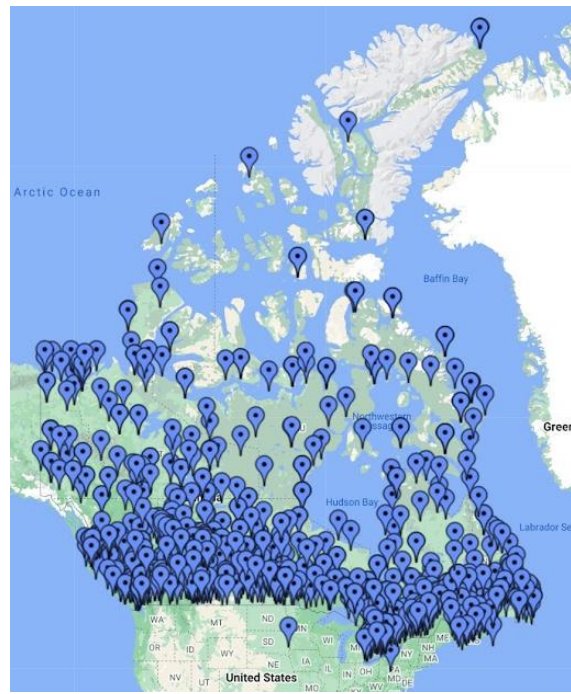


Figure 1.2: Environment and Climate Change Canada network of automatic weather stations (as of 2022-11-12).

In the past decade, the scientific community progressed significantly to fill gaps with an improved empirical understanding of snow processes implemented in models (e.g.: albedo properties: Larue et al., 2020; snow metamorphism: Madore et al., 2018; vegetation effect: Gouttevin et al., 2018; thermal conductivity: Domine et al., 2019). The data allows simulating snow conditions in remote and inaccessible regions (Dong, 2018). The scarcity of data from polar regions has led to serious limitations for developing Arctic applications (Gouttevin et al., 2018; Domine et al., 2019) and snow representation in climate models (Langlois et al., 2014). The lack of data can lead to problems as shown by Domine et al. (2019), reporting issues in simulating snow density profiles for Arctic conditions. However, remote sensing and models could be used to fill observational gaps at various scales when driven and developed with sufficient training and validation *in situ* data.

Modern satellite missions like the PLÉIADES 1 constellation can capture images of the Earth's surface with a resolution of 0.7 m if set to panchromatic mode (EOS, 2021), which delivers a picture sampled over the full visible (VIS) electromagnetic spectrum. The VIS spectrum ranges roughly from 400 nm to 800 nm and the human eye perceives these wavelengths as different colours. In the past, the revisiting time of a satellite over a specific area had been a limiting factor, which was solved with constellation missions. Satellite missions operating in the VIS are restrained by three factors: 1) they are limited to deriving SCE only, 2) atmospheric conditions must be cloud-free, and 3) measuring is only possible during daylight hours. To bridge this gap, satellites and applications using the microwave spectrum have been developed. Microwave sensors are independent of sunlight and can penetrate through cloud layers. The GLOBSNOW project utilizes several sensors at 19 GHz and 37 GHz to deliver d_s and SWE at a resolution of approximately $25 \text{ km} \times 25 \text{ km}$ (GLOBSNOW, 2021). SWE describes the amount of liquid water stored in the snowpack and is crucial to understand and predict the momentary and future state of ecosystem hydrology, where snow is often the main freshwater source (Levasseur et al., 2021). Other publications cover space-borne approaches, e.g., by Chang et al. (1982), Kelly (2009) and Takala et al. (2011), all focusing on the microwave domain used for large-scale monitoring. However, the coarse resolution of these tools can cause problems when studying processes at the local scale and leads to systematic biases in the retrievals (e.g., Foster et al., 2005; Larue et al., 2017; Meloche et al., 2021).

The problems caused by coarse spatial resolution (passive microwaves) or bad atmospheric conditions (optical approaches) can be tackled with an active sensor like a radar (RADio Detection And Ranging), or by lowering the sensors using airborne platforms. As aircraft campaigns are expensive, they are usually not used to monitor changes over time but only during specific campaigns focused on process studies or algorithm development. As

such, previous work focused on using airborne passive microwaves to drive radiative transfer models (Langlois et al., 2008; Langlois et al., 2012) and assimilate satellite observations to drive snow models (Che et al., 2014; Larue et al., 2018). With regards to radar missions, currently no mission dedicated to snow monitoring exists. Radars do, however, deliver better spatial resolution and, because they are sensitive to the dielectric contrast of snow, information on microstructure can be retrieved at certain frequencies. The issue concerning local snow monitoring remains therefore currently unaddressed.

Broadly introduced in recent years, a new platform perfectly addresses the gap between aircraft campaigns (which are expensive) and ground-based measurements (which are spatially limited). This new platform - Remotely Piloted Aircraft Systems (RPAS), known to the wider public as either drone or UAV (Unmanned Aerial Vehicle) - combines the advantage of low flight altitudes (increased resolution) with cost effectiveness and a high flexibility to carry numerous payloads addressing various scientific needs. With RPAS, the repeatedly stated need for high-resolution data (e.g. Bokhorst et al., 2016) can be answered. The availability of RPAS technology has resulted in numerous publications on different geoscientific topics (e.g., Fernandes et al., 2016; Anderson et al., 2019; Chudley et al., 2019; Kramer et al., 2019). RPAS deploy easily, become increasingly popular in the private and the industrial sectors, and regulations are nowadays streamlined. Basic RPAS usually have a digital VIS-camera and can cover much larger areas (Jo and Kwon, 2019) than the traditional method (snow pit). For example, using VIS-cameras mounted on a RPAS combined with the Structure from Motion (SfM) technique has shown good results to derive d_s (Fernandes et al., 2016; Kramer et al., 2019). This motivated the first part of this PhD project, which provides a detailed technique to develop and use a RPAS for snow monitoring and that can handle the harsh arctic winter environment. Two limiting factors arise from this: 1) such approach requires at least two missions (snow-off and snow-on), and 2) it can only deliver d_s

and SCE (no information on the microstructure). Therefore, the second part of this thesis focused on developing an algorithm capable of retrieving Arctic snow stratigraphy using a small, portable radar. The focus lay on developing an approach that required no *a priori* snow information during field campaigns and that is portable enough to be mounted on a RPAS. The final step was then to develop a mapping approach combining the radar-based approach for snow measurements with a high-precision geolocation module (differential Global Navigation Satellite System, dGNSS). While meeting these approaches would support the development of snow models and satellite retrieval techniques, it would also allow for mapping snow characteristics with an adequate resolution using interpolation techniques.

1.3.1 Objectives and hypotheses

The overarching objective is to develop and validate a high-resolution snow monitoring system capable of mapping snow depth (d_s), Snow Water Equivalent (SWE) and stratigraphy in harsh arctic environments. The system must be non-destructive, easily deployed, easily transported, low-cost and operational in frigid temperatures. This main objective motivates the hypotheses and specific objectives:

1.3.1.1 Hypothesis 1 and specific objectives 1

Hypothesis: Technology has advanced to a point that non-engineers can design and build a cost-effective and durable RPAS capable of operating in polar conditions and delivering science-grade data.

Specific objective 1: a) to design, build and test a Do-It-Yourself (DIY) RPAS focusing on durability and flexibility for arctic conditions; b) to deliver accurate d_s information of the arctic winter snowpack using the DIY RPAS and SfM.

1.3.1.2 Hypothesis 2 and specific objectives 2

Hypothesis: It is possible to extract diagnostic geophysical properties of arctic snow from a Frequency Modulated Continuous Wave (FMCW) radar without resorting to a snow pit for every measurement.

Specific objective 2: a) to develop a retrieval algorithm for a FMCW radar to retrieve snow stratigraphy and d_s without using direct snow measurements; b) to validate results by using snow measurements from two regions of the Arctic; and c) to evaluate statistically the influence of the underlying ecotype on the radar.

1.3.1.3 Hypothesis 3 and specific objectives 3

Hypothesis: It is possible to retrofit the FMCW radar system with a dGNSS module to reach a geolocation precision sufficient for extracting several Digital Surface Models (DSMs) for mapping d_s and microstructure.

Specific objective 3: a) to retrofit the FMCW radar system with a high precision dGNSS module; b) to validate interpolated snow information and investigate differences and similarities of the different mapping approaches; c) to optimize data collection by addressing major difficulties while conducting fieldwork with limited infrastructure available.

1.4 THESIS OVERVIEW

The thesis is structured into seven chapters. This first chapter provides a general introduction along with the motivations of this work. Chapter 2 provides scientific background on snow, electromagnetics, and their interactions. In the third chapter, the

methods are presented in general terms whereas a detailed methodology is included in each of the results chapters, of which two are peer-reviewed publications. The third chapter also presents the study sites and the datasets.

Chapters 4, 5 and 6 put forward the results related to the three specific objectives. Chapter 4 presents the first scientific article (Aqhaliat Report, in print) on the RPAS design (specific objective 1) and chapter 5 the second scientific article (Cold Region Science and Technology, under review) about the FMCW algorithm (specific objective 2). Finally, chapter 6 is on the snow mapping capabilities of the FMCW radar using interpolation techniques (specific objective 3). The seventh and last chapter concludes and gives a perspective for future work and developments.

2 BACKGROUND

This thesis primarily aims to describe how to monitor snow state variables from a geospatial context. The first section of this chapter, I describe snow formation and metamorphic processes, focusing on the Arctic snowpack and its evolution. This is followed by a description of the basic concepts of electromagnetic (EM) waves and radar technology. In the last section, I describe snow in the microwave region of the EM spectrum.

2.1 SNOW

This section provides information on snow - how it forms and accumulates, its life cycle, physical properties, processes, and spatiotemporal distribution.

2.1.1 Formation

Snow manifests as a form of precipitation and usually originates from clouds. These can form under different circumstances. A well-known example of cloud formation occurs when an air parcel rises, saturates (water vapour), and then condensates (Kraus, 2000). Condensation cores allow for water droplets or ice crystals to form (average size 10 μm) (Kraus, 2000). Suspended in the air, droplets travel over large distances. If the temperature inside a cloud falls $<-5\text{ }^{\circ}\text{C}$, ice crystals form and turn into snowflakes, following a nucleation process (Kraus, 2000). Two types of nucleation mechanisms exist: heterogeneous and homogeneous. The latter marks a spontaneous process in very cold clouds ($<-36\text{ }^{\circ}\text{C}$) when ice crystals form from supercooled water droplets (Langlois and Barber, 2007; King, 2014). The former includes three processes: deposition of water vapour, immersion freezing and contact–collision (Langlois and Barber, 2007).

Once the ice crystals grow beyond the size of 100 μm (e.g., by collision with other droplets), they reach a falling speed of 0.8 m s^{-1} and precipitation occurs. Whereas the process is called precipitation, the droplets are described as hydrometeors, even before they start

falling towards the surface of the Earth (Kraus, 2000). The shape of the ice crystal depends on air temperature whereas the level of supersaturation will define the complexity of the crystal (Nakaya, 1954; Libbrecht, 2005). Fig. 2.1 shows the Nakaya diagram, which describes the influence of temperature and humidity on the shape of the forming snow crystals and links the diagram to the International Classification for Seasonal Snow on the Ground (ICSSG, 2009).

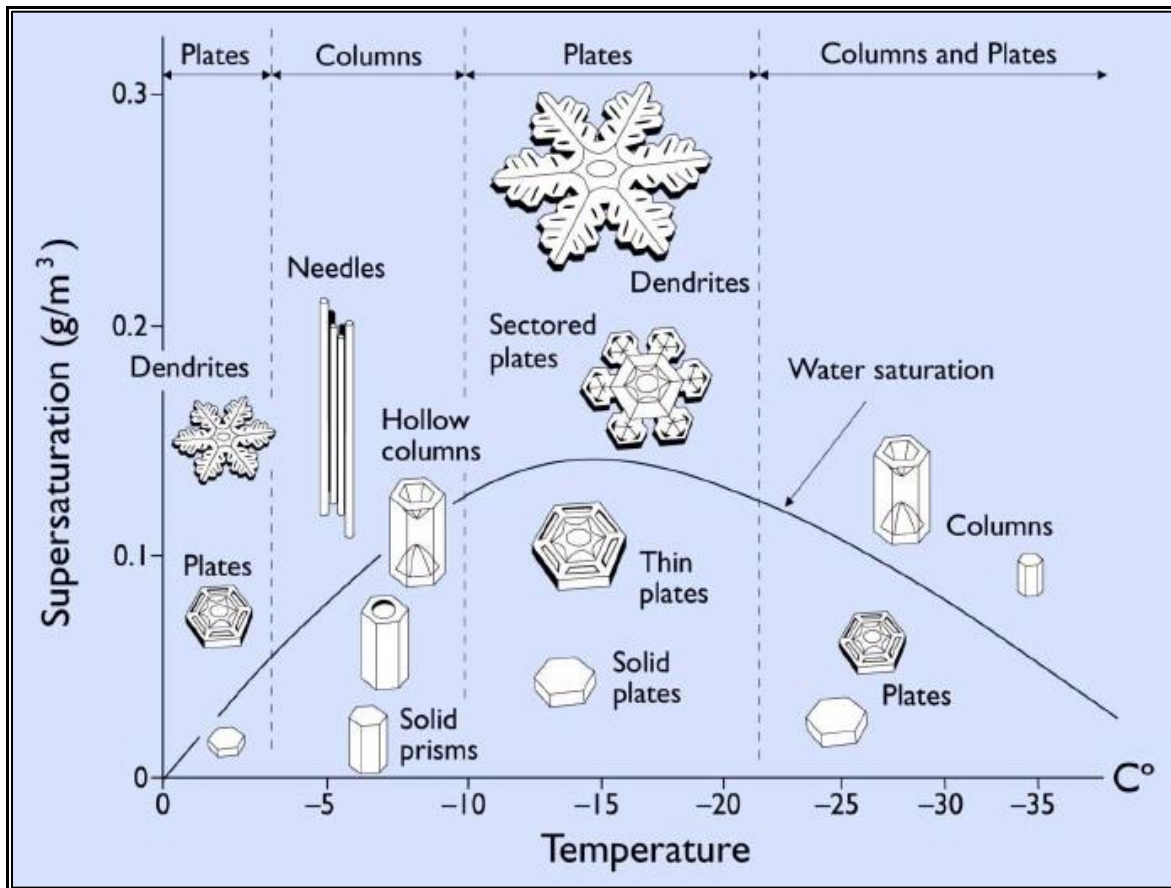


Figure 2.1: The Nakaya diagram describes how temperature and humidity influence the shape of the snow crystal.

With the exception of Rime (PPrm), which is the accretion of supercooled droplets on the ground, all precipitation particles (PP) form inside clouds (ICSSG, 2009). If supersaturation is low and T_{air} is between 0 and -3 °C or below -8 °C, plates (PPpl) will form. If T_{air} is between -3 and -8 °C or below -30 °C, columns (PPco) occur. If supersaturation is high, needles (PPnd) form either between -3 and -5 °C or below -60 °C. The classical snowflake occurs between 0 and -3 °C or between -12 and -16 °C. It is referred to as PPsd,

which stands for stellars and dendrites. If environmental conditions change during the formation, irregular crystals (PPir) appear (ICSSG, 2009). If heavy riming occurs on the still airborne snow crystals, it is defined as Graupel (PPgp) if the size is ≤ 5 mm and as Hail (PPhl) if the size is >5 mm. The last precipitation particle class are Ice pellets (PPip), which can either form from freezing raindrops, refreezing of largely melted snow crystals/flakes or PPgl enclosed in a thin ice layer (≤ 5 mm) (ICSSG, 2009). Whereas PPgp and PPip can occur in the Arctic, PPhl usually forms in thunderstorms.

2.1.2 Accumulation and metamorphism

Once the PP reach the surface of the Earth, they accumulate and form a snowpack. The snow accumulation rate can be defined (adapted from Bromwich, 1988) as

$$S_a = P - NE - \Delta W - Ru \quad (\text{Eq. 2.1})$$

where S_a refers to the snow accumulation rate, P is the precipitation rate, NE the net evaporation, W the horizontal flux of drifting snow, and Ru , the run-off (adapted from King and Tuner, 1997).

Snow crystals undergo a constant evolution as changes in temperature, humidity and wind speed affect the processes that determine the state of the snow (pack). The metamorphism processes are reflected in the different crystal types that are defined in the ICSSG (2009). This classification has been used as a basis for the following section and as it plays no role for this work, the class of Machine-Made snow (MM) is not discussed.

Decomposing and Fragmented precipitation particles (DF) are the first metamorphic stage evolving from PP. It distinguishes between Partly decomposed precipitation particles (DFdc) and Wind-broken precipitation particles (DFbk), which are quite common in harsh arctic environments. DFdc have the perceptible shape of the initial PP, but often first rounding has occurred. The speed of the decomposition is depending on the temperature gradient (TG) of the snowpack where a low gradient will enhance rounding of the grains

through sublimation. This decreases the specific surface area (SSA) of the grains. The SSA is defined as the total surface area of the air/ice interface per unit mass of a snow sample (ICSSG, 2009). The decrease of the SSA reduces the surface free energy which initially decreases the layer strength due to decomposition, but over time it regains cohesion due to sintering. Sintering describes the process of compacting the snowpack by which snow and ice crystals bond together with air temperatures $< 0^{\circ}\text{C}$ (Ramseier and Keeler, 1966).

If the wind speed is up to 10 m s^{-1} , saltation of the snow crystals occurs, and the crystal type is identified as DFbk. Pomeroy and Gray (1990) describe saltation as a horizontal movement of snow on up to a few cm high curved trajectories over the ground. Due to the impacts caused by the movement, the ice crystals break, form new bonds and the snowpack will increase in density. This process is often followed by rounding and is common in the Arctic. It is the initial stage of the Wind Slab (WS), a very hard and dense surface layer which is a common feature in many Arctic regions and plays an important role in this thesis.

From the DFbk, in which rounding has sometimes already started, the Rounded Grains (RG) class RGwp (Rounded grains wind packed) evolves. It is a surface layer of dry snow that develops either into a hard but thin wind crust or a thicker WS. With increasing wind speeds or decreasing particle size, the hardness increases as well. The small size of the particles and the high amount of contact points lead to a high layer strength, which is amplified through sintering. Wind crusts are thin irregular layers that are buried over time and thus can be found deeper in the snowpack when compared to WS which are usually thicker.

Small (RGsr) and Large (RGlr) rounded particles are distinguished by size. If the crystals are $< 0.25\text{ mm}$, RGsr are present. The right side of Fig. 2.2 show RGsr. This type forms under the absence of a strong TG where a decrease in the SSA leads to an overall decrease of the grain diameter. Under such a weak temperature gradient (between 0.1 to

0.3 °C m⁻¹; Colbeck, 1982; Colbeck, 1983; Sturm et al., 2002) the snow is governed by equilibrium metamorphism. This type of metamorphism is characterised by a decrease in SSA where the convex areas of the grains will sublime and mass accumulate in concave areas (i.e. rounding), which in turn will lead to sintering promoting the densification of the layer.

This leads to RGlr, which forms by grain-to-grain vapour diffusion but with the vapour density remaining under the threshold for kinetic growth. Both types grow faster with increasing temperatures but grow slower within very dense snowpacks. Both processes occur in the Arctic snowpacks.

Especially during the coldest parts of the year, the Arctic has strong TG between the air and the frozen ground. With increasing TG, Faceted rounded particles (RGxf) evolve. These are rounded grains that start to develop facets. In addition to the TG, the vapour density needs to exceed a critical point for Faceted Crystals (FC) to develop.

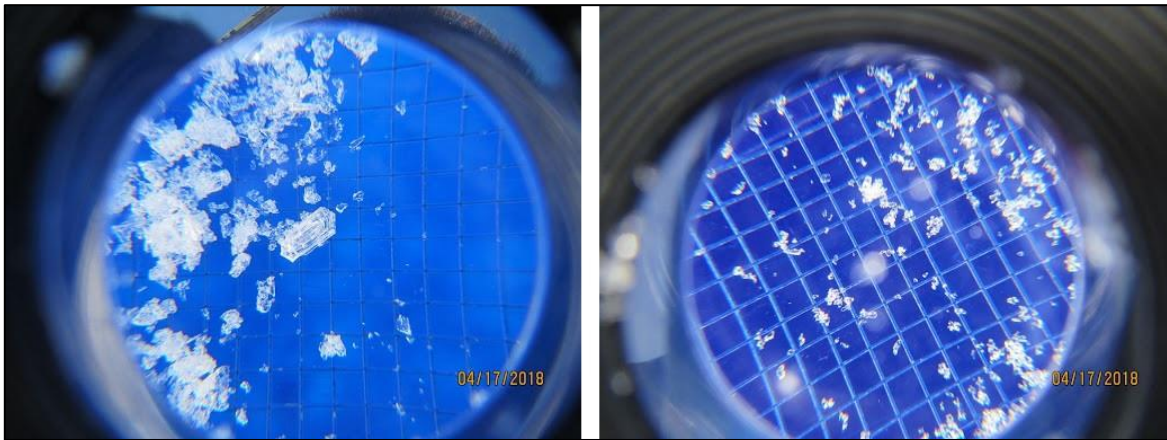


Figure 2.2: Crystals of a DH (left) and RG (right). The latter is a typical grain found in WS. Pictures taken by Simon Levasseur.

Similar to RG, FC forms in dry snow. Dry snow is defined with a Liquid Water Content (LWC) of 0 and occurs at temperatures ≤ 0 °C but is usually well below freezing. If the snow temperature reaches 0 °C but no water is visible under 10x magnification, the snow is considered moist and sticks together when compacted (ICSSG, 2009). The volume fraction is between 0-3 %. If water is visible under magnification but can not be pressed out, the snow

is considered wet with a volume fraction of 3-8 %. This regime is called pendular. Once water can be pressed out of the snow by squeezing, the regime changes to funicular and the snow is considered very wet with a volume fraction of 8-15 %. If 15 % are exceeded, the snow is considered soaked. Melt Forms (MF) occur if liquid water and temperatures above freezing occur. The clustered rounded grains (MFcl) appear if the snow is wet at a low water content (pendular regime). The clusters form to minimize the surface free energy. Rounded polycrystals (MFpc) form after several melt-freeze cycles, which also increases the particle size. In both cases (MFcl and MFpc) an increase in LWC leads to Slush (MFsl), which is wet snow with a high liquid water content (funicular regime). This happens if the water drainage is blocked. At the surface, Melt-freeze crusts can form (MFcr). This form occurs if rain, or melt water wets the snowpack and then refreezes.

As the process is reversible, RGxf evolves into FC but also the FCxr (Rounding faceted particles) into RG. The rounding of the FC starts if the TG decreases. It reduces the SSA while corners and edges are rounded off. Near surface faceted particles (FCsf) develop from RG or other FC classes but can also form from PP or DFdc if a large TG is present near the surface. In the early stage of the development, Solid faceted particles (FCso) form. FCso are the main FC class and are characterised by solid crystals with sharp edges and corners and glassy, smooth faces. The growth rate increases with temperature and the strength of the TG. If the TG persists, the next class of dry snow crystals forms: Depth Hoar (DH). This layer is present in many Arctic snowpacks and plays an important role for this thesis as well.

The lowest layer in the Arctic snowpack is the DH. It can be identified by a grain size of several mm (Fig. 2.2, left). In winter, the air temperature remains low during extended periods of time (Sturm and Benson, 1997). If the TG persists and intensifies, a DH develops (King, 2014) under a minimum temperature gradient of $10\text{--}20\text{ }^{\circ}\text{C m}^{-1}$ through a process called kinetic growth metamorphism to set in (Colbeck, 1982; Miller and Adams, 2009).

Thermally insulated from cold air temperatures by the WS, the temperature of the DH is warmer and thus these TGs can exist over extended periods. The TG can increase when cloud-free conditions are present, and the surface is cooling further due to radiative cooling. Radiative cooling describes the loss of heat if longwave radiation is directly transmitted into space without atmospheric interactions. The density (ρ_s) of DH varies around 250 kg m^{-3} with a typical height of 15 cm (Royer et al., 2021).

In general DH forms by grain-to-grain vapour diffusion. In addition to the large TG, the excess vapour density must be high enough to favor kinetic growth. With similar conditions required as for FCso, the Depth Hoar Hollow cups (DHcp) form. If the high TG continues and the snow completely recrystallizes into low density snow, Hollow prisms will form (DHpr). Under similar conditions, Chains of depth hoar (DHch) may form over time. The crystals arrange themselves during the metamorphism in vertical chains with few lateral bonds. The final stage, which takes the longest period of time to form and can grow from any of the previous stages, are the Large striated crystals (DHla). Whereas the previous stages decreased in bonding (strength), this type regains some strength due to new crystal initiation. DH and FC crystals in polar snowpacks can exceed a density of 300 kg m^{-3} and is then referred to as hard or indurated DH. In the absence of a TG, DH may revert to RG as they start to round off again. This affects all DH classes but once the rounding has started, the class is referred to as Rounding depth hoar (DHxr). The process reduces the SSA and the crystals round off at corners and faces lose their relief.

Surface hoar crystals (SHsu) form if the snow surface is cooling below T_{air} whereas the relative humidity of the air increases. The crystals grow via kinetic growth via transfer of water vapour towards the snow surface. If the TG decreases, the crystals start to round and Rounding surface hoar (SHxr) appears. Cavity or crevasse hoar (SHcv) form near cavities if water vapour can be deposited under calm, still conditions.

Ice Formations (IF) emerge either from rain or melt events. Ice layer (IFil) can be found if rain or melt water percolates into a cold snowpack and refreezes. This type usually keeps some permeability. Ice columns (IFic) require draining water within flow fingers, which describe a vertical path of water transport through the snowpack. Highly stratified snowpacks and cold temperatures favor this development. Basal ice (IFbi) forms at the bottom of the snowpack if the layer is impermeable. A rain crust (MFrc) appears if freezing rain hits the snow. It forms a thin and transparent layer. Similar in appearance is the sun crust (IFsc), which forms if melting occurs at the surface and then refreezes by radiative cooling. Thus, this form builds during clear weather with intense solar radiation.

2.1.3 The Arctic snowpack

In the previous section I described the formation and accumulation of snow in the atmosphere, its distribution on the ground and metamorphic processes. In my thesis, the two dominant layers of the arctic snowpack, Depth Hoar (DH) and Wind Slab (WS) (Fig. 2.2), play a crucial role. As DH has been discussed in detail before, the following section will describe the WS in more detail.

Compared to the DH layer, the WS has a higher ρ_s (around 300 kg m^{-3}) and can consist of multiple grain types. The thickness of this layer varies and can reach more than 30 cm. The WS is forming from freshly fallen snow ($\rho_s = 50\text{--}150 \text{ kg m}^{-3}$, Pomeroy et al., 1998) and requires sustained periods of wind (King, 2014). A snowpack continuously exposed to such winds forms a WS, which is the regular case for many polar regions. The wind redistributes the snow via wind drifting which is one of the major factors governing snow depth variability (Meloche et al., 2022; Groot Zwaafink et al., 2013). Depending on the wind speed, three types of transport are distinguished. The earlier described saltation is responsible for about 80 % of the total snow drift (Langlois, 2007). Experiments from Summer et al. (2017) suggest that this is a necessary condition for wind-packing, but they

also state that not all drifting snow events lead to wind crusts. For wind speeds $< 5 \text{ m s}^{-1}$, creeping is the main mode of transport. The crystals are rolling over the surface and account for about 10 % of the total snow drift (Langlois, 2007). In their experiments, Kosugi et al. (1991), found similar behaviour. At 5 m s^{-1} , snow ripples are forming, and they estimate at least 6 % of the total snow drift can be allocated to creeping. The final 10 % of snow drift, called turbulent diffusion, is attributed to higher wind speeds (Langlois, 2007).

2.1.4 Seasonal life cycle and spatial variability of the Arctic snowpack

Throughout the seasons, the snowpack undergoes several stages. In the northern hemisphere, snowfalls start between autumn and winter, depending on the latitude and the local conditions. During this season, the insulation properties of the fallen snow have a significant impact on the surface energy balance. This is explained by a low thermal diffusivity as the snow traps a proportion of air (Langlois and Barber, 2007). The insulation can increase the ground thermal regime by several degrees Celsius (Goodrich, 1982) and protects the vegetation below from the cold air temperatures. The first part of the winter, before it reaches the lowest air temperatures, is a cooling period. In the Arctic, this period is marked by a large variety of snow depths, which consequently influences the thermodynamic state of the snow (Langlois et al. 2007). Due to the low temperatures and a very dry environment, wind and topography are the main processes behind the variability of d_s (Meloche et al., 2022). Once winter reaches its lowest temperatures, the TG metamorphism becomes the dominant process governing snow microstructure (Langlois and Barber, 2007). Increasing air temperatures characterize the spring season (Serreze et al., 1993). During the progression throughout spring, the hours of daylight increase and thus the amount of solar irradiation arriving on the surface increases as well. With the beginning of the melt season, the albedo of tundra snow drops rapidly (Grenfell and Perovich (2004). This is followed by

the advanced melt, which is characterised by a snowpack saturated with water where frequent rain events speed up the melting (Dolant et al., 2017).

Many studies have focused on the SCE (Brown, 2000; Cherkauer and Lettenmaier, 2003; Dyer and Mote, 2006; López-Moreno et al., 2013). SCE has a very high spatio-temporal variability, rendering its monitoring quite difficult at all scales. On flat terrain, the snow cover appears level and even, but measurements of d_s reveal a different picture. As recently shown by Meloche et al. (2022), the variability is linked to wind and topography. Hills and other, more distinct features of the landscape are not always fully covered by snow. Due to the lower albedo, these darker areas warm up faster once more incoming radiation arrives on the surface.

2.2 RELEVANT ELECTROMAGNETIC CONCEPTS

EM waves and their propagation are central to many remote sensing theories and applications. In this section, I describe the basic concepts of EM waves, and how they apply to radar RS and GNSS-based surveying.

The EM field combines an electric field (EF) and a magnetic field (M) that travel almost at the speed of light c ($c_{\text{air}} = 299702547 \text{ m s}^{-1}$, $c_{\text{vac}} = 299792458 \text{ m s}^{-1}$) and are perpendicular to each other. Besides their travel speed c , EM waves are characterized by frequency (f) and wavelength (λ). The frequency describes the number of oscillations an EM wave cycles through per second and is expressed in hertz (Hz). The wavelength describes the length between two peaks of an EM wave's cycle and is related to the frequency and speed of light (c) such that:

$$f = \frac{c}{\lambda} \quad (\text{Eq. 2.2})$$

Snow consists of H_2O dipolar molecules. The two hydrogens (H) are connected to the oxygen (O) at a 104.5° angle. Though resulting in a neutral charge, the molecule has a positively and

a negatively charged side. As the EM wave travels through the material, the EF excites the electrons (charge carriers) of the molecule and aligns them (in: Langlois [2007], after Jonscher [1996] and Baker-Jarvis [2000]). Once the wave has passed through, the molecules return to their initial state during a period called “relaxation time” (Logsdon and Laird, 2004). This relaxation time is the temporary delay in the dielectric constant (κ) and depends on viscosity, temperature, and the frequency of the applied electric field (King, 2014). κ is the ratio of the electric permittivity of the material (ε) to the electric permittivity of a vacuum (ε_0) and is defined as

$$\kappa = \frac{\varepsilon}{\varepsilon_0} \quad (\text{Eq. 2.3})$$

The permittivity of the material can be expressed as

$$\varepsilon = \varepsilon' + \varepsilon'' \quad (\text{Eq. 2.4})$$

with ε' expressing the capacity of a material to store energy and being polarized. ε'' denotes the dielectric loss. This describes the capability of the extinction of the incoming energy (Langlois, 2007; King, 2014). Polarization explains how E is oscillating along the direction of propagation.

The theoretical concept assumes that an EM wave propagates in a vacuum. In this project, I work with EM waves interacting with snow and thus I need to adjust for it by using the Refractive Index (RI). For dry snow, the RI is determined by ρ_s (Warren, 2019). This will be explained in more detail later on.

The loss of incident energy is described by the process of absorption and is an important factor considering microwave propagation in the snowpack. With increasing permittivity or increasing LWC, absorption increases as well (Williams et al., 1990). The incoming microwave is partially scattered at the surface. This process is governed by the roughness of the surface and the differences in the dielectric properties of the material (King,

2014). The part of the energy that is not reflected, transmits into the snowpack and changes the incident velocity and direction (Venkataraman et al. , 2007).

2.2.1 Radar

RADAR (Radio Detection And Ranging) uses EM waves to determine the distance to an object. Different types of radar exist, and they have wide technical applications (weather observations, airspace control, navigation, threat detection, etc.). This paragraph introduces the basic concept of a radar system and its relevant characteristics for this project.

2.2.1.1 Pulse radar

The pulse radar probably exemplifies the best-known type of radar, and the underlying principle perfectly illustrates the basic idea of a radar. We know that an emitted EM pulse is constantly travelling at the speed of light and is reflected at objects in the distance (PRadar, 2022). A radar system uses a transmitter to create an energy pulse at t_0 and then emits it into space via the antenna (PRadTut, 2022). The size of the pulse increases along with the distance, an important factor for footprint considerations. The footprint describes the area of illumination on the ground once the pulse arrives. At the same time as the radar switches the antenna to receiving mode, the pulse travels with c towards an object (PRadTut, 2022). Once it reaches the object (t_1), the pulse is reflected towards the receiver. When the pulse reaches the receiving antenna (t_2), the difference in time is calculated and we can determine the distance using c and dividing the result by 2 (two-way travel time) (PRadTut, 2022). If the medium is not a vacuum, the distance must be corrected with the RI.

Given that this thesis work uses a radar close to the surface (usually $< 1\text{m}$ above ground) to detect changes in the stratigraphy, a pulse radar is not suitable as the pulse length determines the minimum operational range. To achieve a resolution of 3 cm , the pulse length would need to be as short as 1^{-10} s whereas a short radar pulse is defined in the range of 1^{-6} s

(PRadar, 2022). Thus, another type of radar is required that allows to measure objects that are very close.

2.2.1.2 CW radar

A Continuous Wave (CW) radar emits a continuous wave instead of a single pulse. The CW radar measures the change of rate of the target's range (target velocity) by measuring the doppler shift of the returned signal (Engineering Funda, 2017). The doppler shift describes the change of frequency of the EM wave based on the motion of the transmitter, target or both (BrainGrain, 2018). Fig. 2.3 explains the principle.

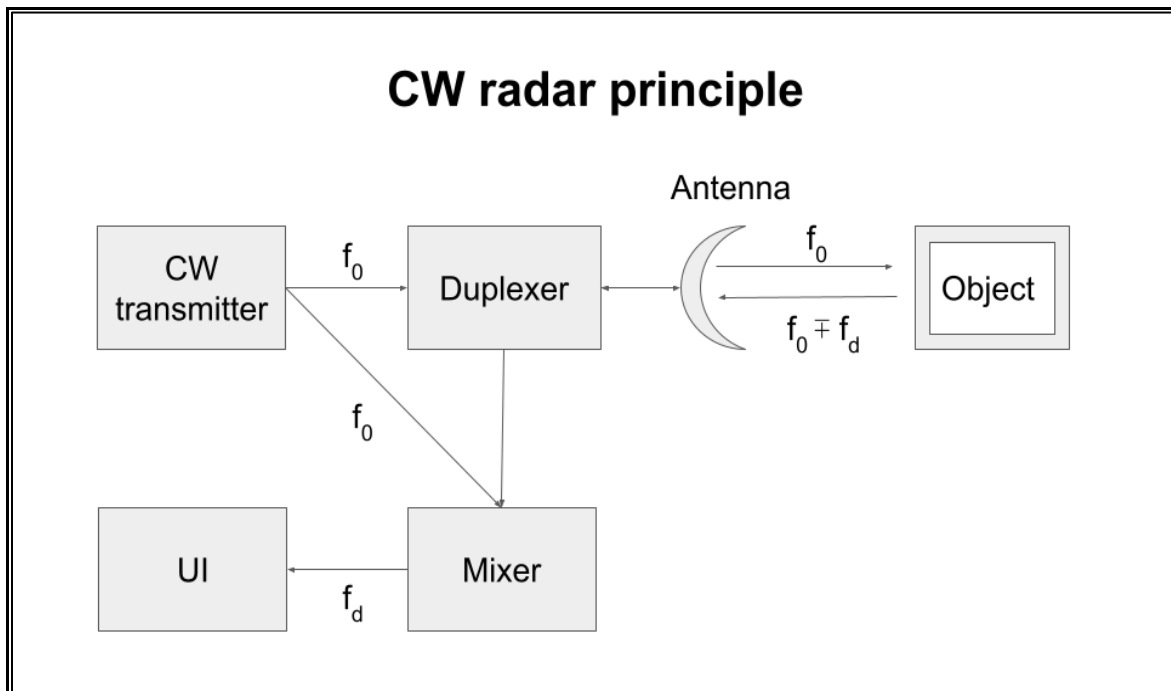


Figure 2.3: CW principle. The CW transmitter continuously emits an EM wave f_0 . Via the duplexer, the signal is sent by the antenna towards the object. The duplexer switches the antenna from transmit to receive and the antenna will receive the returning signal. The mixer receives f_0 and $f_0 \mp f_d$. Then it isolates f_d , which is shown e.g. on the User Interface (UI). If the antenna is stationary, this equates to the target's velocity. Adapted from Engineering Funda (2017).

The CW radar only assesses f_d (doppler frequency), thus it can't evaluate the distance to the target as f_d is depending on a relative change of distance between radar and object. If f_d is added (+) to f_0 , it means that the distance between radar and object is decreasing. In case it is subtracted from f_0 , the distance has increased (Engineering Funda, 2017). As the CW radar

can't determine the range to an object, a modified version of this radar type is necessary. By modulating the frequency of the signal during the measurement, range detection is possible.

2.2.1.3 FMCW radar

A Frequency Modulated Continuous Wave (FMCW) transmits a chirp (sine wave whose frequency is modulated over time). This chirp is used as a proxy for a time marker which allows the distance measurement (Texas Instruments, 2018). As the minimum range is comparable to the transmitted wavelength, the radar can measure at very small ranges with a high accuracy. For 24 GHz, the wavelength is at about 1.2 cm.

Fig. 2.4 visualizes the concept of a signal of the FMCW in the form of a sine wave. The top left panel shows the chirp and how its wavelength changes over time (x-axis). The lower left panel shows the same chirp in the frequency domain instead of its amplitude (A). On the y-axis, the frequency ranges between 23.5 and 26 GHz, which is the operational range of the used radar and equates to a bandwidth B of 2.5 GHz. By using

$$\Delta d > \frac{c}{2B} \quad \text{Eq. 2.5}$$

and Δd being the range resolution, the radar has a resolution of 6 cm. In the present case, the duration of the chirp is 1 μ s, which is also known as ramp time (RT). Together with B, RT defines the rate (S) at which the chirp ramps up.

Before I explain how the distance measurement is achieved, it is important to understand the operational process of the radar (Fig. 2.5). A synthesizer transmits the chirp via the transmitting antenna (T_x , blue line in Fig. 2.4, top right) but it is also sent to the mixer (FMCWtut, 2022). The receiving antenna (R_x , green line in Fig. 2.4, top left) receives the signal. Note that the T_x chirp and the R_x chirp are identical in their form, just with the time delay τ . τ is twice the distance to the object, typically much smaller than RT and thus negligible (Texas Instruments, 2018).

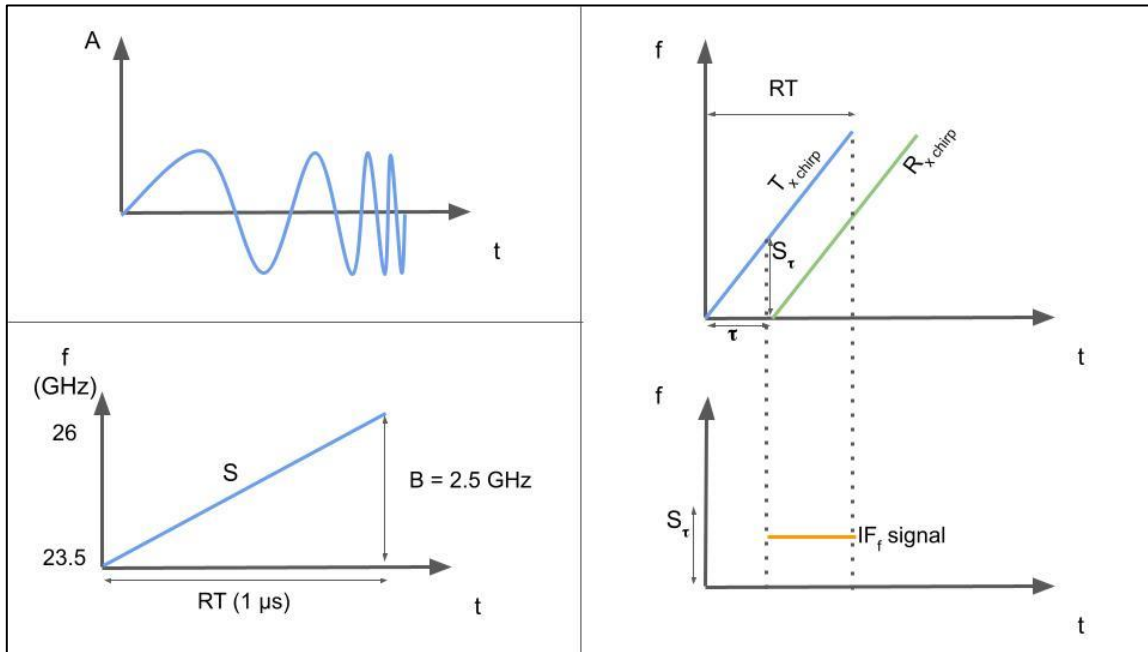


Figure 2.4: FMCW signal considerations. Adapted from (Texas Instruments, 2018).

By mixing the R_x signal and the T_x signal, the mixer calculates the Intermediate Frequency (IF_f). The IF_f is a constant frequency tone that reflects the distance to the object (Texas Instruments, 2018). The IF is also known as a beat frequency. This stems from audio engineering and serves as an analogy for what happens with the EM waves. The top of Fig. 2.6 shows two audio signals, one at 50 Hz, one at 60 Hz. Each frequency played by itself sounds like a beep tone with a small difference in pitch. When overlaying both frequencies, constructive and destructive wave interferences create a regular sound pattern which sounds like a techno beat. If both frequencies are at their maximum amplitude, they create a maximum constructive interference, which sounds like a beat. If one frequency is at its minimum while the other is at its maximum, the waves cancel each other out and the result is silence. This is shown in the lower part of Fig. 2.6. The processing happens in the mixer of the FMCW system with the EM signals. FMCW radars detect targets in multiple distances (Texas Instruments, 2018), which are in my case layers of distinct ρ_s . These multiple targets would add more R_x lines in Fig. 2.4, just with an offset in the x-direction. Consequently, more IF lines would appear as well.

The ‘beat’ in the IF_f frequency is the necessary time marker but the original frequencies must be reconstructed for the distance measurement. A Fourier Transformation deconstructs the wave pattern and transforms the signal from the time domain into the frequency domain. The resulting peaks in the frequencies directly correspond to the range of the object.

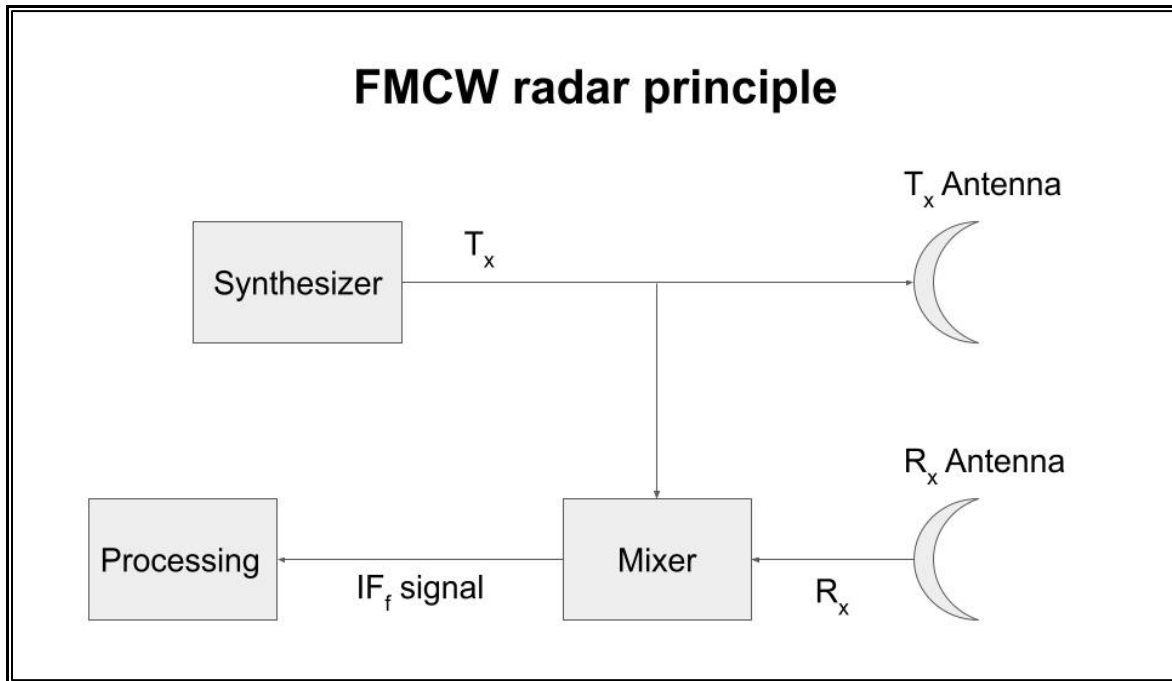


Figure 2.5: FMCW principle. Adapted from Texas Instruments (2022).

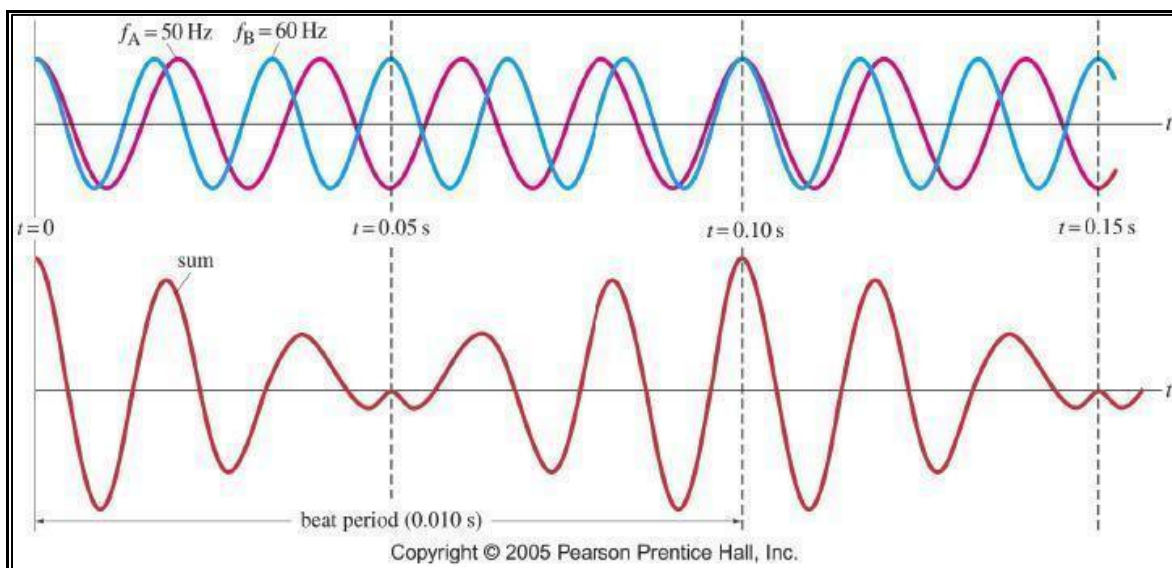


Figure 2.6: Wave interference and its resulting beat frequency.

For the radar we have calculated a range resolution of 6 cm, which is more than the given wavelength at about 1.2 cm. To improve the range resolution artificially, we use the zero-padding technique (Cohen, 2019). While the signal is still in the time domain, zeros are added after the signal, as can be seen in Fig. 2.7. The radar offers different zero padding options and we used a zero-padding factor of 8 as it maximizes the frequency interval and allows to better interpret the results. By the manufacturer's setting, this adds 896 zeros behind the signal which achieves the equivalent of a 0.7 cm resolution.

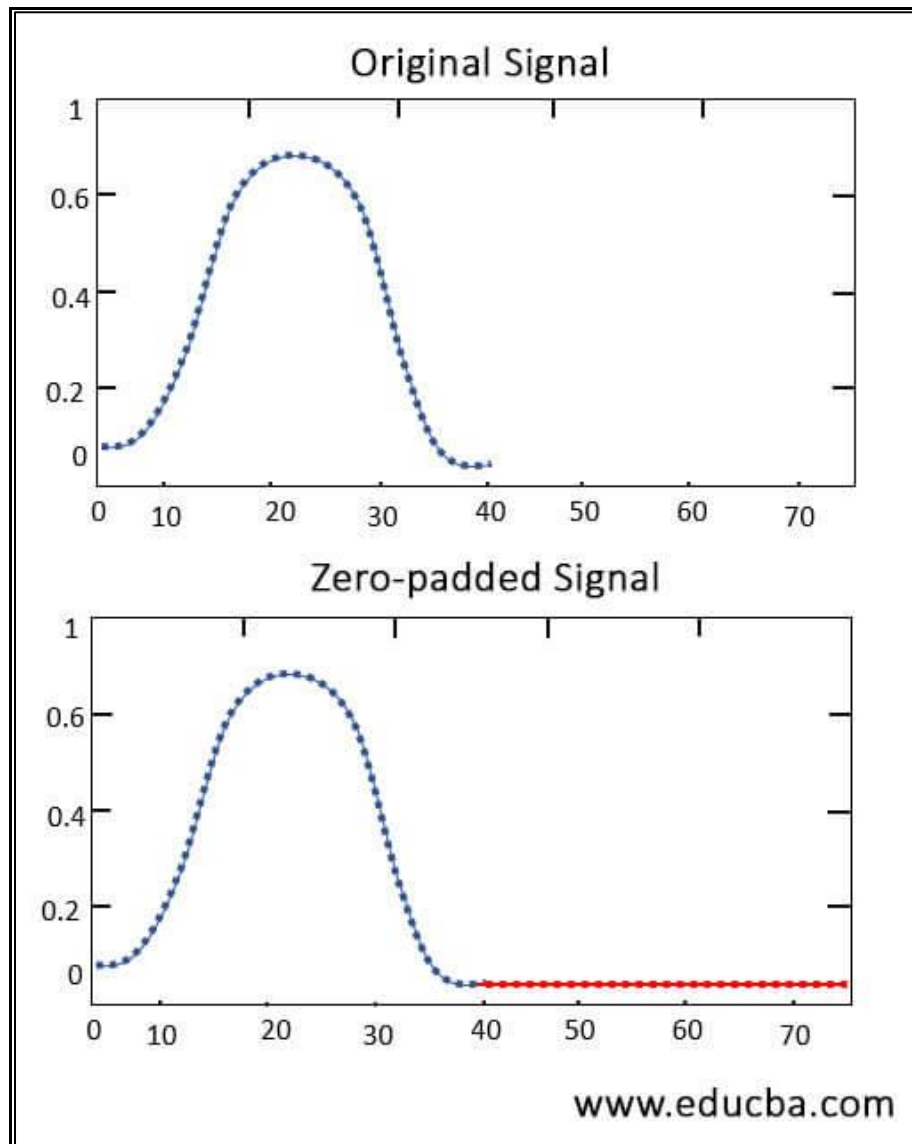


Figure 2.7: Principle of zero padding. Picture taken from www.educba.com.

The last step is a Fourier transformation. This process unmixes the overlapping frequencies by switching from the time into the frequency domain (3Blue1Brown, 2018). The zero padded signal results in a finer resolution in the frequency domain.

2.3 SNOW IN THE MICROWAVE REGION

2.3.1 Properties

As the porous air space in the snowpack is not considered a relevant source of absorption or scattering for microwave remote sensing (King, 2014), it is not further discussed here. ρ_s and LWC are the main factors describing the dielectric properties of snow (in Marshall et al., 2005).

LWC changes the amount of microwave absorption and scattering. This is due to the dipole structure of H_2O and its easy dielectric polarisation if an electric field is applied. At a temperature of 0 °C, liquid water has a maximum ϵ'' at about 9 GHz (microwave energy dissipates here), which shows the sensitivity to LWC of many microwave radar systems. Lower temperatures will lower ϵ'' due to increasing viscosity of liquid water. This is similar to ice, though the solid state minimizes the capability of the H_2O molecule to reorientate itself under the influence of an electric field. ϵ'' of ice has a very small dependency of temperature and frequency (King, 2014). For dry snow, different authors have shown that the permittivity is a function of ρ_s (Cumming, 1952; Tiuri et al, 1984). King (2014) describes how the stratigraphy of the snowpack influences microwaves. Changes in stratigraphy often come together with changes in ρ_s . At the transition, this can produce backscatter due to the change in dielectric properties. An example is the interface between WS and DH. ρ_s increases linearly with increasing permittivity. In dry conditions and depending on their wavelength, microwaves can penetrate deep into the snowpack. An increase in relative permittivity (e.g.

by an increase in LWC) reduces the penetration depth. With increasing E , scattering increases as well due to the relatively decreasing difference between E and wavelength.

Shallow snowpacks (<1 m) are difficult to measure with pulse radars as the required short pulses are hard to realise on the hardware (Marshall et al., 2008). FMCW radars deliver measurements of the snowpack with a vertical resolution of 1–3 cm (Marshall et al., 2008). This allows the retrieval of the stratigraphy through the sharp dielectric contrasts between layers. The Air Snow Interface (ASI) usually stands apart because of its sharp change in density (Marshall et al., 2008). The Snow Soil Interface (SSI) is much harder to differentiate especially if low-density mosses, lichens, and grasses dominate the ecotype (Holmgren et al., 1998). Snowpacks under 50 cm present similar characteristics, and a misinterpretation can lead to large errors in the retrieved d_s .

As seasonal arctic snowpacks are often shallow, Marshall et al. (2008) recommends the Ka-band frequencies of 26–40 GHz as the higher frequencies reveal more details of the snowpack. In the case of this work, the radar is using a bandwidth of 23.5–26 GHz. For deeper snowpacks, lower frequencies offer a higher penetration depth at the cost of detail. Marshall et al. (2008) suggests using Ku-frequencies (14–18 GHz), whereas even deeper snowpacks can be monitored using C-band (2–6 GHz or lower).

2.3.2 Absorption and scattering

Snow is a porous material that consists of ice crystals, air and liquid water. The degree of LWC changes the level absorption and scattering in the microwave region (King, 2014). The dipole structure of H_2O is largely responsible for this as the permanent polar structure allows for an easy dielectric polarization under the influence of an electric field (Glen and Paren, 1975) that causes a molecular reorientation (Baker-Jarvis, 2000). Under normal circumstances, the snow in Cambridge Bay is considered dry with the exception during the

melt-season or during rain-on-snow events. For microwave remote sensing, air is not considered a significant source of absorption and scattering (King, 2014).

2.3.3 Refractive Index and Snell's law

When an electromagnetic wave crosses the boundary from one medium of specific density into another, the speed of propagation changes and the angle of incidence is different to the angle of reflection. This is described in Snell's law:

$$\frac{RI_2}{\sin\theta_2} = \frac{RI_1}{\sin\theta_1} \quad (\text{Eq. 2.6})$$

with Θ_1 being the angle of incident and Θ_2 the angle of refraction. This is stylized in Fig. 2.8.

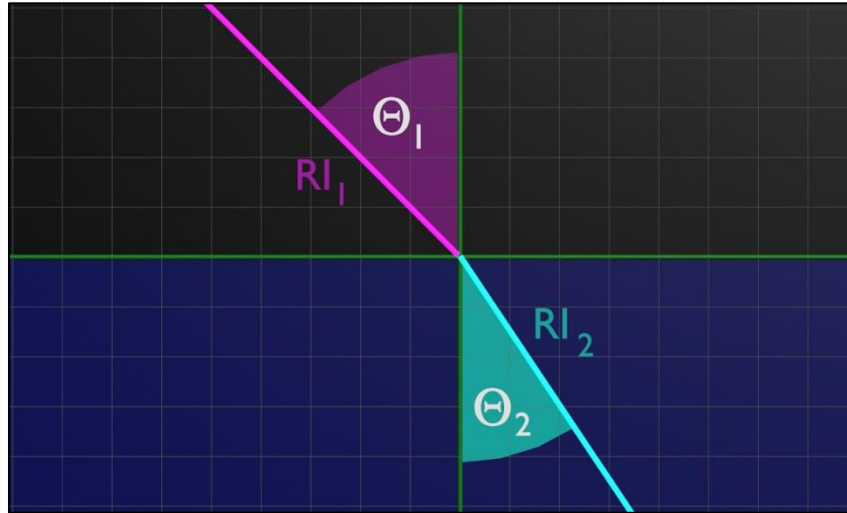


Figure 2.8: Snell's law. In purple is the incident process and its material in black. In turquoise, the refractive process, and its material in blue.

This must be applied to the returning radar signal to correct for the change in propagation speed. In my case, the radar was in a nadir position and the correction as done after Pomerleau et al. (2020):

$$h_s \cong \frac{h_{rad} - h_{air}}{\sqrt{\epsilon_{sd}}} \quad (\text{Eq. 2.7})$$

with h_s being the snow depth, h_{rad} the height of the radar above ground, h_{air} the height of the radar above the snow and ϵ_{sd} the mean effective permittivity. Behind this is the concept of

the Refractive Index (RI), which is a dimensionless number describing the ability of the medium to bend light. For my work, I have

- 1) removed h_{rad} from the equation. The radar is only a few cm above the surface and the RI for air is 1.0003. Thus, the estimated difference is negligible.
- 2) split the snowpack in two separate layers with their respective different densities. The two different snow depth measurements have been added. Fig. 2.9 shows how this has been applied.

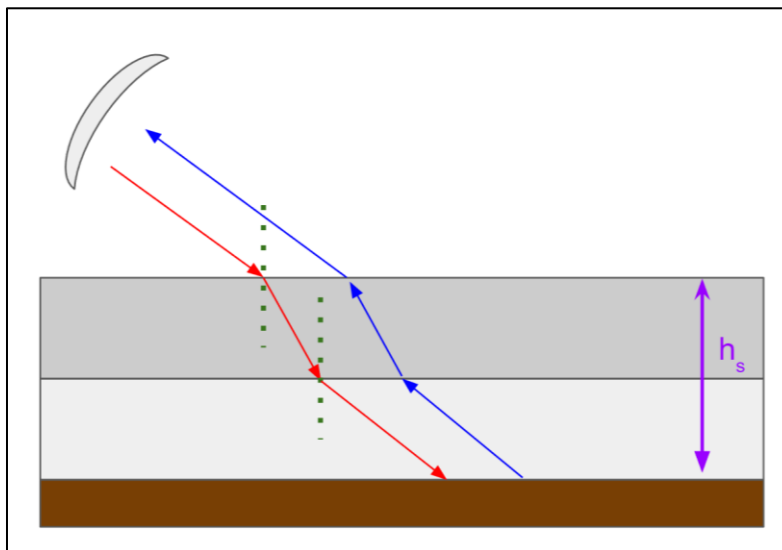


Figure 2.9: The figure shows the separation of the snowpack in two layers and how Snell's law has been applied. h_s is the total snow depth and the two gray layers distinguish Depth Hoar (bottom) and Wind Slab (top). The red and blue arrows are the incident and reflected angle with the dotted green line marking the interfaces.

The higher the RI, the slower the light propagates through the medium. In the case of Arctic snow, the layer of density of Depth Hoar is much lower than the density of the Wind Slab (examples given in chapter 5). Therefore, a distinction between both layers is meaningful to correct the return of the radar signal.

3 DATA AND METHODS

In this chapter, I present an overview of the three research sites of this thesis. This is followed by an overview of the general methods and data being used.

3.1 RESEARCH SITES

The main research site is located in Greiner Lake Watershed in Nunavut, Canada hereinafter referred to as CB (Cambridge Bay), as CB is the nearest community. Most of the scientific data have been collected at CB over several field campaigns since 2015. The second site is Trail Valley Creek (TVC), near Inuvik, Northwest Territories, with one campaign in 2019. The third site is the research station SIRENE (Site Interdisciplinaire de Recherche en ENvironnement Extérieur) at the Université de Sherbrooke. This site has been used for developing and testing the hardware components. Fig. 3.1 shows the locations on a map.



Figure 3.1: Overview of the three research sites and areas for the project. Background map: Google Hybrid.

3.1.1 Greiner Lake Watershed

The Greiner Lake Watershed (GLW) lies on south-eastern Victoria Island, about 10 km to the east of CB, the only local community and base for many research projects. The GWL coordinates are 69° 13.4' N and 104° 50.4' W with an area of approximately 1500 km², (Fig. 3.2). This site is my main research site and was part of the studies in chapter 4 and chapter 5.

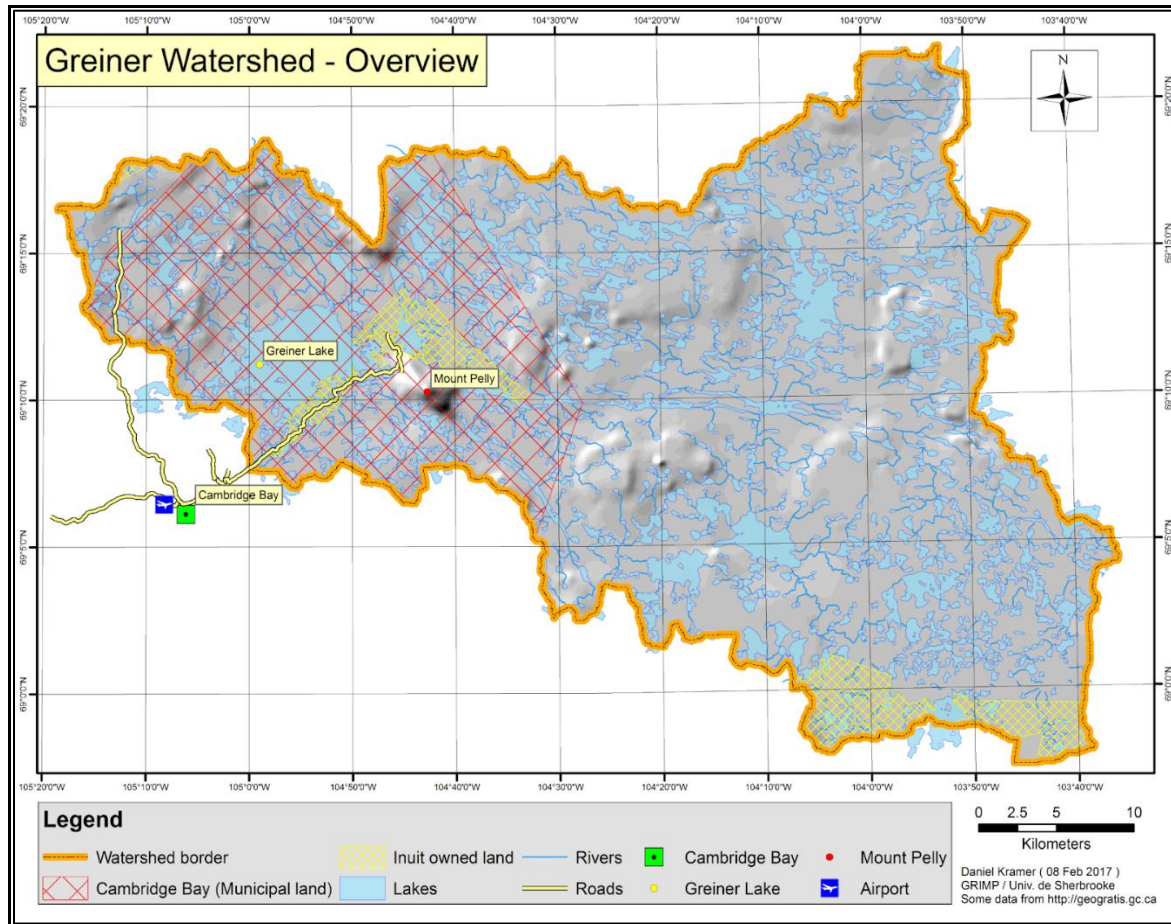


Figure 3.2: Greiner Lake Watershed and Cambridge Bay. In grey, the relief of the area; in blue lakes and rivers. With the exceptions of a few small mountains, the area is relatively flat. Data taken from www.openstreetmap.org and <https://geogratis.gc.ca>.

Polar Knowledge Canada (PKC) has selected the northern shore of Greiner Lake to serve as a pilot Intensive Monitoring Area (IMA) (McLennan, 2016). Ponomarenko et al. (2019) provided a very precise map with ecotypes of the IMA, shown in Fig. 3.3. A newer yet unpublished version is available to our group and covers a larger area. More and more research groups are focusing on the IMA and its direct surrounding area. An Automatic

Weather Station (AWS) (operated by PKC) is located about 500 m from the southern border of the IMA. In the short-term future, two Eddy-Covariance will be deployed in the IMA. The *Groupe de Recherche Interdisciplinaire sur les Milieux Polaires* (GRIMP, “Interdisciplinary research group on polar environments”) operates another AWS about 20 km to the southeast of the IMA.

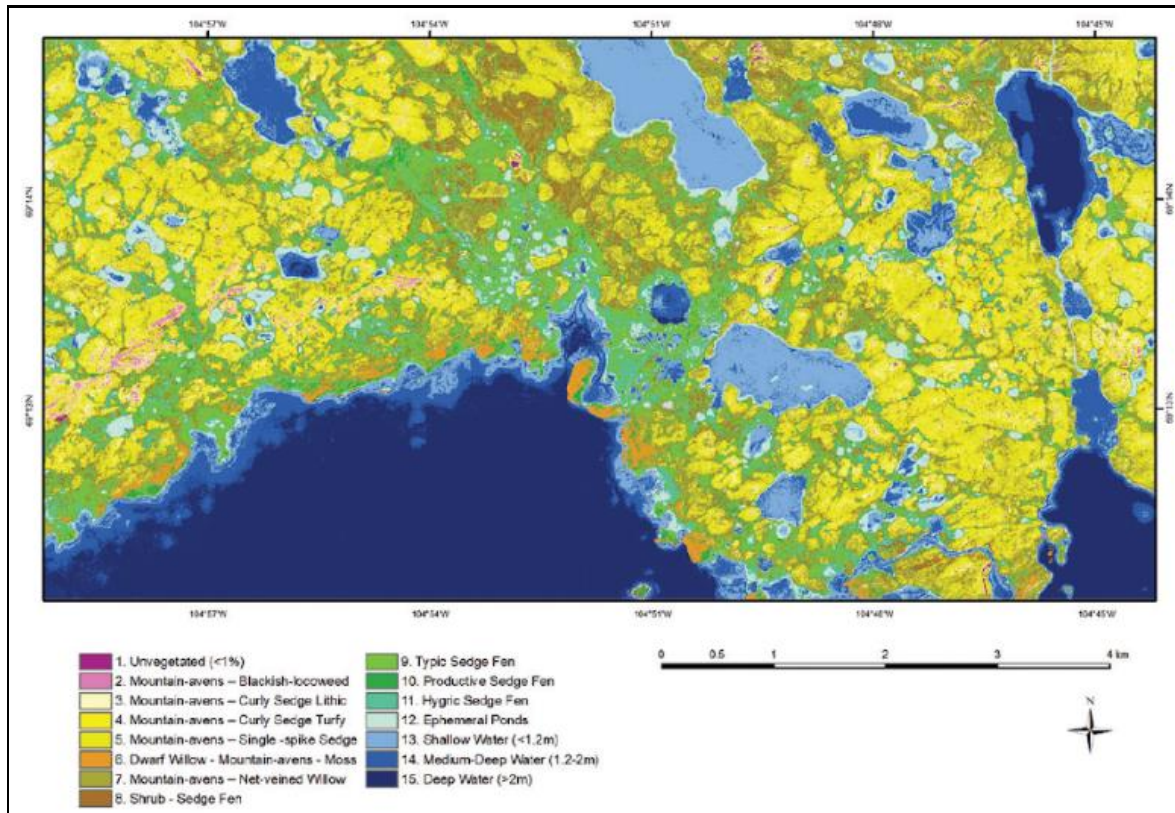


Figure 3.3: Ecotypes of the IMA, from Ponomarenko et al. (2019).

3.1.2 Trail Valley Creek

Wilfrid Laurier University manages the TVC research camp located about 50 km northeast of Inuvik, a town in the Northwest Territories, Canada, near the Mackenzie River Delta. The area is 60–100 m a.s.l. (Quinton and Marsh, 1999). Research, including snow modelling efforts, has been conducted since 1995 and auxiliary datasets are available (Wrona et al., 2017). The Circumpolar Arctic Vegetation Mapping Project Team (2003) classified the region as on the southern boundary of bioclimatic zone E, consisting of open and shrub

tundra with occasional, small tree stands. We collected snow and radar data during an expedition in January 2019 (mid-winter conditions). The area has more complex terrain features than CB, and the rivers form small valleys. Since 2012, a variety of sensors offer meteorological data. Quinton and Marsh (1999) cite several authors describing the area as having continuous permafrost and being dominated by hummocks with a diameter ranging from 0.4–1 m. Cryoturbation and periglacial processes influence the soil heavily. See Fig. 3.4 for a model of the camp in a landscape derived from RPAS data. This location has been part of the SIRA-development (chapter 5). SIRA stands for Snow-and-Ice-Radar.



Figure 3.4: 3D model of the TVC campsite and immediate surroundings. x- and y-scales to scale, but z-scale altered for a better presentation. Underlying height data has been provided by Branden Walker.

3.1.3 SIRENE Research station

The small research station SIRENE (*Site Interdisciplinaire de Recherche en ENvironnement Extérieur*, “Interdisciplinary Research Site for the Outdoor Environment”) is located next to the Université de Sherbrooke in Sherbrooke, Quebec, Canada. As covid-restrictions made it impossible to work in CB, this site has been used to develop the technical approach towards precise snow mapping presented in chapter 6. After its initial use for RS

projects related to agriculture, it was unused for many years. Since summer 2020, the *Département de géomatique appliquée* mobilized to re-establish SIRENE as a place for developing and building instruments and systems for ongoing research projects. The location is at 45°22'25.08" N and 71°55'22.86" W. Fig. 3.5 shows the station. The height data and texture images are derived from the RPAS flights done for this project. The station is modelled, and photographs are projected on the side. Please note that scales and photographs are edited for a better perception and are not on a 1:1 scale. The turquoise area covers the east-pointing hill with the E-rail (green) above. The blue pillars mark the location of the Ground Control Points (GCP) 1 to 3. The area coloured in red delineated the southern pointing hill with the S-rail above in purple and the red pillars indicate the position of GCP 4 to 6.

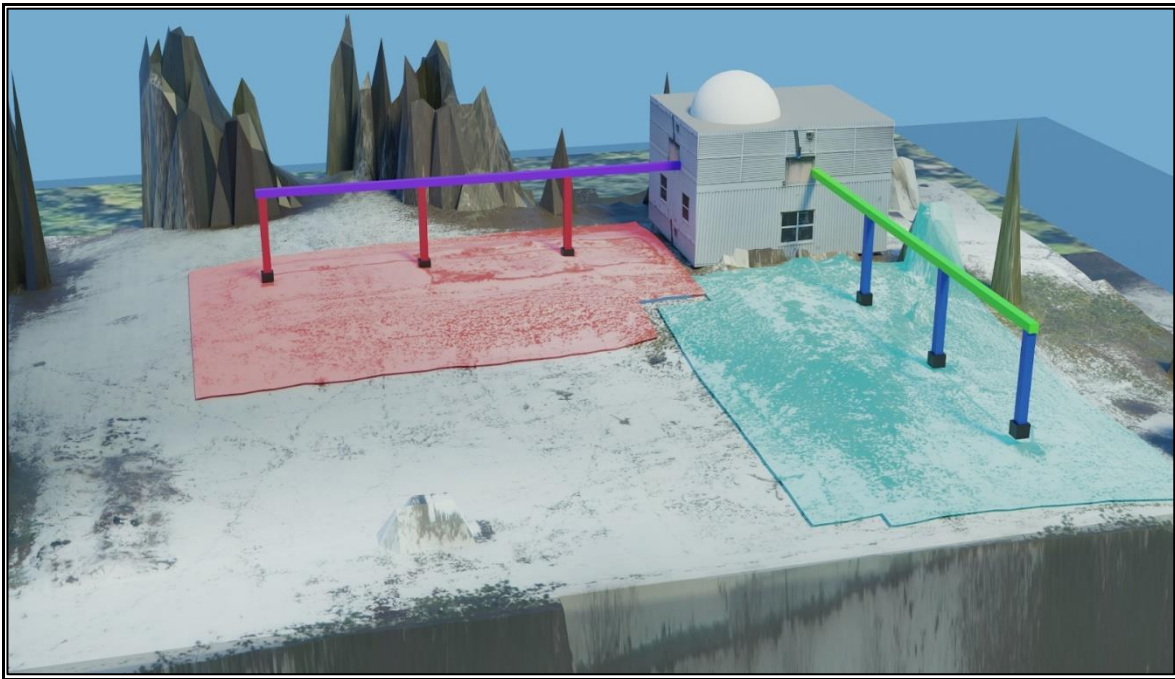


Figure 3.5: Overview of the SIRENE station and surrounding area as a combination of RPAS data and modelling. Patrick Menard produced picture material of the station, with background information retrieved from Google Hybrid. The station is area elevated. This model only serves presentation purposes and is thus not to scale.

3.2 DATA AND METHODS

I start this section with brief notes on each science chapter. This is followed by descriptions of the general methods that have been used to achieve the different scientific objectives. Each of the descriptions indicate in which chapter it was used.

3.2.1 Notes

Chapter 4 (RPAS)

During the PhD project, the official terminology has changed from UAV to RPAS. Both terms are used interchangeably throughout the thesis, but I always use the same term in a single chapter for consistency purposes.

Chapter 5 (SIRA)

The main device on the SIRA system is a Ka-Band 24 GHz FMCW radar. It's manufactured by IMST sentireTM from the sR-1200 series. The operating frequency is 24.25 GHz with a bandwidth of 2.5 GHz. It has one transmitting channel, two receiver channels and is connected to a Raspberry Pi (RPi) through an ethernet connection. The measuring range is between 0.6–307 m, but our results show that the device can measure at smaller distances. Likewise, with the lowest stated operational temperature is -40 °C but we could successfully perform measurements at around -50 °C. The operation voltage given is 10.5–13 V and has a standby consumption of 3 W. During operation, the unit uses 4.5 W. A LiPo-flight battery, used for GRIMP's aircrafts, powers the system.

I modified a Raspberry Pi 4 to control the device to an Access Point through the Wi-Fi connection of a mobile phone. I used the software Termux to send commands to the RPi and execute different scripts containing the measurement settings and for downloading the data. This setup was extremely successful in Arctic conditions. The data has been stored in the txt format with a header section describing the location, date, time and channel. The main data

is stored in a matrix. For the surveying experiment (details in chapter 6), I integrated a “M+” unit from Emlid to retrieve a GNSS signal from space, and a LoRa antenna to retrieve the correction from the base station. The base station is a Emlid RS2.

Chapter 6 (Mapping)

Originally, I planned to combine the technical development of the mapping system together with a further study of the influence of ecotypes and soil roughness on the SIRA signal (as described in the ‘future work’ paragraph of chapter 4). Due to the travel restrictions of the last two years, this chapter has been altered. I used SIRENE as a development site for the SIRA-mapper, and focused on different retrieval methods for snow depth maps and their comparison.

3.2.2 Snow pits and snow depth measurements

I used snow pits and snow depth measurements in every chapter for the validation of the remote sensing approaches. Snow pits offer detailed information on snow physical properties such as grain size and density, stratigraphy, and hardness. Chapter 4 required only snow depth measurements, but with a high accuracy on each measurement position. For chapter 5, I used detailed snow pits. During fieldwork, we measured the snow temperature per layer, T_{Air} and T_{Ground} . To measure snow grain size and type, we took a small sample of each layer and inspected it under a magnifying glass over a crystal card (gridded plate). We measured the snow density with density cutters and a scale to measure the weight of the volume defined by the density cutter. We inspected the stratigraphy visually and tested the hardness haptically. To determine the total snow depth (TSD) and that of each layer, we used a metre stick. We measured bulk SWE (Snow Water Equivalent) with a tube collecting a snow core and then weighted it. We retrieved layer-based SWE via density and depths

measurements. Fig. 3.6 shows a schematic conceptualized by J. King (unpublished). For chapter 6, I simplified the snow pits to snow depth and density measurements.

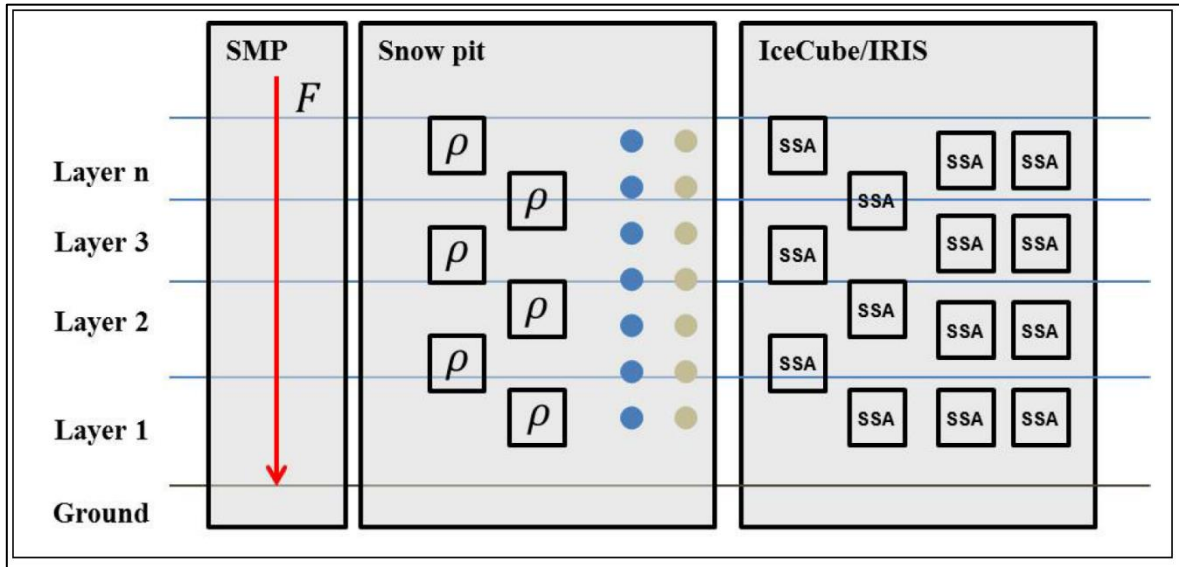


Figure 3.6: Concept for snow pit measurements. Blue dots show the spots for temperature measurements and yellow dots, spots for snow grain samples. As this graphic is a concept, variations may occur during fieldwork.

Digging snow pits has been the reference method for validating other techniques like RS-approaches and modeling. Tab. 3.1 shows the advantages and disadvantages of the snow pit technique. As a person does a snow pits, the accuracy can be set to fulfill the requirements of the scientific goal and is less limited than e.g. the set technical specification from a sensor in space. Further, any quantity can be added to snow pit measurement, leaving snow pits flexible and open to implement new ideas. The basic snow pit is a fairly simple process that does not require high-tech tools to generate results. The drawbacks of snow pits will be discussed in Chapter 4, as one of the goals of this work is to develop techniques to counter those limitations.

3.2.3 Satellite-based geolocation procedures

Geolocation procedures have been essential for chapter 4 and 6. In chapter 4, I used the standard procedure for the autopilot in the RPAS. In both chapters I used advanced concepts

to improve the accuracy and precision of the GCPs. For chapter 6, I introduced another advanced concept to be able to map each location in real time.

Table 3.1: Snow pits: Pros and Cons.

Snowpit	
Pros	Cons
<ul style="list-style-type: none"> - Very accurate - Any quantity - Simple 	<ul style="list-style-type: none"> - One point in space - One point in time - Destructive - Subjective - Time-consuming - Footprint

3.2.3.1 Standard positioning

The U.S.-American Global Positioning System (GPS) is probably the best known GNSS. Though its development started in the late '70, the system was fully operational in 1993 (Hein, 2020). Shortly after, the Russian system GLONASS came online and in recent years, China's BeiDou and the European's Galileo have been launched (Hein, 2020). Aside from the global systems, regional setups also exist, for example the Japanese Quasi-Zenith Satellite System (QZSS). Depending on the system, three orbits are used for GNSS:

- **Geostationary Earth Orbit (GEO):** Satellite in the GEO orbit Earth directly above the equator. Observed from the ground, the satellite seems to be fixed to one point in the sky (Space Weather Service, 2021). The orbit is at about 35787 km above the surface of the Earth (Steigenberge et al., 2013).
- **Inclined Geostationary Orbit (IGSO):** At a similar height as the GEO, this orbit has an inclination of 55° and an orbit revolution of 23 h and 56 min (Steigenberge et al., 2013).

- **Medium Earth Orbit (MEO):** Mostly used for GNSS systems at an altitude of 27900 km, and inclination of 55° and a revolution time of 12 h and 53 min (Steigenberge et al., 2013).

Retrieving a three-dimensional position requires at least four satellites. As two GNSS systems are fully operational (and two are almost fully operational) and most modern receivers being able to receive signals from either, the requirements are almost always met (Hein, 2020). GNSS frequencies are in the L-band (1-2 GHz), details in tab. 3.2. L-band frequencies are weather independent but heavily occupied. This can cause interferences—though negligible according to Hein (2020). Other frequencies exist but are also crowded (S-band) or have severe drawbacks (C-band) like a higher required signal power or higher costs for receivers (Hein, 2020). A GNSS system counts three components: a) the space segment consisting of the orbiting satellites; b) the control segment including the infrastructure to control the space segment; and c) the user segment, consisting of the user and the equipment. The GNSS radio signal works at a frequency of about 1.5 GHz. The positioning process relies on trilateration (Novatel, 2015), a process that allows estimating a position if three (or more) other points and their distance are known (Novatel, 2015; Yang et al., 2020; Wang and Park, 2020).

More advanced GNSS units that receive the GNSS signal on multiple frequencies are more and more common. Some atmospheric disturbances are frequency-dependent, and a better precision can be reached by comparing multiple frequencies. In this project, I used single- and multi-frequency receivers. More details on the topic can be found e.g. in Hamza et al. (2021).

GNSS units have multiple applications. In snow sciences, we commonly use them for general positioning or mapping. An example is the Magnaprobe, which allows mapping of d_s (Sturm and Holmgren, 2018). Most single receiver units have a limited precision of 2–5

metres (Hein, 2020). To improve the precision to a survey-grade level, different techniques are available.

Table 3.2: GNSS systems and their frequencies. Adapted from Hexagon (2021).

GNSS system	MHz range	cm range
GPS	1176.45–1575.42	25.48–19.03
GLONASS	1202.025–1609.3125	24.94–18.63
Galileo	1191.795–1575.42	25.15–19.03
BeiDou	1176.45–1575.42	25.48–19.03

Radio waves from about 5 cm to 10 m can travel unhindered through the atmosphere, whereas it blocks longer ones. GNSS systems are transmitting their signal in the MHz range, listed in tab. 3.1. Real-life frequencies are more specific, here I listed only the lower and upper limits. In centimetres, the frequencies range from 18.63 to 25.48 cm, which shows that they are in the middle of an atmospheric window. Nevertheless, GNSS signals interfere with certain atmospheric conditions, reflections on the ground and artificial disruptions (wanted and unwanted). As the power of the signal is relatively weak, interference can happen easily. On the atmospheric side, ionospheric storms can cause severe propagation errors in GNSS signals (Bouya et al., 2013), but also dynamic changes in the ionosphere regarding the electron content and structure that can cause performance issues (Terkildsen and Olivares, 2018).

3.2.3.2 Advance positioning methods

The differential GNSS (dGNSS) is a common technique based on two GNSS units, one serving as a base and the other as a rover. The base can either be an official reference station or a station created locally. The position of the base is very well known as it collects GNSS signals over an extended period, reducing uncertainties. The base transmits the corrected position to the rover, e.g., via a radio link. Official base stations present the advantage of

operating continuously (resulting in the best possible correction) and it only requires a rover on the user side. In remote regions, official stations are often too far away as the correction is only valid for a certain area. Building a local base station solves the problem: a dGNSS unit on a tripod recording the position for several hours. The rover is moving from position to position for the survey. See Fig. 3.7 for the dGNSS principle.

I used Real-Time-Kinematic (RTK) to position the SIRA in real time (chapter 6). This requires the base to transmit the correction via radio and is necessary to synchronize the GNSS-position with the radar measurement. For GCP-measurements, I used RTK and PPK (Post-Processing-Kinematic). For PPK, the rover records the satellite signals, and the position is retrieved during post processing. The last concept I utilised to improve the position of the base is the Precise Point Positioning (PPP). This method is accurate up to 3 cm and only requires a single unit (Novatel, 2015). The unit records the GNSS signal over time and the position is corrected during post-processing. For post-processing, I used the free service from Natural Resources Canada.

3.2.4 Ground Control Points (GCP)

I used GCPs in chapter 4 and chapter 6 to improve the RPAS-based retrievals. In this study, I combined GCPs and digital cameras. GCPs are targets on the ground that are easily recognizable by the airborne sensor and have a very well-known position. Martínez-Carricondo et al. (2018) advice to deploy GCPs in the (Region Of Interest) ROI with a density of 0.5–1 GCP per 10,000 m² and a stratified distribution to minimize altimetry errors. To avoid planimetry errors, they recommend an edge distribution, including the corners and sides of the ROI. To achieve a high enough precision, a suitable survey method must be used, and Agüera-Vega et al. (2017) suggest dGNSS as one option. As the GCPs must be easily identifiable on the images, bright colours and unnatural shapes work well. I used this recommendation for the flights in CB, but not at the SIRENE as the area is small (5,000 m²).

At SIRENE, I used parts of the permanent structure as GCP so they can be use in future. For SIRENE, the method of acquisition was via the RTK and the correction factor was received from the cellular network. We used the official reference station in Sherbrooke (CANNET-SHER). In CB, we used PPP for the base and PPK for the GCPs.

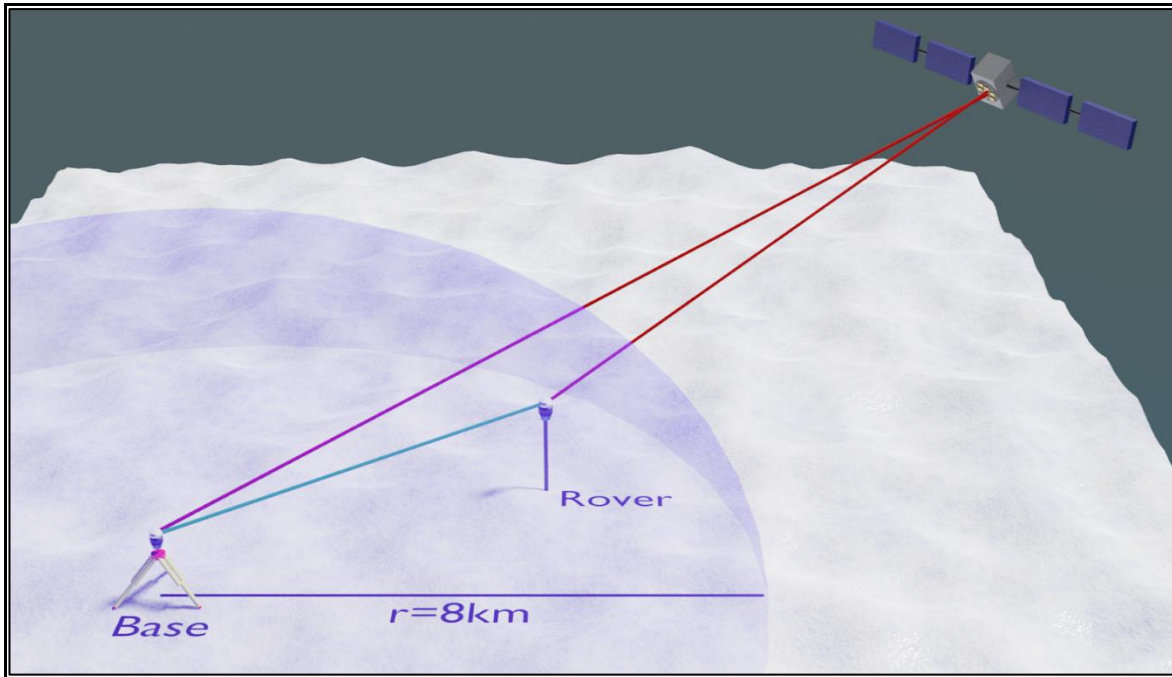


Figure 3.7: dGNSS principle: Red lines represent the time signal sent by the navigation satellite and received by the rover and the base station. The green line is the correction signal sent from the base station to the rover via the LoRa radio. The blue sphere is the effective radius of LoRa as given from the manufacturer.

3.2.5 Digital representations of the surface

For chapter 4 and chapter 6, I produced different types of maps. Three common types of the digital representation of the Earth's surface (Geodectics, 2021) are

- **DEM** (Digital Elevation Model): The most basic type that only includes elevation data. All natural (e.g., trees) or artificial (e.g., buildings) objects are removed.
- **DSM** (Digital Surface Model): This type adds all natural and artificial structures.

- **DTM** (Digital Terrain Model): This type adds information like rivers or ridges to the DEM.

They minimally combine the latitude (Lat), longitude (Lon) and elevation of a given landscape. In chapter 6, I added another type of digital representation: the Digital Snow Surface Model (DSSM). It provides a distinction between the solid earth representation (DSM) and the snow surface (DSSM). Further, to make an easier and more readable distinction between the solid surface and the snow surface, I use “DSM” to refer to DEMs and DSMs.

4 DESIGNING A DO-IT-YOURSELF (DIY) UNMANNED AERIAL VEHICLE (UAV) FOR ARCTIC RESEARCH PURPOSES AND PROVING ITS CAPABILITIES BY RETRIEVING SNOW DEPTH VIA STRUCTURE-FROM- MOTION.

4.1 INTRODUCTION TO ARTICLE

My motivation for this article was to design and build a RPAS platform that can carry different scientific payloads, is resilient to harsh arctic conditions and is cost-effective. This addresses the three general issues of working in the North:

- 1) Areal snow depth observations (i.e. sparse data) will be addressed by taking images of larger areas.
- 2) As the design is specifically tuned for Arctic conditions, the harsh environment is implicitly addressed and should not inhibit operations.
- 3) The DIY-character addresses cost-effectiveness as the price is a fraction of a comparable drone. At the time of writing the article, not commercial drone was able to operate under the expected conditions.

Our first decision was to either buy a commercial RPAS or go through the development process of a Do-It-Yourself system (DIY). As a group, we decided in favour of a DIY system as it has two critical advantages over commercial RPAS: 1) Primarily, it is a white box as all components are known. This makes it easier to repair and maintain the aircraft during fieldwork. Spare parts can be brought, which leads to 2) the fact that all electronic parts can be reused, thus reducing the costs for future projects.

As a scientific objective, I decided to evaluate the potential of a DIY RPAS flying in arctic conditions to retrieve TSD using a method proposed by Fernandez et al. (2018). They used SfM to measure snow depth via images in the VIS. In Tab. 3.1, the drawbacks of the snow pit are shown. To tackle these, RPAS-based SfM is ideally suited as takes images over a larger area and thus avoids the single point measurement. As the method is non-destructive, further flights can be done (potentially countering the one point in time issue). Further, the images are objective, and results are reproducible. The time-consuming aspect is addressed as it takes about the same time to conduct a flight as it takes to dig a snow pit, at least under the conditions found in Cambridge Bay.

Another concern is the footprint of the measurement. On the left side of Fig. 4.1, the footprint of an avalanche probe is shown. We use avalanche probes to determine the location of the snow pit, usually aiming for the average found depth of the local area. The right part of the figure shows the cross section of a wall in a snow pit. This demonstrates one difficulty in comparing different types of snow measurements: Whereas the avalanche probe has a single point, placing all snow measurements of the snow pit over one spot of the ground is impossible. The snow pit needs a certain degree of horizontal space and thus already these measurements are not taken exactly over the same spot, which may lead to uncertainties. SfM circumvents this problem fully, as the entire taken picture is the footprint. Summarising the attributes of SfM, all drawbacks of snow pits are addressed.

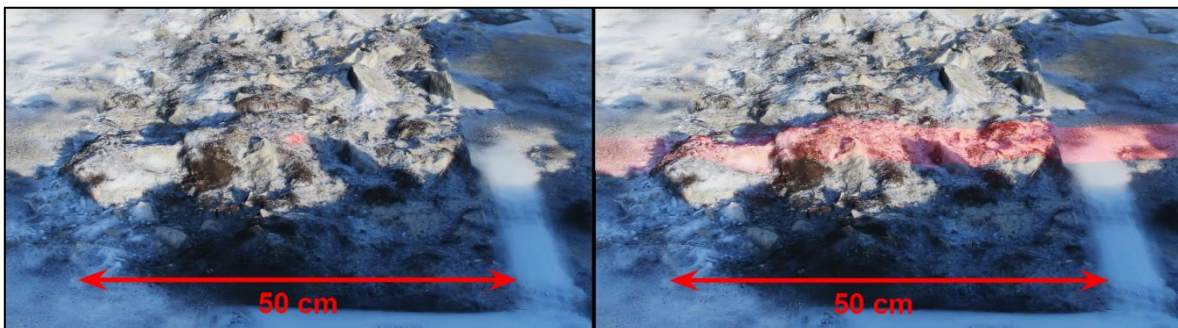


Figure 4.1: Footprint of a snow probe (red dot, left image) and the wall of the snow pit (red line, left image).

In this chapter, we show that it is possible to retrieve snow information matching the accuracy available in the literature using a self-made platform. As an aircraft type, we decided on a power glider as it fulfilled all our requirements. Additionally, it is easier to fly than a normal fixed wing, as it can fly slow. The gliding capability offer increased battery time, which is important in cold and windy environments.

Fig. 4.2 highlights the workflow of the work presented in this chapter starting with RPAS-development from scratch. In the first phase, the scientific needs and requirements are identified, followed with the acquisition of the associated hardware and assembling the platform. It is essential to evaluate the airworthiness of the aircraft, the concept for answering the scientific questions and preparing crew and pilot with a routine. During the first field campaign, numerous flights were conducted gathering information on flight capacity and experience which allowed further improvements on the aircraft: cold-resilience assessment and improvements of each component. All these improvements led to a successful second campaign which is presented in this chapter.

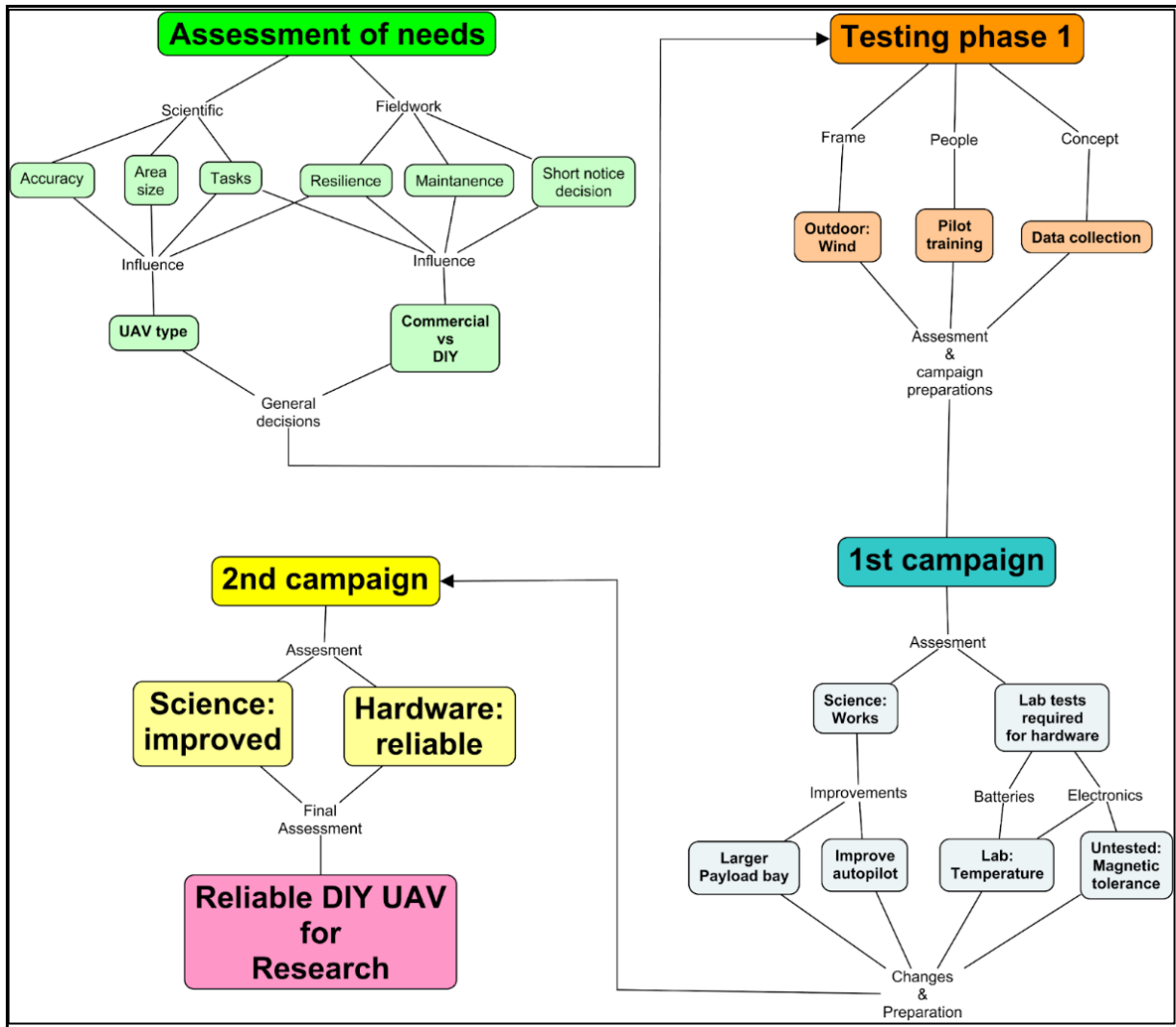


Figure 4.2: Schematic of the workflow to develop a DIY UAV.

4.2 DESIGNING A DO-IT-YOURSELF (DIY) UNMANNED AERIAL VEHICLE (UAV) FOR ARCTIC RESEARCH PURPOSES AND PROVING ITS CAPABILITIES BY RETRIEVING SNOW DEPTH VIA STRUCTURE-FROM-MOTION.

D. Kramer^{1,2}, J. Meloche^{1,2}, A. Langlois^{1,2}, D. McLennan³, B. Chapdelaine⁴, C. Gauthier-Barrette¹,
A. Royer^{1,2}, and P. Cliche¹

¹ *Centre d'Applications et de Recherches en Télédétection (CARTEL), Université de Sherbrooke, Québec, Canada*

² *Centre d'études nordiques, Québec, Canada*

³ *Polar Knowledge Canada, Canadian High Arctic Research Station, Cambridge Bay, Nunavut, Canada*

⁴ *Institut interdisciplinaire d'innovation technologique, Sherbrooke, Québec, Canada*

**Daniel.kramer@usherbrooke.ca*

Citation:

Kramer, D., Meloche, J., Langlois, A., McLennan, D., Chapdelaine, B., Gauthier-Barrette, C., Royer, A., Cliche, P. 2019. Designing a Do-It-Yourself Unmanned aerial Vehicle for Arctic research purposes and proving its capabilities by retrieving snow depth via structure-from-motion. Aqhalat 2019, Polar Knowledge Canada, p. 43-62. DOI: 10.35298/pkc.2019.05

4.2.1 Abstract

Unmanned Aerial Vehicles (UAVs) have become commonplace in many scientific applications, including operations in harsh environmental conditions. However, off-the-shelf UAVs capable of this type of work are very expensive and offer limited flexibility for custom payloads. Cost-effective and customized UAV system capabilities for site exploration, mapping, surveying, and atmospheric profiling in the Arctic are needed. The goal of this project was to develop a do-it-yourself (DIY) platform from simple, pre-manufactured components capable of flight operations in extreme arctic and polar winter conditions. This approach provides the flexibility to fly a range of sensor payloads for different applications and allows for easy on-site modifications and low-cost repairs. A highly customized payload example is the Ka-band radar used by the research team (circa 700 grams (g), 200 x 130 x 150 millimetres (mm)) and more common examples are cameras like the MAPIR Survey 3 (circa 50 g, 59 x 41.5 x 36 mm). Where some manufacture warranties (like senseFly) require the UAV to be sent in even for minor repairs, on-site modifications and repairs can keep the costs to operation a DIY UAV low. To meet this goal, different components were tested under controlled conditions to verify their functionality in extreme cold temperatures and their compatibility with devices used during fieldwork. To further validate the scientific capability of the DIY UAV system design, a small area near Cambridge Bay, Nunavut, Canada was surveyed to retrieve snow depth via Structure-from-Motion (SfM). This produced a snow depth map with a horizontal resolution of 6 cm. The calculated snow depth, with a root mean square error (RMSE) of 16 centimetres (cm) (13 cm without points over vegetation), matches values found in the literature that were retrieved at lower latitudes using much more expensive platforms. The main UAV type studied in this project can operate safely in temperatures as low as -40 degrees Celsius (°C) and at even colder temperatures, though with slightly reduced capabilities. The DIY UAV design is currently limited to a

maximum wind speed of 10 metres per second (m/s), including a large safety margin. Next steps include the development of a rotary-wing aircraft to carry a radar system capable of snow and ice profiling and a fixed-wing aircraft to fly in wind speeds over 10 m/s.

4.2.2 Introduction

Unmanned Aerial Vehicles (UAVs) are frequently used in many geoscientific fields (Anderson et al., 2019) and arctic research applications (Chudley et al., 2019). Arctic scientific applications will greatly benefit from the possibilities that UAVs offer. For example, traditional methods of snow depth acquisition (Langlois et al., 2010), like manual measurements with an avalanche probe or digging a snow pit, are time consuming and limited to a small area which leads to representativeness problems. UAVs can cover a much larger area (Jo and Kwon, 2019), avoid spatial interpolation, and can easily track changes in an area over time (e.g., vegetation). Furthermore, by better representing local processes (snow distribution versus roughness/topography) that are difficult to represent with the coarser spatial resolution of satellite imagery, UAVs can also reduce modelling uncertainties (Rutter et al., 2014).

UAV technology is developing quickly, and usability is improving. Nevertheless, the harsh environmental conditions of polar regions put considerable strain on aircraft that can be challenging for simple, off-the-shelf solutions (DJI, 2015). In addition, these systems are often closed and don't allow parameter modifications or easy on-site maintenance and repair. Advanced systems, like the senseFly eBee or the Microdrones md4-3000, can handle harsh environmental conditions better, but their price tags, which can exceed US\$ 30 000, can be restrictive. Furthermore, these advanced systems do not usually allow for modifying payloads or attaching systems or sensors for specific scientific requirements. The alternative is the do-it-yourself (DIY) approach. This makes it possible to make specific alterations to an aircraft for the desired task. It also allows for easy repairs and modifications during field

campaigns to address problems that arise. An additional benefit is the ability to re-use the electronics in different UAVs, which significantly lowers the price for new aircraft as a new frame can usually be acquired for under US\$ 200. The philosophy behind the technical part of this paper is to construct simple and low-cost UAVs that can operate in the Arctic and meet scientific standards in surface state retrievals accuracy. Care was taken to avoid complicated procedures with airspace authorities, in this case Transport Canada (TC). Site selection and tasks were designed to meet all TC exemptions (e.g., distance to builtup areas, airspace class, and flight altitudes and distances). While this design limits flying opportunities, it avoids the wait time associated with requesting and obtaining Special Flight Operations Certificates (SFOCs)¹ and allows for last minute science-based decisions on flight needs. To show that this approach can meet scientific standards for data acquisition this paper aims to provide:

- Technical details of the project's approach, including hardware and software information, and lessons learned from past campaigns; and
- An example of application by retrieving snow depth data using structure-from-motion (SfM), validated using field measurements.

Consequently, the article is divided into two main sections: first, a description of the technical solutions, experiments, and experiences of operating a UAV in the Arctic, and second, a demonstration of the capabilities of the DIY-UAV system design in retrieving snow depth in the Arctic.

¹ The regulations from Transport Canada changed as of June 1, 2019. The restrictions in place during the project are no longer in effect. The new regulations that will be in effect for future flight missions can be found at: <https://www.tc.gc.ca/en/services/aviation/drone-safety/new-rules-drones.html>.

4.2.3 UAV development and overview

This section discusses the configurations of the different aircrafts and the environmental influences on the materials and electronics. Some experiments were conducted in a controlled environment (weather chamber), whereas other tests and observations were done during fieldwork. Notably, operating near the geomagnetic pole (e.g., Cambridge Bay, 1500 kilometres (km)) while using a magnetometer can cause problems flying UAVs. Manual flight may be necessary, as most UAVs use a magnetometer to determine the heading while flying on autopilot. Rotary-wing or multicopter aircrafts strongly rely on magnetometers for orientation because of the ability to hover or fly with low speed. In comparison, fixed-wing aircrafts can estimate heading solely from the tracking of the previous global positioning system (GPS) point navigation (Ader and Axelsson, 2017). Cimoli et al., (2017) used a rotary-wing in the Arctic and report briefly on their experience: *“GPS and compass navigation are compromised at high latitude (due to magnetic field interference) [...] It is recommended that pilots be prepared to perform the survey in manual mode.”*

From personal experiences and reports from colleagues, fly-aways on random trajectories occurred with older versions of DJI products. With newer versions, the autopilot switches automatically to altitude hold/manual mode when trying to fly in full automatic/GPS mode. While manual flying is possible, very advanced flying skills are required to obtain good measurements from the sensors carried on the UAV. For instance, if a SfM approach is planned, angle, speed, and camera timing must be controlled to provide sufficient overlap between the photographs. An alternative is to record video instead of photographs. However, this requires more intensive post-processing and lowers the resolution of the images. For the purpose of this project, it was decided to only use GPS for navigation on the aircraft, with

additional reliance on autopilot calibration. For this reason, the DIY UAV design is a fixed-wing frame. The autopilot can be used without a magnetometer and fixed-wing aircraft are better suited for longer flight time, which is good for mapping. A DJI Phantom 3 Professional aircraft was also used in manual mode for comparison on several occasions.

4.2.3.1 Batteries

The following section describes the battery tests that were conducted to identify potential flying times in different temperature conditions. The focus of this testing was to better understand battery performance, e.g., how long will a battery last on a certain load, independent of UAV-type, wind-speed, or other factors. Knowing battery-performance is an important aspect of planning flight missions as it impacts decisions on parameters like flight-lines, cover area and expected flight time under the prevailing weather conditions. For the fleet used in this project, Lithium polymer batteries were selected. These batteries are widely used for UAVs, as they “offer the optimal compromise of moderate specific energy, high specific power, and high cycle life” (Abdilla et al., 2015; Mulgaonkar et al., 2014). The long-term goal is to cover similar distances as commercially available UAVs (e.g., 1000 square metres (m²), while being able to switch payload on site.

Test set-up

Power consumption was estimated by analyzing a real flight log from a fixed-wing aircraft (BlitzRCWorks Skysurfer Pro, see Fig. 4.7, left) carrying no payload. The flight took place under good conditions (< 10 metres per second (m/s) wind, around 0 degrees Celsius (°C)). The amperage (A) used during the flight varied between 1 A and 25 A, and most power was consumed during takeoff and climb. When gliding, almost no power was needed, so an average of load of 16 A was calculated to replicate ‘normal’ flight consumption. Table 4.1 lists the batteries tested. The constant discharge refers to the rate at which the battery can

continuously discharge itself without being damaged. The peak discharge characterises the battery's ability to discharge a higher amount than the constant discharge over a short period of time. The schematic of the experiment is shown in Figure 4.3.

Table 4.1: Batteries used in experiments. All batteries have 4 cells.

Battery	mAh	V	Wh	Constant Discharge	Peak Discharge
Phantom PH3	4480	15.2	68	N.A.	N.A.
Turnigy 4.0 Nano-tech	4000	14.8	59.2	30 C	40 C (10s)
Turnigy 4.0 Multistar	4000	14.8	59.2	12 C	24 C
Turnigy 5.2 Multistar	5200	14.8	76.96	12 C	24 C

Test types and protocol

Three types of tests were conducted.

Test type 1: During the test, a constant high load (16 A) was applied at a specific temperature. Before, the test the battery was kept at room temperature to simulate keeping a battery warm (e.g., near body) while being out in the field.

Test type 2: Before, the test the battery was frozen to a specific temperature to simulate the battery being transported on the field, without temperature protection. As in Test type 1, the applied load was 16 A.

Test type 3: During the test, a small low load (1 A) was applied to investigate the effect of cold temperatures on battery life. Before, the test the battery was kept at room temperature.

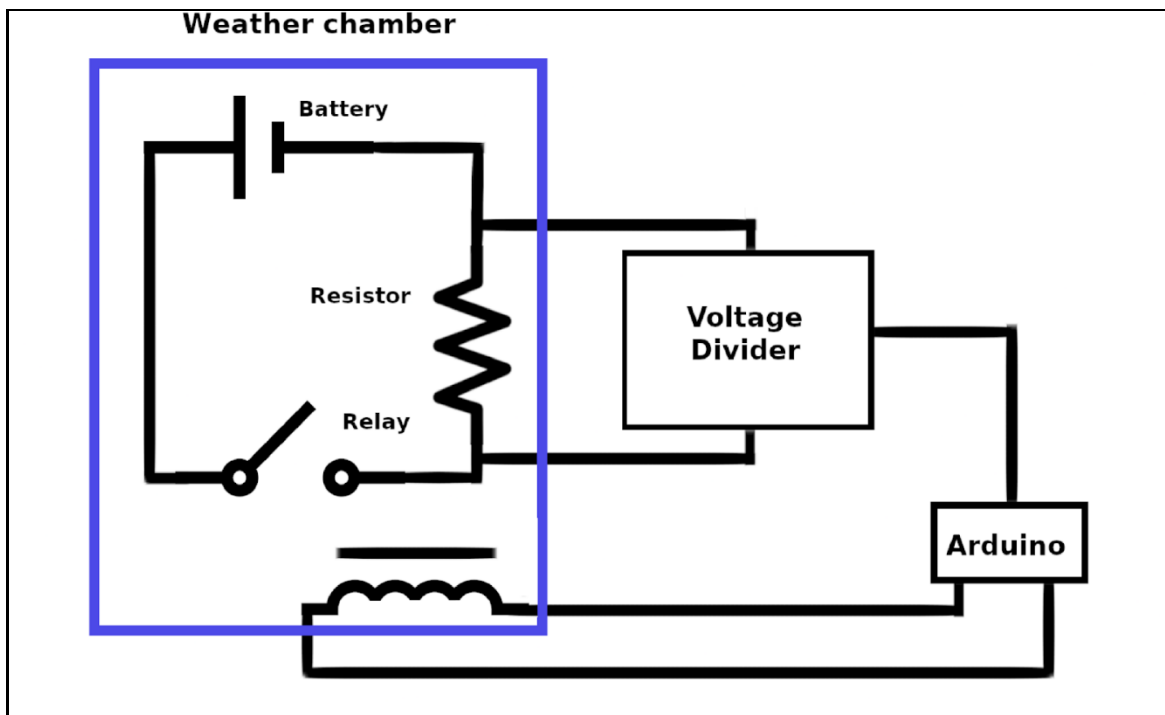


Figure 4.3: Experimental set-up.

The following protocol was used to standardize the tests:

- 1) All parts of the circuit are connected, and two freezers are used. One is held at a constant temperature, in which the battery is inserted. The other was set to $-80\text{ }^{\circ}\text{C}$ to cool the load (several resistors). The resistors are controlled by an Arduino microcontroller, which is connected to a relay. The resistors are used to simulate the load applied during a flight.
- 2) During test types 1 and 2, the freezer is set and kept at a desired temperature. The temperature ranges from $-20\text{ }^{\circ}\text{C}$ to $-40\text{ }^{\circ}\text{C}$, which reflects normal conditions during fieldwork. The tests were conducted at $10\text{ }^{\circ}\text{C}$ intervals. Results from test type 3 ranged from $+4\text{ }^{\circ}\text{C}$ to $-40\text{ }^{\circ}\text{C}$.

3) A fully charged battery was placed in the freezer and connected to the circuit. Batteries were always placed in the same position/orientation/ part of the freezer to avoid random factors influencing the results.

4) At the start, after about 350 seconds (s), and at the end of each test, the resistance (R) was measured to verify that the load was constant and there was no resistor malfunction.

5) To prevent battery damage, the system automatically shut down when the battery reached 12.6 volts (V) (3.15 V per cell). Further explanation follows in the Results section.

6) For each setting, the test was repeated 3 times per battery (except for test type 3, further explanation follows below).

Results

For all tests, R was in a range between 0.93 and 0.98 ohm (Ω). Therefore, the load during the tests was as planned.

Test type 1

Fig. 4.4 compares the discharge of the three different battery types at three different temperatures. The Phantom 3 battery heated up so much in the first test, that further testing with this battery was discontinued. In repeated testing, the performance of each battery was relatively similar, though there are visible differences between battery types. As batteries lose strength over time, it is important to note that no record was kept of the battery cycles. The Multistar 4.0 and 5.2 were almost new, and the Nano-tech 4.0 had been in use for about two years. At 5200 milliampere per hour (mAh), the Multistar 5.2 had the highest capacity, while at 4000 mAh, the Multistar 4.0 and Nano-tech 4.0 had the same capacity. The Multistar

4.0 and Nano-tech 4.0 have different C-ratings (maximum safe current draw)— the Nano-tech rating is higher (25 to 50 °C) than the Multistar 4.0 (12 °C).

All three batteries had a sharp decline in capacity at about 14.5 V. In Figure 4.5, each battery type is presented in its own graph, which also show the different temperatures. The Nano-tech 4.0 (top graph) is the most sensitive to temperature. It loses about 3 minutes of operational time at -40 °C (7.35 minutes (min)) in comparison to -20 °C (10.28 min). The Multistar 4.0 (middle graph) loses just over 1 minute of time at -40 °C (11 min) in comparison to -20 °C (12.16 min). The Multistar 5.2 (bottom graph) loses almost exactly 1 minute of time between -20 °C and -40 °C. In all three cases, the results represent mean values over the three tests performed with each battery at each temperature.

Test type 2

The first test was conducted at -20 °C and the battery was exposed to the cold for 30 min. As the load was applied, the voltage immediately dropped under 12.6 V. As this was the upper end of the temperature test, no further tests were conducted. Only the Nano-tech 4.0 was tested. It was assumed that other LiPo-batteries, though maybe of a slightly different chemical composition, would react in a similar way.

Test type 3

The protocol described in the previous section was repeated at five different temperatures with the Nano-tech 4.0 (see Fig. 4.6). Notably, the test at -8 °C had to be conducted under real conditions outside at night with variable temperatures. The equipment at the time of the test was not able to cool to a temperature above -20 °C. For the temperature at +4 °C, a conventional fridge was used while the other tests were performed in a controlled weather chamber. Results depicted in Figure 4 suggest that the impact of temperature on the

discharge capability is rather low at -20 °C, but a significant change can be observed at lower temperatures (at about 50 minutes into the test).

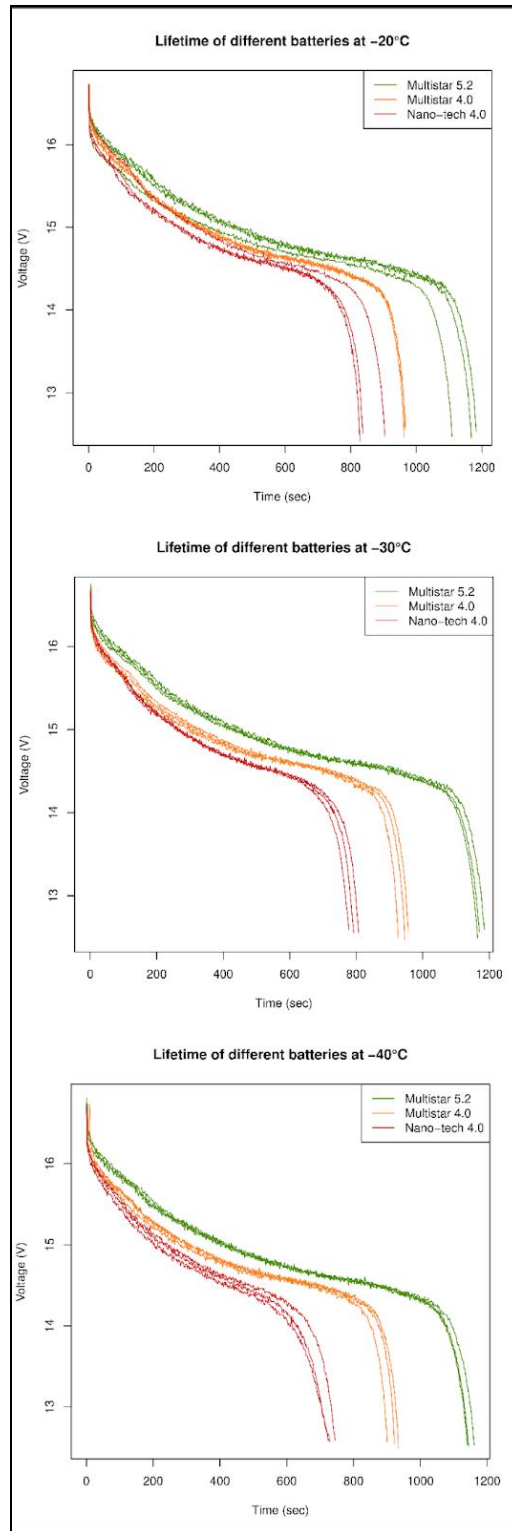


Figure 4.4: Comparison of three different batteries at three different temperatures.

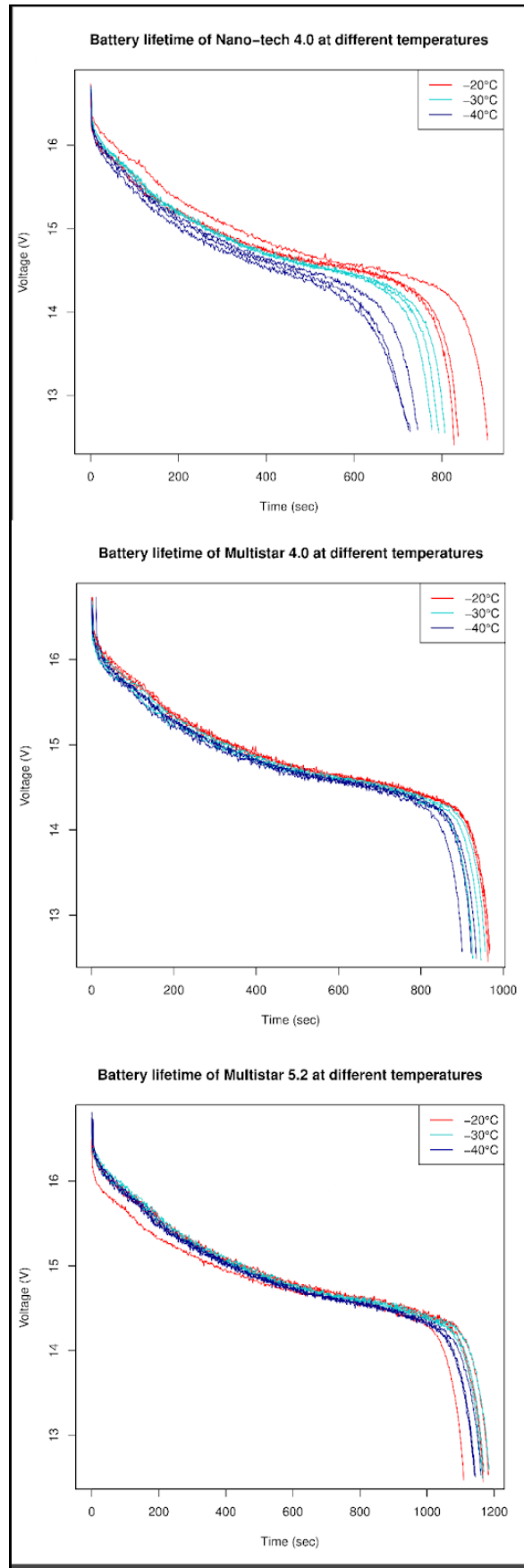


Figure 4.5: Results for three different battery types at three different temperatures.

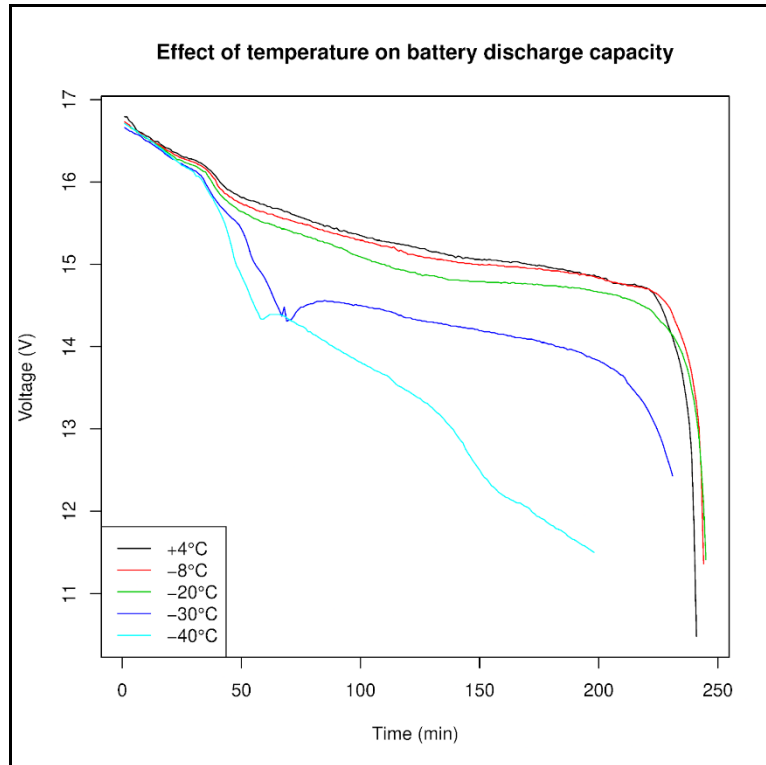


Figure 4.6: Long-term exposure of a battery to different temperatures. Note the distinct drop of discharge capacity at around 50 min for temperatures < -30°C.

Discussion

Test type 1

Battery age appears to play an important role. The Nano-tech 4.0 significantly underperforms the others, despite having specifications that are comparable to the Multistar 4.0. Table 4.2 presents the average operation time for each battery at each temperature (average of three tests). Voltage was measured and recorded throughout the test as well as the time at which the battery reached 14.50 V for the first time. The results are similar to values found in the literature, e.g., Winslow et al. (2016). After this interval, battery capacity drops sharply. To avoid damage to the battery, its voltage should never drop below 12 V, although an extra 0.5 V buffer was built into the project design. The 12 V is a combined result from 4 cell batteries, each with a lower limit of 3 V. The typical cell has an operational

range from 2.3 to 4.2 V (Salerno and Korsunsky, 1998), but the 3 V is a widely used rule-of-thumb as the V-drop is not linear. This test allows us to better estimate flight times, assuming a constant load. The load used for testing was high enough to underestimate rather than overestimate flight times. As mentioned earlier, the difference between the Nano-tech 4.0 and the Multistar 5.2 (and to some degree the Multistar 4.0) is almost 3 minutes when compared at -20 °C and -40 °C, respectively. Since the Nano-tech 4.0 is by far the oldest battery, this finding suggests it is reasonable to repeat this type of experiment as a ‘good habit’ with older batteries before deployment to ensure airworthiness and estimate discharge-time. The purchase of a new battery is not a big expense and could significantly increase safety and flight time.

Table 4.2: Time in seconds until the battery reaches 14.50 V. Shortly after this value, voltages for all batteries drop sharply until reaching the cut-off limit of 12.5 V. The displayed value is the mean of 3 tests.

	Nano-tech 4.0	Multistar 4.0	Multistar 5.2
-20°C	617s	730s	897s
-30°C	537s	702s	897s
-40°C	441s	654s	832s

Test type 2

Due to the different chemical compositions, this value might differ for each battery type/manufacturer. However, the test results indicate the best practise is to keep the batteries warm until the last moment. Since the research sites are usually ≥ 30 minutes away from accommodations, measures must be taken.

Test type 3

A difference was found between the voltage measurements taken at the end of the experiment and those taken once the battery was removed from the weather chamber and allowed to warm up. Ideally, the battery should be tested under no load in both conditions. The impedance of the battery increases as the temperature lowers (Wang, 2015). This phenomenon demonstrates that a temperature drop causes a loss of discharge capacity, which is mainly caused by an increase of the internal resistance of the battery. This lowers the discharge rate and capacity (Wang, 2015). From a practical standpoint, the significant loss of discharge capacity between -20 °C and -30 °C is not particularly relevant for the purposes of this design project. Since the typical flight times are under 50 minutes and the typical load draw from the battery is higher, the battery would be empty before the cold had an impact.

4.2.3.2 *Frames*

Various commercially available platforms were tested for the design project including two DIY fixed-wing platforms (both motor glider) and one off-the-shelf rotary-wing platform. To begin UAV operations, test flights were conducted as part of various campaigns in Southern Ontario, Nunavut, and Quebec. The initial price tag for our DIY system was about US\$ 1 250, which is comparable to the cost of a low-end, off-the-shelf solution like the DJI Phantom 3 Professional.

The DJI Phantom 3 Professional was used to represent an off-the-shelf system and well-known platform. While it is a different type of UAV (rotary wing) that cannot be compared in every aspect to fixed-wing frames, it serves as a benchmark for testing. The DJI Phantom 3 Professional produced results quickly and was a good tool to start UAV

operations. This device was used in the Bay of Quinte region (Southern Ontario, Canada; 44°43'06.5370"N, 77°35'46.6923"W) for a snow mapping campaign in 2017 and in the Greiner Lake Watershed near Cambridge Bay (Nunavut, Canada; 69°14'11.78"N, 104°52'55.10"W) during a summer campaign in 2018. During the snow mapping campaign in the Bay of Quinte, there were a few issues with the DJI Phantom 3 Professional, but it was able to fly using the autopilot setting. Unfortunately, this was not possible in the Greiner Lake Watershed summer campaign. We assume the relative proximity to the magnetic North Pole interfered with the magnetometer readings needed for orientation and forced the pilot to fly manually.

The first DIY platform built and tested was the BlitzRCWorks Skysurfer Pro. This aircraft has no payload bay and required customization. The flying weight of the aircraft is stated as 650 grams (g) by the manufacturer. The customization included adding 117 g for the camera (GoPro 6) and 485 g for a larger battery. Following this, the take-off weight was 1 252 g and put the engine to the limit of its propulsion capabilities. The customized design was able to retrieve data and was used on a winter and a summer campaign in Cambridge Bay, as well as on test flights in the Sherbrooke area (Quebec, Canada).

While the build was easy, the test flights identified a few problems. Notably, the Electronic Speed Controller (ESC) on the BlitzRCWorks Skysurfer Pro did not work below 0 °C. This finding led to testing all electronic components in the weather chambers instead of focusing solely on battery discharge abilities. In addition, the aircraft has a very limited payload capacity and, lacking previous experience, the most powerful battery that would fit in the aircraft was used to ensure sufficient power during flight. The advantages of the BlitzRCWorks Skysurfer Pro platform are its low price (around US\$ 75 for the frame) and its gliding properties. It is easy to fly and a great platform to inexperienced pilots. However,

glider planes have problems in higher wind speeds (the maximum wind speed deemed safe in testing was 10 m/s).

The second DIY platform built and tested was the Finwing Penguin (about US\$ 200). This aircraft has a designated payload bay (with some modification it can fit a Sony A6000, weight: 468 g, dimension: 120 x 67 x 45 mm) and can carry up to 900 g payload (manufacturer's specifications). The aircraft all-up weight (AUW) shall not exceed 2.4 kilograms. The aircraft was easy to build and can be done in a short amount of time. Compared to the BlitzRCWorks Skysurfer Pro, which was also at its AUW, the Finwing Penguin felt more comfortable in the air. Its hardware is more robust than the BlitzRCWorks Skysurfer Pro and the aircraft performed better for the testing purposes. As a motor glider, strong winds remain a problem, but it was still comfortable to fly in 10 m/s (wind in 2 m height, not measured higher up at an altitude of 50 to 70 m) in the Fly-By-Wire-mode (assisted flying) and was acceptable in manual flight mode. A summary of the pros and cons of the various DIY platforms tested can be found in Table 4.3, with pictures of the different platforms in Figure 4.7.



Figure 4.7: From left to right: Skysurfer, Penguin, interior of the Penguin, DJI Phantom 3 Pro.

4.2.3.3 Electronic components

The electronic components are exposed to cold conditions during transport to the site and the flights themselves. To ensure a working aircraft in cold conditions, all electronic components were tested in a controlled freezer. This test was separate from the battery test, since the batteries are stored in warm conditions. For the experiments, the electronics parts were left in the freezer at the indicated temperature for a minimum of one hour. Fig. 4.8 shows the wiring of the electronic components tested.

This test was not conducted for the DJI Phantom 3 Professional (the benchmark, off-the-shelf platform), as operational ranges were provided by the manufacturer (DJY, 2015). Table 4.3 lists the X-UAV Talon for reference, however this platform has not yet been used in fieldwork. Cameras were not tested either, as they are not critical for safe flights.

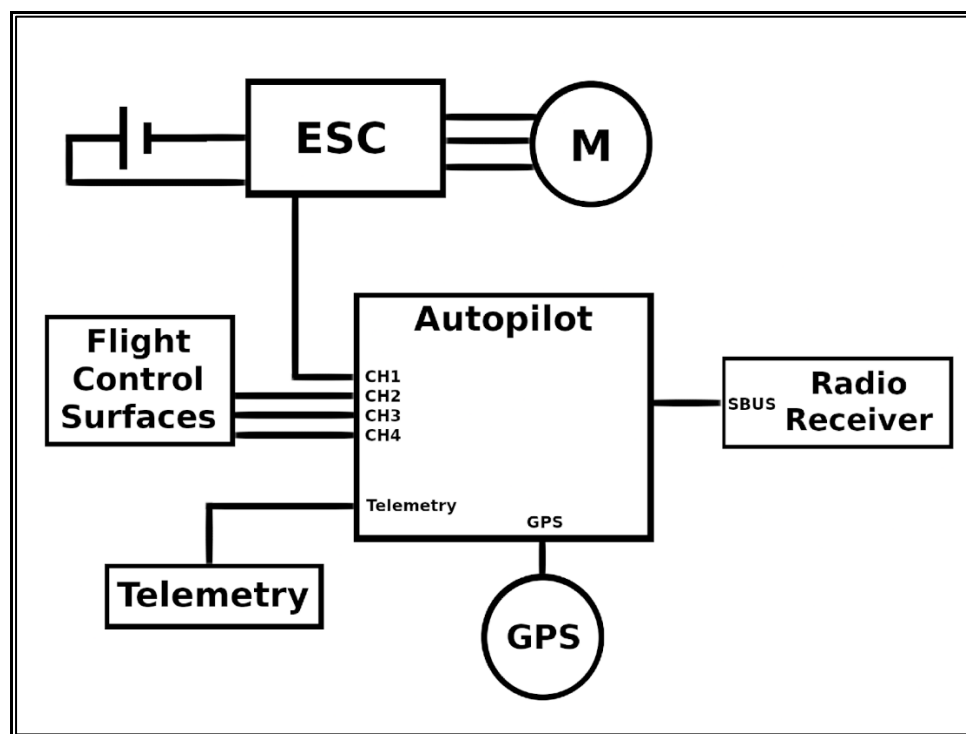


Figure 4.8: Wiring diagram of the electronics.

Results and discussion

As shown in Table 4.3, the operational temperature range of the aircrafts differ. As the BlitzRCWorks Skysurfer Pro stopped operating at -5 °C, tests were not continued below this limit. Similarly, tests for the Finwing Penguin and X-UAV Talon were not conducted above -15 °C, as they had already been shown to be operational down to -40 °C and with limitations to -50 °C. The BlitzRCWorks Skysurfer Pro can only be used in above-zero temperatures, as the ESC stops working below 0 °C. The ESC directly controls the engine and thus is essential for automated flight. Manual flights during fieldwork are still possible and have been conducted between -20 °C and -30 °C. The Finwing Penguin and X-UAV Talon have proven to be fully operational down to -40 °C, though at -50 °C the servo motors that control pitch, yaw, and roll had a reduced range of movement. Based on these results, both aircrafts can be flown down to temperatures around -40 °C. This test also showed that the other components like GPS, telemetry module, radio receiver, and autopilot (in this case Pixhawk 2) are operational in the tested temperatures.

Mounted sensors

To date, only two types of cameras have been used in the DIY UAV system design. The main camera system used during fieldwork is a GoPro 6. In addition to having a robust, waterproof design, the GoPro 6 can be used in temperatures around -30 °C for the duration of two flights and preparation (about 1 hour). The other camera used is the standard camera on the DJI Phantom 3 Professional. This was used during summer missions and produced reliable results, which are presented in the next chapter. A small camera (MAPIR Survey 3, circa 50 g, 59 x 41.5 x 36 mm) and a small frequency-modulated continuous wave (FMCW) Ka-band radar system (circa 700 g, 200 x 130 x 150 mm) will be mounted on the DIY UAV design in 2019–2020. The radar system has already been used during fieldwork in

temperatures around -40 °C and has shown no signs of cold-related limitations. It will be used for UAV-based snow and ice thickness retrievals (Pomerleau et al., 2018).

Table 4.3: As the Skysurfer stopped operating at -5°C, tests were not continued below this limit. Similarly, tests for the Penguin and Talon were not conducted above -15°C, as they had already been shown to be operational down to -40°C and with limitations to -50°C. The ‘X’ means that the electronic device failed the test, the check mark that the test was successful and a check mark in brackets that the electronic device still worked, but at a reduced capacity.

Model	Temp. (°C)	ESC / arming	Servo	Comment
SkySurfer Pro	0	√	√	
	-5	x	√	
	-10	x	√	
	-15	x	√	
	-20	x	√	
	-30	x	√	
	-40	Na	Na	Tests were not conducted.
	-50	Na	Na	
Finwing Penguin	-10	Na	Na	Tests were not conducted.
	-15	Na	Na	
	-20	√	√	
	-30	√	√	
	-40	√	√	
	-50	√	(√)	Servos not moving at full range.
X-UAV Talon	-10	Na	Na	Tests were not conducted.
	-15	Na	Na	
	-20	√	√	
	-30	√	√	
	-40	√	√	
	-50	√	(√)	Servos not moving at full range.

4.2.3.4 Summary and outlook

The ability to customize specific UAVs for all needs and to change frames and re-use electronics make the DIY approach good for medium-sized research groups that can afford the manpower to build a DIY system. Another advantage of the DIY approach is high independence in the field if repairs and troubleshooting are required. With new technology

General operations

- To further customize payloads and general aspects of the ‘interior’ design, the DIY UAV system design uses a 3D printer. Many parts are available online or can be designed quickly. While polyactic acid was found to be an adequate material in most circumstances, an ecofriendly acrylonitrile butadiene styrene material was used for most purposes. The 3D-printed plastic parts were less brittle than expected.
- To reach the research sites it takes ≥ 30 minutes by snowmobile. These trips are hard on any material. Since experiments with heating the aircraft did not work well, the current best practise is to allow the frame to cool down and simply cushion it for the hard ride. Since some glues (e.g., underside of Velcro-strips) lose adhesiveness in the cold, it is better to use mechanical mounting where possible.
- Experiments also showed it is important to keep the batteries warm until the last moment. Initially, 4000 mAh batteries were used. After conducting the test series, 5200 mAh batteries were mainly used. This switch increases the weight and reduces the payload capacity for sensors, but the additional flight time makes up for this.
- While hard landings can occur, surface scratches can be repaired easily with Tuck Tape, superglue, and epoxy.

4.2.3.5 *Future work and development*

In the early stages of the development, it was necessary to take manual control of the aircraft several times (ESC-failure, autopilot settings, etc.). During campaigns in spring and summer 2019, the problems have been solved and the autopilot is working great. For the purpose of flight operations in polar winter conditions, fixed-wing UAVs will be used for most missions, unless specific requirements are needed (e.g. hovering and low altitude flights for radar measurements). Plans to build a quadcopter in late 2019 will enable flights with the new FMCW radar system. Another future development will be to increase payload flexibility.

Work is also currently underway to develop a mounting system that will support both DIY and off-the-shelf systems with a small adapter unique to the UAV. Being able to mount independent payloads on any system will allow scientists to conduct research most efficiently. As of 2019, several reasonably priced, off-the-shelf UAVs (e.g., the DJI Phantom 4 RTK and DJI Matrice 600 Pro, which are both under US\$ 10 000) have entered the market. The great advantage of newer off-the-shelf UAVs is the plug-and-play capability. This enables inexperienced users to achieve reasonable results in very short time. However, inexperienced users typically have a lesser understanding of how the UAV works and limited manual flight experience. Since operations take place in a challenging environment, that adds a lot of stress due to its natural conditions, this is a concern.

4.2.4 UAV – Application: Snow Depth Retrieval

This section demonstrates the capabilities of the project's DIY UAV system design in retrieving snow depth in the Arctic. The technique used for retrieving snow depth from UAV is based on the structure-from-motion (SfM) workflow described below. This technique is widely used by scientists and surveyors (Fernandes et al., 2018). From this workflow, precise topographic maps are obtained and can be used for many applications,

including temporal evolution of landslides (Turner et al., 2015), and reconstruction of an historical building (Murtiyoso et al., 2017).

4.2.4.1 Introduction

This section demonstrates the capabilities of the project's DIY UAV system design in retrieving snow depth in the Arctic. The technique used for retrieving snow depth from UAV is based on the structure-from-motion (SfM) workflow described below. This technique is widely used by scientists and surveyors (Fernandes et al., 2018). From this workflow, precise topographic maps are obtained and can be used for many applications, including temporal evolution of landslides (Turner et al., 2015), and reconstruction of an historical building (Murtiyoso et al., 2017).

- Nolan et al., (2015) mapped snow depth in Alaska by aircraft, using SfM with a consumer grade camera. They were able to achieve 10 cm precision on snow depth for arctic snow where influences of vegetation and other factors were minimized.
- Cimoli et al., (2017) mapped snow depth in Svalbard and Greenland with UAVs but used a terrestrial DSM to acquire snow-off conditions in summer. They measured a range root mean square error for multiple sites from 5 to 18 cm.
- Bühler et al., (2016) mapped snow depth in alpine terrain with UAVs. Their study shows that SfM works for snow depth in alpine terrain to an acceptable accuracy, with an RMSE of 0.07 m to 0.15 m in meadows and an RMSE of less than 0.3 m in areas with bushes or tall grass.

The SfM workflow uses multiple images to create a three dimensional (3D) reconstruction. The first step is to find features (or tie points) that appear in multiple images. These points are found by using the Scale Invariant Feature Transform (SIFTs) detection

algorithm (Lowe, 2004). An initial 3D reconstruction can be done using estimated camera parameters (position and orientation), which yields to a 3D point cloud. This process is optimized by using Bundle Adjustment (Granshaw, 1980).

Snow depth retrieval Application

For the purpose of this project, ground control points (GCP) with well-known positions were used to refine camera parameters and provide a GPS datum for the point cloud. This project used Agisoft Photoscan version 1.4.3 and the GCPs were acquired using a differential GPS (dGPS) system that consists of a Trimble Net R9 with Trimble Zephyr Geodetic antenna as a base station, and a u-blox receiver as a rover. A base station point was measured from 5 hours static acquisition with a sampling interval of 1 second. Then the position was refined using Precise Point Positioning (PPP) from Natural Resources Canada.

The relative accuracy of the targets is 0.5 cm on the X-/Y-axes and 1 cm on the Z-axis. This is the accuracy from the dGPS software used (EZSurv version 3.98.374 from Effigis Geo Solution), but absolute positioning accuracy depends on the PPP result from the base station ($X, Y, Z = (2, 3, 5 \text{ cm})$). The absolute positioning error matters when two sets of measurements are compared, e.g., to differentiate two DSMs, whereas relative positioning refers to the accuracy within each set. For example, the accuracy of GCPs specified in Agisoft Photoscan during the DSM calculation is relative to positioning. The absolute accuracy on the other hand would impact the overall error of the snow depth map.

One major issue is the link to the absolute accuracy of the base station. For winter and summer flights, the base station was not set on the same point, which led to more uncertainties in positioning. A rod was driven into the ground to create a static point for future field campaigns. The risk that the rod will rise from cryoturbation remains low in this area. It will be important to set up the base station for winter and summer flights on this point so

that the absolute error in positioning can be eliminated. A correction had to be made by adding 10 cm to winter DSM from a known snow free zone that had negative snow depth. The snow free zone was barely covered by snow, but rocks were clearly visible. This small area had an average snow depth of -13 cm, so a 10 cm correction was applied to the entire snow depth map (i.e., winter DSM). Again, because the base station was not set on the same point, this offset is also on the same order of magnitude if the uncertainty of the two points ($z = 5$ cm) from the PPP result are added. With a snow free zone, one can improve co-registration of both DSMs (Nolan et al., 2015).

A total DSM was constructed by merging multiple flight zones surveyed over two to three days (see Table 4.4). Conducting validation measurements from snow probing is time consuming and they were done immediately after each flight, limiting the number of flights per day. Dates for the different flight can be found in Tab. 4.4. Different light conditions are not optimal as they induce an error in the 3D reconstruction process from the SfM workflow and must be considered. Manual measurements of snow depth were conducted for validation of the DSM using an avalanche probe, geolocated with the dGPS antenna. Notably, the typical hand-held GPS of new devices, like the Magnaprobe (Sturm, 2018), do not have a sufficient X, Y, Z precision since the DSM pixel size is approximately 5 cm. These measurements were done with an avalanche probe paired with the same dGPS system used for the GCPs. This provides excellent correspondence between validation points and the map derived by UAV. Given the very high spatial variability of snow depth and the pixel resolution of approximately 4 to 6 cm retrieved from the SfM approach, such a precision is essential. In total, 155 validation points (see Figure 8) were taken and are spread throughout the mapped area of 40 000 m². For more information on the study site see Appendix B.

4.2.4.2 Results and discussion

Agisoft Photoscan was used to process all images. Fig. 4.9 shows both the DSM and the orthophoto of snow-on and snow-off conditions. The resolution of the DSM is 4 cm for the summer flight and 6 cm for winter flight. A total of 18 GCPs (see Figure 4.9) were used for optimizing camera parameters and positions. No GCPs were available for external validation so it is not possible to provide an external estimation of the precision of the DSM. The error per GCP is 8 cm on average (see appendix D) and is therefore intrinsic to the optimization because it reduces the difference between the true position of GCP and GCP position on the point cloud by optimizing camera parameters (more details on GCPs can be found in Appendix A and D). In the future, the DIY UAV design will feature a dGPS system that will provide fixed solution (real-time kinematic precision) for all pictures taken during flight. This will allow use of most GCPs for evaluating the precision of the DSM and leave 3 to 4 GCPs for optimization (if needed). This is necessary to maximize the precision and robustness of the DSM and to detect systematic errors (James et al., 2017; Goetz et al., 2018).

In Figure 4.9 (a), a zone of vegetation can be seen on the west and rockier ground on the east. The vegetation can be characterized by shrubs and segdes, more specifically *Salix richardsonii* and *Carex aquatilis*. This impacts the precision of the snow depth map as highlighted in Fig. 4.10. The uncertainty arises from snow compaction on vegetation where the DSM summer surface (i.e., vegetation surface) is lower under compacted snow. This is in agreement with higher RMSE values recorded by Nolan et al., (2015) and Bühler et al., (2016) in vegetated areas. As for the winter DSM, there is clear influence of the wind on the snow, leading to compacted snow drifts (see Appendix C for full size orthophoto). These snow drifts provide lot of contrast to the picture and make it easier to detect points in multiple images, even though the pictures are mostly white. Some GCPs appear to be outside of the DSM/orthophoto (Fig. 4.9). This is an artificial effect, as only the regions with enough

overlap between pictures are used for creating the DSM. The overlap between both DSMs is equivalent to the snow depth map (see Figure 8). Also shown in Fig. 4.10, there are 155 validation points, with an average of 33 cm snow depth.

Table 4.4: DSM description for summer and winter flights. Both flights were in manual mode.

DSM	UAV	Flight	Additional Info
Snow on (winter)	Sky Surfer Pro (Fixed wing)	Mode: Manual Zone: 40000m ²	No. images: 548 Resolution (DSM): 6 cm Altitude: 20-50 m
Flight	Date		Area (m²)
	1	2018-04-23	20000
	2	2018-04-26	20000
Snow off (summer)	DJI Phantom 3 (Multi rotor)	Mode: Manual Zone: 40000m ²	No. images: 709 Resolution (DSM): 6 cm Altitude: 50 m
Flight	Date		Area (m²)
	1	2018-07-11	10000
	2	2018-07-17	10000
	3	2018-07-25	20000

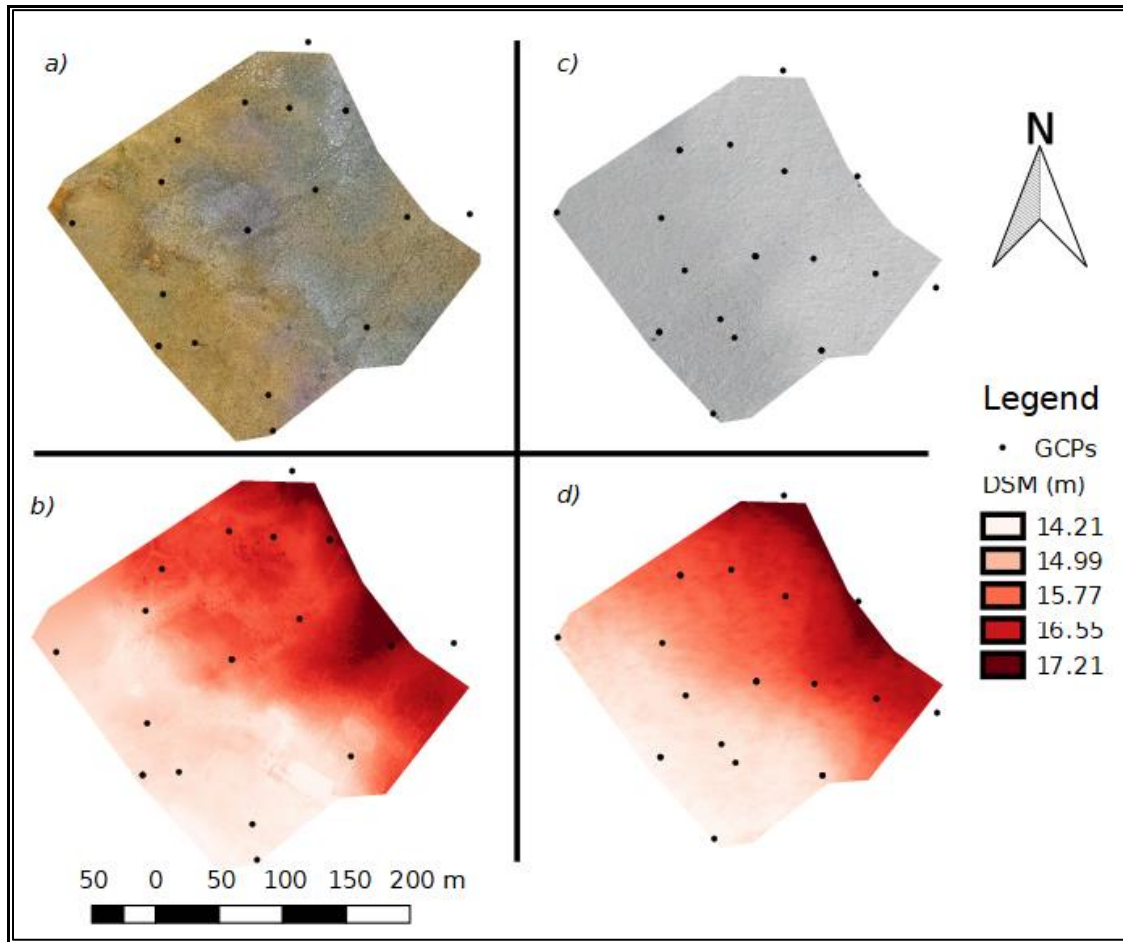


Figure 4.9: Orthophoto and DSM images of the study site near Cambridge Bay (69°13'19.66" N, 104°53'54.91" W). The upper left (a) shows the orthophoto from the summer flight with more vegetation on the left and more rocks on the right. The lower left (b) shows the resulting DSM from the summer flight. On the right side (c) and (d) show the orthophoto and DSM results for the winter flights.

Fig. 4.11 shows the comparison between snow depth from validation points and from the dDSM UAV map. The orange line represents the best correspondence between validation points and the UAV map. Validation points over vegetation are marked in red and were removed on the second graph in Fig. 4.11. Vegetation areas were identified using a combination of photographs from the DIY UAV design and ground observations. It can be seen in Tab. 4.5 that these vegetation points have an impact on the correlation and the RMSE. Overall, the RMSE is 16 cm, which is comparable to the literature.

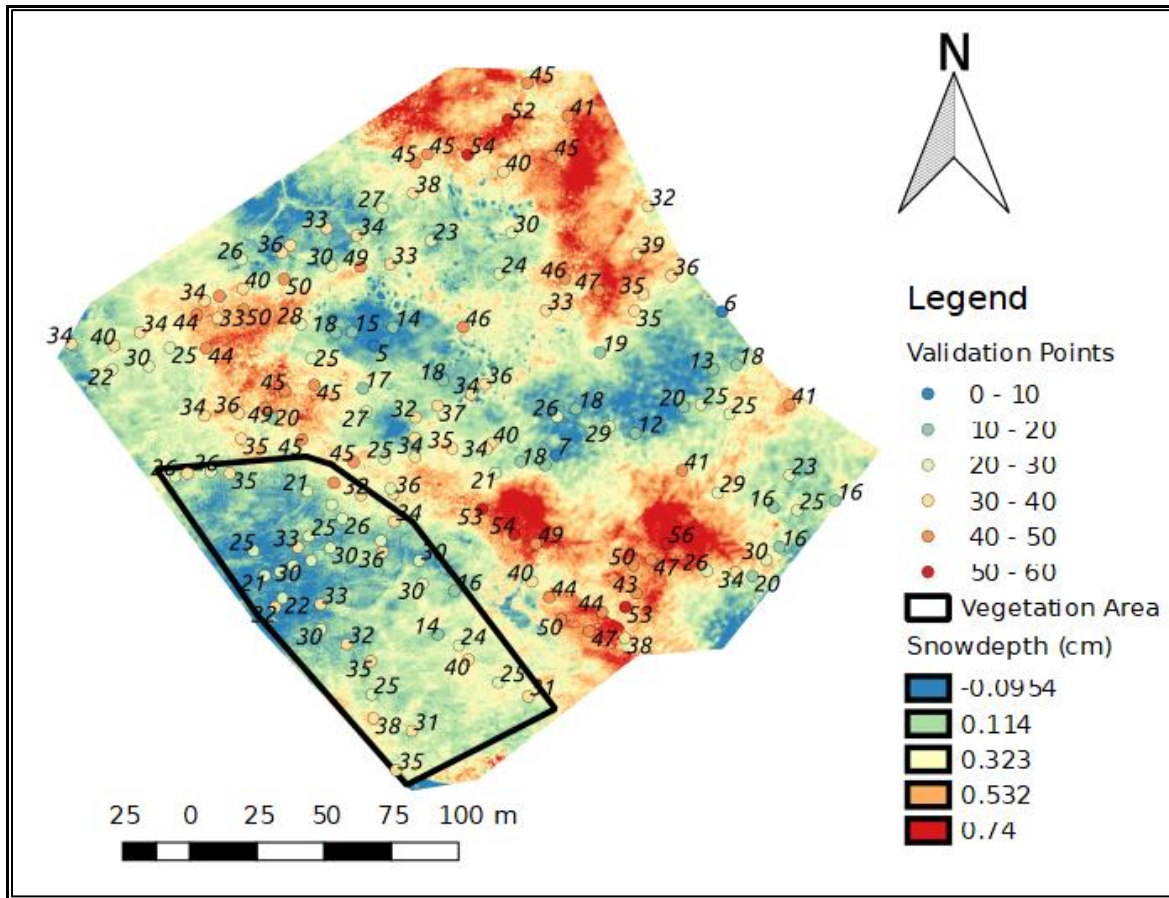


Figure 4.10: Snow depth map resulting from the SfM approach. The delimited area in black shows negative results and is due to the influence of the vegetation.

Compared to work in alpine regions or tundra environments, the arctic snowpack near Cambridge Bay is rather small with an average of 33 cm, measured in early spring (April 2018). Therefore, micro-topography and vegetation have a stronger influence on the map accuracy. Improvements are possible for Global Navigation Satellite System handling and processing (as explained above) with the 10 cm off correction applied to the winter DSM. Further improvements will also be possible by switching from manual flights to automated flights, as a constant altitude and constant overlap will increase the uniformity of the point cloud. Additionally, setting the camera to fixed camera parameters and flying zones on the same day will give constant light conditions and reduce reconstruction uncertainties of the point cloud (Bühler et al., 2017). A higher-resolution camera will also be tested for better DSM results (see Appendix A for camera info).

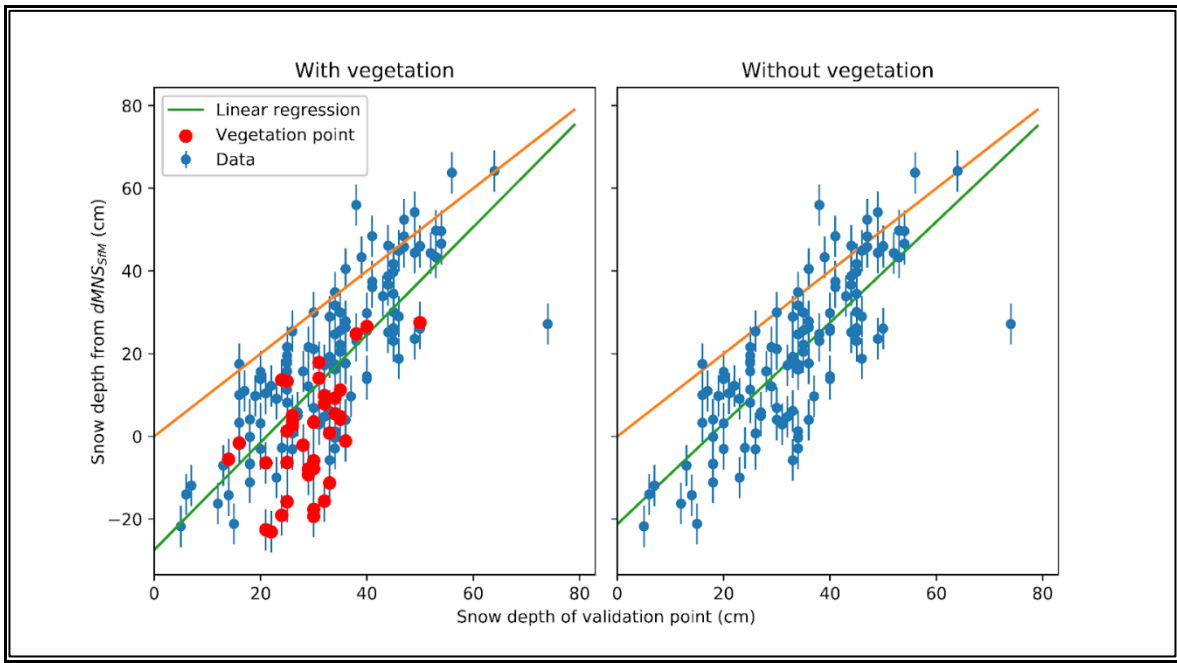


Figure 4.11: Regression between the validation points and the UAV points.

Table 4.5: Linear regression parameters and RMSE from snow depth validation points.

	With Vegetation	Without Vegetation
a	1.30	1.22
b	-18	-11
No. of points	155	118
RMSE	16cm	13cm
R²	0.57	0.64
p-value	2.14e ⁻³⁰	1.66e ⁻²⁷

4.2.5 Conclusions

This project aimed to build an aircraft capable of flying in winter conditions in the North, as such the focus was on material testing for cold temperatures. Batteries and electronics were tested at various temperatures to understand their limitations before using them in the field. Initially, there were no battery preferences. For the experiments, different sized and shaped batteries were purchased for use in this project and others, such as powering the radar system. Being able to have a variety is beneficial and allows for battery selection based on mission requirements. The fixed-wing DIY UAV designs are close to their maximum payload, so somewhat smaller batteries are preferred on these missions. In contrast, the yet-to-be-built quadcopter will benefit from more lifting capacity, so the battery size will matter less.

Currently, an additional Finwing Penguin aircraft has been purchased. It has a stronger engine than the BlitzRCWorks Skysurfer Pro, was easier to fly in wind, and was easier to prepare and maintain in the field. The next steps will include designing and building a quadcopter for the radar system. It currently requires a system capable of relatively low and slow flight. While a glider can provide the later, low flights (under 5 m) are too risky. Additionally, the hovering ability will make it easier to aim for nadir measurements. Small deviations will occur and the research team will have to decide whether to counter them with a gyroscope or an electronic accelerometer. The latter has the benefit of being lighter, the former of actually achieving nadir. In addition, working more frequently on the X-UAV Talon platform will allow future flights in higher wind speeds.

In terms of scientific applications, the next intuitive step is to add a Normalize Difference Vegetation Index (NDVI) layer to the snow depth map. This will establish an empirical relationship between snow depth bias and vegetation type. This could also lead to

a finer scale analysis of snow-shrub interaction (Sturm et al., 2001). Furthermore, an analysis of micro-topography is planned using a topographic index, such as an upwind slope index, with dominant wind to better understand the snow redistribution processes (Winstral et al., 2002). This can be useful in soil thermal applications. This type of map is rather rare in the Arctic given all the logistical constraints highlighted in this work. Despite the scarcity of the available data to date, future snow depth information at high resolution will be beneficial for hydrology (melt timing, geochemical processes), permafrost (active layer monitoring) and ecology (habitat characterization). Many physical processes at this level influence larger-scale processes, and detailed snow distribution maps could be used to analyze sub-pixel variability of snow models or surface state retrievals (i.e., snow water equivalent) derived from coarse resolution satellite imagery.

4.2.6 Acknowledgements

The authors would like to thank David Rancourt and Alexis Lussier-Desbiens for their training and support in building and modifying our frames. Their knowledge and experience in UAV design contributed significantly to the success of our flights. This project was funded through Polar Knowledge Canada, the National Science and Engineering Research Council for Canada, and the Fonds Québécois de la recherche sur la nature et les technologies. Special thanks to the staff of the Canadian High Arctic Research Station and the community of Cambridge Bay, Nunavut, for their tremendous logistical support during the field campaigns.

4.2.7 Appendix

Appendix A

Description (Tab. 4.6) of both cameras used for the snow depth map, the Go Pro had to be used in linear mode to avoid the fisheye distortion from these types of action cameras however, this reduces the resolution. We also recorded and tested videos (instead of photographs) while flying which led to a loss of spatial resolutions and much heavier post-processing.

Table 4.6: Camera parameters used in both DSM.

Camera	mode	Sensor	FOV	Resolution
GoPro 6 (winter DSM)	normal	1/2.3" CMOS	122°	Photo: 12MP
				Video: 8 MP
	linear		85°	Photo: 8 MP
				Video: 5 MP
Phantom 3 Pro (summer DSM)	normal	1/2.3" CMOS	94°	12 MP
Sony a6000 (future work)	normal	23.50mm x 15.60mm CMOS	73°	24 P

Appendix B

Here is a map (Fig. 4.12) that shows our study site in Cambridge Bay, Nunavut, Canada. More specifically, it is located in Greiner Lake Watershed.

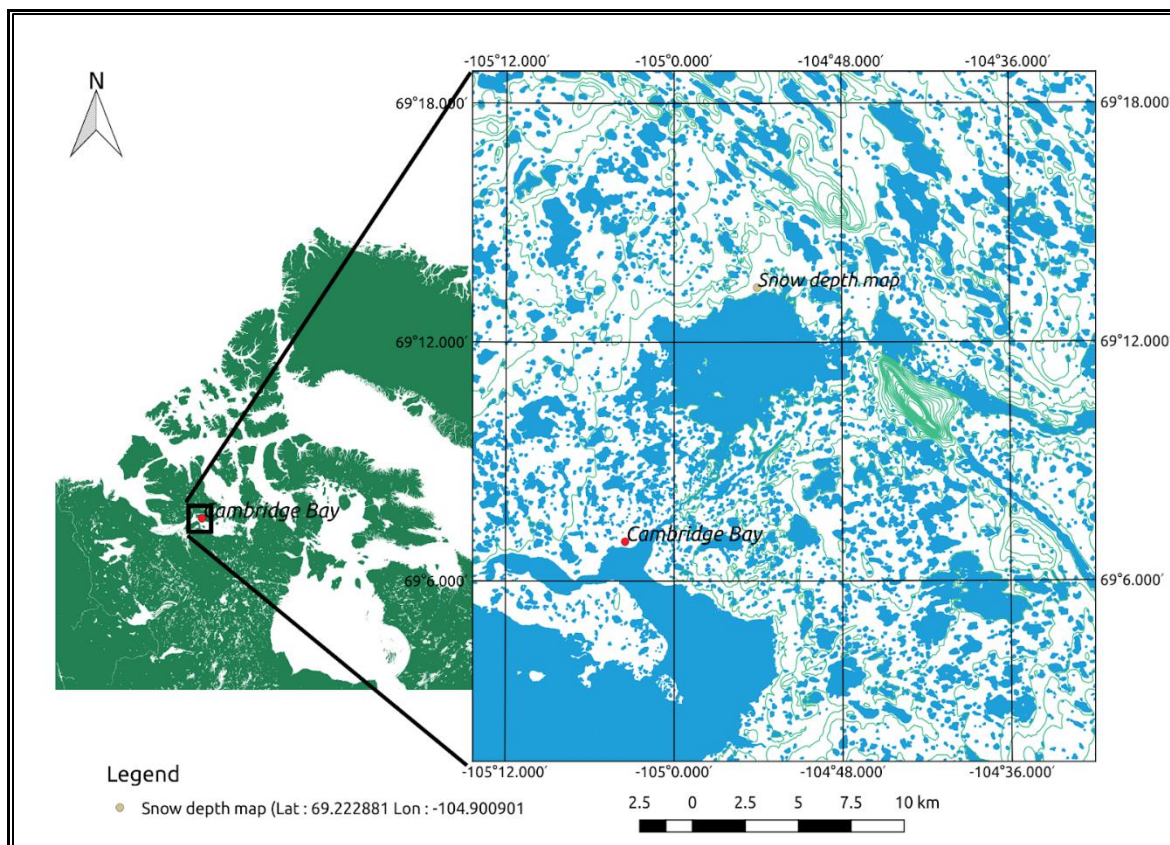


Figure 4.12: Map of study site at Greiner Lake Watershed.

Appendix C

Fig. 4.13 shows an overview of the orthophotos for April flights where snow spatial patterns caused by wind can be observed. The zone in black is the snow free zone used to apply the 10 cm correction.

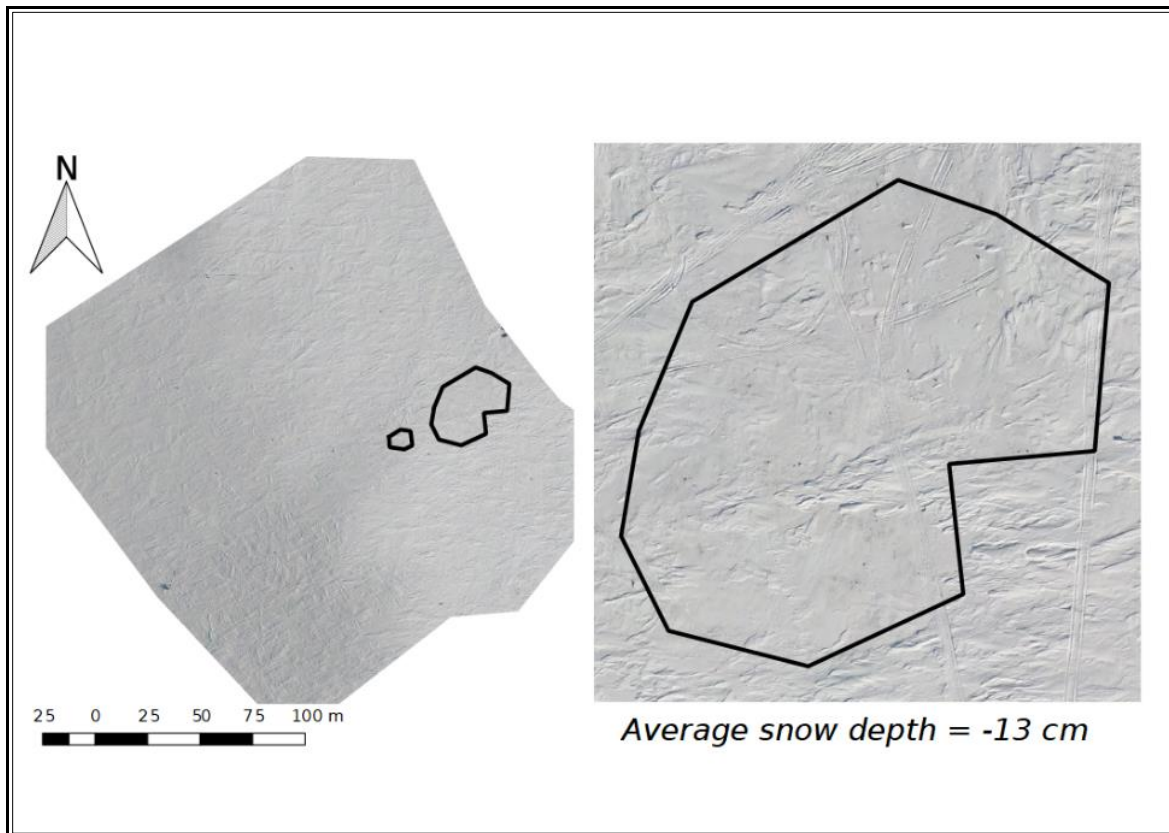


Figure 4.13: Orthophotos from April-flights.

Appendix D

Ground control points (GCPs) with their position accuracy related to the GPS system and the difference (Error (m)) between the position and the 3D model. Fig. 4.14 and Fig. 4.15 are screenshots from Agisoft Photoscan software.

Markers	Easting (m)	Northing (m)	Altitude (m)	Accuracy (m)	Error (m)	Projections	Error (pix)
<input checked="" type="checkbox"/> 101	503990.002000	7679155.692000	14.802000	0.005/0.012	0.028189	11	0.365
<input checked="" type="checkbox"/> 102	503924.449000	7679084.147000	14.112000	0.005/0.012	0.048929	12	0.767
<input checked="" type="checkbox"/> 103	503921.187000	7679108.808000	14.281000	0.005/0.012	0.058068	14	0.515
<input checked="" type="checkbox"/> 104	503869.852000	7679144.885000	14.388000	0.005/0.012	0.225831	10	0.589
<input checked="" type="checkbox"/> 105	503844.497000	7679142.810000	14.362000	0.005/0.012	0.111675	13	0.335
<input checked="" type="checkbox"/> 106	503906.737000	7679222.762000	15.545000	0.005/0.012	0.055086	4	0.135
<input checked="" type="checkbox"/> 201	503844.516000	7679142.837000	14.365000	0.006/0.016	0.118750	12	0.257
<input checked="" type="checkbox"/> 202	503906.727000	7679222.769000	15.551000	0.005/0.006/0....	0.050462	16	0.255
<input checked="" type="checkbox"/> 203	503847.647000	7679178.554000	14.611000	0.006/0.007/0....	0.029599	11	0.399
<input checked="" type="checkbox"/> 204	503784.159000	7679227.752000	14.868000	0.006/0.007/0....	0.106292	13	0.387
<input checked="" type="checkbox"/> 205	503846.518000	7679256.293000	15.020000	0.006/0.007/0....	0.148801	13	0.166
<input checked="" type="checkbox"/> 206	503857.960000	7679285.157000	15.722000	0.006/0.007/0....	0.083373	11	0.321
<input checked="" type="checkbox"/> 307	503904.894000	7679311.262000	16.051000	0.006/0.007/0....	0.065924	11	0.424
<input checked="" type="checkbox"/> 308	503949.014000	7679352.993000	17.370000	0.005/0.006/0....	0.027096	10	0.326
<input checked="" type="checkbox"/> 309	503935.949000	7679307.399000	16.135000	0.005/0.006/0....	0.080173	14	0.435
<input checked="" type="checkbox"/> 310	503975.339000	7679305.502000	16.586000	0.005/0.006/0....	0.056571	18	0.146
<input checked="" type="checkbox"/> 403	503954.077000	7679250.819000	15.961000	0.005/0.012	0.034524	11	0.311
<input checked="" type="checkbox"/> 404	504018.222000	7679231.977000	16.939000	0.005/0.013	0.024358	27	0.179
<input checked="" type="checkbox"/> 405	503975.348000	7679305.466000	16.591000	0.005/0.012	0.063655	30	0.198
<input checked="" type="checkbox"/> 406	504061.918000	7679233.983000	16.859000	0.005/0.013	0.069560	13	0.240
Total Error							
Control points					0.088421		0.353
Check points							

Figure 4.14: Detailed GCP-info from summer DSM.

Markers	Easting (m)	Northing (m)	Altitude (m)	Accuracy (m)	Error (m)	Projections	Error (pix)
<input type="checkbox"/> h101	503978.188000	7679133.123000	14.520000	0.005/0.007/0....		1	0.000
<input checked="" type="checkbox"/> h102	503926.303000	7679206.179000	15.461000	0.005/0.007/0....	0.174172	33	0.315
<input checked="" type="checkbox"/> h103	503850.712000	7679147.313000	14.394000	0.005/0.007/0....	0.123419	16	0.268
<input checked="" type="checkbox"/> h104	503892.990000	7679083.866000	13.925000	0.005/0.007/0....	0.033347	5	0.179
<input checked="" type="checkbox"/> h105	503909.732000	7679142.972000	14.579000	0.005/0.007/0....	0.079232	15	0.206
<input checked="" type="checkbox"/> h106	503898.660000	7679157.426000	14.531000	0.005/0.007/0....	0.095781	15	0.167
<input checked="" type="checkbox"/> h201	503926.097000	7679206.254000	15.364000	0.005/0.006/0....	0.148914	11	0.417
<input checked="" type="checkbox"/> h202	503866.532000	7679288.746000	15.821000	0.005/0.006/0....	0.109120	22	0.247
<input checked="" type="checkbox"/> h203	503770.092000	7679240.462000	14.778000	0.005/0.006/0....	0.002791	4	0.007
<input checked="" type="checkbox"/> h204	503850.527000	7679147.378000	14.302000	0.005/0.006/0....	0.122511	15	0.272
<input checked="" type="checkbox"/> h205	503870.563000	7679195.289000	14.702000	0.005/0.006/0....	0.102609	22	0.266
<input checked="" type="checkbox"/> h206	503852.197000	7679236.112000	15.068000	0.005/0.006/0....	0.036849	17	0.190
<input checked="" type="checkbox"/> h301	504006.304000	7679268.453000	17.202000	0.005/0.006/0....	0.016234	13	0.153
<input checked="" type="checkbox"/> h302	503947.821000	7679350.767000	17.616000	0.005/0.006/0....	0.021583	18	0.140
<input checked="" type="checkbox"/> h303	503866.535000	7679288.737000	16.038000	0.005/0.006/0....	0.106522	26	0.184
<input checked="" type="checkbox"/> h304	503906.376000	7679293.081000	16.165000	0.005/0.006/0....	0.073502	33	0.273
<input checked="" type="checkbox"/> h305	503948.947000	7679272.426000	16.285000	0.005/0.006/0....	0.034830	46	0.189
<input checked="" type="checkbox"/> h306	503926.115000	7679206.239000	15.597000	0.005/0.007/0....	0.095605	30	0.219
<input checked="" type="checkbox"/> h402	503977.996000	7679133.203000	14.678000	0.005/0.007/0....	0.048365	12	0.170
<input checked="" type="checkbox"/> h403	504068.110000	7679181.896000	16.492000	0.005/0.007/0....	0.007212	8	0.038
<input checked="" type="checkbox"/> h404	504020.517000	7679192.817000	16.455000	0.005/0.007/0....	0.030709	12	0.455
<input checked="" type="checkbox"/> h405	503971.808000	7679204.446000	16.144000	0.005/0.007/0....	0.059606	13	0.207
Total Error							
Control points					0.086695		0.242
Check points							0.000

Figure 4.15: Detailed GCP-info from winter DSM.

Appendix E

We can separate the components in our UAV into two different categories (Fig. 4.16):

1) mechanic (frame) and 2) electronic. First, the frame is the actual UAV itself. In our case the type is a fixed-wing. It is followed by all the electronics inside (related to the autopilot). One of the advantages of the DIY-approach is that you can re-use and cross-use the electronics for different UAVs (incl. fixed- and rotary-wing).

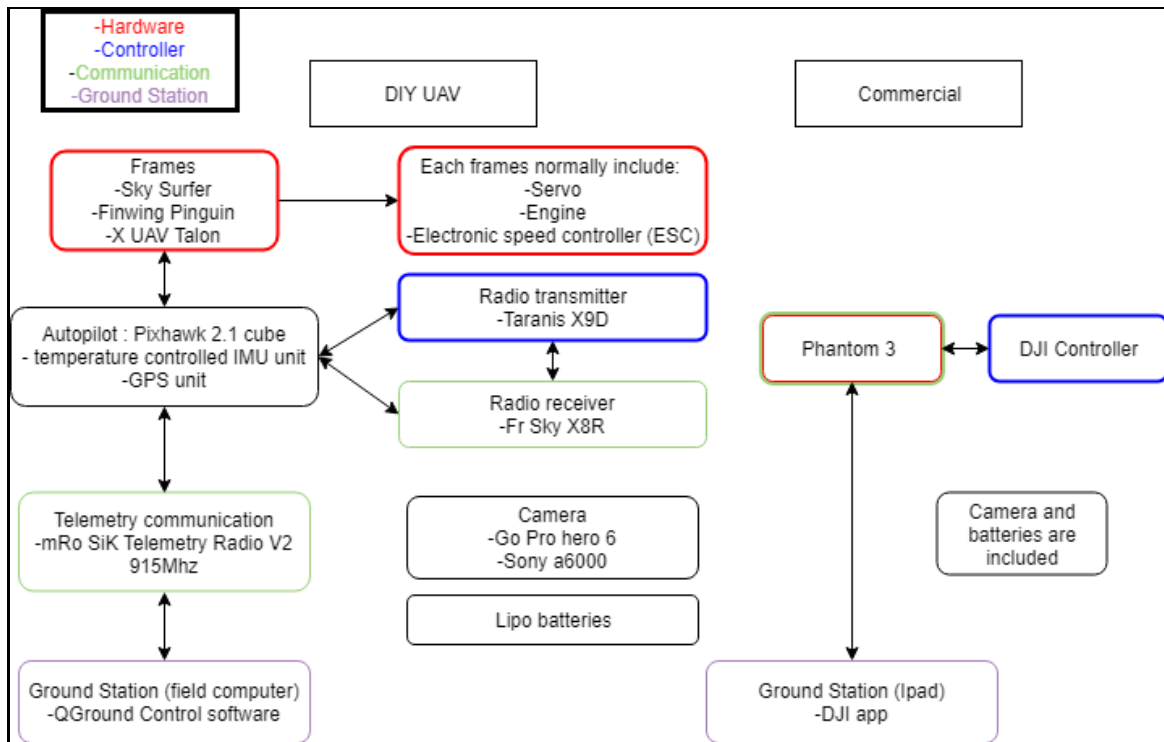


Figure 4.16: DIY-components (left) vs. Commercial components (right).

4.3 COMMENTARY

4.3.1 Comparison to the literature

In this study, we had an average snow depth of 33 cm with an RMSE of 16 cm. This leads to an error of 48.5 %. At a first glance, this sounds like a large error. Thus, a comparison to the literature is necessary to show that our results are in absolute terms similar, but in relative terms we encounter a large error since we are operating at several limits.

4.3.1.1 *Relative and absolute margins*

Our method is based on Fernandes et al. (2018), who states that “Current UAV imaging methods may have a practical lower limit of ~30 cm SD due to the combined errors in estimating the snow-covered and snow-free surface elevation”. With the given snow depth in Cambridge Bay, we are operating at and partially below this practical limit. They achieve an error of 0.02 m and 0.11 m, compared to our error of 0.16 m (0.13 m without vegetation), thus our error margin is only slightly higher.

Gun et al. (2021) studied snow depth over lake ice and compares their results to different environmental settings. For glaciers and open natural environments, they find RMSEs of under 0.3 m and for vegetated areas of up to 0.5 m. The environment in Cambridge Bay can be described as an open natural environment with small vegetation. In either case, we outperform this. Gun et al. (2021) achieve an RMSE of 0.06 – 0.08 m with an average snow depth of 60 cm, leading to an error of 10-13 %. The snow depth in Cambridge Bay is only half of that, so the relative errors increase. Further, Gun et al. (2021) took their measurements over lake ice, usually a smooth surface if compared to the open tundra in Cambridge Bay.

Walker et al. (2020) mapped snow depth in Trail Valley Creek (TVC), an open tundra environment. Their RMSE is 0.15 m, comparable to ours. Nevertheless, they encounter snow depths of up to 3 m (compare fig. 4.17). Thus, the relative error is much smaller.

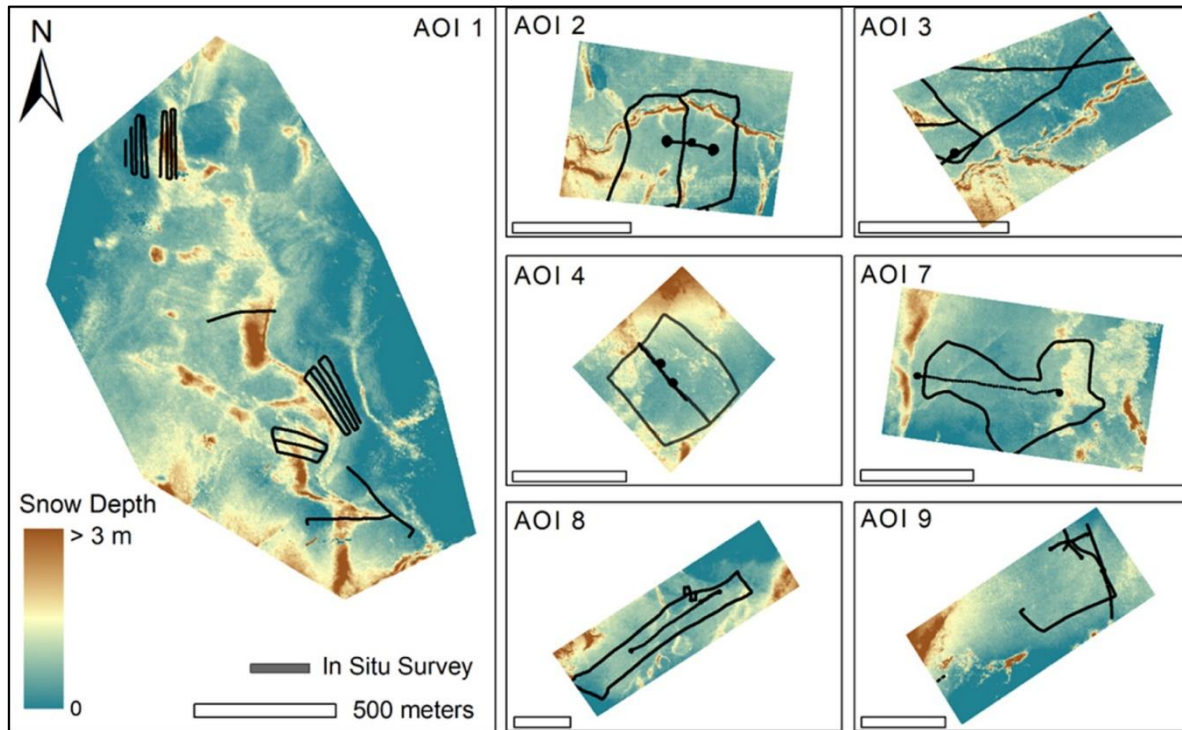


Figure 4.17: Results from Walker et al. (2020). Please note the snow depth coloring. Comparable to Cambridge Bay are only the bluest parts.

Dickson (2022) uses SfM for snow depth measurement for Coastal British Columbia. Their initial RMSE-range is 0.36 – 0.59 m. After a bias-removal for ground classification, an RMSE of 0.08 m was achieved for open areas (e.g. roads). In off-road situations, the best result had an error of 0.18 m.

All these examples show that we have achieved the initial goal to built and operated a DIY RPAS in the Arctic that collects data comparable to the literature. Only the local conditions and the difficulties working in remote regions lead to a larger relative error.

4.3.1.2 Remarks on the reference method

As a reference method, we use an avalanche probe with a pointy top. The Arctic snow is often very hard, sometimes permeated by (several) layers of ice. A lot of force is necessary

to push the probe through these layers and it frequently requires multiple attempts. It is entirely possible that an over-probing occurs, meaning that the top of the probe is pushed into the ground. Despite a frozen ground, the probe can penetrate a small amount, esp. if the ground is covered by e.g. a thin layer of moss. Other terrain features or larger vegetation is not considered either and it would be difficult to account for that as it would require the removal of snow over the area. The rock could land between two rocks, which the SfM-method would see as one feature (despite high resolution cameras). This introduces an unquantifiable error to the comparison of both methods, which has nothing to do with SfM itself.

4.3.1.3 Fieldwork in the North

Campaigning in remote regions introduces another problem. Usually, the time spend in the area is limited to days or weeks. It is not feasible to wait for perfect conditions and usually every opportunity is taken that allows to take measurements. Compared to studies in more accessible areas, it introduces an uncertainty as well. Similar to the previous point, it is hard to quantify or avoid.

4.3.2 Comparison to snowpits

Tab. 4.8 summarizes the advantages and disadvantages of RPAS-based SfM. The advantages counter most of the disadvantages of the snow pit (Tab. 3.1). The aerial aspect removes the single point issue of the snow pit measurements. The images are objective and allow other to redo the work easily and it also addresses the footprint: In a sense, the image is equivalent to the footprint and thus as large the area of the footprint is, the large the amount of data that can be used. As the RPAS is flying over the area, it is a non-destructive method and allows for repetition (more than one point in time possible). The method allows further to do measurements in inaccessible or dangerous terrain, e.g. during high avalanche danger.

The greatest disadvantages of the methods are the heavy dependency on a variety of technology (flight-related electronics, positioning, imaging) and fairly good weather. The

RPAS can fly in the cold, but heavy winds (>10-15 m/s) or rain/snowfall would inhibit operations. From a scientific perspective, the RPAS collects only one measurement (snow depth) but requires initially two missions to retrieve the snow-off data. This is not cost effective and may impede using the device if there is only a winter mission possible.

Table 4.7: Advantageous and disadvantageous of SfM.

SfM	
Pros	Cons
<ul style="list-style-type: none"> - Aerial - Objective - Non-destructive - Dangerous / inaccessible areas 	<ul style="list-style-type: none"> - Tech-heavy - Weather depending - No snow characteristics - Two missions necessary

4.3.3 Towards the next chapter

Maps of snow depths are required by the scientific community. Thus, it would make sense to find a method to counter the disadvantageous of SfM. The Snow-and-Ice-RAdar (SIRA) is a small, compact radar controlled by a Raspberry Pi. Both items are robust and simple to use. With this radar, it is possible to measure quantities inside the snowpack and combined with a precise positioning system, it would be possible to counter all drawbacks of the SfM. The first step, the development of an algorithm to retrieve snow depth and stratigraphy of Arctic snow from the SIRA, is the aim of the following chapter. The modification of the SIRA to collect a precise 3D position and consequently produce maps of retrieved snow information will be addressed in chapter 6.

5 ASSESSMENT OF ARCTIC SNOW STRATIGRAPHY AND WATER EQUIVALENT USING A PORTABLE FREQUENCY MODULATED CONTINUOUS WAVE RADAR.

5.1 INTRODUCTION TO ARTICLE

In the previous chapter, I elaborated on the development of a platform to carry different payloads, while being able to operate in Arctic conditions. I used the SfM-method to counter the disadvantages of snow pits. In a similar fashion, I wanted to develop a new method that can counter the disadvantageous of SfM (Tab. 4.8).

SfM requires two mission (costly) and delivers only snow depth. A sensor with the ability to see into and through the snowpack would be ideal. It would detect snow layers and the ground, consequently countering both drawbacks of SfM. SIRA, the Snow-And-Ice-Radar developed by Pomerleau et al. (2020), fulfils these criteria. It is small and robust, but it was lacking the following attributes:

1. No algorithm for Arctic snow existed.
2. The existing algorithm was not able to distinguish the ground unless the distance was known, or a metal plate was used.
3. Snow density must be available to correct the measurements.
4. No high-precision geolocation unit was implemented.

If the four points could be solved, it would address the need for representativeness and statistical distribution (Langlois, 2022; Meloche, 2022) that are necessary to tackle limitations in remote sensing approaches (Tsang et al., 2022) and the need for the

development of an Arctic snow model (Domine, 2019). Points 1-3 are the focus in this chapter, whereas chapter 6 will find a solution for geolocation issue.

To retrieve snow information from SIRA, snow density needs to be known. Consequently, for each radar measurement, snow measurements were conducted to collect density data associated with the SIRA signatures. This is time consuming as for each SIRA measurements we had to dig a snowpit. Thus, an empirical approach was developed using an average density based on previous field campaigns for each of the two main snow layers in the Arctic: DH and WS. The data analysis has also shown that the underlying ecotype seems to have an influence on the achieved radar accuracy. Unfortunately, not enough radar measurements per ecotype are available to produce a reliable statistic.

Fig. 5.1 displays the workflow of the development of the algorithm to tune SIRA to Arctic snow conditions. The chosen empirical approach used data from manual snow pits over several seasons and two research sites (Greiner Lake Watershed near Cambridge Bay, Nunavut, Canada) and the Trail Valley Creek research camp (near Inuvik, Northwest Territories, Canada). As mentioned above, the Arctic snowpack can be simplified in two main layers that have been used to predetermine the radar profiles.

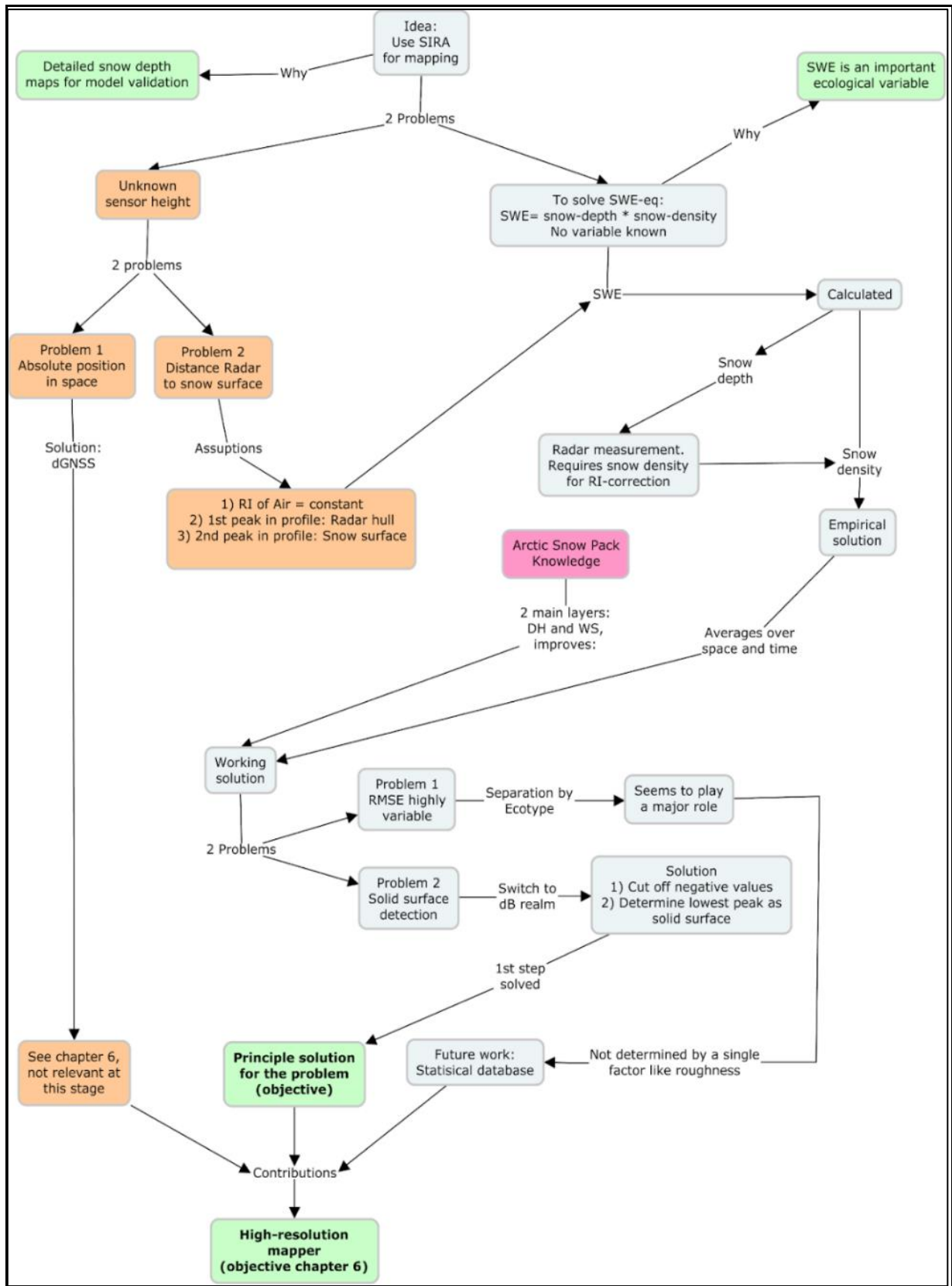


Figure 5.1: Workflow of the algorithm-development for SIRA.

5.2 ASSESSMENT OF ARCTIC SNOW STRATIGRAPHY AND WATER EQUIVALENT USING A PORTABLE FREQUENCY MODULATED CONTINUOUS WAVE RADAR

Daniel Kramer ^{a,b}, Alexandre Langlois ^{a,b}, Alain Royer ^{a,b}, Jean-Benoît Madore ^{a,b}, Joshua King ^c, Donald McLennan ^d, and Érika Boisvert-Vigneault ^a

^a *Centre d'Applications et de Recherches en Télédétection (CARTEL), Université de Sherbrooke, Québec, Canada.*

^b *Centre d'études nordiques, Québec, Canada*

^c Climate Research Division, Environment and Climate Change Canada, Toronto, Ontario, Canada

^d Polar Knowledge Canada

Citation

Kramer, D., Langlois, A., Royer, A., Madore, J. B., King, J., McLennan, D., & Boisvert-Vigneault, É. (2023). Assessment of Arctic snow stratigraphy and water equivalent using a portable Frequency Modulated Continuous Wave RADAR. *Cold Regions Science and Technology*, 205, 103683. <https://doi.org/10.1016/j.coldregions.2022.103683>

5.2.1 Abstract

There is significant spatial variability in snow cover characteristics across the Arctic. Current physical or empirical approaches to simulate or measure snow state variables suffer from poor spatial and/or temporal resolutions. Our current understanding of the spatio-temporal variability in Arctic snow cover leads to uncertainties in existing snow property retrievals from space or in models, thus leading to a poor representation of the snow cover in various climate models and reanalysis products. In this paper, we developed a method to derive total snow depth from a ground-based radar as well as distinguishing the two main layers generally observed in Arctic snowpacks: Depth Hoar and Wind Slab. This algorithm was developed for a 24 GHz Frequency Modulated Continuous Wave radar. The novelty of our approach resides in the fact that no validation snow pits are required if previous data on snow conditions (snow depth and density) are known. The impact of the underlying ecotypes on the radar-derived snow stratigraphy was also investigated. The RMSE of the snow depth ranges from 3.5 to 25 cm, but mostly varies between 10 and 15 cm (< 25%). The RMSE is based on snow pit data that has a corresponding radar measurement.

Keywords

Arctic snow; FMCW; radar; ecotype; snow pit; snow depth retrieval

5.2.2 Introduction

During winter, up to 80% of the landmasses of Eurasia and North America can be covered with snow (Shi et al., 2016), which plays a crucial role in the surface energy balance due to its high albedo and low thermal conductivity (Sturm et al., 1997; Giese and Hawley, 2015; O’Neil and Burn, 2017). In the Arctic, an accelerated warming has been recorded over recent decades, caused by a series of positive climate feedbacks (Serreze and Barry, 2011; IPCC, 2019). The warming amplification of the Arctic, also referred to as the arctic amplification, has been robustly linked over the last 40 to 50 years to negative anomalies in snow cover extent (Mudryk et al., 2018; Bormann et al., 2018; Thackeray et al., 2019) and an increase in winter liquid water precipitation over maritime regions of the Arctic (Callaghan et al., 2011; Langlois et al., 2017). Furthermore, changes in vegetation have also been reported by Zhang et al. (2018), who highlighted that shrub vegetation is expanding in response to the recent warming. Vegetation impacts snow depth and stratigraphy (Gacitúa et al., 2013; Busseau et al., 2017; Park et al., 2018; Royer et al., 2021), contributing to a high spatio-temporal variability in snow distribution which is challenging to both simulate and retrieve using remote sensing technique (Langlois et al., 2012; Gouttevin et al., 2018; Domine et al., 2019).

There is a critical need to improve techniques for monitoring snow state variability at high spatial resolution, as it was highlighted for example by Bokhorst et al. (2016). In particular, scarcity of data on the snow state leads to important limitations in model development for Arctic applications (e.g. Gouttevin et al., 2018; Domine et al., 2019), snow representation in climate models (Langlois et al., 2014) and poor performance in satellite retrievals of snow properties (Foster et al., 2005; Larue et al., 2017). Larue et al. (2017) stated that snow grain size (specifically Depth Hoar) has a strong impact on passive microwave

(PMW) retrievals (Langlois et al., 2012). PMW observations have been collected since the 1980s (e.g. Chang et al., 1982; Foster et al., 2005; Kelly et al., 2003). These approaches suffer from coarse spatial resolution, when local changes in mass (i.e. Snow Water Equivalent (SWE) affecting water availability) and/or microstructure (i.e. metamorphism affecting energy transfer) can't be distinguished despite their important implications for the ground thermal regime and the surface energy balance as a whole (Lemmetyinen et al., 2018). SWE is an important variable describing the state of the snowpack given that it is conditioned by density and thickness, which are driven by processes such as metamorphism, and mass balance change. Past studies, linking airborne (Langlois et al., 2008, 2012) or satellite (Che et al., 2014; Larue et al., 2017) brightness temperature measurements to snow models, have led to improvements in SWE retrievals, but the poor spatial resolution and limited availability of the meteorological and snow data remain an important restriction. This has led research efforts to develop snow state variable retrievals using active microwave sensors that have a finer spatial resolution. However, very few satellite missions are available at frequencies higher than X-band, which is outside of user requirements from a global snow retrieval perspective (Lemmetyinen et al., 2018).

Traditionally, direct snow measurements techniques for snow observations have proven their value by providing robust and detailed snow information and serve as a baseline reference for the development of models and remote sensing techniques. However, direct snow measurements methods remain time-consuming and have limited spatial coverage, especially in remote regions (e.g. Bergstedt et al., 2018; Zweng et al., 2018). Therefore, radar-based methods, as presented in a review by Marshall and Koh (2008), have been developed where snow depth can be derived if snow density is known. Frequency Modulated Continuous Wave (FMCW) radar can assess the stratigraphy of the snowpack, as demonstrated by Laliberté et al. (2021). They were able to identify highly contrasted layers

of density and snow grain morphology. Furthermore, such approaches allow the quantification of water percolation, as well as detection of refreezing crusts that can be of use in various applications such as hydrology and avalanche hazards assessment (Lalibert'e et al., 2021). Nevertheless, all available methods require direct snow measurements of either snow depth or snow density, which is a strong limitation for covering a larger area with radar observations.

This study examines the potential of using a lightweight and portable FMCW radar to monitor snow depth and snow stratigraphy at high spatial resolution and with centimetric vertical resolution. Furthermore, by using FMCW snow measurements, we seek to improve our empirical understanding of the spatial and temporal variability of the processes affecting snow microstructure and energy transfer. The main objective of this paper is to develop a method to quantify snow depth, stratigraphy and SWE using a FMCW radar at the watershed scale. The specific objectives of this paper are to:

- a) Empirically derive Refraction Indexes (RI) for Depth Hoar (DH) and Wind Slab (WS) that can be used in Arctic environments without further measurements of snow density and;
- b) From a) derive total snow depth (ds), SWE and stratigraphy (i.e. dDH and dWS thickness) assuming a two-layer snowpack that is representative of Arctic snowpacks (Royer et al., 2021);

5.2.3 Data and methods

5.2.3.1 Study sites

Combined snow pits and radar measurements were taken in January 2019 in Trail Valley Creek (TVC) and in the Greiner Lake Watershed near Cambridge Bay in March 2019 (CB1) and April 2019 (CB2). For the empirical determination of the average ds and snow

density (ρ_s) for depth hoar and wind slab, we added additional CB snow pits (no radar data) from 2015 to 2018 to a total of 240 pits. The two sites are shown in Fig. 5.2 with a broader view of the region. TVC is located in the Northwest Territories (Canada) near Inuvik and Cambridge Bay in Nunavut (Canada).

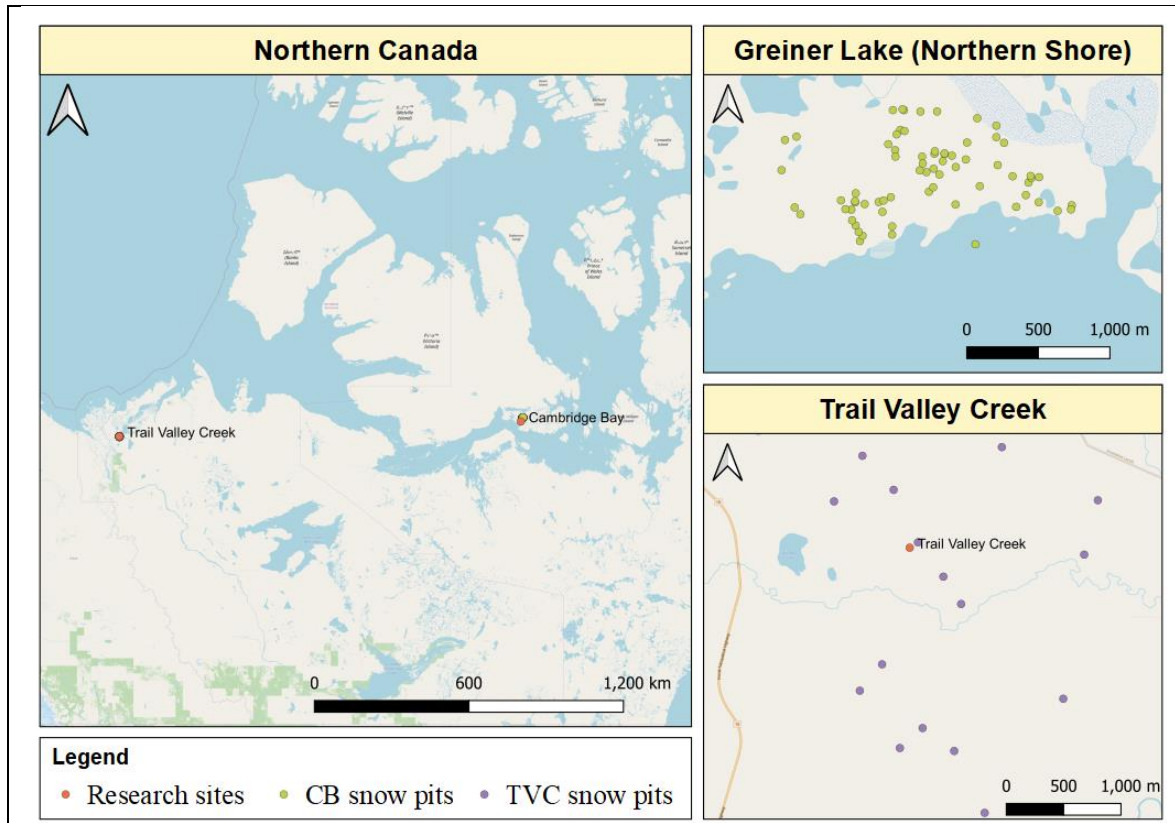


Figure 5.2: Location of main research sites and locations of snow pits/FMCW radar measurements. The coordinates of the TVC station are 68°44'31.29" N; 133°29'57.02" W, and for the northern shore of Greiner Lake 69°13'12.19" N; 104°54'2.12" W. Data taken from www.openstreetmap.org and <https://geogratis.gc.ca>.

a) Cambridge Bay

The Greiner Lake watershed covers an area of about 1500 km² and is located on Victoria Island (Nunavut, Canada) near Cambridge Bay. The watershed lies at 69°13.4' N; 104°50.4' W and is classified as a tundra landscape with base rich vegetation typical of Bioclimatic Zone D (Raynolds et al., 2019). The area is characterized by dwarf shrubs on 3 upland sites and low shrub – sedge fens and sedge fens on lower slopes and landscape depressions. It is a habitat for several large mammals such as muskoxen, caribou and Arctic

wolves. Smaller animals such as the rough-legged hawk, peregrine falcon, glaucous gull and Arctic fox can be found as well Ponomarenko et al. (2019). In general, the snow in the Cambridge Bay region can be characterized by a low-density depth hoar layer on top of the soil, which is in turn covered by a high-density wind slab layer. The typical snow depth varies between 30 and 40 cm and the snowpack is strongly influenced by wind, which is the most significant process driving snow depth variability (Meloche et al., 2021). In the vicinity of the watershed, two automatic weather stations (AWS) are deployed and equipped with a standard set of meteorological sensors (temperature, humidity, wind, snow depth).

As part of our radar accuracy analysis, we considered the impact of the underlying ecotype (ET) on the radar signal. The ecotype description is only available for the Cambridge Bay area and a detailed description can be found in Ponomarenko et al. (2019). Their research group provided us with an updated yet unpublished map. A summary of the ecotypes can be found in Table 5.2. By attributing an ecotype to each snow pit, we wanted to 1) determine the impact of the ecotype on the retrieval accuracy and 2) the influence of different ecotypes on the snow stratigraphy derived from the FMCW radar. To calculate the surface roughness, we used the data and method presented in Meloche et al. (2020). They used a standard compact camera (Canon Powershot Elph 160 5.0 mm) and Agisoft Metashape to process the data. Via the Structure-from-Motion approach, a 3D surface can be derived from 2D pictures. The images need sufficient overlap (60–80%) to determine enough tie points (same points in at least two pictures). From this, a point cloud for the roughness metrics calculation can be extracted. Meloche et al. (2020) used three metal plates for scaling inside the images to achieve a precision of 0.1 mm. They derived the soil roughness by using the height standard deviation (or root mean squared height) of an area of 0.5 m² (measured in all directions of the x-y plane). We used the same dataset for this study, but we utilised the maximum peak-to-mean roughness metric instead of the root mean squared height based. This is based on

the idea that the radar is sensitive to the “highest” point of the surface. The points are perpendicular to a fitted plane.

Table 5.1: Brief description of ecotypes occurring in this study. Data from Ponomarenko et al. (2019).

Ecotype	% in study area	Vegetation height	Comments
6. Hydric sedge fen	3.4	<30 cm	Occurs usually on flat lowlands with normal snow accumulation.
7. Sedge fen	4.1	<30 cm	Permafrost can be close to the surface.
10. Shrub - Sedge - Mountain avens	8.1	<40 cm	Low shrubs with an herb layer.
11. Subhygric communities	12.8	<15 cm	Perennial parts of vegetation of about 3 cm in height; Normal snow accumulation in winter; A lot of low shrubs; Herbs and grass are well developed.
12. Productive Mesic - Subhygric communitie	1.5	<15 cm	Shrubs and small vegetation; Moss is composing most of the biomass
13. Turfy Mountain avens - Curly sedge (open <25%)	12.8	<15cm	Not available.

b) Trail Valley Creek

TVC is located about 50 km northeast of Inuvik (Northwest Territories, Canada), where the predominant land cover consists of open and shrub tundra, with small, isolated tree stands, and is found near the southern boundary of the bioclimatic Zone E (CAVM Team,

2003). The site is managed by the Wilfrid Laurier University, and research on cold regions hydrological processes and modelling has been conducted here since 1995. Auxiliary datasets such as high-resolution land cover, digital elevation models and meteorological observations are available for the basin (Wrona et al., 2017). The snow in TVC is similar to snow in CB with a wind slab overlaying a depth hoar. The main difference resides in the fact that the snowpack is thicker given the higher amount of precipitation in the region.

5.2.3.2 *Radar description*

The Snow and Ice Radar (SIRA) is the commercial 24 GHz IMST sentire™ sR-1200 Series FMCW radar and has been described in detail in Pomerleau et al. (2020). A summary can be found in Table 5.3. It is controlled by a Raspberry Pi© (RPi model 3 B+) that has a user interface accessible through a smartphone. The total field of view of the radar is 65° in azimuth and 24° in longitudinal direction, which results in a 0.43 m² footprint at one metre above the surface. The bandwidth of the radar used is 2.5 GHz with a ramp time of 1 ms. We used a zero-padding factor of 8 to interpolate the signal in the time domain. The radar has two separate channels that provide two returns (subchannels), one for the real part, one for the imaginary part of the signal. The radar output is given in decibels (dB), but for averaging the channels, we needed to transform the dB value into Volts [V]. To calculate the average received power (P_{rec}) of each channel pair ($C_{1, real}$, $C_{2, img.}$ and $C_{3, real}$, $C_{4, img.}$), the following equation was used:

$$\overline{P_{rec}} = (C_r^2 + C_i^2)^{\frac{1}{2}} \quad (\text{Eq. 5.1})$$

An FMCW radar transmits a continuous wave with a frequency chirp. The returned signal is mixed with the original signal transmitted from the radar to produce a beat frequency, which is proportional to the time for the round trip of the signal (Brooker, 2005). The standard equation for FMCW, as described in Brooker (2005), is:

$$f_B = \frac{\Delta f}{t_m} \frac{2R}{c} \quad (\text{Eq. 5.2})$$

with f_b being the beat frequency, t_m the temporal length of the chirp, c the speed of light, R the distance covered by the signal (return trip) and Δf the total frequency bandwidth. We use the equation given by Marshall et al. (2005) to calculate R :

$$R = \frac{1}{2} v_s T_{2w} \quad (\text{Eq. 5.3})$$

with v_s being velocity of propagation in snow and T_{2w} being two-way travel time. v_s can be described as:

$$v_s = \frac{c}{\sqrt{\epsilon_s}} \quad (\text{Eq. 5.4})$$

and $\overline{\epsilon_s}$ the mean dielectric constant of snow. To correct the radar measurement for the existing snow properties, we use the Refractive Index (RI):

$$RI = \sqrt{\epsilon'_s} = \sqrt{1 + 1.7\rho_s + 0.7\rho_s^2} \quad (\text{Eq. 5.5})$$

with ϵ_s given by Tiuri et al. (1984) for the real part of the dielectric constant, depending only on snow density in dry conditions. Since we can only retrieve a distance measurement from the radar (i.e. d_s), we developed an empirical approach to estimate ρ_s , which will be explained in the next section as part of our new approach.

After averaging 10 measurements of each channel to determine a single d_s , we transformed the signal back to dB. We found that by removing all negative dB values, we were able to remove all reflections below the snow-soil interface, thus making the peak detection easier. To detect the peaks, we firstly determined the difference between two consecutive values in the data (difference function). Then we applied a difference function on the result as this will detect a sign-change and thus if the amplitude increases (+) or decreases (-). This identifies the peak values (Fig. 5.3).

During the field campaigns, we selected snowpit sites following different criteria to fulfill several research interests. At each measurement site, before digging the pit, we held

the radar horizontally over the snow surface. Each measurement cycle takes about 5 s. The radar was handheld above the surface (the legs of the system were not long enough to always keep the radar out of the snow. Please note that snowpits are sampled as a point measurement whereas the radar measurements have a footprint. The validation snowpits have been dug in the following fashion: The stratigraphy was measured visually with an interpretation of the layers along with hardness measurements (via hand test, see ICSSG, 2009). The layer depth has been measured with a ruler and for the ρ_S , a density cutter (100 cm³) has been used. The density has been measured with a vertical resolution of 3 cm. At the same interval, snow temperature, grain size and type were recorded.

Table 5.2: SIRA characteristics.

SIRA summary	
Hardware	
Operating Frequency	23.5 - 26 GHz
Number of Channels	1 Tx, 2 Rx
Antenna Characteristics	65° Azimuth, 24° Elevation
Dimensions	98mm * 87 mm * 42.5 mm
Weight	280 g
Penetration depth after Pomerleau et al. (2020)	
Ice at 0°C to -30°C	0.8–1.57 m
Snow at 0°C <ul style="list-style-type: none"> • 150 kg m⁻³ • 400 kg m⁻³ 	6.78 m 2.05 m
Snow at 275 kg m ⁻³ 0°C -20°C -40°C	3.26 m 4.78 m 6.38 m

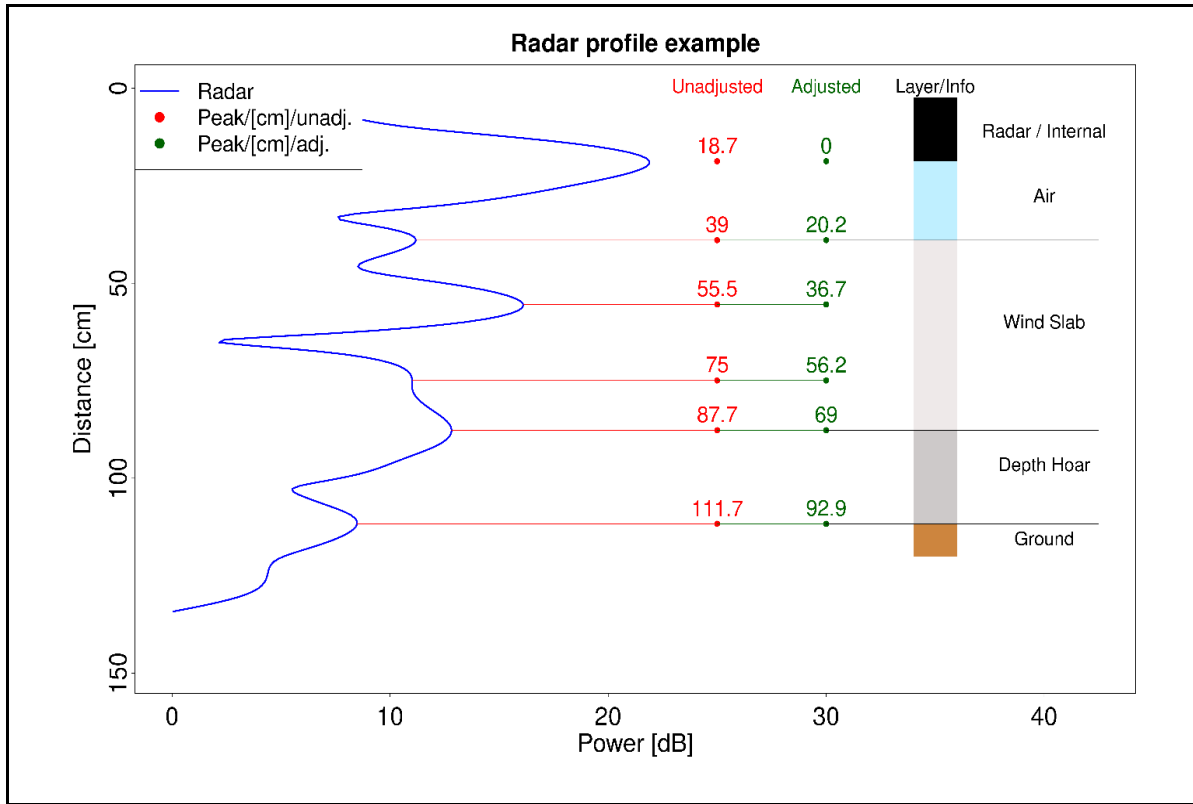


Figure 5.3: The figure shows R_{avg} from one of the snow pits during a campaign in Cambridge Bay. The blue line shows the return signal in decibels [dB] (x-axis) and the distance [cm] on the y-axis. The red lines mark the detected peak and the red points, the vertical distance in cm. These are raw values that are not corrected for the RI. The green lines/points show the adjustment for an offset cause by the radar plastic cover. These also are not corrected for the RI. The Layer/Info part shows the sectioning of the data after our methodology. The black part is aforementioned plastic cover and is used as the 0-point. The light blue part is the layer of air and is not corrected for RI (RI of air is close to 1), followed by the wind slab layer, which consists in this case of three peaks. The lowest two peaks enclose the depth hoar and everything below the lowest peak is considered ground. The peaks are identified by calculating the difference between two consecutive points along the profile twice enabling inflexion points to be identified.

5.2.4 Snow depth retrieval

In large parts of the Arctic, the snowpack can be simplified to a depth hoar layer below a wind slab, e.g. reported by Benson and Sturm (1993), Sturm et al. (2001), King et al. (2018) and Royer et al. (2021). Based on this simplification, we hypothesized that the deepest signal return from within the snowpack (furthest distance from the radar) corresponds to the frozen ground (see Fig.5.3) while the peak above it is either inside the depth hoar or the depth hoar / wind slab interface. Thus, it is likely to be a depth hoar measurement and we determined it as such. The uppermost peak of the profile corresponds to the protective cover

of the radar itself, followed by the peak of the air-snow interface. The next two peaks are within the wind slab. The deepest two peaks are the previously mentioned depth hoar - wind slab interface and then the depth hoar - soil interface. Please note that we are using the term depth hoar for the lowest layer, although our approach does not distinguish depth hoar from the wind slab based on the measurement itself, but by definition.

a) Empirical calculations

Our empirical calculation includes 240 pits from 2015 to 2019 over several campaigns and seasons in the two regions. We calculated averages of ρ_s and d_s for depth hoar and wind slab respectively and derived the empirical RI values specific to each layer. We used Eq. 5 to derive the RI. Hereinafter they are referred to as “individual RI”: iRI , and thus 240 values of iRI_{DH} and iRI_{WS} are available. Then we calculated the averaged or “generalized RI” (gRI) for depth hoar and wind slab as well, which we want to use as an empirical substitute to reduce the number of validation measurements necessary in future campaigns.

b) Snow depth and water equivalent (SWE) retrievals

55 pits have a corresponding radar and SWE measurement. The radar distance was then corrected using the iRI and gRI . We had to remove 12 outliers because the layer thickness measured by the radar showed a difference of more than twice of what was measured in the pit and could not be explained with supplementary data. This will not exclude extreme (but real) areas of deeper snow like gullies and only remove unrealistic returns. We calculated SWE using the measured in-situ dS and ρS . For the radar-based SWE retrievals, we used the empirically measured ρS and the radar-derived dS .

5.2.5 Results

5.2.5.1 *Snow measurements and empirical calculations of RI*

Table 5.4 shows the number of pits (n) for each year and each site. The overall average d_s is 37 cm, varying between 27.5 and 46.3 cm given the different years. The average d_{DH} is 14.4 cm, varying between 11.1 and 20.8 cm, while the d_{WS} is 22.9 cm, varying between 16.4 and 26 cm. One notable difference between the campaigns of CB and TVC is the ratio of depth hoar and wind slab. In TVC, the depth hoar layer represents on average 55% (45% for wind slab) of the total snow depth, while the depth hoar value is 38% (62% for wind slab) for CB. Overall, the total snow depth is quite shallow. It was measured every year during the same March–April period (exception: TVC, mid-January) so that year-to-year changes in snow depth are rather governed by intra-seasonal effects (wind redistribution, temperature, precipitation) than by inter-seasonal effects. Via the Random Forest method, Meloche et al. (2022) have shown that wind and topography correlate strongly with snow depth. In open tundra, the maximum snow depth is typically reached in the early winter. Afterwards changes are largely controlled by erosion and sublimation which will densify the snowpack (Pomeroy and Brun, 2001). The average density (all sites and years combined) of the depth hoar density (ρ_{DH}) layers is 258 kg/m^3 , corresponding to an average gRI of 1.22. For the wind slab layers, the average wind slab density (ρ_{WS}) is higher (wind packed) with 317.9 kg/m^3 and an associated gRI of 1.27. For both cases, the standard deviation is 0.04.

To better understand the sensitivity of the radar measurements to the RI, we examined the effect on the calculated snow depth based on the variability of the smallest RI, the average RI and the largest RI for ‘the average snowpit’. This is based on the data from each individual snow pit (not the average values shown in Table 5.4). The lowest and highest calculated RI for the depth hoar are 1.12 and 1.34, while the values for the wind slab are 1.15 and 1.4. This equates to a difference of 2.1 cm (depth hoar) and 3.5 cm (wind slab) for the average snow

depth. This shows that using a gRI, which is a little less accurate than the iRI, has a much smaller impact on the final accuracy than the given uncertainty via the RMSE for total snow depth (RMSEd), which is on average 14.3 cm. As we want to reduce the amount of snowpits necessary for validating radar measurements, we think that this approach can be used in future campaigns.

Table 5.3: Yearly and campaign averages of total snow depth, depth hoar and wind slab thicknesses. Results are presented yearly for each CB campaign between 2015 and 2019 (2019: 2 campaigns) and are averaged for that period. TVC data from a single campaign is shown in the second last column. The last column shows the overall average of all sites together. σ is the standard deviation, Snow depth is given in cm, ρ_s in kg·m³. The RI is unit less. d_{DH} is the measured depth of the depth hoar and d_{WS} the measured depth of the wind slab.

	CB 2015	CB 2016	CB 2017	CB 2018	CB 2019	All CB	TVC 2019	All
n	38	32	41	36	69	216	24	240
d_s / σ	32 / 18.9	27.5 / 12.4	46.3 / 17.9	36.2 / 13.1	39.5 / 22.7	37.1 / 19.3	37.7 / 10.07	37.2 / 18.5
DH / σ	12.5 / 7	11.1 / 5.4	15.4 / 6	15.7 / 6.5	13.6 / 7.2	13.7 / 6.7	20.79 / 5.45	14.4 / 6.9
$DH\%d_s$	39	40.2	33.2	43.3	34.5	38.1	55.1	40.9
WS / σ	19.5 / 16.6	16.4 / 9.6	31.1 / 15.4	20.6 / 12.9	26 / 19.4	23.5 / 16.6	16.94 / 7.9	22.9 / 16.4
$WS\%d_s$	61	59.8	67.1	57.1	65.8	62.2	44.9	59.3
$\overline{DH}_\rho / \sigma$	249.8 / 38.2	230.2 / 35.4	255.4 / 40.1	249.3 / 37.1	295.9 / 33	262.6 / 43.6	218.36 / 25	258.2 / 44.1
$\overline{WS}_\rho / \sigma$	314.3 / 53.8	290 / 26.2	360.1 / 36.1	305.1 / 44.4	321.6 / 44	320.2 / 47.5	293.13 / 45.7	317.5 / 47.9
$\overline{DH}_{RI} / \sigma$	1.21 / 0.03	1.2 / 0.03	1.22 / 0.03	1.21 / 0.03	1.25 / 0.03	1.22 / 0.04	1.19 / 0.02	1.22 / 0.04
$\overline{WS}_{RI} / \sigma$	1.27 / 0.05	1.25 / 0.02	1.3 / 0.03	1.26 / 0.04	1.27 / 0.04	1.27 / 0.04	1.25 / 0.04	1.27 / 0.04

5.2.5.2 *Snow depth and water equivalent retrievals*

Table 5.5 shows the results from the radar-based retrievals of snow depth using empirical values of RI. Please note that the averages of measured ds , d_{DH} and d_{WS} thicknesses are slightly different from the results presented in Table 5.4 (multi-year average) given that only the pits with coinciding radar measurements were considered. The Pit-column shows the manually measured pit data, the iRI-column the derived ds using the individual RI (pit-based) and gRI provides the derived thicknesses using the generalized results, meaning that the calculations were based on the results of Table 3 (last column). On average, the radar-derived snow thickness is overestimated by 8 cm with an $RMSE_{ds}$ of 14.3 cm. The RMSE is based on the pit vs. the gRI corrected radar measurement. The derived values from both the iRI and gRI are almost identical at 55.3 cm and 55.8 cm, which corresponds to an average overestimation of ds of 17.2%. For d_{DH} , the iRI overestimates by 5.4% and the gRI by 4.3%. The d_{WS} -overestimation is 29.9% (iRI) and 30.9% (gRI). The difference between iRI and gRI is again rather small. Despite the rather small overestimation of the snow thickness of 5% and a similar standard deviation, the RMSE of the depth hoar depth measurement ($RMSE_{d_{DH}}$) is relatively high likely due to soil roughness creating a large variability in snow depth within the field-of-view. For the d_{WS} (similar standard deviation), the overestimation is 30.9% with a $RMSE_{d_{WS}}$ of 29.1%. For ds , the values are mixed. The standard deviation is similar, but the overestimation is in-between d_{DH} and d_{WS} . Though the RMSE for d_{DH} (61.6%) and d_{WS} (59.1%) are high, the RMSE for ds is 30%. Therefore, we think that we can use this method to map snow depth since we capture snow depth on average well and have a comparable standard deviation.

Table 5.5 shows the calculated SWE using in-situ averages of ps for depth hoar and wind slab along with radar-derived thicknesses. The SWE is calculated separately for each layer and then added up. We only used the thicknesses derived from the gRI given the small

differences compared to the iRI. Overall, the derived SWE is overestimated by 13% for the bulk SWE. In all three cases, the high values of standard deviation highlight the high spatial variability in layering and thickness. The RMSESWE is 35% (bulk).

Table 5.4: The table shows data for all pits that have a corresponding radar measurement. The left column presents the data from the manual measurements, whereas the middle (individual RI, iRI) and the right column (gRI) shows the radar results. Results in the right column (gRI) are based on a generalized RI from the previous section. The last row shows the total SWE [mm].

	Pit	iRI	gRI
n	43		
d_s / σ / RMSE	47.6 / 21.7	55.3 / 21.1 / 14.2	55.8 / 21 / 14.3
DH / σ / RMSE	18.5 / 7.1	17.5 / 6.9 / 11.2	17.7 / 7 / 11.4
WS / σ / RMSE	29.1 / 19.4	37.8 / 22.8 / 16.9	38.1 / 23.8 / 17.2
SWE / σ / RMSE	146.9 / 86.7	----	166.6 / 70.3 / 51.4

5.2.5.3 Ecotypes

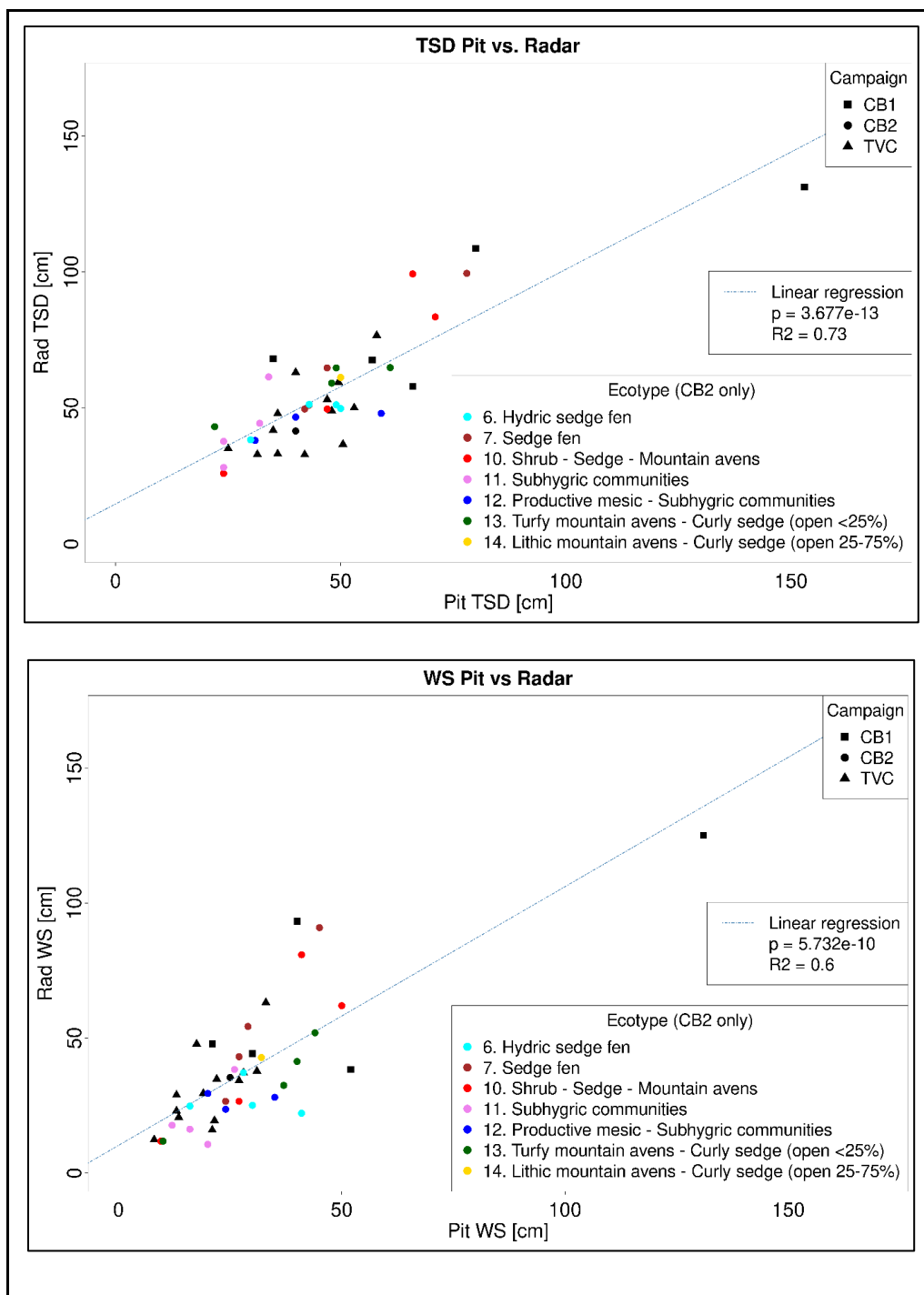
For several different ecotypes, we evaluated if the accuracy of the retrieval is affected by ground characteristics. The occurring ecotype that have both a radar and manual measurement, are 6) Hydric sedge fen, 7) Sedge fen, 10) Shrub - Sedge - Mountain avens, 11) Subhygric communities, 12) Productive mesic – Subhygric communities and 13) Turfy mountain avens – Curly sedge (open <25%). Please note that per ET, only 3–4 pits contribute to the statistic and thus the results should be interpreted as preliminary. Given that ecotype information is only available for CB, 23 pits were compared during this analysis. The d_s is captured by the radar across different ecotypes with a RMSE ranging from 6 to 17.9 cm (see Table 5.6 for more details). The values are similar to those shown by Meloche et al. (2021) using RPAS-based measurements. Similar RMSE values are observed for the d_{DH} with best values <5 cm for ET 10 and ET 12. As for d_{WS} , the RMSE ranges from 4.7 to 27.4 cm. For

d_{DH} , the RMSE has a much larger range (18.7–108.8%) whereas the RMSE_ d_{WS} covers a range from 13.7 to 51%. The three scatter plots in Fig. 5.4 show the manually retrieved d_s plotted against the radar retrieved snow depth for d_s (top), d_{WS} (middle) and d_{DH} (bottom). The three campaigns are distinguished by symbols and ETs have been coloured (only available for CB). The results show that total d_s ($R^2 = 0.7$) and d_{WS} ($R^2 = 0.6$) are clustered along the regression line, but d_{DH} ($R^2 = 0.1$) is not. The thickness retrieval for the d_{DH} has a higher RMSE leading to a statistically non-significant relationship with the observed data. The retrieved values are within the range of observed values, with a high RMSE likely caused by surface roughness or vegetation. To understand the impact of ecotypes on the retrieval accuracies, we extracted roughness values using structure-from-motion. For the 6 ecotypes available for this study, the peak-to-mean values are used as a roughness metric (Meloche et al., 2020) and varied between 2.2 and 3.9 cm for the peak-to-mean average and 9.6 and 27.6 cm for the maximum distance. The RMSE_ d_s varies between 12.6 and 38.9%. The analysis is constrained by the limited number of observations in each ecotype and therefore will be the subject of future investigations.

The reason why the wind slab retrieval performs better is likely due to the easier determination of the air-wind slab interface and being a thicker layer. This has led to a good performance in retrieving d_s (Table 5.5). The depth hoar retrieval has uncertainties in the vertical determination of the wind slab-depth hoar interface as this is determined by our assumption. Our results indicate further that the roughness and ecotype decrease the precision with which we can measure.

Table 5.5: The table shows the results for the different snow parameters and roughness for each ET.

EC-type	6. Hydric Sedge Fen	7. Sedge Fen	10. Shrub - Sedge - Mountain Avens	11. Subhygric communities	12. Productive Mesic - Subhygric communities	13. Turfy Mountain Avens - Curly sedge (open <25%)
n pits	4	4	4	4	3	4
Roughness						
Rough max.	15.3	10.2	27.6	13	16	9.6
Rough max. avg.	9.7	8.3	12.2	9.7	7.6	5.3
Peak-to-Mean avg	3.7	3.1	3.3	3.9	3.3	2.2
Snow						
TSD pit / σ	43 / 9.2	52.5 / 17.14	52 / 21.3	28.5 / 5.3	43.3 / 14.3	45 / 16.4
TSD rad / σ / RMSE	47.7 / 6.3 / 6	66.2 / 23.2 / 15	64.6 / 33.1 / 17.9	42.9 / 14 / 16.7	44.2 / 5.4 / 8.5	58 / 10.2 / 14.4
TSD-RMSE-%	12.6	22.7	27.7	38.9	19.2	24.8
DH pit / σ	14.3 / 4.1	21.3 / 7.89	20.1 / 4.3	10 / 2.3	17 / 6.6	12.3 / 3.7
DH rad / σ / RMSE	20.4 / 7.6 / 10	12.5 / 7.1 / 13.6	19.3 / 3.9 / 3.6	22.2 / 9.6 / 14.9	17.2 / 7.6 / 4.9	23.6 / 9.7 / 15
DH-RMSE-%	49	108.8	18.7	67.1	28.5	63.6
WS pit / σ	28.7 / 10.2	31.3 / 9.4	31.9 / 17.7	18.5 / 5.97	26.3 / 7.8	32.8 / 15.4
WS rad / σ / RMSE	27.3 / 6.7 / 11.6	53.7 / 27.3 / 27.4	45.3 / 31.7 / 20.9	20.7 / 12.2 / 8.3	27.1 / 3.1 / 6.8	34.4 / 17 / 4.7
WS-RMSE-%	42	51	46.1	40.1	25.1	13.7
DH% of TSD pit	33.3	40.6	38.7	35.1	39.3	27.3
DH% of TSD rad	42.3	18.9	29.9	51.4	38.9	40.7
SWE						
SWE pit / σ	136.4 / 33.7	166.8 / 57.71	167.9 / 74.5	95.2 / 14.5	138.9 / 47.5	131.9 / 50.6
SWE rad / σ / RMSE	139.2 / 17.9 / 21.55	202.8 / 75.7 / 40.8	193.6 / 104.1 / 43.7	123.1 / 41.8 / 36.8	130.3 / 12.9 / 30.1	170 / 35.5 / 45.1



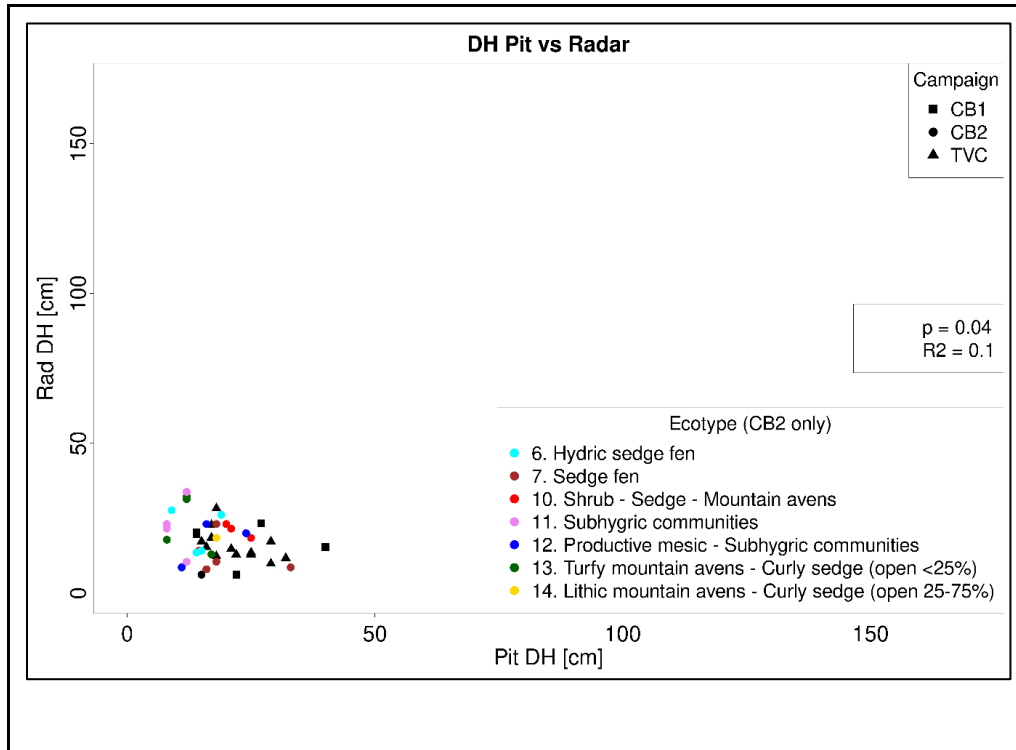


Figure 5.4: The figures show radar-retrieved d_s against the manually retrieved d_s . The campaigns are separated by symbols and for CB2, ecotypes are presented in different colours. A regression line has been added for total d_s and d_{ws} , which have shown to be statistically significant.

5.2.6 Discussion

5.2.6.1 Empirical calculation

For measured values of d_s , d_{DH} and d_{ws} in CB, data from 2019 lies within the range of the other years and is very close to the interannual average. The slightly increased standard deviation of the wind slab layer (and thus total snow depth) for 2019 can be explained by the following two points: 1) The data spans across two different campaigns, one in March and one in April. The extended time period allowed for more changes in the snowpack. 2) During the March campaign, we were focusing on deeper snow measurements (not related to this work) but included the data here to demonstrate that the algorithm can handle a variety of snow conditions. Values of ρ_{DH} and ρ_{ws} and the associated RIs lie within the interannual

range, so we concluded that 2019 was an average year in terms of snow characteristics in CB.

For the TVC dataset, similar ds were found, but with a different ratio of depth hoar and wind slab. The large depth hoar ratio from TVC can be explained by a stronger temperature gradient which sustains strong kinetic metamorphism (Colbeck, 1980; Langlois and Barber, 2007). Colbeck (1982) and Miller and Adams (2009) have shown that a minimum T-gradient of 10–20 °C m⁻¹ is required for kinetic growth metamorphism. We derived an average temperature gradient of 35 °C m⁻¹ for TVC compared to 19 °C m⁻¹ in CB. Thus, the more pronounced depth hoar layer in TVC was expected. Another factor for the larger depth hoar ratio could lie in the present microtopography (hummocks and tussocks), which is linked to the ground thermal regime (Gouttevin et al., 2018).

The difference between the RMSE of iRI and gRI for ds, d_{WS}, and d_{DH} is ≤ 0.3 cm. This increase is small compared to the RMSE-values ranging from 3.6 cm (best case) to 27 cm (worst case). Using a gRI is particularly relevant given that being independent from prior snow information or many validation pits, it will allow us to use the radar as a mapping tool.

5.2.6.2 Snow depth and SWE retrievals

The RMSE of d_s is 14.3 cm, but one should keep in mind that we compare a point measurement (metre stick) with a footprint (radar). With the radar at 50 cm above ground, the footprint covers an area of 0.11 m². The available pictures of the ground used to derive the roughness show many features like rocks, small trenches, and vegetation. Looking at the large RMSE-differences of the radar per ecotype, it seems clear that either the ecotype or the roughness influences the signal strongly. We had to remove 12 outliers and we think that these can be explained by the placement of the radar. In this version of the SIRA, we are not yet able to correct for off-nadir measurements. As it is not placed far from the ground, the

contribution to the error might not be large, but we also cannot quantify this precisely. We are developing a newer version that has the ability to correct for the tilt of the radar. A further reason for the outliers could be a very rough surface (rocks, vegetation) within the field of view. Due to the small amount of available measurement, we were not yet able to determine this with statistical significance. We know from other experiments that the radar can achieve a higher accuracy if more parameters are known (e.g. exact height above ground). As we can't know the conditions under the snow, we think the best way to approach this problem is having a large reservoir of snowpits per ecotype to build a more reliable statistic, including roughness measurements.

Our SWE measurements have an RMSE of about 30% for d_s (RMSE based on manual vs. radar estimated measurements). As we do the calculation for depth hoar and wind slab separately, and then add the values, we think that any improvement on determining the vertical location of the wind slab – depth hoar interface will influence the accuracy positively.

5.2.6.3 *Ecotypes*

At first, we checked the aspect, slope, and water availability (ridge vs. valley, distance to the next water body), but we were not able to detect a relation between the snow pit and the range of the RMSE for the snow depth retrieved by our radar. None of the slopes have an incline steeper than 5° and during the snow season, the surface appears to be flat. As indicated by Gacitúa et al. (2013) and others, snow depth is influenced by the underlying vegetation. Our technique differentiates between wind slab and depth hoar and takes ecotype and roughness into account. For wind slab and snow depth, we were able to derive statistically significant measurements. In the best cases, the RMSE was as low as 4.7 cm (13%) for d_{ws} and 6 cm (12.6%) for d_s . For d_{DH} , the results are acceptable with 3.6 cm (18%) in good cases. Comparing the worst cases (Table 5.6), we can see that the largest uncertainties are made while measuring the depth hoar. We assumed that the smaller the roughness is, the better our

technique would perform. But the roughness for ET 7 is comparatively low compared to the other ecotypes, nevertheless the RMSE for all snow depth measurements is high. On the contrary, ET 11 has comparatively high roughness values but the RMSE for d_{DH} is one of the lowest of all ecotypes (18%). From these two points we conclude that another factor than roughness has to play a role. For example, vegetation height might play a role as the it is higher for ET 7 than for ET 11 (see Table 5.2). But we would like to point out again that we have a maximum of only 4 pits per ecotype. More fieldwork is required to investigate this further.

5.2.7 Summary and future work

Snow data scarcity contributes to errors in model development and satellite retrievals of snow state variables. Furthermore, existing retrieval algorithms have coarse spatial resolutions, rendering it very difficult to retrieve high accuracy of d_s and SWE (Chang et al., 1982; Kelly, 2009; Takala et al., 2011; Lemmetyinen et al., 2018). To fill this gap, we developed an algorithm capable of deriving snow depth and distinguishing between depth hoar and wind slab using a small FMCW radar at a high spatial resolution. We derived empirical values of ρ_s for depth hoar and wind slab, from which we calculated the corresponding RI for each layer. On this basis, we procured a radar-based d_s retrieval technique and used it to determine SWE. We have shown that the RMSE for the d_{DH} was higher than d_{ws} and d_s , which we think is attributed to uncertainties in the vertical location of the wind slab-depth hoar interface and the underlying roughness and ecotype. Using the radar-derived d_s and the empirically estimated ρ_s , we achieve a SWE-estimation with a RMSE of 35%.

By separating the radar-retrieved dataset by ecotype, we observed great differences in the accuracy of the radar. We examined the influence of the surface roughness but couldn't find a clear pattern. As none of the ecotypes have >4 observations, we can only discuss the

effect of the ecotypes on the retrieval accuracy preliminary and further measurements are necessary. Our preliminary findings show that ET 6 (Table 5.6) has the lowest RMSE for d_s even though the roughness values are comparable to ET 11, which has the highest RMSE for d_s . We want to mark and measure areas (roughness, vegetation) during the summer while the vegetation is better visible. Then we want to repeat the measurements at the exact same spot during winter. After the radar measurement and a full snowpit, we want to excavate the area and measure the same quantities and compare them to the summer values. By comparing the differences, we hope to find how much of the error can be attributed to the roughness of the ground and how much to the vegetation above.

Notwithstanding rather low roughness values, ET 7 has a RMSE of 108.8% for the d_{DH} . By studying the ecotype and roughness during summer and winter, we hope to better determine the interface between depth hoar and wind slab for the different ecotypes. This will be important as we want to map areas of snow depth with the radar. As we have a high-resolution map of the different ecotypes available, we can better describe the errors by subdividing the map in areas with expected low and high accuracy.

Overall, our approach can be used by researchers working in similar areas. Simplifying the snowpack into two layers and using empirical values to fill missing measurements has been demonstrated successfully.

All hardware can be acquired under 5000 USD and is thus available for smaller research groups or local communities. We think that SIRA has great potential towards monitoring larger areas of snow including the distinction of the two main snow layers and retrieving SWE. The system is under constant development, and we have already integrated an RTK-dGNSS (Real-Time-Kinematic differential Global Navigation Satellite System) module with a positioning accuracy in the cm range (5 cm vertical and 2 cm horizontal). We

plan to map the spatial distribution of depth hoar, wind slab layer thickness and total snow depth.

These maps could be useful for developing and validating snow models or satellite-based approaches to predict and monitor the state of the snow. To address the path length change for off-nadir measurements, we plan to integrate an IMU. We have mounted SIRA under a remotely piloted aircraft system (RPAS) to avoid snow disturbance and on a snowmobile to be able to conduct such measurements in all weather conditions or where RPAS flights are impossible due to restricted airspace.

Credit author statement

- Daniel Kramer: data analysis, writing, developing the method. Others: partial data analysis, partial writing, participated to the sampling design, revision of manuscript.

Declaration of Competing Interest

- The authors declare that they have no known competing financial interests or personal relationships that could have appeared to influence the work reported in this paper.

5.2.8 Acknowledgements

We thank Julien Meloche, Simon Levasseur, Patrick Cliche, Coralie Gautier, Guillaume Couture, Caroline Dolant, Chlo'e Martineau, Ludovic Brucker, Branden Walker, Peter Toose, Chris Derksen, Arvids Silis, Shawn Marriot, Johann Wagner, Sergei Ponomarenko and Christopher Arko for their help in the field, technical support and/or scientific advice.

This work was funded by Polar Knowledge Canada, the Canadian Foundation for Innovation, ECCC Grant & Contribution Program and the Fonds de recherche — Nature et technologies.

5.3 COMMENTARY

5.3.1 Footprint, over probing and ecotypes

The footprint differences of the previous methods have been addresses. SIRA adds a new shape of footprint (Fig. 5.5) with further consideration. SfM uses the full image as a footprint and delivers a DSM in postprocessing. A DSM shows the surface of the area (e.g. top of the vegetation), whereas a snow pit and the avalanche probe reach the bottom. SIRA illuminates an area, thus the microtopography affects the returned signal. A worst-case example would be:

- The top of the shrub would be detected by SfM (canopy).
- SIRA gets a return from a branch further down.
- The avalanche probe hits the ground.
- The snow pit measurements are done at best possible spot, which might not be where the prob hit.

This example shows how difficult it is to interpret the different signals and methods and that there is natural grey zone of precision without one method having the advantage.

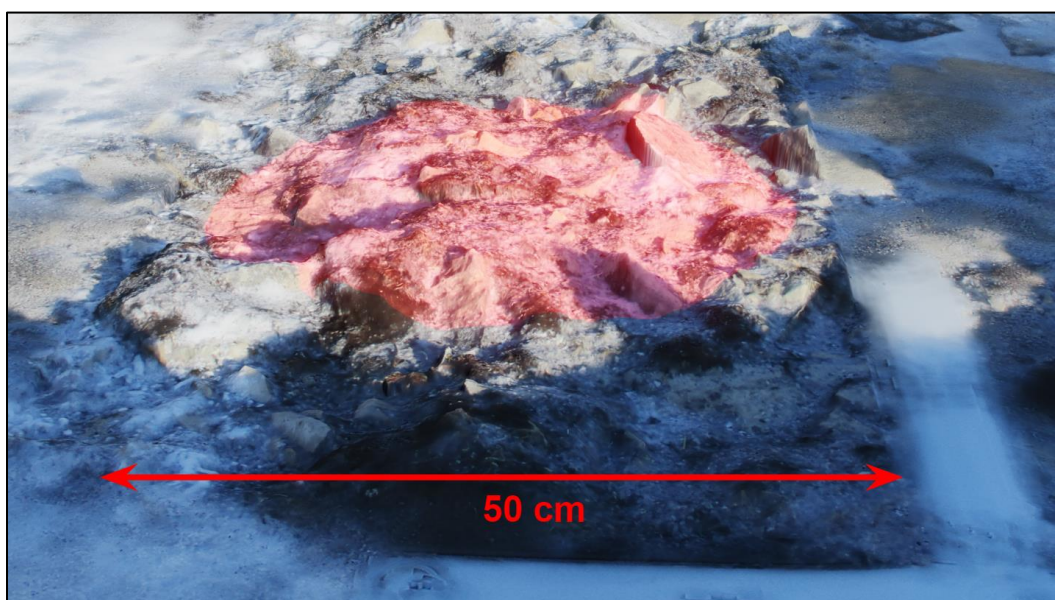


Figure 5.5: Footprint of SIRA (not to scale).

5.3.2 Towards the next chapter

This chapter has addressed three out of four points that are required to have a new mapping tool available to support the scientific community by developing new model and Remote sensing techniques, mainly producing maps of snow distribution to improve e.g. the certainty of values that are used to describe the snow properties in a spaceborne passive microwave approach (Meloche, 2022). Table 5.6 summarizes the strengths and weaknesses of using FMCW for snow measurements.

Table 5.6: Advantages and disadvantages of the FMCW measurements.

FMCW	
Pros	Cons
<ul style="list-style-type: none">- Objective- Non-destructive- Snow characteristics- Weather independent	<ul style="list-style-type: none">- One point in space- One point in time

To develop the algorithm for Arctic snow, the SIRA was used stationary. The remaining task was to modify the SIRA to enable mapping, which will be done in the next chapter.

6 HIGH PRECISION MAPPING OF SNOW DEPTH WITH THE SIRA

6.1 INTRODUCTION TO THE CHAPTER

In chapter 4, we developed a DIY RPAS that can handle rough conditions in the Arctic and deliver scientific data that matches recent literature. This was followed by the chapter on adapting the SIRA algorithm to arctic snow conditions. Shown in Table 5.6, the remaining weaknesses of the FMCW method can be condensed into the single measurement problem: During the development of the algorithm, only a single point was taken in space and now repetitive measurements were possible as the necessary snow pit destroyed this option. As the algorithm has been worked out, a snow pit for every measurement is not necessary and with an appropriate geolocation upgrade, the SIRA could be used for spatial and temporal measurements.

To produce a high-resolution snow map, two pieces of information must be known as precisely as possible: The exact horizontal position (latitude, longitude) and the TSD. As the TSD-retrieval has been covered in the last chapter, I will focus in this chapter on the positioning. By using dGNSS (differential Global Navigation Satellite System), we can determine the precise 3D position of the SIRA. With the accurate 3D position, I am able to extract the following layers and surfaces:

- 1) Air-Surface-Interface (ASI), which is the top of the snowpack that is exposed to the atmosphere. Via interpolation of multiple measurement locations, this surface creates the ‘Digital Snow Surface Model’ (DSSM).
- 2) Snow-Soil-Interface, which is the bottom of the snowpack that touches the ground. Similar to 1), multiple measurements create the DSM.
- 3) The difference between 1) and 2) creates the layer of TSD.

- 4) With the restrictions describes in chapter 5, the additional layer between Depth Hoar and Wind Slab can be extracted as well.

For interpolation, I used the TIN-interpolation method (Triangulated Irregular Networks). Further, I compared them to other mapping techniques and evaluated the potential of cross using these techniques.

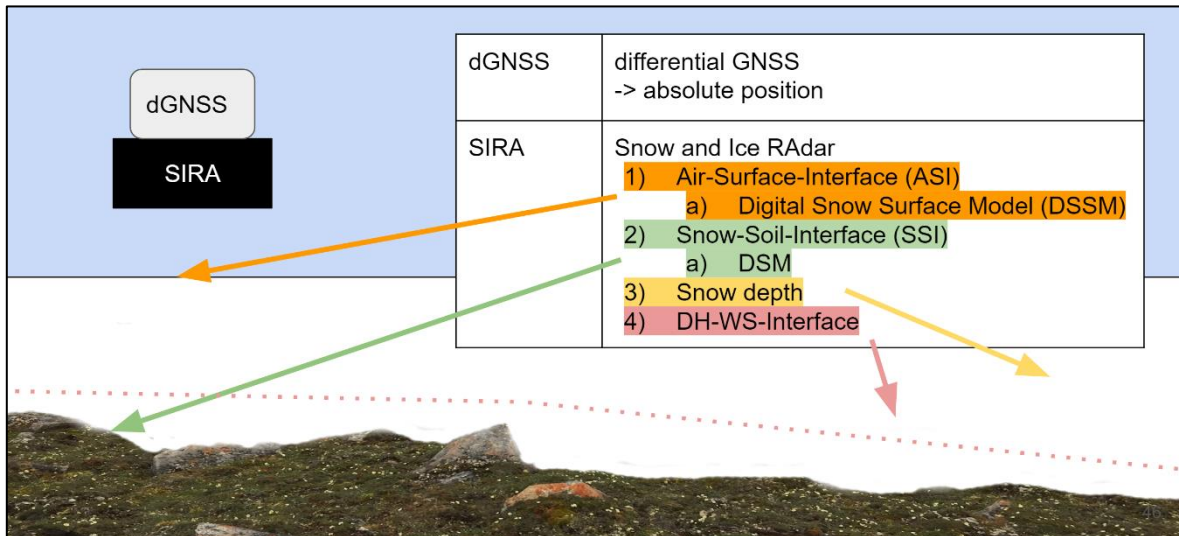


Figure 6.1: The figure shows the different surfaces and layers that the SIRA can map.

Fig. 6.2 illustrates the schematic of this chapter. I retrofitted the SIRA with the necessary hardware and conducted the measurements. To analyze and compare the SIRA maps, I produced a reference data set with the best possible accuracy and a RPAS-based data set as it is a common method widely used in the scientific community. Table 6.1 lists important acronyms relevant to mapping with a brief explanation.

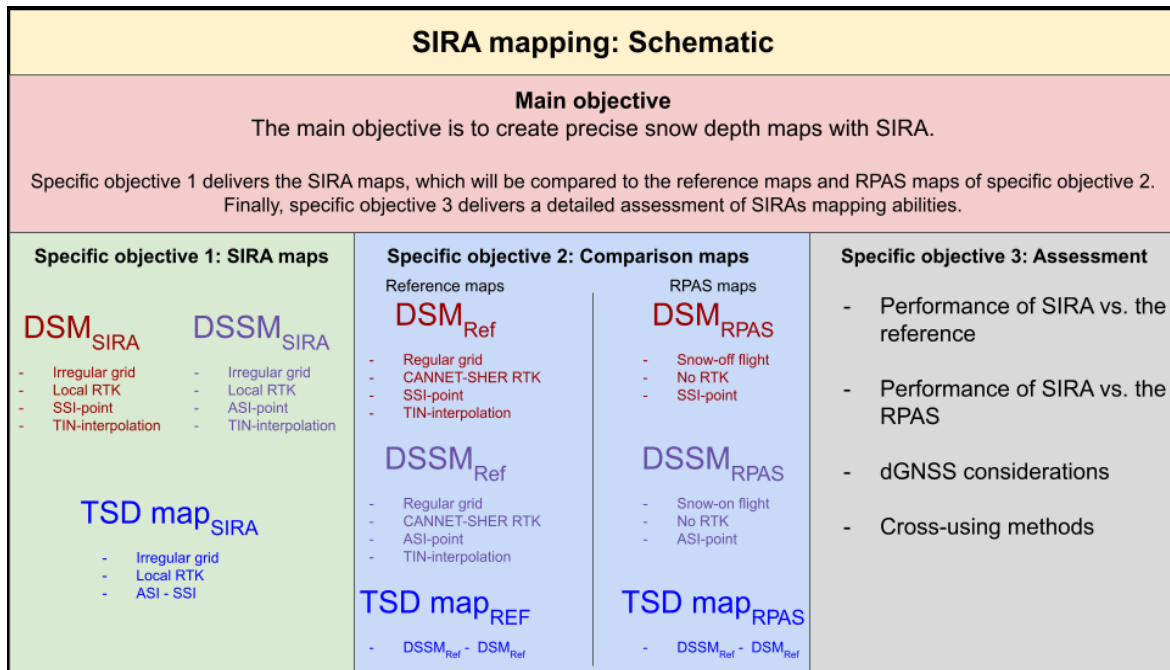


Figure 6.2: Schematic for this chapter including the specific objectives.

Table 6.1: Important acronyms for this chapter.

Acronym	Description
ASI	Air-Snow-Interface: Describes (the position) where air and snow have their boundary (snow surface).
DSM _{index}	Every DSM represents the solid surface of the Earth. The index explains the acquisition method, e.g. Ref for the reference method.
DSSM _{index}	Similarly, to the DSM, the DSSM describes the snow surface. The index references to the acquisition method.
PPP	Precise Point Positioning
RTK	Real-time Kinematik
SSI	Soil-Surface-Interface: Describes (the position) of the boundary between the solid Earth and the layer above (snow or air).
TIN	Triangulated irregular network
TSD map _{index}	This describes the map of TSD with the index explaining the data acquisition method.

6.2 HIGH PRECISION MAPPING OF SNOW DEPTH WITH THE SIRA

6.2.1 Introduction

Digging snow pits is the traditional method to retrieve snow information because of their high level of detail. They are used as a reference and a calibration tool for models and remote sensing (RS) retrieval techniques. Data obtained from an individual field campaign generally represents only a few points in space and time (e.g., Zweng et al. 2018; Bergstedt et al. 2018). To address this gap, several RS techniques were developed over the past few decades to increase the spatial and temporal coverage of snow retrievals using various types of frequency. For example, optical sensors operating in the VIS spectrum can be used to derive the snow spatial extent but are often limited by cloud cover. Additionally, VIS sensors depend on solar illumination, a major constraint when working in high latitudes due to the polar night. Despite having a high spatial resolution, VIS can't directly deliver information about the state of the snowpack such as snow depth (total snow depth, TSD), snow volume nor microstructure (Foster et al., 2005; Larue et al., 2017). This led to the development of retrieval approaches using passive microwave (PMW) sensors, which are less dependent on atmospheric conditions, solar illumination (Chang et al., 1982; Mätzler, 1987) and can measure TSD and snow water equivalent (SWE). This said, PMW sensors offer poor spatial resolution, provoking high uncertainties in the retrieval of snow state variables because of pixel heterogeneity (Meloche et al., 2021).

It's possible to increase the spatial resolution of the retrieved data by lowering the altitude of the sensors, for example, by mounting them on an aircraft instead of a satellite. While the spatial resolution would increase, the spatial coverage would drastically decrease, an aircraft indeed being able to cover only a limited area and fewer to none repetition over time, resulting in a very poor temporal resolution. Furthermore, those campaigns are extremely expensive and continued monitoring is usually not possible. As demonstrated in

Meloche et al. (2021), the need for high-resolution maps of TSD and SWE exists. They showed that combining high-resolution maps of TSD and SWE with retrieved PMW SWE satellite data allows a better characterization of the sub-pixel variability—or what is governing spatial variability—in turn, enhancing our understanding of satellite retrievals. Meloche et al. (2021) compared point measurements of TSD (snow pits) to a TSD map obtained from a Remotely Piloted Aircraft System (RPAS) to quantify local variability. RPAS are frequently used to map TSD over small areas; they combine a low-cost approach with a high-resolution retrieval (Kramer et al., 2019). They used the Structure-from-Motion (SfM) technique to reshape 2D images into 3D information, from which they can extract TSD, as presented by Fernandez et al. (2018). Following their work, Kramer et al. (2019) have developed a low-cost RPAS specialized for winter fieldwork. It successfully demonstrated the retrieval of TSD maps by creating two Digital Surface Models (DSM): one for snow-on and another for snow-off conditions that are then subtracted to obtain the TSD map. Although great for low cost, precision and spatial resolution, the downside of the SfM approach is that two missions (snow-on, snow-off) are necessary. Further, no information on the snow microstructure can be extracted. This could be retrieved from PMW sensors but that would yield a much coarser resolution.

Active sensors such as radar (RADio Detection And Ranging) can obtain information on snow microstructure, TSD and SWE (Marshall and Koh, 2008; King et al., 2018). Frequency Modulated Continuous Wave (FMCW) radar, as presented in a review by Marshall and Koh (2008), can measure the dielectric constant of snow (ϵ_s) from which TSD can be derived if the snow density (ρ_s) is known. These methods require *in situ* measurements of either TSD, ρ_s or both, which is a strong limitation when covering larger areas. This motivated the work of Kramer et al. (2021) who addressed the issue by developing an empirical approach that needs limited to no prior snow information using FMCW

measurements (Ka-band, 24 GHz). In recent years, specialized FMCW radars have become lightweight and affordable enough to be used in the research community. In their study, Kramer et al. (2021) used such a lightweight device: the Snow-and-Ice-radar (SIRA). It was developed by Pomerleau et al. (2020), and given that a FMCW radar at 24 GHz doesn't depend on solar illumination, is relatively cheap and lightweight, it combines the best of both worlds; it also delivers high-resolution information on snow characteristics that is impossible to obtain from an optical sensor in the VIS. An alternative to the radar approach are LIDARs (Light Detection and Ranging) for high resolution mapping, but LIDARs neither give information on the snow stratigraphy nor can they derive snow depth and solid surface at the same time.

Therefore, this chapter puts the focus on the next intuitive step following chapter 4 and chapter 5: Developing an approach that uses the SIRA for mapping TSD over larger areas. A mobile platform for the SIRA is necessary to transport the system and to allow precise 3D positioning. Two platforms are optimal for carrying the SIRA: snowmobiles and RPAS. In this study, I used the former, given I have not yet adapted our RPAS to carry the SIRA. Further, I want to assess the mapping potential of the system and it's easier to perform the task from a snowmobile because it's independent from the weather, reduces administrative preparation and a snowmobile can better accommodate changes in weight, size, and layout of the SIRA as whole. For mapping purposes, I need Digital Surface Models (DSM; i.e., ground/snow-off) and Digital Snow Surface Models (DSSM; top of snow). All previous considerations are culminating to the following objective with associated specific objectives (SO):

Objective: Development of the SIRA mapper for snow depth

The main objective is to develop SIRA into a system that has validated TSD mapping capabilities. After several hardware and software modifications of the original SIRA, described in Pomerleau et al. (2020) and Kramer et al. (2021), I formulated the following tasks based on the specific objectives:

- | | |
|-----------------------------|---|
| Specific objective 1 | <p>Create a TSD map using the SIRA including</p> <ul style="list-style-type: none">• A DSM from the dGNSS* (differential Global Navigation Satellite System) positions.• A DSSM from the dGNSS positions and SIRA;• A TSD map extracted directly from the SIRA measurements. <p>*The process of using a base and a rover is known as dGNSS positioning and will be explained in the next section.</p> |
| Specific objective 2 | <p>Create comparison maps. Each method will produce a DSM, a DSSM and a TSD map. These will be compared to the SIRA results.</p> <ul style="list-style-type: none">• Reference maps: The reference maps are utilizing a metre stick attached to an avalanche probe with a dGNSS module for positioning mounted on top.• RPAS maps: RPAS are nowadays commonly used for mapping and thus a comparison is apparent. This method is using the SfM technique presented in chapter 4. |
| Specific objective 3 | <p>Assessment of SIRAs mapping qualities.</p> <ul style="list-style-type: none">• Analysing the performance of the SIRA mapper compared to the reference maps and to the RPAS maps.• Investigating the influence of the dGNSS as a source of error. |

- With three precise methods, an assessment of cross-using the different approaches is examined.

The reference maps and the SIRA maps require an interpolation from point data into an area. In this study, I used Triangular Irregular Networks (TINs) as the interpolation method.

6.2.2 Methodology

6.2.2.1 Study site

As a study site, I selected the local research station SIRENE (Fig. 6.2). The site is near the University of Sherbrooke (Southern Quebec, Canada) and includes a workshop. The winter air temperature ranges from -5 °C to -17 °C (Dolant et al., 2016).

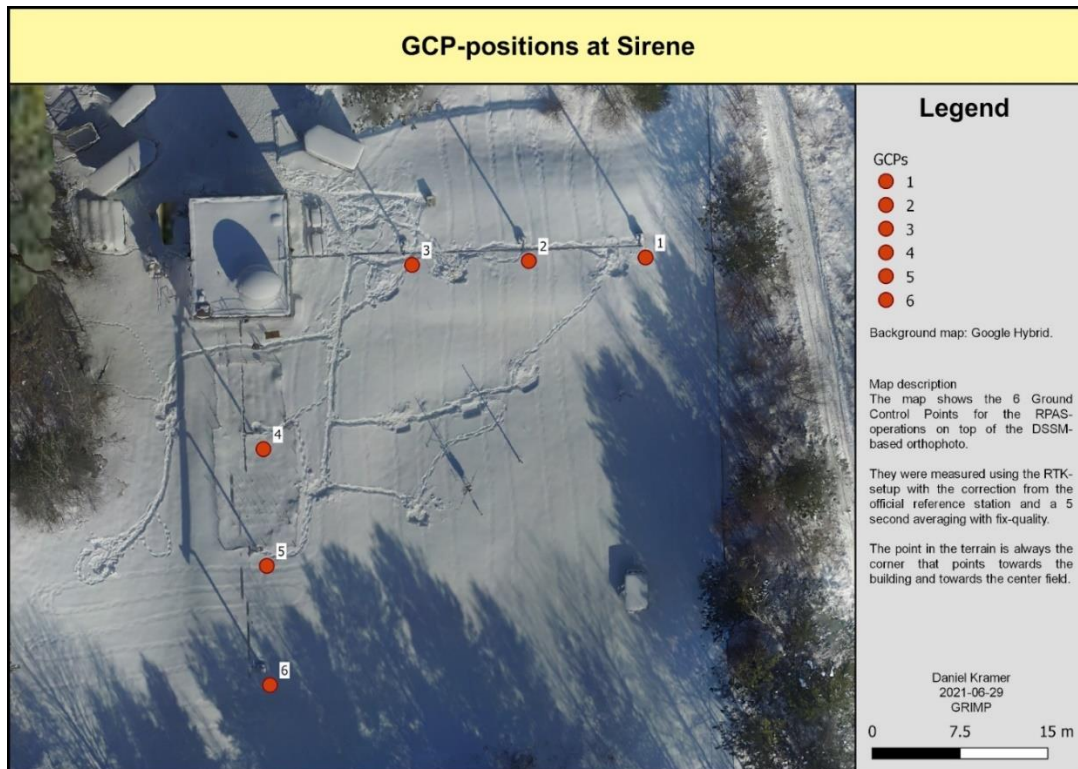


Figure 6.3: The research station SIRENE and the location of the Ground Control Point (GCP).

6.2.2.2 *SIRA*

The SIRA system was described in detail in Pomerleau et al. (2020). Kramer et al. (2021) described the upgrades necessary for and the TSD detection algorithm. To use the SIRA for snow mapping, I implemented further modifications:

- Mounting SIRA on a sledge to be pulled over the snow.
- The system is now controlled by Raspberry Pi[®] (RPi) version 4.
- A bubble level ensured that no measurement was taken with an angle more than 4° off-nadir, which minimizes the error of the retrieved path length.
- A survey-grade dGNSS module (Emlid[®] Reach M+) was retrofitted for precise 3D positioning.

The principle behind retrieving TSD from SIRA has been explained in Pomerleau et al. (2020) and Kramer et al. (2021). In short, I determine TSD by measuring how much time the signal takes to travel to and from the different surfaces (ASI, SSI). As the signal travels in the air at (almost) the speed of light, we know the theoretical travel distance (i.e., radar distance). The propagation speed changes inside the snowpack so that I had to use the Refractive Index (RI) to retrieve the “real” distance and thus TSD. The RI was derived from snow density measurements.

For this experiment, I mounted SIRA on a sledge and kept it about 20 cm above the ASI (Fig. 6.3). The dGNSS unit delivers the precise location of the SIRA and its position above the solid surface. The SIRA retrieves the points for ASI and SSI via the radar measurement. Then I use a TIN-interpolation to derive the DSM_{SIRA} and $DSSM_{SIRA}$.

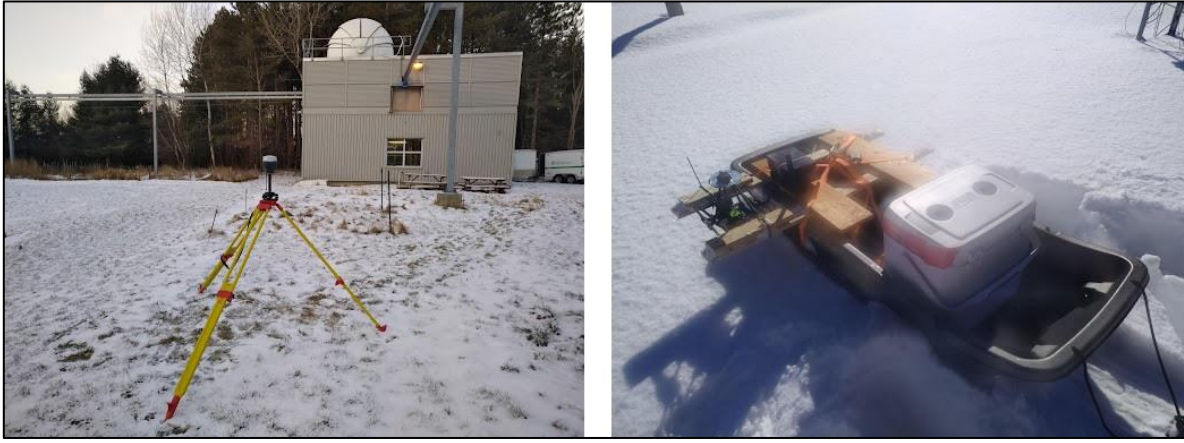


Figure 6.4: Base station and ground conditions (left), SIRA setup (right).

I took 15 SIRA measurements over the same field of view over 4 hours and I used snow pit measurements to verify the SIRA measurements. The peak detection of the SIRA signal is based on two functions that identifies the vertical position of a sign change in the amplitude if a peak shows (Kramer et al., 2021; Laliberté et al., 2021).

Another change from the original settings described in Kramer et al. (2021) is the reduction from 10 separate measurements that are averaged into one measurement to a single measurement. Despite the downside of relying on a single measurement per point, considering the forward motion of the radar during the measurements is more important. The SIRA can take one measurement every 4–5 seconds including the processing time onboard the RPi.

6.2.3 Mapping

After preparing the SIRA for the local conditions and mounting it on a sledge, the following description shows how I achieved a precise mapping. Real-Time Kinematic (RTK) positioning permits retrieval of a precise position in real time as it is a differential positioning method. Differential positioning requires a base station with a very well-known position. The station collects satellite geometry data, compares it to its own and transmits a correction

factor to the rover unit. With the correction factor, the rover can increase its position precision while moving around and, in this case, take measurements.

6.2.3.1 *Reference maps*

To validate the SIRA maps, I need reference data. Thus, I created a DSM_{Ref} , a $DSSM_{Ref}$, and a $TSD\ map_{Ref}$. As a base station, I used the official reference station in Sherbrooke (CANNET-SHER), which has a known position-error of a few millimetres (CANNET fact sheet). The correction was transmitted via a cellular network. As a rover, I used an Emlid RS2 mounted on a 2 m pole to increase its visibility to satellites. The RS2 is a dual frequency receiver, which means it receives GNSS signals on two different frequencies, which reduces its sensitivity to e.g. atmospheric disturbance.

In surveying, three terms are used to indicate the precision of the position. The precision is increasing from “single” (worst) over “float” (medium) to “fixed” (best). Whereas fixed positions are often < 5 cm, float positioning can range from several centimetres up to 5 m (Hall et al., 2010). Based on this, I only accepted fixed solutions to contribute to the reference measurements.

Without recording secondary data, it’s impossible to tell the exact offset at each point. Table 6.2 shows the calculated errors given by the software. All data has undergone an orthometric and antenna height correction. Natural Resources Canada (NRCan) gives an orthometric correction factor of -27.137 m for the area of SIRENE. The measurements were taken on a regular grid with the points being 3.5 m apart.

Table 6.2: RTK DSM error, expressed as RMS (root mean squared error). First three columns stand for the base station, and the last column for the rover. Errors must be summed up. The values are in m.

RMS Easting	RMS Northing	RMS Elevation	RMS Lateral
0.0110	0.0112	0.0135	0.0157

After adding the errors from the base and the rover, the achieved precision has an uncertainty of about 2.5 cm on all axes. To collect the TSD map_{Ref}, I attached a metre stick to the 2 m pole and measured the TSD with a precision of 1 cm.

6.2.3.2 *SIRA maps*

Remote regions usually don't have a base station and a cellular network available for correcting the position. To reflect this in my work, I created a local base station. Hence, I mounted the RS2 on a tripod and recorded the position for 30 min. Then, it transmitted the correction factor via LoRa (Long Range) radio. As this setup doesn't achieve the same precision as when using an official base station, I improved the precision during post-processing via PPP. To do so, I set the RS2 to record the satellite geometry and then applied the PPP technique. A recording time of 4–6 hours is usually a sufficient acquisition time of the satellite geometry. NRCAN offers a free PPP service that I exclusively used for this project.

In my case, the rover is an Emlid M+. This unit is much smaller than the RS2 and can be used on e.g. a RPAS. The M+ unit is a mono frequency unit and was mounted near the SIRA and thus only a few centimetres above the snow. For the horizontal rover positioning, I achieved an average uncertainty of 2.5 cm. For the vertical precision, the uncertainty is <5 cm. This uncertainty confirmed, as expected, that the setup was less precise than with the official reference station.

The M+ handed its position via a NMEA-string (National Marine Electronics Association) to the SIRA. Aside from the position itself, it gives a fix-quality estimation for each measurement. When processing the data, I only accepted measurements with a fix of 4 or 5. According to the Trimble fact sheets (Trimble 2021), a fix quality of 4 gives a precision with fixed integers and a fix quality of 5 with float integers. In post-processing, each measurement has been corrected for the PPP-calculated position of the base.

An important note on the mapping setup:

The SIRA derives its 3D position via the dGNSS module, but it retrieves ASI and SSI using radar. Both are independent measurements and e.g. a low position precision does not affect the TSD measurement and vice versa. Nevertheless, if the SIRA measurement is used for mapping, both independent measurements play into the overall map precision.

6.2.3.3 *Interpolation*

As the SIRA and the reference technique deliver point data, it is necessary to interpolate this into an area if a continuous map of TSD is desired. In this study, I solely used the Triangulated Irregular Networks (TIN) to interpolate the point data. In the case of DSM and DSSM, I extrapolated the surface point using TINs, whereas for the TSD maps, each TIN describes a snow depth layer.

A TIN creates a surface between three nearest neighbouring points of measurements. In my case, I used the QGIS-implemented function that uses the Delaunay triangulation method. This method ensures a network of non-overlapping triangles which preserves the precision of the original data set. This leads to a high resolution in areas with a lot of data points and a lower resolution in areas with fewer data points.

TIN calculations tend to be less efficient when compared to raster data processing but are frequently used for high-precision modelling of small areas (ESRI, 2016). For a small site like SIRENE measuring a highly variable quantity like TSD, this method of interpolation is ideal.

6.2.3.4 *RPAS maps*

Using a digital camera on a RPAS, researchers and surveyors use this frequently to acquire precise maps of an area. Thus, I want to compare the SIRA results to what a RPAS

can achieve. In snow research, it is possible to extract TSD if flights are conducted in summer (snow-off, DSM_{RPAS}) and in winter (snow-on, $DSSM_{RPAS}$) conditions. Both maps are created using Structure-from-Motion (SfM), which requires an overlap between the RPAS photographs that allow the algorithm to find tie points (common features found in multiple images). A density cloud was extracted from the tie points to create a DSM as described in Fernandez et al. (2018).

To increase the precision of RPAS-based position of features in the images, it's common practice to deploy Ground Control Points (GCP). These must 1) be easily recognizable in the captured images and 2) have a very well-known position. I established the GCPs using the RTK method and the CANNET-SHER correction, leading to a centimetre precision. For this study, 6 GCPs have been deployed. There are different possibilities to arrange the GCPs. For this study, I decided to place the GCPs on the permanent structure of SIRENE to allow easy use in the future use. The layout can be seen in Fig. 6.2.

The snow-off flight happened in clear sky conditions, and the ground showed a very thin snow layer. I chose those conditions because it can help to reduce the uncertainty in TSD retrieval because vegetation can cause an error as it was described in Kramer et al. (2019). For example, high grass can be misinterpreted by the SfM algorithm and create the DSM on the grass surface. But as this is compacted under snow, the $DSSM_{RPAS}$ can appear lower than the DSM_{RPAS} , leading to negative TSD. I performed the snow-on flight under a clear sky as well.

6.3 RESULTS

6.3.1 Reference maps

The DSM_{Ref} is shown in Fig. 6.4. The data is corrected for orthometric height and the distance between antenna and ground. The map shows an altitude between 300–312 m a.s.l. but note that this excludes the building of SIRENE (red-bordered square). I used brake lines

to exclude it from the TIN-calculation. Important features appearing on the map are the two elongated hills, extending in a straight line to the S and the E, that are about 1–1.5 m higher than the large grass area in the SE corner. Both hills have a mounted metal rail running from the station several metres above the ground. The SW corner is the lowest part on the map with about 300 m a.s.l. Trees and high vegetation edge the NW corner, but this method doesn't capture them. I marked contour lines at 50 cm intervals with red lines.

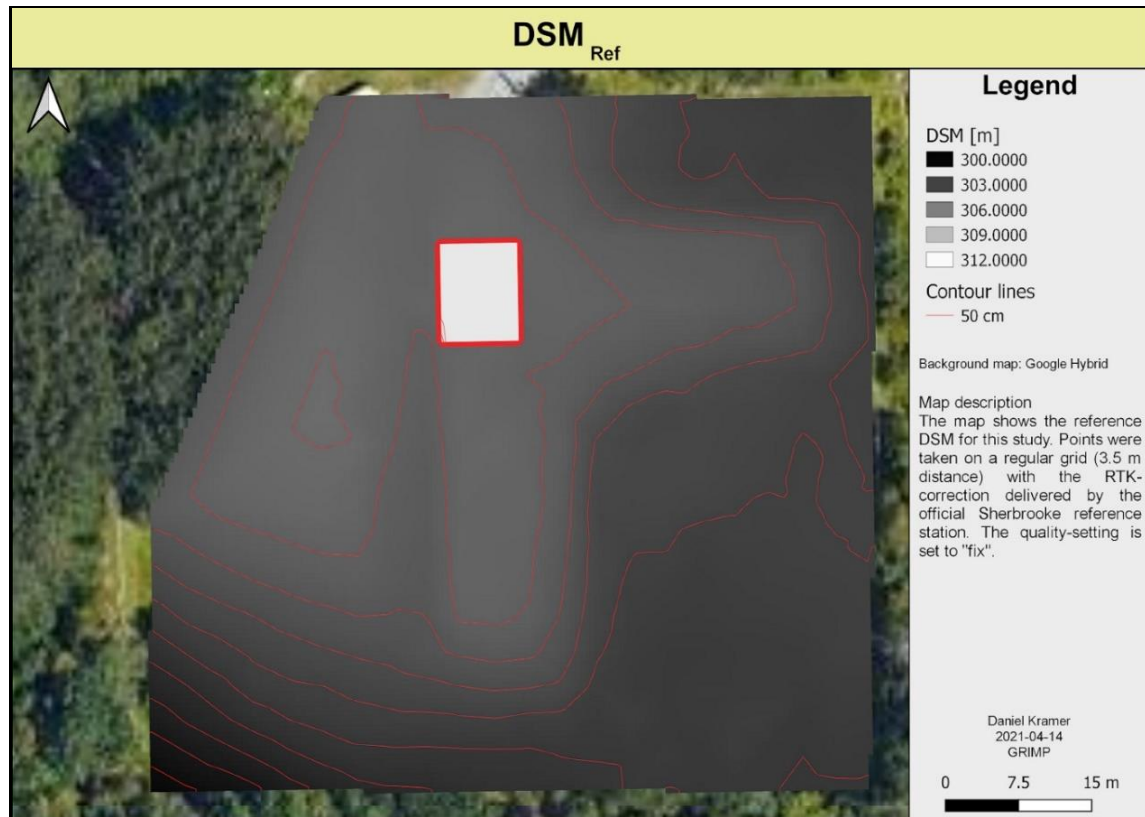


Figure 6.5: Map of the DSM_{Ref}. The red-bordered square delineates the station building. Contour lines are shown in red at 50 cm intervals (thick red lines). Height given in metre a.s.l.

Fig. 6.5 shows the TSD map_{Ref} with a horizontal precision of <2.5 cm and the vertical precision of <5 cm for each measurement point. The TSD ranges between 25 cm and 40 cm with three exceptions:

- SE corner: Three spots of deeper snow are close to several high trees. The snow accumulation may have happened by wind deposition due to the change from forest to open terrain, but without available wind data, I can't confirm this.
- NE corner: The second deeper spot reflects a similar situation.

- S rail: Below the rail is a patch of higher vegetation. This might have caused the higher snow accumulation or could be an artefact as the probe might have penetrated through the vegetation layer.

I have calculated the $DSSM_{Ref}$ by adding the TSD data to the DSM_{Ref} , but it isn't shown as it alike Fig. 6.4, just with slightly elevated values for the altitude.

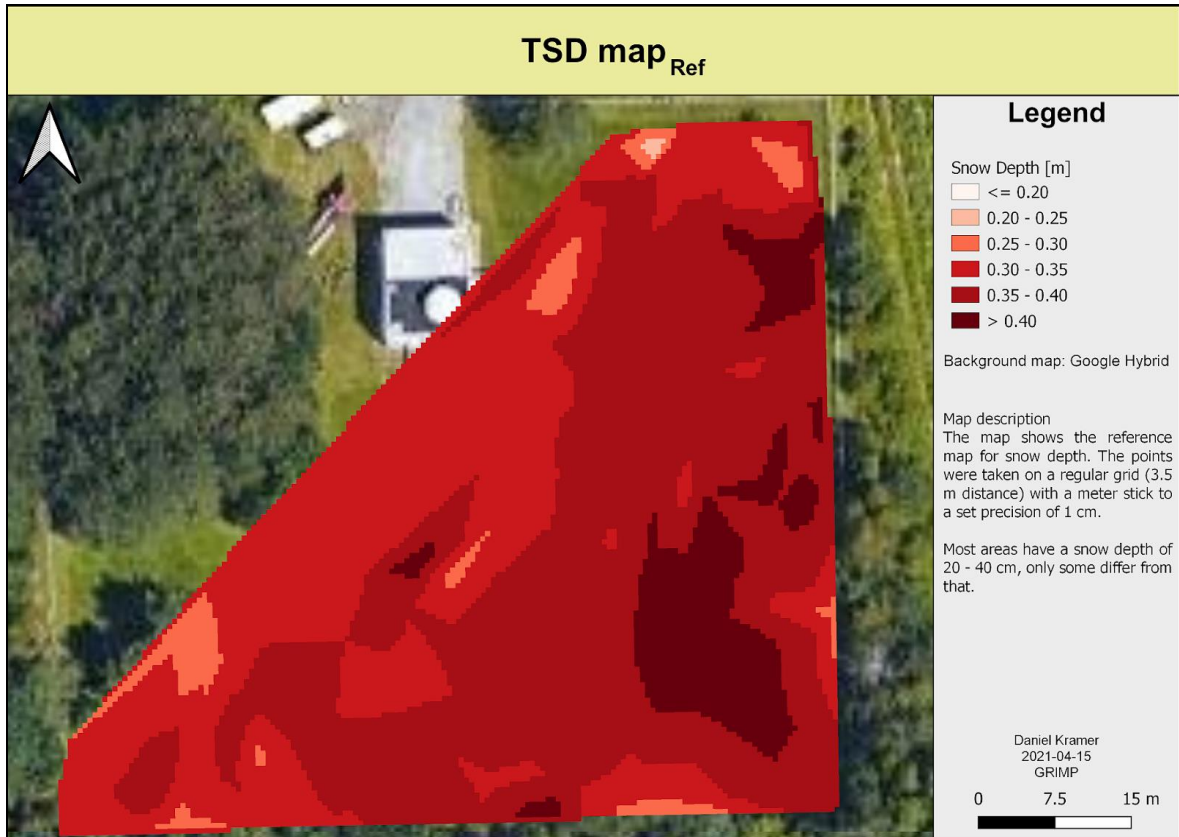


Figure 6.6: TSD mapRef measured with a metre stick and a dGNSS module.

6.3.2 Local snow conditions

As described earlier, I need a RI to calculate the TSD via the SIRA. During the day of the SIRA measurements, I dug a validation snowpit to retrieve the necessary data. ρ_s based on 4 measurements vertically distributed over the snowpack (equal intervals). Table 6.3 presents the results for the important variables.

Table 6.3: Reference and SIRA measurements for the validation snow pit.

	SIRA to ASI	SIRA to SSI	TSD	ρ_s	RI
Reference	14.5 cm	54.5 cm	40 cm	230 kg·m ⁻³	1.2
SIRA	13.2 cm	50.8 cm	37.6 cm	—	—
Difference	-1.3 cm	-3.7 cm	-2.4 cm	—	—

6.3.3 SIRA measurements and maps

6.3.3.1 Measurements

After applying s and the RI to the SIRA measurements, I find a TSD of 37.6 cm for the validation snowpit, which is 2.43 cm less than the reference measurement. Despite that the snow conditions at SIRENE can't be described as arctic snow, ρ_s and the RI show comparable values as in Kramer et al., (2021), which supports their claim to use empirical RIs in different regions once the average conditions are known. Table 6.4 shows the spatial results for the reference measurements and the SIRA measurements.

I took 176 valid measurements with a TSD_{SIRA} of 30.5 cm. The SIRA underestimates the average TSD by 5.5 cm but has a comparable standard deviation. The RMSE is 9.2 cm, which is about 30% and no outliers were removed. This is comparable to Kramer et al. (2021) with an RMSE of 29% after removing outliers. I decided to not remove outliers in the present case as I know the ground under the snow at SIRENE, which is flat and grassy, compared to a variation of ecotypes in Kramer et al. (2021).

Table 6.4: This table shows the results of TSD measurements taken over the area of SIRENE.

	Reference [cm]	SIRA [cm]
TSD	36	30.5
SD	4	6.8
RMSE		9.2

6.3.3.2 Maps

The DSM_{SIRA} is presented in Fig. 6.6 and the colour scheme is exactly as in Fig. 6.4. In general, the maps look similar as the S and E hills stand out distinctly, and the SW corner appears lower than the rest of the map. The 50 cm contour lines appear similar though a bit less regular as in the reference map. The DSM_{SIRA} shows one false measurement: In the SE corner is a white spot with a difference of about +1.5 m, which disqualifies it for a real feature as the area is known and there is no matching counterpart.

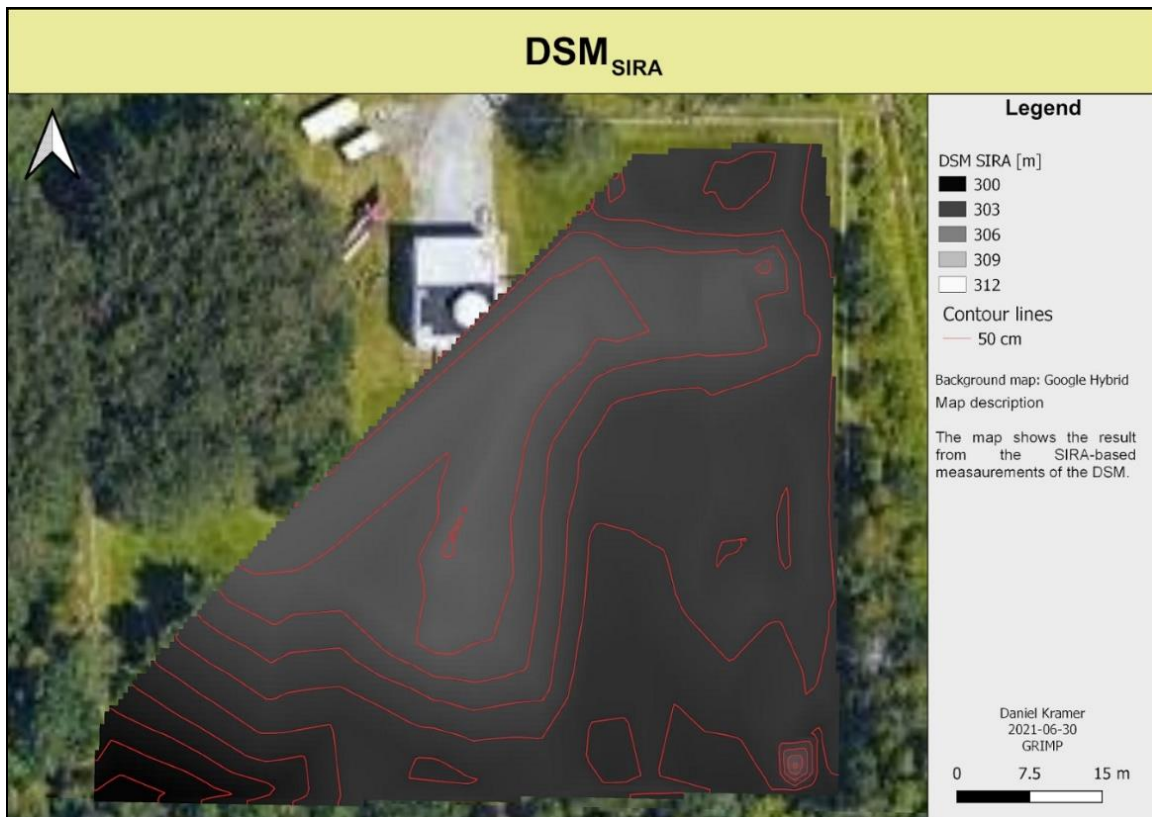


Figure 6.7: DSM_{SIRA} with the elevation given a.s.l. and contour lines with 50 cm intervals (red lines).

The TSD map_{SIRA} is depicted in Fig. 6.7. Generally, the derived TSD is similar at each location compared to the TSD map_{Ref}. At several locations, differences can be observed:

- Whereas the TSD map_{Ref} appears uniform on the snow distribution with larger patches of similar TSD, the TSD map_{SIRA} has an irregular pattern with many different patches of TSD.
- The areas with deeper snow are rather in the centre of TSD map_{SIRA} of the map and one spot in the E. The feature in the E is at a similar position on the TSD map_{Ref} but the deeper snow is shifted a bit from the center to the E.
- As the TSD map_{SIRA} appears whiter, SIRA's general underestimation of TSD is visible.

Similar to the DSSM_{Ref}, the DSSM_{SIRA} is not shown as it would appear very like the DSM_{SIRA}.

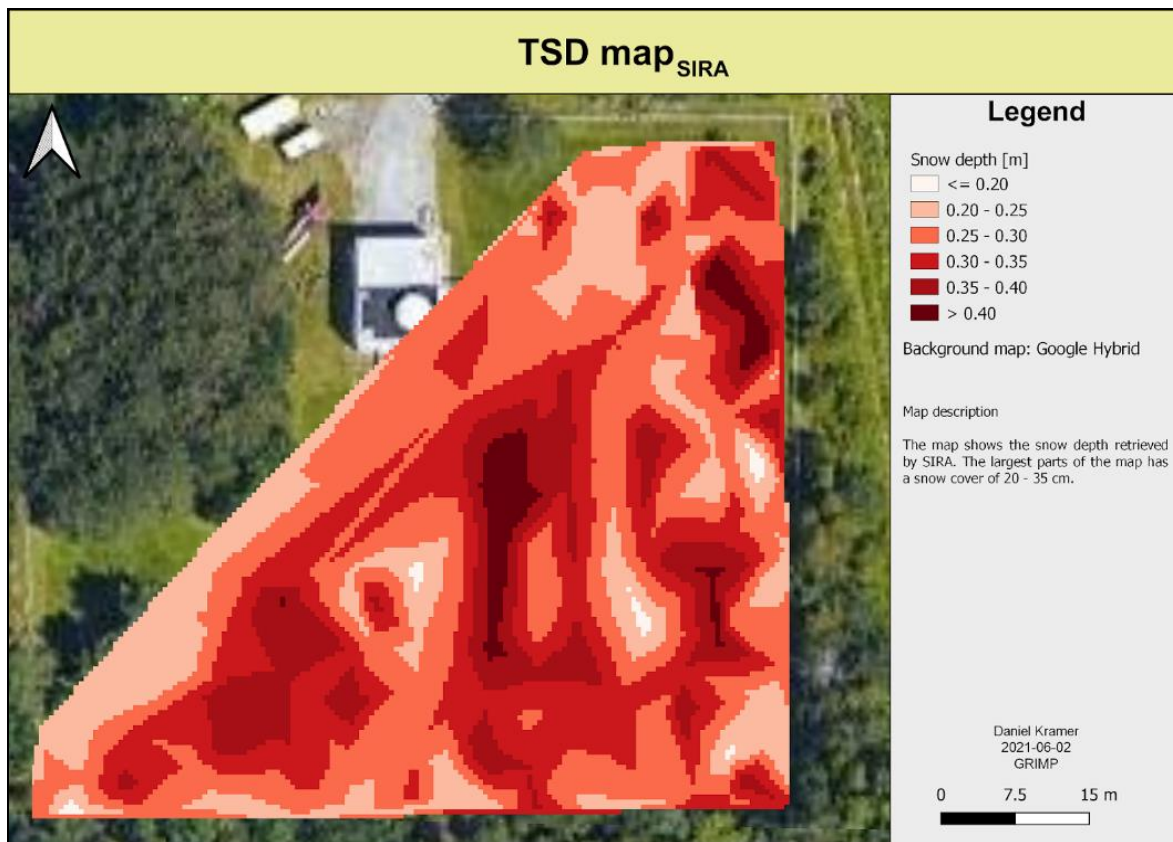


Figure 6.8: Snow distribution based on the SIRA retrievals.

6.3.4 RPAS flights

6.3.4.1 GCPs

I used a RPAS that has an internal GNSS unit, allowing for a coarse geolocation of the images. As the precision is in the meter range, it remains sufficient for many types of projects (for example visualization), but for accurate surveying, the precision needs to be within the centimetre range. I can achieve this by either upgrading the RPAS with a dGNSS system or via post-processing. In this study, I chose the latter path. To improve the precision in post-processing, a common technique is to deploy GCPs. These points are easily distinguishable in different images (e.g. with a VIS camera) as they are usually brightly coloured targets on the ground or on permanent parts of a structure (as in this study). The GCPs are located in the corners of the pillars holding up the metal rails along the S and E axis, on the little hills (see Fig. 6.2). The GCPs are always in the corner that is facing towards the building (SIRENE) and towards the open field in the SE of the map. Using the fixed quality setting, the location of the GCPs is accurate within 1–2 cm. The absolute coordinates are shown in Tab. 6.5. The data is corrected for the orthometric and antenna height.

Table 6.5: Coordinates of the GCPs.

GCP	Latitude	Longitude	Easting	Northing	Elevation
GCP1	-71.92265272	45.37385236	271154.31	5028637.8	305.009
GCP2	-71.92278028	45.37384961	271144.36	5028637.94	304.984
GCP3	-71.92290802	45.37384706	271134.32	5028637.97	304.985
GCP4	-71.92306563	45.37370884	271121.39	5028623.09	304.963
GCP5	-71.92306184	45.37361886	271121.34	5028613.08	304.995
GCP6	-71.92305796	45.3735289	271121.29	5028603.07	304.996

6.3.4.2 RPAS maps

The first retrieved map is the DSM_{RPAS} (Fig. 6.8). The flight happened in December 2019 with a thin layer of snow present on the ground with grass still appearing through the

snow and thus conditions were met as described earlier. In contrast to the other methods, the RPAS distinguishes all objects on the ground. Visible are the station (white square in the centre North), the trees (mainly W/SW), the trailers (N of the station) and other features like tables (near the station) or high vegetation (two horizontal lines in the S/SE). These are also easily distinguishable via the contour lines. Slim structures show only partly, for example, the metal rails along the S and E axis. Although clearly visible in the raw pictures, the SfM method was unable to retrieve them outright.

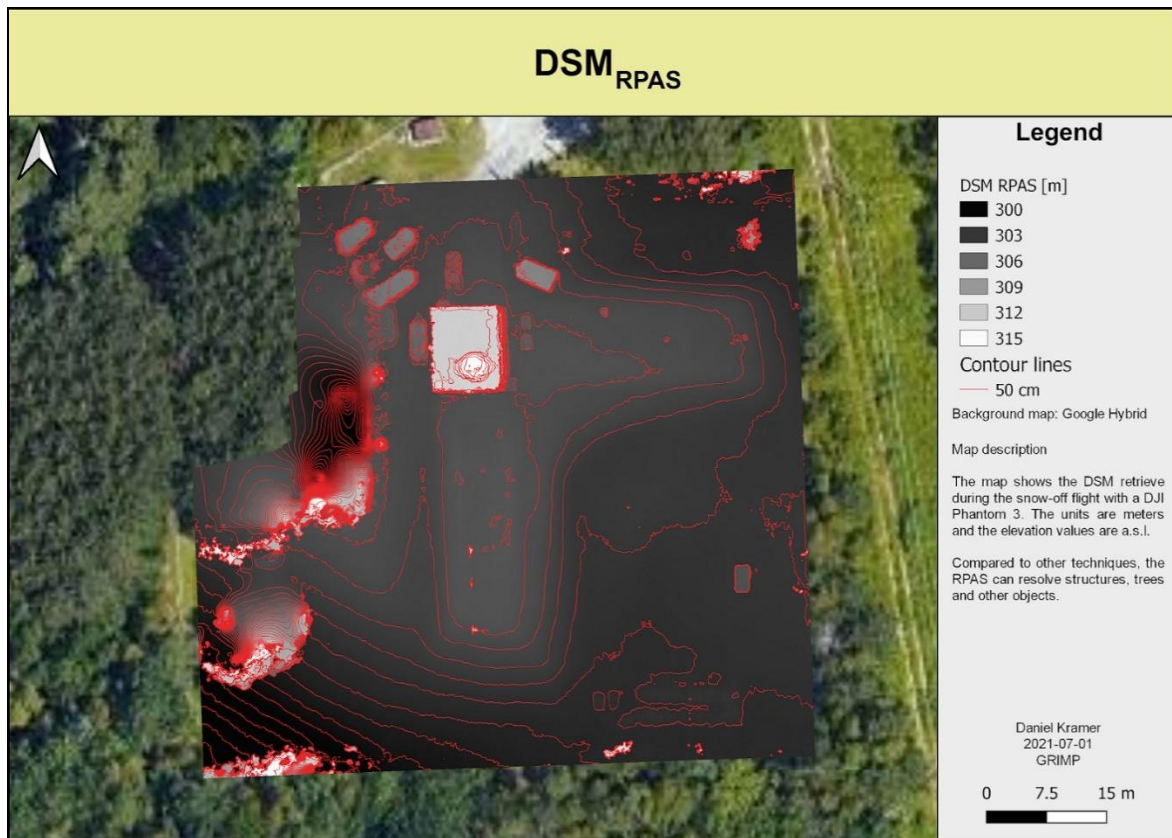


Figure 6.9: Derived DSM from the RPAS flight during snow-off conditions. Units are in metres and a.s.l. and the contour line interval (red) is 50 cm.

To retrieve the TSD via a RPAS, a $DSSM_{RPAS}$ is required. For the same reason as for the $DSSM_{Ref}$ and $DSSM_{SIRA}$, it is not shown. Please note that the SW corner was not resolved by the snow-off flight and thus lead to a false TSD estimation. The missing information can likely be attributed to not having enough overlap. The TSD map_{RPAS} is shown in Fig. 6.9. The footpaths and the snow pits near the station (white lines) are clearly depicted, as these

compacted areas show a lower TSD. We can also see the snow that was removed from the pits, appearing as a darker patch near each pit (thus higher TSD). The thin black lines going to the S and E of the station are the rails and present a large TSD because the DSM_{RPAS} did not resolve them whereas the DSSM_{RPAS} resolved them partially. The two hills below are clearly visible as TSD increases towards the S of the field. Several external objects are visible as white spots indicating a very low TSD, for example the building. All values <20 cm are shown in one category, including negative values. The SE and N edges of the map show very deep snow (>60 cm). Whereas the northern edge is outside the study area, the south-eastern side requires an explanation.



Figure 6.10: TSD map_{RPAS}. TSD is given in metres.

6.4 ANALYSIS

6.4.1 Snow

SIRA underestimates the average TSD by 5.5 cm (Table 6.4), whereas Kramer et al. (2021) found an overestimation of about 5 cm for their arctic study site. Nevertheless, the TSD is comparable, and the RI is with 1.2 similar (only the second digit varies). It shows that

despite different snowpacks, the RI is very similar and thus can be used in different areas after an initial verification.

SIRENE is covered mostly by a flat, grassy ground whereas the ecotypes in the Arctic show a greater variation regarding small surface features (rocks, shrubs, etc.). This is reflected in a higher standard deviation for the Arctic (45%) versus SIRENE (11%) (Table 6.4). The standard deviation for TSD_{SIRA} is 21.7% whereas for the Arctic dataset, it's 37.6%. This result points in a similar direction as for Kramer et al. (2021), meaning that the ecotypes play a profound role in the radar interactions.

The precision of RMSE is comparable in both studies and shows that the algorithm achieves a similar precision. The RMSE for the TSD retrieved from SIRA is 27.1% whereas it's 25.6% for Arctic snow.

6.4.2 Map evaluations

6.4.2.1 TSD maps

Fig. 6.10 shows the TSD differences between the SIRA and the reference measurements. Generally, the differences are rather small with a majority of the values being <10 cm in difference. The distribution follows no obvious pattern. Areas in red cover open and protected parts (e.g., trees) as much as flat and inclined areas. In agreement with the snow statistics, the underestimated areas are larger than the overestimated areas.

Fig. 6.11 shows TSD differences between the RPAS and SIRA (Please note the different scale of the legend). It shows good agreement (within 10 cm difference) along the two rails and in the eastern part of the map. In the central party of the field towards the S, the differences grow to 10 - 30 cm. The large differences in the SW corner are expected as the snow-on flight didn't capture this corner properly, which is visible in the $DSSM_{RPAS}$ (not shown).

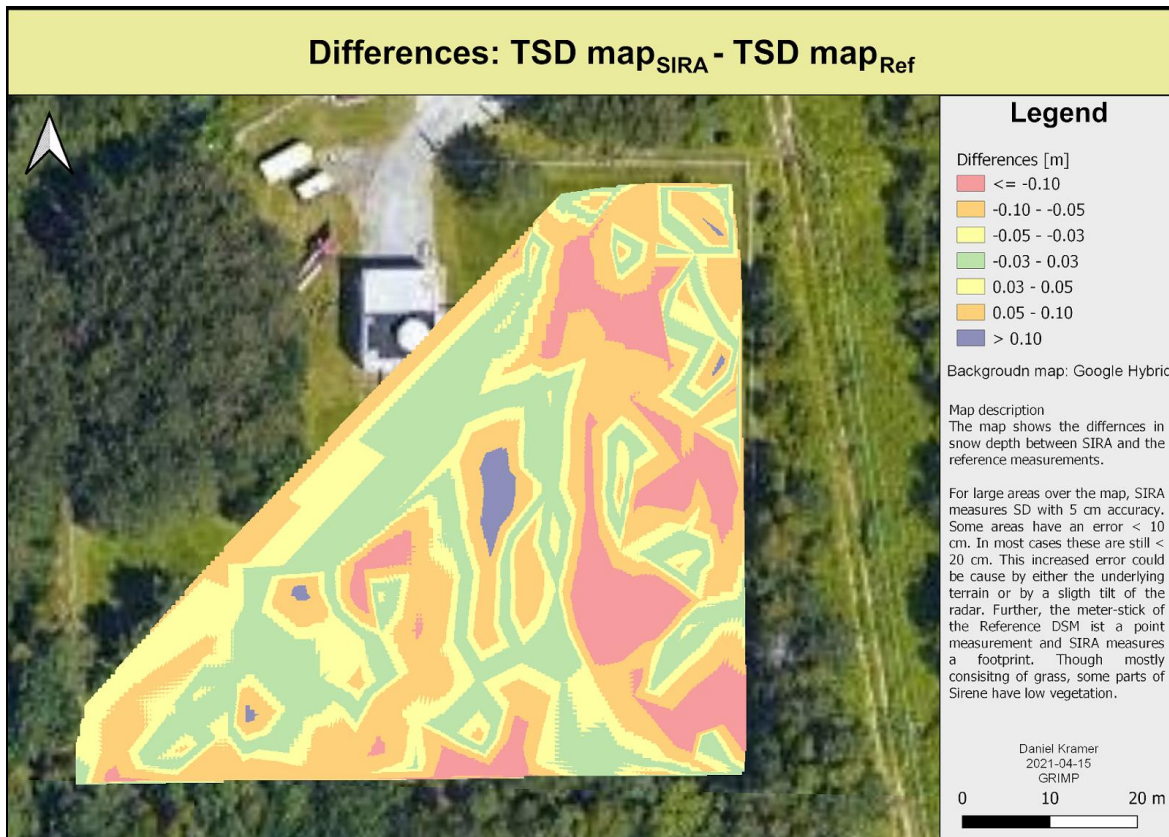


Figure 6.11: Differences in TSD between the SIRA and the reference measurements.

The DSM_{RPAS} shows a gradual increase of discrepancy moving towards the SW corner when compared to the DSM_{Ref} . This corner is surrounded by trees from three sides and an additional tree stands in the centre. The presence of trees may have caused too low an overlap in the snow-off flight. Both flights were performed during winter, when there were no leaves. The difference could arise from different light conditions, slightly different flight patterns or the ground conditions.

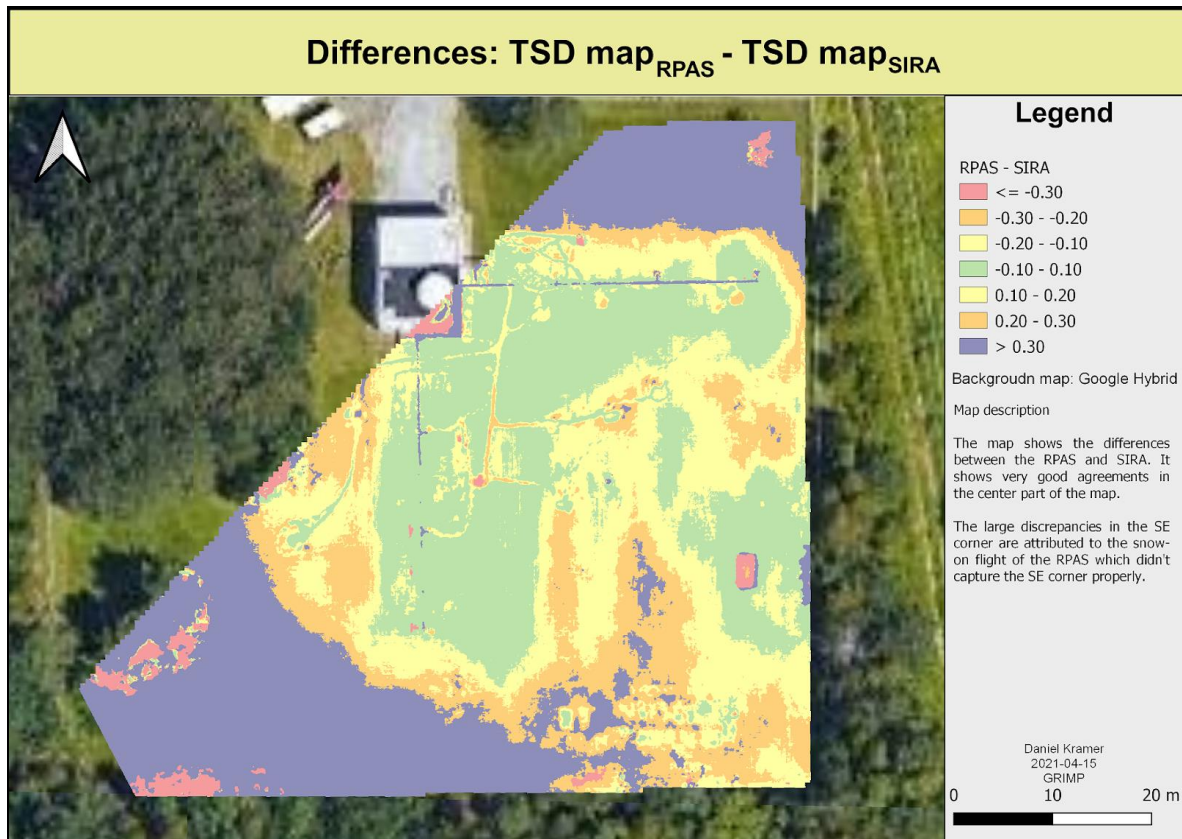


Figure 6.12: Difference between TSD_{RPAS} and TSD_{SIRA}.

6.4.3 Cross-use of methods

Data sets from remote regions are usually rare and expensive. As the DSM_{RPAS} demonstrates, it can easily happen that a data set has been collected but during the analysis it shows (partial) errors. Thus, it would be a great advantage to use different surveys in a cross-use, meaning that the DSM is delivered from one type of survey and the DSSM is delivered by another type. As the previously shown maps are in good agreement and the precision is high, I did this and replaced the faulty DSM_{RPAS} with the DSM_{Ref}. Then I subtracted the DSM_{Ref} from the DSSM_{RPAS} to retrieve the resulting TSD map. In the final step, I calculated the difference between this TSD map and the TSD map_{Ref}. The result is shown in Fig. 6.12. The map shows that there is in general a good agreement between the TSD_{Ref} and the here presented TSD_{cross}. For SIRA and RPAS data, Kramer et al. (2019) and Kramer et al. (2021) showed RMSE-values around 10 - 15 cm, which are similar to the differences in the shown map.

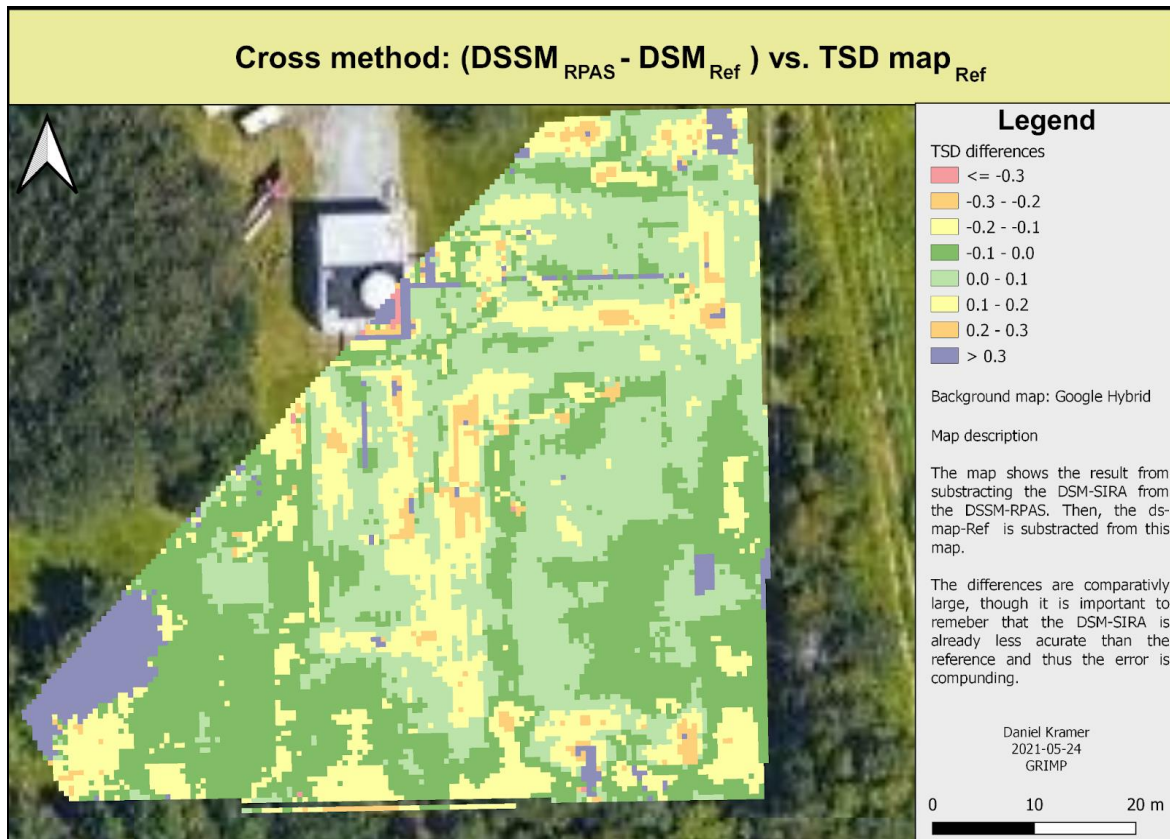


Figure 6.13: Differences between the $ds\ map_{Ref}$ and the calculated ds map combining the DSM_{Ref} with the $DSSM_{RPAS}$.

6.4.4 Surveying aspects

6.4.4.1 Fix-quality of dGNSS signal

The satellite reception plays an important role for the precision of the geolocation. Fig. 6.13 shows the southern, central edge of SIRENE. The red dot has a low fix-quality (1) and the green dots have a high fix-quality (4 or 5). For a), the point has been left in the TIN-calculation and shows a difference of 3.53 m between the DSM_{Ref} and the DSM_{SIRA} . In b), the point has been removed and the TIN-estimation is only -10 cm from the reference. This demonstrates two important points: 1) Removing points with a too low fix-quality is important to ensure a good DSM and 2) that choosing TINs as an interpolation method is a valid option. 1) improves the DSM by removing a point of high uncertainty and 2) shows that the method estimates altitude at the missing point with a high accuracy.

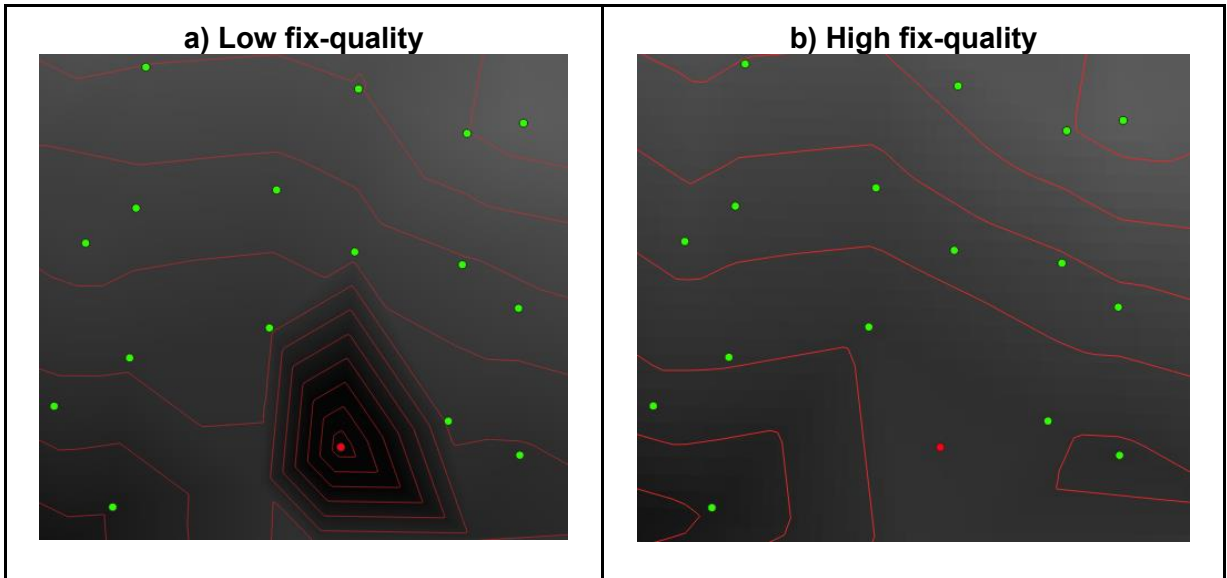


Figure 6.14: The maps show the importance of a data quality check. At the red point, a low fix-quality of 1 has been used during the TIN calculation. In b), the point has been removed.

6.4.4.2 Differences for TSD

I also want to evaluate the removal of a low fix-quality point for the resulting TSD. At the same point, the SIRA measured a TSD of 31.7 cm. The reference measurement is 37.4 cm, which leads to a difference of -5.7 cm. The related figure is 6.14. If the point is not removed, the difference between the SIRA and the reference measurement is -5.5 cm. If the point is removed, the difference is -6.3 cm. This leads me to the following conclusions:

- A difference of 0.8 cm is small compared to an RMSE of 9.2 cm. Thus, the radar measurement itself has a much larger error margin. This is especially true if the size of the radar footprint is taken into account.
- The uncertainty of position with a low fix-quality can be up to several meters. SIRENE has only a few terrain features where a positioning error may not lead to large total errors (as can be seen in this example). But in areas with a) more pronounced terrain features or b) where ecotypes play an important role on the radar precision, it is better to remove this large uncertainty.

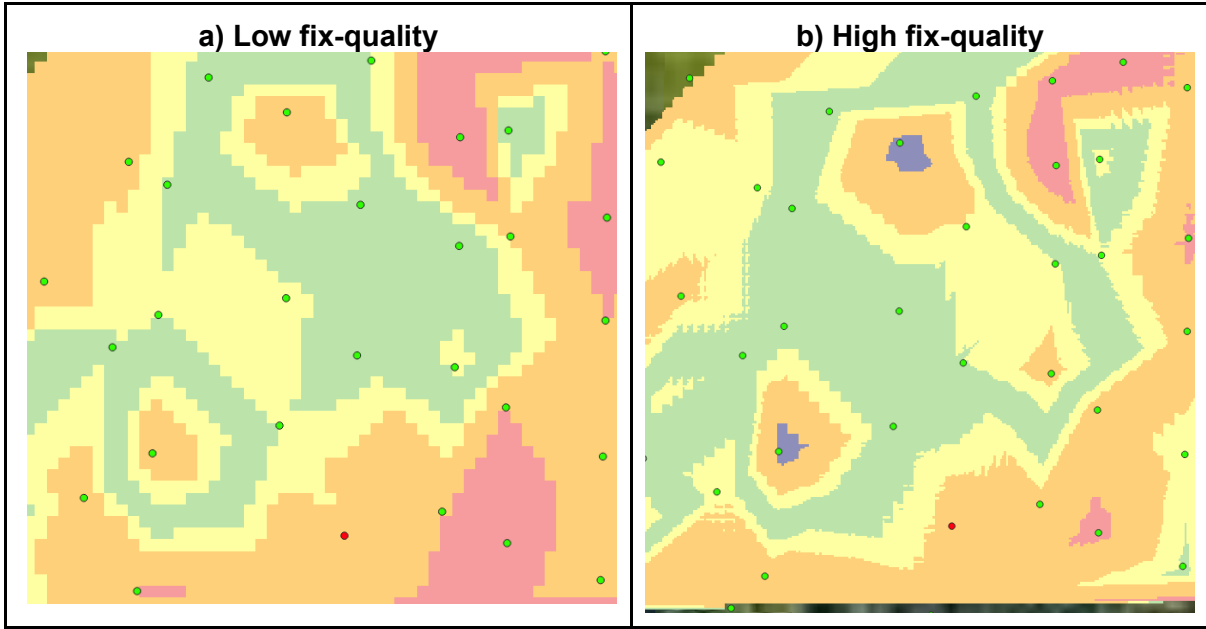


Figure 6.15: Difference in TSD-estimation with low fix-quality (a) and high fix-quality (b).

6.4.4.3 DSM-retrievals

As the DSM-retrieval with the SIRA is new, I want to examine how this method performs in comparison to the reference method and the common RPAS method. The results are illustrated in Fig. 6.15. Part a) shows the $DSM_{SIRA} - DSM_{Ref}$. The SIRA consistently underestimates the height by 20 - 60 cm. Part b) expresses the results $DSM_{RPAS} - DSM_{Ref}$ with most values being in the range of ± 20 cm from the reference in the central area. Part c) shows $DSM_{SIRA} - DSM_{RPAS}$. Similar to the comparison to the DSM_{Ref} , in this case the SIRA underestimates large parts of the map by 20 - 60 cm. I think that the differences can be attributed to the following methodological differences:

1. For both the DSM_{Ref} and the GCPs of the DSM_{RPAS} , I used a RS2 unit to measure the points. The RS2 is a dual-frequency receiver. The SIRA has an implemented M+ unit, which is a mono-frequency receiver.
2. For all points of the DSM_{Ref} and the GCPs for the DSM_{RPAS} , I utilized a 2m-pole with the RS2 unit mounted on top. This ensures better satellite reception. The M+ is mounted close to the radar and thus usually <1 m above the surface.

3. For the DSM_{Ref} and DSM_{RPAS} , I used the official CANNET-SHER station for correcting the position. For the DSM_{SIRA} , I set up a local base station. The type of station is much more mobile and suitable for remote fieldwork but delivers a lower precision for the correction.

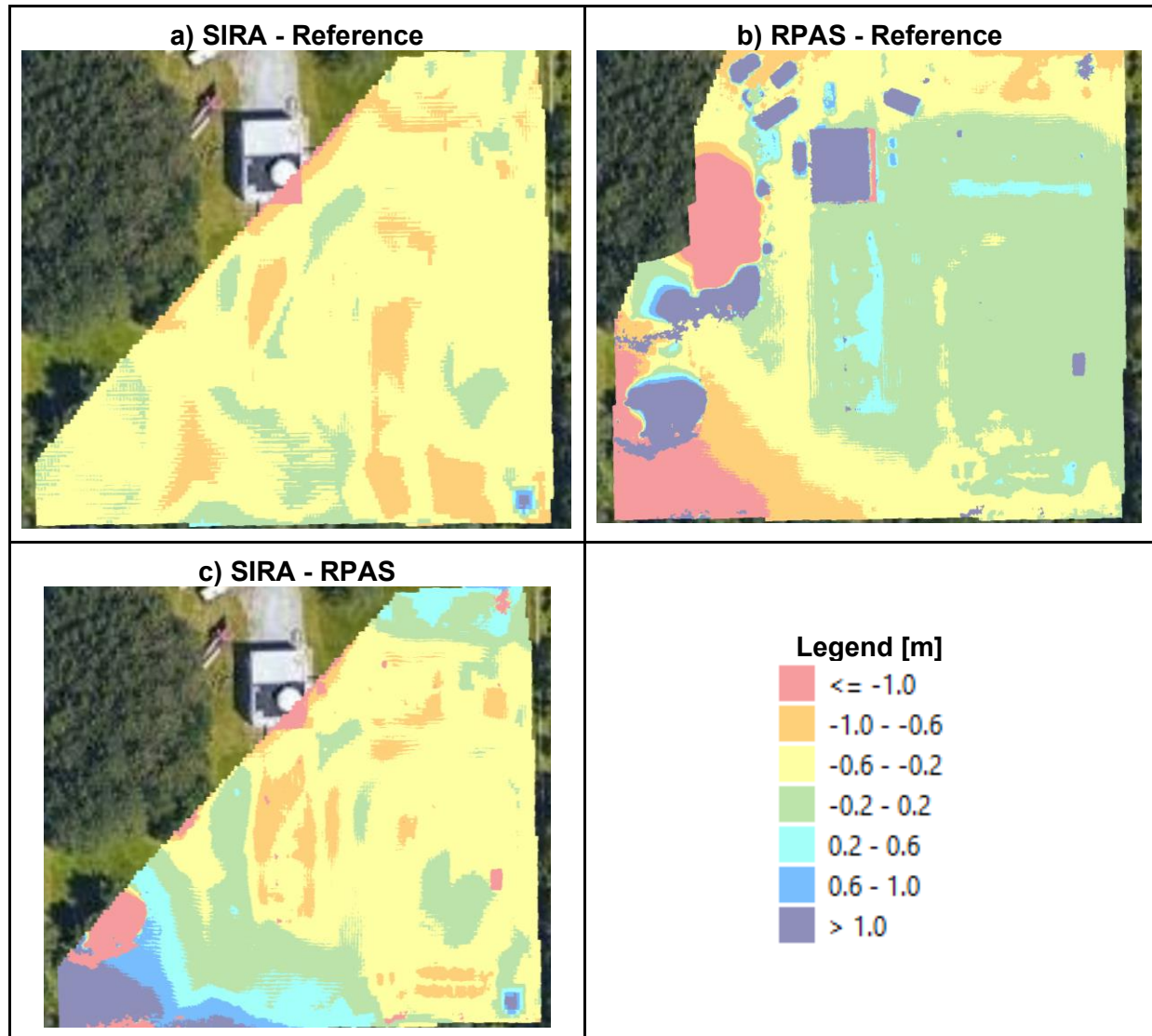


Figure 6.16: DSM comparison between the different methods. The units are given in m.

I want to make one final point on the DSM-retrieval with SIRA:

An offset of 20 - 60 cm is large if the snowpack above is only about 40 cm. This would make the cross-use of methods impossible. Nevertheless, for example the Arctic-DEM has a

resolution of 2 m and thus the results delivered by the SIRA are a great improvement. Further, the SIRA delivers several relevant parameters in a single deployment and can be mounted on a vehicle. This reduces costs by avoiding a second campaign (RPAS method) or by slow data accumulation (reference method).

6.5 CONCLUSION AND FUTURE WORK

The goal of this chapter was to develop and demonstrate the mapping capabilities of the SIRA. After retrofitting the system with a dGNSS unit, I used the SIRA to capture a DSM, a DSSM and a TSD map. Then I produced similar maps with a reference setup and with an RPAS. Finally, I compared the different results and assessed the outcome.

To fulfil the first specific objective, I did the necessary hardware modifications to the SIRA. Then I dug a snowpit at SIRENE to collect ρ_s and TSD to modify the algorithm for the local snow conditions and for reference data. With a TSD of 40 cm, a ρ_s of 230 kg m⁻³ and an RI of 1.2, the values are similar to what I encountered in Cambridge Bay and Trail Valley Creek (chapter 5). 176 valid measurements showed a TSD_{SIRA} of 30.5 cm, which underestimates the TSD_{Ref} by 5.5 cm and a RMSE of 9.2 cm. The three resulting SIRA-maps were produced in the following fashion: I set up a dGNSS station and corrected the SIRA-position via the correction given by said station. The dGNSS gives the precise 3D-position of the SIRA in space. The radar collects the relative positions of the ASI and the SSI. With these three pieces of information, all maps can be derived. The DSM_{SIRA} is calculated by subtracting the distance to the SSI from the vertical part of the 3D-position. The TSD map_{SIRA} is obtained solely by the radar measurement, thus the distance between SSI and ASI. The DSSM_{SIRA} can be extracted either by subtracting the ASI distance from the vertical part of the 3D position or by adding TSD to the DSM_{SIRA}.

For the second specific objective, I produced the same type of maps with a reference system and with an RPAS. For the reference system, I mounted a dGNSS modul on top of a

2 m pole and corrected the position via cellular network to the official CANNET-SHER reference station. I attached a metre-stick to the pole to collect the TSD. From this, I was able to retrieve all three maps. For the RPAS, I conducted two flights, one snow-off (resulting in a DSM) and one snow-on (resulting in a DSSM). From the difference of the two, I calculated the TSD map. My goal in the third specific objective was to assess the map of the SIRA in comparison to a reference map and to the commonly used RPAS-based retrieval. The results show that the derived TSD maps are very similar with the SIRA map diverging only in a few spots more than 10 cm from the reference data. Compared to the TSD map_{RPAS}, the SIRA outperforms the RPAS in TSD precision.

Then I compared each of the DSMs. In this case, the DSM_{SIRA} diverges with a general underestimation of 20 - 60 cm from the reference map. The RPAS performs better, not digressing more than ± 20 cm of the reference. As the DSM_{RPAS} had a large error in the SE corner, I performed a cross-use of methods, meaning that I used the DSSM_{RPAS} and subtracted it from the DSM_{Ref} instead of the DSM_{RPAS}. Then I subtracted it from the TSD map_{Ref}. The results show a very good agreement often within ± 10 cm of the reference. This shows that in the future, we can use different methods in case of faulty data sets given that we achieve survey precision for all methods. This is very helpful for remote (and thus expensive) fieldwork. This claim is supported by my last analysis: Estimating the influence of the fix-quality of the dGNSS signal. If measurements are accepted that do not have a high fix-quality, the resulting maps have a lower precision. With the lower precision, e.g., no cross-use of methods could be done as the positioning errors are much larger than the estimated TSD.

In the future, the presented SIRA-mapper can be used to collect maps of TSD and DSMs in remote regions. Together with the algorithm presented in chapter 5, a simple snow stratigraphy can be derived as well. The combination of both, a simple stratigraphy and high

precision maps, can support e.g. work on PMW. Further, the principle can be adapted to a similar radar that is under development with a dual Ku band (13.5 GHz and 17.25 GHz). These are the same frequencies as for the “Terrestrial Snow Mass Mission”. Thus, the SIRA mapper can provide insights in the radar-snow-interaction and provide maps for ground truthing.

6.6 ACKNOWLEDGEMENT

Many thanks to Gabriel Couët for supporting this work with the dGNSS base station and his expertise in surveying and with QGIS. Further, I want to thank Julien Meloche for conducting the flights and Érika Boisvert-Vignault for helping during the snow measurements.

6.7 COMMENTARY

This chapter has overcome the last two drawbacks of the SIRA. With the use of the dGNSS version, it is possible to map larger areas quickly, even in difficult conditions. During a field campaign in April 2022, we collected snow data near Cambridge Bay and will work on two publications. The second article will in large represent the content of this chapter, but with data from the North instead of SIRENE. The first article will compare different snow interpolation methods for tundra snow. As of now, this comparison does not exist.

7 CONCLUSION

7.1 SUMMARY

Given the very high spatio-temporal variability of snow, many models suffer from a poor representation of the snow surface as models need *in situ* data for validation and development. To address this gap, the overarching goal of this thesis was to develop a high-resolution snow mapping tool based on a radar system, specifically designed for arctic conditions during winter field missions. The system had to be light and little time consuming to construct sound snow datasets in harsh arctic conditions. More specifically, the three predominant environmental conditions with regards to our work were extreme cold, sustained winds and geomagnetic disturbances for the RPAS work. Conducting fieldwork in the arctic remains expensive, thus requiring an optimization of the time available with a high level of flexibility and on-site maintenance to collect high quality datasets. The approach of the different topics addressed in this thesis reflects those concerns.

In chapter 4, I explained how we developed a DIY RPAS platform that can carry a VIS camera and deliver snow information comparable to those found in recent literature using commercial and (partially) much more expensive options (e.g., Nolan et al., 2015; Cimoli et al., 2017; Fernandes et al., 2018). Lab experiments and field deployments proved that our RPAS platform can operate in harsh Arctic environments. Using the SfM approach we retrieved a d_s RMSE of about 13 cm (35 %). Results also showed that the effect of vegetation when working with SfM can enhance the RMSE to about 16 cm (43 %). From the modifications made to the platform, neither geomagnetic disturbances, wind speeds (at 2 m height) over 10 m/s nor temperature down to -40 °C negatively affected the aircraft. When this work started, very little literature was available covering the engineering and the science side of RPAS in the Arctic, thus motivating the need for an interdisciplinary study. However,

the novelty of this work lies in the combination of the DIY approach to build a specialized RPAS, involving estimations for environmental conditions like temperature impact on flight batteries, and retrieval of high-quality snow data matching recent literature. Thus, other groups can use this work as a guideline to build and fly their own RPAS for specific research applications and environmental conditions that commercial RPAS solutions often do not cover.

Results from chapter 5 detailed, first, how to adapt a FMCW radar to arctic snow conditions. Second, we evaluated the potential for mapping by developing an algorithm that is (mostly) independent of prior snow information while handling an unknown sensor height. The SIRA is able to retrieve snow depth with a RMSE of 14.3 cm (25 %), partially outperforming the RPAS SfM results from chapter 4. Furthermore, the method developed can distinguish DH and WS layers and derive SWE, which is a main advantage compared to VIS techniques that cannot penetrate the snow. Nevertheless, the distinction between the layers is affected by the underlying ecotype. By using the dB realm and cutting off any values < 0 dB, I found a reliable method to determine the vertical location of the soil snow interface, a problem raised in Marshall et al. (2008) and Holmgren et al. (1998). This said, lingering uncertainties remain and approaches to reduce errors in estimating the surface roughness using SfM (Meloche et al., 2020), along with distinguishing the ecotypes, based on Ponomarenko et al. (2019), have been analyzed. Overall, with a footprint of about 0.4 m^2 , SIRA fills a gap between satellite-based (Marshall et al., 2008) or airborne-based resolutions (Kolpuke et al., 2020) and snowpits.

The next intuitive step, presented in chapter 6 was to equip the SIRA with a dGNSS unit to ensure a precise geolocation allowing to map of d_s using the methods presented in chapter 5. I compared manual (avalanche probe), RPAS and SIRA results on snow depth retrieval to evaluate the pros and cons of each method. I also evaluated the cross-use of

methods deriving surface models to address potential data gaps and the needs of specific applications (ex. no summer campaign available, meaning the SfM technique can not be used). Results from this chapter showed that the dGNSS unit delivers a precision that a) derives snow information with high accuracy and b) is adaptable to various approaches (i.e. snowmobile and RPAS). From the scientific point of view, when compared to direct snow depth measurements, the SIRA delivers a good precision while informing on stratigraphy. Both require an interpolation of the measurements to retrieve a map of d_s . On the contrary, the RPAS delivers spatially distributed snow depth but suffers from requiring two flights (snow off and snow on), no information on stratigraphy is available and is sensitive to weather conditions. This work is of particular relevance given that Windstral et al. (2014) found that the snow cover needs to be presented with a resolution of 100 m to force or develop models properly. Further, Baba et al. (2019) defined a similar resolution regarding the influence on the underlying DEM. Grünewald et al. (2013) used a grid size of 400 m for statistical snow modelling with elevation, slope and northing: all good predictors for snow distribution. The dGNSS-based SIRA will improve the resolution drastically. Indeed, it can produce snow depth maps of a few metres in spatial resolution with a few centimetres' accuracy.

7.2 LIMITATIONS

7.2.1 RPAS

In the early phase of the data collection, the autopilot of the DIY RPAS has failed on several occasions and manual flights were necessary. A human pilot can not follow a grid pattern with the same precision and the exact required overlap, especially with a glider plane compared to a rotary wing. Thus, those inaccuracies affect the data quality. The commercial RPAS autopilot suffered from problems due to magnetic disturbances. In both cases, I assume that improving the autopilot would yield better results for the tie points as more images would

overlap. Over several campaigns, we modified the autopilot settings, and the DIY RPAS has flown reliably.

As tested during experiments in the lab and on several campaigns, the RPAS can operate safely in temperatures down to -40°C . For the lab experiments, we inferred that the RPAS can still operate with most of its functions in temperatures down to -50°C , but such harsh conditions impose few limits because we rarely encounter such low temperatures during campaigns. On the other hand, wind speed remains the main limit to the systems performance. After several flight tests, we conclude that the RPAS can operate in wind speeds up to 10 m s^{-1} at 2 m height. This is a rule of thumb as we did not measure the wind speed at an altitude of 50–100 m. The plane flew stable, but the difference in speed above ground when flying upwind or downwind created variability in the overlap between photographs, thus affecting the precision of the retrieved DSM maps due to a lower number of tie-points. Thus, we should limit flights to wind speeds $<10\text{ m s}^{-1}$.

The achieved DSM resolution of 6 cm with both the GoPro 6 and the DJI Phantom 3 internal camera on 50 m flight altitudes resulted in a snow depth retrieval RMSE of 35%. Lowering the altitude or using a camera with a higher resolution would lead to an increased resolution on the ground and potentially to a lower RMSE. Occasionally, it is necessary to control the aircraft manually to ensure flight safety or if major problems with the autopilot occur. Manual flight patterns are not as exact as patterns performed with the autopilot, which may lower the quality of the resulting data set.

7.2.2 SIRA

The SIRA is distinguishing DH and WS based on an assumption. As the distinction is not based on a physical measurement, the algorithm works only with the right conditions (presence of DH). As demonstrated in chapter 6, we can modify the algorithm and the assumptions to adapt for different snow and environmental conditions that need to be

considered when planning field campaigns. Another point that needs consideration is the quality control for snow depth measurements. Very deep snowpits, though not representative for the area, may occur naturally, but the quality control settings may eliminate them from the data set analysis. Nevertheless, if the system is used for mapping, the discrepancy for very deep snowpits need to be considered when assessing the statistical performance of the retrievals. Also, when doing single measurements, holding the SIRA in a nadir position is essential. A level was recently added to help reduce errors in positioning, but an IMU would further improve the measurements as it would allow to account for any rotation along the axis during data processing.

The presence of liquid water or wet snow also impose severe limitations for the SIRA, which can happen during melt or rain-on-snow events. This limits the penetration of the radar wave into the snow drastically. For now, it is impossible to know which ecotype lies below the snow surface. As the SIRA requires undisturbed snow, we can only determine the ecotype after the measurement. In the future, using available high-resolution ecotype maps could address this problem (based on Ponomarenko et al., 2019), and developing a dGNSS solution, an augmented reality application for a mobile phone or preselecting specific GNSS locations could solve the issue.

7.2.3 Surveying

In principle, all research sites get good satellite reception as the terrain is flat and there are few structures that could obscure the signal (Caamano et al., 2020; Kubo et al., 2020). Nevertheless, three factors remain uncertain. The first one regards the constantly changing satellite geometry. The user on the ground has no influence on how the satellites travel and can only record the signal as it is. If an unfortunate geometry occurs, the position will be recorded with a lower precision.

The second concern relates to the sampling of the satellite geometry over several hours. Operating in very cold environments limits the battery time of the receivers and we had occasionally shutdowns. Further, even if the receiver finishes all its assigned tasks in an area, it may have to stay longer to acquire the minimum time enabling good final data.

Thirdly, the base station can operate in a limited range that can fluctuate regarding environmental conditions. As of now, this problem is only theoretical as our experiments always happened within the range of the base station. To date, the SIRA can not correct off-nadir measurements, which could be solved using an IMU as mentioned above.

7.3 ONGOING CONTRIBUTIONS AND FUTURE WORK

Aside from the science itself, I have focused a lot on developing and implementing new technologies in research and teaching. In this section I want to describe the contribution I have made that were directly on indirectly part of this work. This is followed by a section on future work.

7.3.1 Ongoing contributions

7.3.1.1 SIRA User interface

After the interface between the IMST radar and the Raspberry Pi was built by team members, I have modified the WiFi-connection of the Raspberry Pi and set it to an “Access Point”. This allows the user to access the Pi via a smart phone and thus control the hardware and download data on site. Also, modifications to a script can be made on the fly and without any physical connection to the device. This setup has been proven very robust and flexible during fieldwork. It is used in our Arctic as well as avalanche team.

7.3.1.2 SIRA geolocation

During the development of the SIRA-algorithm (chapter 5), I equipped the Raspberry Pi with a simple GPS unit. After initial test haven been successful, I have implemented the

Emlid system to enable dGNSS geolocation (chapter 6). This setup is used by a master student working on a method to ρ_s . The setup has been modified by the team to build SIRA-version mounted on a pole. It is not used for mapping but to retrieve the exact location to e.g. determine the underlying ecotype. This adaptation contributes to two master projects, one in the avalanche and one in the arctic team.

7.3.1.3 *RPAS development*

The decision to develop the RPAS has significantly increased the knowhow in our group on electronics and lead to the utilisation of different materials and modern technologies. To customize the aircraft, we started with 3D-printing. The technique itself is now used in many other applications within and outside of the team. This project has further been a foundation for other scientific developments, most noticeable here the adaptation of using the SfM-method to measure surface roughness.

7.3.1.4 *Other contributions*

In the course of writing this thesis, I have supported other research projects and efforts. I have put a lot of time and effort in maintaining and modifying the G.R.I.M.P. automatic weather station near Cambridge Bay and supporting PKC on site with their stations.

I have been teaching regularly courses at the University Centre in Svalbard on polar meteorology and snow. This led to the implementation of multimedia content for teaching and science, incl. Virtual Reality applications, instructional videos (<https://www.earth.no/resource/frost-a-video-about-the-videos>) and video games (<https://www.earth.no/resource/iwalk-how-to-create-a-walkable-map>). As the time of writing, a discussion is ongoing in the department of implementing theses techniques at the University of Sherbrooke as well.

7.3.2 Future work

Utilising already existing RPAS d_s data, I want to combine the approaches from chapter 4 and 5. During earlier field campaigns, we have collected several d_s -maps_{RPAS}. I want to use the empirically found value for ρ_s to produce maps of bulk SWE for areas of up to 200 m². In the future, these areas can be extended quickly. This gives researchers the opportunity to estimate SWE on the local scale without relying on coarse space borne products or expensive airborne campaigns.

It would be interesting to collect more SIRA-measurements for each ET, incl. measurements on footprint and surface roughness. This will help to clarify the uncertainties in accuracies of the SIRA retrievals that I observed over the different ETs. Together with a further investigation of ice layer detection within the arctic snowpack, this work will support research efforts on ungulates populations (Langlois et al., 2017). Ungulates have seen a strong decline related to Rain-on-Snow events as newly formed layers of ice or areas of high snow density impede easy access to food. This aerial validation helps snow simulations to better predict the size, health, and migration routes of ungulates. This knowledge can be applied to the RPAS-based maps as well.

SIRA is capable of detecting lake ice with an accuracy of 2 cm (Pomerleau et al., 2020). For the freeze-up season of 2022, we plan to deploy SIRA on a small floating dock next to the SIMB sensor (Cheng et al., 2014) for comparison of the early on ice detection. Afterwards, we want to mount the SIRA on a DJI Matrice 300 to fly thin ice profiles over the lake and produce accurate maps of ice thickness. In the early season, this would primarily be a safety feature to determine when other scientific work can start. More generally, lake ice plays an important ecological and hydrological role (Cheng et al., 2014; Prowse et al. 2011). As shown in chapter 5, the SIRA is also capable of determining d_s over the ice.

The “Terrestrial Snow Mass Mission”, a Canadian satellite under development, will provide moderate resolution (500 m) measurements for the northern hemisphere via a synthetic aperture radar (SAR). The radar will operate on 13.5 and 15.25 GHz. These are the exact same frequencies as on G.R.I.M.P.s new radar (will be acquired in 2022). Despite the differences between the approaches of SAR and FMCW, the methods developed in chapter 5 and chapter 6 will be directly applied to the new radar to develop retrieval procedures and validation maps.

7.4 CLOSING COMMENTS

The Arctic plays a major role in the global ecosystem and is of major concern from the climatic perspective. The work presented in the thesis aimed at providing solutions for many of the practical aspects of conducting fieldwork in harsh arctic environments. Other researchers and members outside the polar research community can use the DIY RPAS we developed as a blueprint. Such a platform performing individual tasks helps to respect tight research budgets.

Aside from the Arctic-specific experiments on issues related to low temperature, our project also demonstrates that a group that is not focused on engineering can build a DIY RPAS. To combine a RPAS (chapter 4), a SIRA (chapter 5) and a dGNSS (chapter 6) benefits the whole community as this method can serve in high-risk areas (avalanche terrain, ice roads) when direct human access would be dangerous.

A non-destructive system to measure d_s (chapter 5) and high-precision geolocation (chapter 6) will provide new opportunities to include high-resolution snow maps into model forcing and validation, which plays a major role in predicting the future state of the planetary climate.

8 REFERENCES

3Blue1Brown (2019), But what is the Fourier Transform? A visual introduction, <https://www.youtube.com/watch?v=spUNpyF58BY&t=232s>, [link accessed 2022-05-13]

A

Agüera-Vega, F., F. Carvajal-Ramírez, and P. Martínez-Carricondo (2017), Assessment of photogrammetric mapping accuracy based on variation ground control points number using unmanned aerial vehicle, *Measurement*, Vol 98, pp. 221-227, <https://doi.org/10.1016/j.measurement.2016.12.002>.

Anderson, K., Westoby, M.J., James, M.R. 2019,. Low-budget topographic surveying comes of age: Structure from motion photogrammetry in geography and the geosciences. *Progress in Physical Geography: Earth and Environment*, 43(2):163–173. Retrieved from: <https://doi.org/10.1177/0309133319837454>.

B

Baba, M. W., S. Gascoin, C. Kinnard, A. Marchane, and L. Hanich (2019), Effect of Digital Elevation Model Resolution on the Simulation of the Snow Cover Evolution in the High Atlas, *Water Resource Res.*, Vol. 55, Iss. 7, <https://doi.org/10.1029/2018WR023789>

Baldwin, M. P. and T. J. Dunkerton (1999), Propagation of the Arctic Oscillation from the stratosphere to the troposphere, *Journal of Geophysical Research*, Vol. 104, No. D24, pp. 30937 - 30946

Baker-Jarvis, J. (2000), A generalized dielectric polarization evolution equation, *IEEE Transactions on Dielectrics and Electrical Insulation*, 7, 374-386.

Barry, R., and T. Y. Gan (2011), *The Global Cryosphere: Past, Present and Future*, Cambridge University Press, ISBN 9781139496698, 489 p.

Benson, C. S. and M. Sturm (1993), Structure and wind transport of seasonal snow on the Arctic slope of Alaska, *Ann. Glaciol.*, 18, pp. 261-267, DOI: <https://doi.org/10.3189/S0260305500011629>

Bergstedt, H., S. Zwieback, A. Bartsch, and M. Leibman (2018), Dependence of C-Band Backscatter on Ground Temperature, Air Temperature and Snow Depth in Arctic Permafrost Regions, *Remote Sensing*, 10(1), 14, <https://doi.org/10.3390/rs10010142>

Bokhorst, S., Pedersen, S.H., Brucker, L. et al. (2016), Changing Arctic snow cover: A review of recent developments and assessment of future needs for observations, modelling, and impacts, *Ambio* 45, 516–537, <https://doi.org/10.1007/s13280-016-0770-0>

Bormann, K. J., R. D. Brown, C. Derksen, and T. H. Painter (2018), Estimating snow-cover trends from space, *Nature Climate Change*, Vol. 8, pp. 924–928,

Bouya, Z., Terkildsen, M., and M. Francis (2013), Monitoring and forecasting Regional Ionospheric perturbations over Australia based on GNSS techniques, *EGU General Assembly 2013, held 7-12 April, 2013 in Vienna, Austria, id. EGU2013-3856, bibcode: 2013EGUGA..15.3856B*

BrainGain (2018), CW RADAR / Dopplerradar | Hochfrequenztechnik, <https://www.youtube.com/watch?v=BedgbVqCqEk>, [link accessed 2022-05-14]

Bromwich, D. H. (1988), Snowfall in High Southern Latitudes, *Rev. of Geophys.* Vol. 26, No. 1, pp. 149-186, <https://doi.org/10.1029/RG026i001p00149>

Brooker, G. M. (2005), Understanding Millimetre Wave FMCW Radars, *1st International conference on Sensing Technology, 21-23.11.2005, Palmerston North, New Zealand*

Brown, R. D. (2000), Northern Hemisphere snow cover variability and change 1915–97, *Journal of climate*, 13(13), 2339-2355.

Brown, R. D., and B. E. Goodison (2005), Snow cover, *Encyclopedia of Hydrological Sciences*, John Wiley & Sons, Ltd, ISBN: 9780471491033, DOI: 10.1002/0470848944

Busseau, B.-C., A. Royer, A. Roy, A. Langlois, and F. Domine (2017), Analysis of snow-vegetation interactions in the low Arctic-Subarctic transition zone (northeastern Canada), *Phys. Geogr.*, Vol. 38, Issue 2, pp. 159-175, <https://doi.org/10.1080/02723646.2017.1283477>

C

Caamano, M., O. G. Crespillo, D. Gerbeth, and A. Grosch (2020), Detection of GNSS Multipath with Time-Differenced Code-Minus-Carrier for Land-Based Applications, *IEEE, 2020 European Navigation Conference (ENC), 23-24 Nov. 2020, Dresden, Germany, DOI: 10.23919/ENC48637.2020.9317340*

Callaghan, T. V., M. Johansson, R. D. Brown, P. Y. Groisman, N. Labba, V. Radionov, R. G. Barry, O. N. Bulygina, R. L. H. Essery, D. M. Frolov, V. N. Golubev, T. C. Grenfell, M. N. Petrushina, V. N. Razuvaev, D. A. Robinson, P. Romanov, D. Shindell, A. B. Shmakin, S. A. Sokratov, S., and D. Yang (2011), The Changing Face of Arctic Snow Cover: A Synthesis of Observed and Projected Changes, *A Journal of the Human Environment* 40(sp1):17-31. 2011, doi: <http://dx.doi.org/10.1007/s13280-011-0212-y>

CAVM Team (2003), Circumpolar Arctic Vegetation Map. (1:7,500,000 scale), Conservation of Arctic Flora and Fauna (CAFF) Map No. 1. U.S. Fish and Wildlife Service, Anchorage, Alaska. ISBN: 0-9767525-0-6, ISBN-13: 978-0-9767525-0-9

Chang, A. T. C., J. L. Foster, D. K. Hall, A. Rango, and B. K. Hartline (1982), Snow water equivalent estimation by microwave radiometry, *Cold Regions Science and Technology*, Vol. 5, Iss. 3, pp. 259-267, [https://doi.org/10.1016/0165-232X\(82\)90019-2](https://doi.org/10.1016/0165-232X(82)90019-2)

Che, T., X. Li, R. Jin, and C. Huang (2014), Assimilating passive microwave remote sensing data into a land surface model to improve the estimation of snow depth, *Remote Sensing of Environment*, Vol. 143, pp. 54-63, <https://doi.org/10.1016/j.rse.2013.12.009>

Cherkauer, K. A., and D. P. Lettenmaier (2003), Simulations of spatial variability in snow and frozen soil, *J. of. Geophys. Res: Atmosphere*, Vol. 108, Issu. D22, <https://doi.org/10.1029/2003JD003575>

Cheng, B., T. Vihma, L. Rontu, A. Kontu, H. Kheyrollah Pour, C. Duguay & J. Pulliainen (2014), Evolution of snow and ice temperature, thickness and energy balance in Lake Orajärvi, northern Finland, *Tellus A: Dynamic Meteorology and Oceanography*, 66:1, DOI: 10.3402/tellusa.v66.21564

Chudley, T.R., Christoffersen, P., Doyle, S.H., Abellan, A., Snooke, N. 2019. High-accuracy UAV photogrammetry of ice sheet dynamics with no ground control. *The Cryosphere*, 13(3):955–968. Retrieved from: <https://doi.org/10.5194/tc-13-955-2019>.

Cimoli, Emiliano, Marco Marcer, Baptiste Vandecrux, Carl E. Bøggild, Guy Williams, and Sebastian B. Simonsen (2017), Application of Low-Cost Uass and Digital Photogrammetry for High-Resolution Snow Depth Mapping in the Arctic; *Remote Sensing* 9 (11): 1–29. <https://doi.org/10.3390/rs9111144>

Clark, M. P., J. Hendrikx, A. G. Slater, D. Kavetski, B. Anderson, N. J. Cullen, T. Kerr, E. Ö. Hreinsson, and R. A. Woods (2011), Representing spatial variability of snow water equivalent in hydrologic and land-surface models: A review, *Water Resources Research*, Vol. 47, Iss. 7, <https://doi.org/10.1029/2011WR010745>

Cohern, M. X. (2019), Frequency resolution and zero-padding, <https://www.youtube.com/watch?v=oh7WvhlkxnU&t=10s>, [link accesses 2022-05-14]

Colbeck, S. (1980), Thermodynamics of snow metamorphism due to variations in curvature, *J. of Glacio.*, 26 (94), pp. 291 - 301, doi:10.3189/S0022143000010832

Colbeck, S.C. (1982), An Overview of Seasonal Snow Metamorphism, *Rev. of Geophys. s and Space Phys.*, Vol. 20, Iss. 1, pp. 45-61, <https://doi.org/10.1029/RG020i001p00045>

Colbeck, S.C. (1983), Theory of metamorphism of dry snow, *Journal of Geophysical Research*, 88, 5475-5482. <https://doi.org/10.1029/JC088iC09p05475>

Connolly, R., M. Connolly, W. Soon, D. R. Legates, R. G. Cionco, and V. M. V. Herrera (2019), Northern Hemisphere Snow-Cover Trends (1967–2018): A Comparison between Climate Models and Observations, *Geoscience*, Vol. 9, Iss. 3, <https://doi.org/10.3390/geosciences9030135>

Cumming, W. A. (1952), The dielectric properties of ice and snow at 3.2 centimeters, *Journal of Applied Physics*, 23(7):768–773.

D

Derksen, C. et al. (2021), Development of the Terrestrial Snow Mass Mission, *IEEE International Geoscience and Remote Sensing Symposium IGARSS*, pp. 614-617, doi: 10.1109/IGARSS47720.2021.9553496.

Dickson, T. (2022), RPAS-SfM snow depth and snow density mapping in disturbed vegetated mountainous environments of Coastal British Columbia, Master thesis, University of Victoria (BC)

Dolant, C., A. Langlois, B. Montpetit, L. Brucker, A. Roy, and Alain Royer (2016), Development of rain-on-snow detection algorithm using passive microwave radiometry, *Hydr. Proc.*, Vol. 20, Iss. 18, pp. 3184-3196, <https://doi.org/10.1002/hyp.10828>

Dolant, C. A. Langlois, L. Brucker, A. Royer, A. Roy, and B. Montpetit (2017), Meteorological inventory of rain-on-snow events in the Canadian Arctic Archipelago and satellite detection assessment using passive microwave data, *Physical Geography*, Vol. 39, Iss. 5, <https://doi.org/10.1080/02723646.2017.1400339>

Domine, F., G. Picard, S. Morin, M. Barrere, J.-B. Madore, and A. Langlois (2019), Major Issues in Simulating Some Arctic Snowpack Properties Using Current Detailed Snow Physics Models: Consequences for the Thermal Regime and Water Budget of Permafrost, *Journal of Advances in Modeling Earth Systems*, Vol. 11, Iss. 1, pp. 34-44, <https://doi.org/10.1029/2018MS001445>

Dong, C. (2018), Remote sensing, hydrological modeling and in situ observations in snow cover research: A review, *Journal. of Hydrology*, Vol. 561, pp. 573-583, <https://doi.org/10.1016/j.jhydrol.2018.04.027>

Dyer, J. L., and T. L. Mote (2006), Spatial variability and trends in observed snow depth over North America, *The Cryosphere*, Vol. 33, Iss. 16, <https://doi.org/10.1029/2006GL027258>

E

Engineering Funda (2017), Doppler RADAR or Continuous wave RADAR in RADAR Engineering, <https://www.youtube.com/watch?v=Xwo1qdzWAgk>, [link accessed 2022-05-18]

EOS (2021), Earth Observation System, <https://eos.com/find-satellite/pleiades-1>, link accesses on 2021-07-14

ESRI (2016), What is a TIN surface, ArcGIS Desktop help, <https://desktop.arcgis.com/en/arcmap/10.3/manage-data/tin/fundamentals-of-tin-surfaces.htm>, [link accessed on 2021-05-01],

F

Fernandes, R., F. Canisius, S. Leblanc, M. Maloley, S. Oakes, C. Prevost, and C. Schmidt (2016), Assessment of UAV Based Photogrammetry for Snow Depth Mapping: Data Collection and Processing, Geomatics Canada Open Technical Report

Fernandes, R., Prevost, C., Canisius, F., Leblanc, S. G., Maloley, M., Oakes, S., Holman, K. et Knudby, A. (2018): Monitoring snow depth change across a range of landscapes with ephemeral snowpacks using structure from motion applied to lightweight unmanned aerial vehicle videos; Cryosphere, vol. 12, no 11, p. 3535-3550.

FMCWtut (2022), Frequency-Modulated Continuous-Wave Radar (FMCW Radar), <https://www.radartutorial.eu/02.basics/Frequency%20Modulated%20Continuous%20Wave%20Radar.en.html>, [link accessed 2022-05-10]

Foster, L., C. Sun, J. P. Walker, R. Kelly, A. Chang, J. Dong, and H. Powell (2005), Quantifying the uncertainty in passive microwave snow water equivalent observations, Rem. Sens. of Envir., Vol. 94, Issue 2, pp. 187-203, <https://doi.org/10.1016/j.rse.2004.09.012>

G

Gargano, D., G. Vecchio, and L. Bernardo (2010), Plant–soil relationships in fragments of Mediterranean snow-beds: ecological and conservation implications, *Plant Ecology*, Vol. 207, pp. 175–189, <https://doi.org/10.1007/s11258-009-9663-7>

Gacitúa, G., C. Bay, M. R. Pedersen, and M. P. Tamstorf (2013), Quantifying Snow and Vegetation Interactions in the High Arctic Based on Ground Penetrating Radar (GPR), Arctic, Antarctic, and Alpine Research Journal Vol. 45, Iss. 2, <https://doi.org/10.1657/1938-4246-45.2.201>

Geodetics (2021), DEM, DSM & DTM: Digital Elevation Model – Why It’s Important, [accessed 2021 Jul 22] <https://geodetics.com/dem-dsm-dtm-digital-elevation-models/>

Giese, A. L., and R. L. Hawley (2015), Reconstructing thermal properties of firn at Summit, Greenland, from a temperature profile time series, *Journal of Glaciology*, Vol. 61, Iss. 227, pp. 503 - 510 DOI: <https://doi.org/10.3189/2015JoG14J204>

Glen, J. W. and Paren, J. G. (1975), *The electrical properties of snow and ice. Journal of Glaciology*, 15:15-38.

GLOBSNOW (2021), link accessed 2021-07-14, https://www.globsnow.info/index.php?page=Snow_Water_Equivalent#:~:text=The%20SW E%20product%20is%20projected,geometry%20of%20the%20pixels%20varies.

Goodrich, L. E. (1982), The influence of snow cover on the ground thermal regime, *Can. Geotech. J.*, 19, pp. 421-432

Golledge, N. R. (2020), Long-term projections of sea-level rise from ice sheets, *WIREs climate change*, Vol. 11, Iss. 2, <https://doi.org/10.1002/wcc.634>

Gouttevin, I., M. Langer, H. Lowe, J. Boike, M. Proksch, et al. (2018), Observation and modeling of snow at a polygonal tundra permafrost site: Spatial variability and thermal implications, *The Cryosphere*, Copernicus 2018, 12 (11), pp. 3693-3717, DOI : 10.5194/tc-12-3693-2018

Grenfell, T. C., and D. K. Perovich (2004), Seasonal and spatial evolution of albedo in a snow-ice-land-ocean environment, *Journal of Geophysical Research – Oceans*, Vol. 109, Iss. C1, <https://doi.org/10.1029/2003JC001866>

Gunn, G. E., B. M. Jones, and R. C. Rangel (2021), Unpiloted Aerial Vehicle Retrieval of Snow Depth Over Freshwater Lake Ice Using Structure From Motion, *Front. Remote Sens., Sec. Unoccupied Aerial Systems (UASs and UAVs) Vol. 2 – 2021*, <https://doi.org/10.3389/frsen.2021.675846>

Grünewald, T., J. Stötter, J. W. Pomeroy, R. Dadic, I. Moreno Baños, J. Marturià, M. Spross, C. Hopkinson, P. Burlando, and M. Lehning (2013), Statistical modelling of the snow depth distribution in open alpine terrain, *Hydrol. Earth Syst. Sci.*, 17, 3005–3021, <https://doi.org/10.5194/hess-17-3005-2013>, 2013.

Groot Zwaafink, C. D., A. Cagnati, A. Crepaz, C. Fierz, G. Macelloni, M. Valt, and M. Lehning (Feb. 2013). “Event-driven deposition of snow on the Antarctic Plateau: analyzing field measurements with SNOWPACK”. In: *The Cryosphere* 7.1, pp. 333–347. doi: 10.5194/tc-7-333-2013

H

Hamza, V., B. Stopar and O. Sterle (2021), Testing the Performance of Multi-Frequency Low-Cost GNSS Receivers and Antennas, *Sensors* 2021, 21, 2029. <https://doi.org/10.3390/s21062029>

Hein, G. (2020), Status, perspectives and trends of satellite navigation, *Satellite Navigation*, 1, 22, 10.1186/s43020-020-00023-x.

Holmgren, J., M. Sturm, N. E. Yankielun, and G. Koh (1998), Extensive measurements of snow depth using FM-CW radar, *Cold Reg. Sci. and Tech.*, Vol. 27, pp. 17–30, [https://doi.org/10.1016/S0165-232X\(97\)00020-7](https://doi.org/10.1016/S0165-232X(97)00020-7)

I

ICSSG (2009), The International Classification for Seasonal Snow on the Ground, International Hydrological Programme of the United Nations Educational, Scientific and Cultural Organization (UNESCO-IHP), Paris, in the series of IHP Technical Documents in Hydrology: IACS Contribution.

IPCC (2019), IPCC Special Report on the Ocean and Cryosphere in a Changing Climate [H.-O. Pörtner, D.C. Roberts, V. Masson-Delmotte, P. Zhai, M. Tignor, E. Poloczanska, K. Mintenbeck, A. Alegría, M. Nicolai, A. Okem, J. Petzold, B. Rama, N.M. Weyer (eds.)].

J

Jo, D., Kwon, Y. 2019. Development of Autonomous VTOL UAV for Wide Area Surveillance. *World Journal of Engineering and Technology*, 7(1):227–239. Retrieved from: <https://doi.org/10.4236/wjet.2019.71015>.

Jonscher, A. K. (1996), Universal relaxation law, *Chelsea Dielectrics press, London*.

K

Kelly, R. E.J., and A. T. C. Chang (2003), Development of a passive microwave global snow depth retrieval algorithm for special sensor microwave imager (SSM/I) and advanced microwave scanning radiometer-EOS (AMSR-E) data, *Radio Science*, Vol. 38, Iss. 4, DOI: 10.1029/2002RS002648

Kelly, R (2009), The AMSR-E Snow Depth Algorithm: Description and results, *J. of Rem. Sens. Soc. Of Jap.*, Vol. 29, No. 1, pp. 307-317

Kendall, R. A., and P. T. Giles (2019), Satellite image analysis of changes in glacier cover in Canada's northern Mackenzie Mountain Range (1987–2017), *The Can. Geogr.*, Vol. 63, Iss.3, Pages 466-477, <https://doi.org/10.1111/cag.12533>

King, J. (2014), Remote Sensing Observations of Tundra Snow with Ku- and X-band Radar, doctoral thesis, Waterloo, Ontario, UWSpace. <http://hdl.handle.net/10012/8218>

King, J., C. Derksena, P. Toose, A. Langlois, C. Larsenc, J. Lemmetyinen, P. Marsh, B. Montpetit, A. Roy, N. Rutter, and M. Sturm (2018), The influence of snow microstructure on dual-frequency radar measurements in a tundra environment, *Rem. Sens. of Envir.*, Vol. 215, pp. 2420-254, <https://doi.org/10.1016/j.rse.2018.05.028>

King, J. C., and J. Turner (1997), Antarctic Meteorology and Climatology, *Cambridge Bay University Press*.

Kolpuke, S., S. Yan, C. Simpson, J. Sutphin, N. Nickerson, O. Reyhanigalangashi, R. Taylor, A. Awasthi, D. A. Braaten, H. P. Marshall, and S. Goginen (2020), *Development and Optimization of Airborne FMCW Radar for High-Resolution Snow Depth Measurements*, *American Geophysical Union, Fall Meeting 2020, abstract #C005-0004*

Kosugi, K., K. Nishimura, and N. Maeno (1992), Snow ripples and their contribution to the mass transport in drifting snow, *Boundary-Layer Meteorology*, Vol. 59, pp. 59–66, <https://doi.org/10.1007/BF00120686>

Kramer, D., Meloche, J., Langlois, A., McLennan, D., Chapdelaine, B., Gauthier-Barrette, C., Royer, A., Cliche, P. 2019. Designing a Do-It-Yourself (DIY) Unmanned aerial Vehicle (UAV) for Arctic research purposes and proving its capabilities by retrieving snow depth via structure-from-motion. Aqhalat 2019, Polar Knowledge Canada, in print

Kramer, D., A. Langlois, A. Royer, J.-B. Madore, J. King, D. McLennan, and É. Boisvert-Vigneault (2021), Assessment of Arctic snow stratigraphy and water equivalent using a portable Frequency Modulated Continuous Wave RADAR, *Cold Region Science and Technology*, under review

Kraus, H. (2000), *Die Atmosphäre der Erde*, Springer Verlag, 3rd edition.

Krogh, S. A., and J. W. Pomeroy (2019), Impact of Future Climate and Vegetation on the Hydrology of an Arctic Headwater Basin at the Tundra–Taiga Transition, *Journal of Hydrometeorology*, Vol. 20, Iss. 2, pp. 197–215, DOI: <https://doi.org/10.1175/JHM-D-18-0187.1>

Kubo, N., K. Kobayashi, and R. Furukawa (2020), GNSS Multipath Detection Using Continuous Time-Series C/N0, *Sensors* 2020, 20(14), 4059; <https://doi.org/10.3390/s20144059>.

Kwok, R. (2018), Arctic sea ice thickness, volume and multiyear ice coverage: losses and coupled variability (1958–2018), *Environmental Research Letters*, Vol. 13, 105005

L

Laliberté, J., A. Langlois, A. Royer, J.-B. Madore, and F. Gauthier (2021), Retrieving dry snow stratigraphy using a versatile low-cost frequency modulated continuous wave (FMCW) K-band radar, *Physical Geography*, <https://doi.org/10.1080/02723646.2021.2008104>

Langlois, A. (2022), *oral communication*.

Langlois, A. (2007), Development of a Snow Water Equivalent (SWE) Algorithm over First-Year Sea Ice using In-Situ Passive Microwave Radiometry, PhD thesis, University of Manitoba

Langlois, A., and D.G. Barber (2007), *Passive microwave remote sensing of seasonal snow-covered sea ice*, *Progress in Physical Geography: Earth and Environment*, Vol. 31, Iss. 6, <https://doi.org/10.1177/0309133307087082>

Langlois, A., R. Scharien, T. Geldsetzer, J. Iacozza, D. G. Barber, and J. Yackel (2008), Estimation of snow water equivalent over first-year sea ice using AMSR-E and surface observations, *Remote Sensing of Environment*, Vol. 112, Iss. 9, pp. 3656-3667, <https://doi.org/10.1016/j.rse.2008.05.004>

Langlois, A., A. Royer, C. Derksen, B. Montpetit, F. Dupont, K. Goïta (2012), Coupling the snow thermodynamic model SNOWPACK with the microwave emission model of layered snowpacks for subarctic and arctic snow water equivalent retrievals, *Water Resource. Res.*, Vol. 48, Issue 12, <https://doi.org/10.1029/2012WR012133>

Langlois, A., J. Bergeron, R. Brown, A. Royer, R. Harvey, A. Roy, L. Wang, and N. Thériault (2014), Evaluation of CLASS 2.7 and 3.5 Simulations of Snow Properties from the Canadian Regional Climate Model (CRCM4) over Québec, Canada, *Journal of Hydrometeorology*, Vol. 15, Iss. 4, pp. 1325-1343, DOI: <https://doi.org/10.1175/JHM-D-13-055.1>

Langlois, A., C.-A. Johnson, B. Montpetit, A. Royer, E. A. Blukacz-Richards, E. Neave, C. Dolant, A. Roy, G. Arhonditsis, D.-K. Kim, S. Kaluskar, and L. Brucker (2017), Detection of rain-on-snow (ROS) events and ice layer formation using passive microwave radiometry: A context for Peary caribou habitat in the Canadian Arctic, *Remote Sensing of Environment*, Vol. 189, pp. 84-95, <https://doi.org/10.1016/j.rse.2016.11.006>

Larue, F., A. Royer, D. De Sève, A. Langlois, A. Roy, and L. Brucker (2017), Validation of GlobSnow-2 snow water equivalent over Eastern Canada, *Rem. Sens. of Envir.*, Vol. 194, pp. 264-277, <https://doi.org/10.1016/j.rse.2017.03.027>

Larue, F., A. Royer, D. De Sève, A. Roy, and E. Cosme (2018), Assimilation of passive microwave AMSR-2 satellite observations in a snowpack evolution model over northeastern Canada, *Hydrology and Earth System Sciences*, Vol. 22, Iss. 11, pp. 5711-5734, <https://doi.org/10.5194/hess-22-5711-2018>

Larue, F., G. Picard, L. Arnaud, I. Ollivier, C. Delcourt, M. Lamare, F. Tuzet, J. Revuelto, and M. Dumont (2020), Snow albedo sensitivity to macroscopic surface roughness using a new ray-tracing model, *The Cryosphere*, Vol. 14, pp. 1651-1672, <https://doi.org/10.5194/tc-14-1651-2020>

Lemmetyinen, J., C. Derksen, H. Rott, G. Macelloni, J. King, M. Schneebeli, A. Wiesmann, L. Leppänen, A. Kontu, and J. Pulliainen (2018), Retrieval of Effective Correlation Length and Snow Water Equivalent from Radar and Passive Microwave Measurements, *Rem. Sens.*, Vol. 10 (2), 170, doi:10.3390/rs10020170

Levasseur, S., K. Brown, A. Langlois, and D. McLennan (2021), Measurement of Snow Physical Properties and Stable Isotope Variations in the Canadian Sub-Arctic and Arctic Snowpack, *Atmosphere-Ocean*, Vol. 59, Iss. 3, <https://doi.org/10.1080/07055900.2021.1962240>

Libbrecht, K. G. (2005), *The physics of snow crystals, Reports on progress in Physics, Vol. 68, No. 4*

Liston, G.E., C. A. Hiemstra (2011), The changing cryosphere: Pan-Arctic snow trends (1979-2009), *Journal of Climatology*, Vol. 24, pp. 5691-5712

Logsdon, S. D., and D. A. Laird (2004), Cation and Water Content Effects on Dipole Rotation Activation Energy of Smectites, *Soil Science Society of America Journal*, 68, 1586-1591.

López-Moreno, J. I., S.R. Fassnacht, J. T. Heath, K. N. Musselman, J. Revuelto, J. Latrond, E. Morán-Tejeda, and T. Jonas (2013), Small scale spatial variability of snow density and depth over complex alpine terrain: Implications for estimating snow water equivalent, *Adv. in Water Res.*, Vol. 55, pp. 40-52, <https://doi.org/10.1016/j.advwatres.2012.08.010>

Lyon, S. W., Destouni, G., Giesler, R., Humborg, C., Mörrth, M., Seibert, J., Karlsson, J., and P. A. Troch (2009), Estimation of permafrost thawing rates in a sub-arctic catchment using recession flow analysis, *Hydrological and Earth System Science*, 13, pp. 595–604, <https://doi.org/10.5194/hess-13-595-2009>

M

Madore, J.-B., A. Langlois, and K. Côté (2018), Evaluation of the SNOWPACK model's metamorphism and microstructure in Canada: a case study, *Physical Geography*, Vol. 39, Iss. 5, <https://doi.org/10.1080/02723646.2018.1472984>

Mantua N. J. and S. R. Hare (2002), The Pacific Decadal Oscillation, *Journal of Oceanography*, Vol. 58, pp. 35-44

Marshall, H. P., G. Koh, and R. R. Forster (2005), Estimating alpine snowpack properties using FMCW radar, *Annals of Glac.*, Vol. 40, pp. 157 - 162, DOI: <https://doi.org/10.3189/172756405781813500>

Marshall, H. P., G. Koh, and M. Sturm (2008), Ultra-broadband portable microwave FMCW radars for measuring snow depth, snow water equivalent, and stratigraphy: practical considerations, *Proceedings of the XXIXth International Union of Radio Science (URSI) General Assembly, August 9-16, 2008*

Martínez-Carricondo, P., F. Agüera-Vega, F. Carvajal-Ramírez, F. Mesas-Carrascosa, A. García-Ferrer, and F. Pérez-Porras (2018), Assessment of UAV-photogrammetric mapping accuracy based on variation of ground control points, *Int. J. of App. Earth Obs. and Geoinfo.*, Vol 72, pp 1-10, <https://doi.org/10.1016/j.jag.2018.05.015>.

Matsumoto, N. (2009), Snow Molds: A Group of Fungi that Prevail under Snow, *Microbes and Environments*, Vol. 24, No. 1, pp 14-20, <https://doi.org/10.1264/jsme2.ME09101>

- Mätzler, C. (1987), Applications of the interaction of microwaves with the natural snow cover, *Remote Sensing Reviews*, 2:2, 259-387, DOI: 10.1080/02757258709532086
- McLennan, D. (2016), CHARS ERA Ecosystem Monitoring - Pilot Phase document, Polar Knowledge Canada, 69 pp.
- Meloche, J. (2022), *oral communication*.
- Meloche, J., Royer, A., Langlois, A., Rutter, N. and Sasseville, V. (2020), Improvement of microwave emissivity of frozen Arctic soils using roughness measurements derived from automated computer vision photogrammetry. In *AGU Fall Meeting Abstracts (Vol. 2020, pp. C004-0003)*.
- Meloche, J., A. Royer, A. Langlois, N. Rutter, and V. Sasseville (2021), Improvement of microwave emissivity parameterization of frozen Arctic soils using roughness measurements derived from photogrammetry, *International Journal of Digital Earth*, Vol. 14, Iss. 10, pp. 1380-1396, <https://doi.org/10.1080/17538947.2020.1836049>
- Meloche, J., A. Langlois, N. Rutter, D. McLennan, A. Royer, P. Billecocq, and S. Ponomarenko (2022), High-resolution snow depth prediction using Random Forest algorithm with topographic parameters: A case study in the Greiner watershed, Nunavut, *Hydrological Processes*, Vol. 36, Iss. 3, <https://doi.org/10.1002/hyp.14546>
- Meier, Wolfgang (2021), Past and recent climate variability and glacier fluctuations across the Southern Patagonian Andes - A multi-parameter approach using tree-ring parameters and remote sensing, Doctoral thesis, Friedrich-Alexander-Univ., Erlangen-Nürnberg, urn:nbn:de:bvb:29-opus4-156116
- Miller, D. A. and E. E. Adams (2009), A microstructural dry-snow metamorphism model for kinetic growth, *J. of Glaciology*, Vol. 55, Issue 194, pp. 1003 - 1011, DOI: <https://doi.org/10.3189/002214309790794832>
- Miteva V. (2008), Bacteria in Snow and Glacier Ice, In: Margesin R., Schinner F., Marx JC., Gerday C. (eds) *Psychrophiles: from Biodiversity to Biotechnology*. Springer, Berlin, Heidelberg. https://doi.org/10.1007/978-3-540-74335-4_3
- Morgunova, M. (2020), Why is exploitation of Arctic offshore oil and natural gas resources ongoing? A multi-level perspective on the cases of Norway and Russia, *The Polar Journal*, Vol. 10, Iss. 1, <https://doi.org/10.1080/2154896X.2020.1757823>
- Mudryk, L. R., C. Derksen, S. Howell, F. Laliberté, C. Thackeray, R. Sospedra-Alfonso, V. Vionnet, P. J. Kushner, and R. Brown (2018), Canadian snow and sea ice: historical trends and projections, *The Cryosphere*, Vol. 12, pp. 1157–1176, <https://doi.org/10.5194/tc-12-1157-2018>

Mudryk, L., M. Santolaria-Otín, G. Krinner, M. Ménégos, C. Derksen, C. Brutel-Vuilmet, M. Brady, and R. Essery (2020), Historical Northern Hemisphere snow cover trends and projected changes in the CMIP6 multi-model ensemble, *The Cryosphere*, Vol. 14, pp. 2495–2514, <https://doi.org/10.5194/tc-14-2495-2020>

N

Nakaya, U. (1954), Snow Crystals, *Journal of Glaciology*, Volume 2, Issue 16, 1954, pp. 444 DOI: <https://doi.org/10.3189/S0022143000016956>

Nolan, M., Larsen, C. and Sturm, M. 2015: Mapping snow depth from manned aircraft on landscape scales at centimetre resolution using structure-from-motion photogrammetry; *Cryosphere*, v. 9, p. 1445-1463.

Novatel Inc (2015), An Introduction to GNSS, <https://novatel.com/an-introduction-to-gnss>, [accessed 2021 June 16].

O

O'Neill, H. B., and C. R. Burn (2017), Impacts of variations in snow cover on permafrost stability, including simulated snow management, Dempster Highway, Peel Plateau, Northwest Territories, *Arctic Science*, Vol. 3, No. 2, <https://doi.org/10.1139/as-2016-0036>

P

Park, H., A. B. Sherstiukov, A. N. Fedorov, I. V. Polyakov, and J. E. Walsh (2014), An observation-based assessment of the influences of air temperature and snow depth on soil temperature in Russia, *Environmental Research Letters*, Vol. 9, No. 6

Park, H., S. Launiainen, P. Y. Konstantinov, Y. Iijima, and A. N. Fedorov (2018), Modeling the Effect of Moss Cover on Soil Temperature and Carbon Fluxes at a Tundra Site in Northeastern Siberia, *J. of Geophys. Res. Biogeosci.*, Vol. 123, Issue 9, pp. 3028-3044, <https://doi.org/10.1029/2018JG004491>

Pirazzini, R., L. Leppänen, G. Picard, J. I. Lopez-Moreno, C. Marty, G. Macelloni, A. Kontu, A. Von Lerber, C. M. Tanis, M. Schneebeli, P. De Rosnay, and A. N. Arslan (2018), European In-Situ Snow Measurements: Practices and Purposes, *Sensors*, 18(7), <https://doi.org/10.3390/s18072016>

PRadar (2022), Radar basics, <https://training.weather.gov/nwstc/NEXRAD/RADAR/Section1-2.html>, [link accessed 2022-05-14]

PRadTut (2022), Pulse Radar, <https://www.radartutorial.eu/02.basics/Pulse%20Radar.en.html>, [link accessed 2022-05-17]

Prowse, T., K. Alfredsen, S. Beltaos, B. R. Bonsal, W. B. Bowden, C. R. Duguay, A. Korhola, J. McNamara, W. F. Vincent, V. Vuglinsky, K. M. Walter Anthony, and G. A.

Weyhenmeyer (2011), Effects of Changes in Arctic Lake and River Ice, *AMBIO*, Vol. 40, pp. 63–74, <https://doi.org/10.1007/s13280-011-0217-6>

Ponomarenko, S., D. McLennan, D. Pouliot, J. Wagner (2019), High Resolution Mapping of Tundra Ecosystems on Victoria Island, Nunavut – Application of a Standardized Terrestrial Ecosystem Classification, *Canadian Journal of Remote Sensing*, Vol. 45, Iss. 5, pp. 551-571, <https://doi.org/10.1080/07038992.2019.1682980>

Pomerleau, P., A. Royer, A. Langlois, P. Cliche, B. Courtemanche, J.-B. Madore, G. Picard, and E. Lefebvre (2020), Low Cost and Compact FMCW 24 GHz Radar Applications for Snowpack and Ice Thickness Measurements, *Sensors* 2020, 20(14), 3909; <https://doi.org/10.3390/s20143909>

Pomeroy, J. W., and D. M. Gray (1990), Saltation of Snow, *Water Resource Research*, Vol. 26, Iss. 7, pp. 1583-1594, <https://doi.org/10.1029/WR026i007p01583>

Pomeroy, J.W. and E. Brun (2001) Physical properties of snow, *In: Snow Ecology: An Interdisciplinary Examination of Snow-Covered Ecosystems* (eds HG Jones, JW Pomeroy, DA Walker, RW Hoham), pp. 45– 126. Cambridge University Press, Cambridge.

Pörtner, Hans-O., et al. (2022), *Climate change 2022: Impacts, adaptation and vulnerability*. Geneva, Switzerland: IPCC.

Q

Quinton, W. L. and P. Marsh (1999), A conceptual framework for runoff generation in a permafrost environment, *Hydrological Processes*, Vol. 13, Iss. 16, pp. 2563 - 2581, [https://doi.org/10.1002/\(SICI\)1099-1085\(199911\)13:16%3C2563::AID-HYP942%3E3.0.CO;2-D](https://doi.org/10.1002/(SICI)1099-1085(199911)13:16%3C2563::AID-HYP942%3E3.0.CO;2-D)

R

Rantanen, M., Karpechko, A.Y., Lipponen, A. et al. (2022), *The Arctic has warmed nearly four times faster than the globe since 1979*. *Commun Earth Environ* 3, 168 (2022). <https://doi.org/10.1038/s43247-022-00498-3>

Ramseier, R. O., and C. M. Keeler (1966), The Sintering Process in Snow, *Journal of Glaciology*, Vol. 6, Iss. 45, pp. 421 - 424 DOI: <https://doi.org/10.3189/S0022143000019535>

Raynolds, M.K., D.A. Walker, A. Balser, C. Bay, M. Campbell, M. M. Cherosov, F. J.A. Daniëls, P. B. Eidesen, K. A. Ermokhina, G. V. Frost, B. Jedrzejek, M. T. Jorgenson, B.E. Kennedy, S. S. Kholod, I. A. Lavrinenko, O. V. Lavrinenko, B. Magnússon, N. V. Matveyeva, S. Metúsalemsson, L. Nilsen, I. Olthof, I. N. Pospelov, E. B. Pospelova, D. Pouliot, V. Razzhivin, G. Schaepman-Strub, J. Šibík, M. Y. Telyatnikov, and E. Troeva (2019), A raster version of the Circumpolar Arctic Vegetation Map (CAVM), *Rem. Sens. of the Env.*, Vol. 232, doi: <https://doi.org/10.1016/j.rse.2019.111297>

Rennert, K.J., G. Roe, J. Putkonen, C. M. Bitz (2009), Soil thermal and ecological impacts of rain on snow events in the circumpolar Arctic, *Journal Climatology*, Vol. 22, pp. 2302-2315

Romanovsky, V. E., D. S. Drozdov, N. G. Oberman, G. V. Malkova, A. L. Kholodov, S. S. Marchenko, N. G. Moskalenko, D. O. Sergeev, N. G. Ukraintseva, A. A. Abramov, D. A. Gilichinsky, A. A. Vasiliev (2010), Thermal state of permafrost in Russia, *Permafrost and Periglacial Processes*, Vol. 21, iss. 2, pp. 136-155, <https://doi.org/10.1002/ppp.683>

Royer A., F. Dominé, A. Roy, A. Langlois, N. Marchand and G. Davesne (2021), New northern snowpack classification linked to vegetation cover on a latitudinal mega-transect across Northeastern Canada, *Écoscience*, Vol. 28, Iss. 3-4, pp. 225-242, <https://doi.org/10.1080/11956860.2021.1898775>

Rutter, N., Sandells, M., Derksen, C., Toose, P., Royer, A., Montpetit, B., Langlois, A., Lemmetyinen, J., and Pulliainen, J. (2014), *Snow stratigraphic heterogeneity within ground-based passive microwave radiometer footprints: Implications for emission modeling*, *J. Geophys. Res.-Earth*, 119, 550–565, <https://doi.org/10.1002/2013JF003017>.

S

Slatyer, R. A., K. D.L. Umbers, and P. A. Arnold (2022), *Ecological responses to variation in seasonal snow cover*, *Conservation Biology* 36.1 (2022): e13727

Space Weather Service (2021), <https://www.sws.bom.gov.au/Educational/5/4/3>, [link accessed 2021-06-17]

Serreze, M. G., J. A. Maslanik, G. R. Scharfen, R. G. Barry, and D. A. Robinson (1993), *Interannual variations in snow melt over Arctic sea ice and relationships to atmospheric forcings*. *Annals of Glaciology*, 17, 327-331. doi:10.3189/S0260305500013057

Serreze, M. C., and R. G. Barry (2011), Processes and impacts of Arctic amplification: A research synthesis, *Global and Planetary Change*, Vol. 77, Iss. 1–2, pp 85-96, <https://doi.org/10.1016/j.gloplacha.2011.03.004>

Shi J C, Xiong C, Jiang L M. (2016), Review of snow water equivalent microwave remote sensing, *Science China Earth Sciences*, 59: 731-745, doi:10.1007/s11430-015-5225-0

Sommer, C., M. Lehning, C. Fierz (2017), Wind tunnel experiments: saltation is necessary for wind-packing, *Journal of Glaciology*, Vol. 63 (242), pp. 950–958, doi: 10.1017/jog.2017.53

Steigenberger P., Hugentobler U., Hauschild A., Montenbruck O. (2013): Orbit and Clock Analysis of Compass GEO and IGSO Satellites, *J. of Geodesy*, doi: 10.1007/s00190-013-0625-4

Stroeve, J., and D. Notz (2018), Changing state of Arctic sea ice across all seasons, *Environmental Research Letters*, Vol. 13, 103001

Sturm, M., J. Holmgren, M. König, and K. Morris (1997), The thermal conductivity of seasonal snow, *Journal of Glaciology*, Vol. 43, Iss. 143, pp. 26 - 41, DOI: <https://doi.org/10.3189/S0022143000002781>

Sturm, M., J. P. McFadden, G. E. Liston, F. S. Chapin, C. H. Racine, and J. Holmgren (2001), Snow–Shrub Interactions in Arctic Tundra: A Hypothesis with Climatic Implications, *J. of Clim.*, Vol. 14 (3), pp. 336-344, [https://doi.org/10.1175/1520-0442\(2001\)014<0336:SSIIAT>2.0.CO;2](https://doi.org/10.1175/1520-0442(2001)014<0336:SSIIAT>2.0.CO;2)

Sturm, M., J. Holmgren, and D. K. Perovich (2002), Winter snow cover on the sea ice of the Arctic Ocean at the Surface Heat Budget of the Arctic Ocean (SHEBA): temporal evolution and spatial variability, *J. of Geophys. Res.* 107, DOI: 10.1029/2000JC000400.

Sturm, M., and J. Holmgren (2018), An automatic Snow Depth Probe for Field Validation campaigns, *Water Resource Research*, Vol. 54, Iss. 11, pp. 9695 - 9701, <https://doi.org/10.1029/2018WR023559>

T

Takala, M., K. Luojus, J. Pulliainen, C. Derksen, J. Lemmetyinen, J.-P. Kärnä, J. Koskinen, B. Bojkov (2011), Estimating northern hemisphere snow water equivalent for climate research through assimilation of space-borne radiometer data and ground-based measurements, *Remote Sensing of Environment*, Vol. 115, pp. 3517-3529, <https://doi.org/10.1016/j.rse.2011.08.014>

Terkildsen, M., and G. Olivares (2018), Ionospheric storm effects on GNSS precise positioning, *42nd COSPAR Scientific Assembly, Held 14-22 July 2018, in Pasadena, California, USA, Abstract id. PSW.3-17-18, bibcode: 2018cosp...42E3356T*

Texas Instruments (2018), Introduction to mmwave sensing : FMCW Radars, <https://www.youtube.com/watch?v=8cHACNNDWD8>, [link accessed 2022-05-13]

Thackeray, C. W., C. Derksen, C. G. Fletcher, and & A. Hall (2019), Snow and Climate: Feedbacks, Drivers, and Indices of Change, *Current Climate Change Reports*, Vol. 5, pp. 322–333

Thompson, D. W. J. and J. M . Wallace (1998), The Arctic oscillation signature in the wintertime geopotential height and temperature fields, *Geophysical Research Letter*, Vol. 25, No. 9, pp. 1297-1300

Tiuri, M., Sihvola, A., Nyfors, E. and Hallikaiken, M. (1984), The complex dielectric constant of snow at microwave frequencies, *IEEE J.l of Ocean. Engin.*, Vol. 9, No. 5, pp. 377-382, DOI: 10.1109/JOE.1984.1145645

Trimble (2021), GGA - Global Positioning System fix data, http://help.t4d.trimble.com/documentation/manual/version5.0/server/NMEARecv_GEN_GGA_Description.htm, [link accessed 2022-05-26]

Tsang, L., Durand, M., Derksen, C., Barros, A. P., Kang, D.-H., Lievens, H., Marshall, H.-P., Zhu, J., Johnson, J., King, J., Lemmetyinen, J., Sandells, M., Rutter, N., Siqueira, P., Nolin, A., Osmanoglu, B., Vuyovich, C., Kim, E., Taylor, D., Merkouriadi, I., Brucker, L., Navari, M., Dumont, M., Kelly, R., Kim, R. S., Liao, T.-H., Borah, F., and Xu, X. (2022): *Review article: Global monitoring of snow water equivalent using high-frequency radar remote sensing, The Cryosphere*, 16, 3531–3573, <https://doi.org/10.5194/tc-16-3531-2022>

V

Van Pelt, J. J., T. V. Schuler, V. A. Pohjola, and R. Pettersson (2021), Accelerating future mass loss of Svalbard glaciers from a multi-model ensemble, *J. og Glac.*, Vol. 67, Iss. 263, pp. 485 - 499, DOI:<https://doi.org/10.1017/jog.2021.2>

Venkataraman, G., Singh, G., and Y. S. Rao (2007), Snow cover monitoring and snow density estimation using ALOS-PALSAR data, *Proceedings of First PI Symposium. Kyoto, Japan*.

Vincent, W. F. (2020) Arctic Climate Change: Local Impacts, Global Consequences, and Policy Implications. In: Coates K., Holroyd C. (eds) *The Palgrave Handbook of Arctic Policy and Politics*. Palgrave Macmillan, Cham. https://doi.org/10.1007/978-3-030-20557-7_31

W

Walker, B., E. J. Wilcox, and P. Marsh (2020), Accuracy assessment of late winter snow depth mapping for tundra environments using Structure-from-Motion photogrammetry, *Arctic Science*, <https://doi.org/10.1139/as-2020-0006>

Wang, J., and J. G. Park (2020), Indoor Positioning Algorithm Based on Channel State Information using Bootstrap Filter, *Proceedings of the 33rd International Technical Meeting of the Satellite Division of The Institute of Navigation (ION GNSS+ 2020)*, , September 2020, pp. 2358-2366, <https://doi.org/10.33012/2020.17590>

Wanner, H., S. Brönnimann, C. Casty, D. Gyalistras, J. Luterbacher, C. Schmutz, D. B. Syphenson, and E. Xoplaki (2001), North Atlantic Oscillation - Concepts and Studies, *Surveys in Geophysics*, Vol. 22, pp. 321-382, DOI:10.1023/A:1014217317898

Warren, S. G. (2019), Optical properties of ice and snow, *Phil. Transac. Of the Roy. Soc. A*, Vol. 377, Iss. 2146, <https://doi.org/10.1098/rsta.2018.0161>

Wei, T., Q. Yan, W. Qi, M. Ding, and C. Wang (2020), Projections of Arctic sea ice conditions and shipping routes in the twenty-first century using CMIP6 forcing scenarios, *Environmental Research Letters*, Vol. 15, 104079

Williams, L., Sugden, D., and Gallagher, J. (1990), Millimetric Radar Backscatter From Snowcover, *Stevenson, Dundee*.

Windstral, A., D. Marks, and R. Gurney (2014), Assessing the Sensitivities of a Distributed Snow Model to Forcing Data Resolution, *J. of Hyrdomet.*, Vol. 15, Iss. 4, pp. 1366-1383 DOI: <https://doi.org/10.1175/JHM-D-13-0169.1>

Woo, M., M. Mollinga, and S. L. Smith, 2007: Climate warming and active layer thaw in the boreal and tundra environments of the Mackenzie Valley. *Canadian Journal of Earth Science*, Vol. 44, pp. 733–743, <https://doi.org/10.1139/e06-121>

Wrona, E., T. L. Rowlandson, M. Nambiar, A. A. Berg, A. Colliander, and P. Marsh (2017), Validation of the Soil Moisture Active Passive (SMAP) satellite soil moisture retrieval in an Arctic tundra environment, *Geophysical Research Letters*, Vol. 44, pp. 4152-4158, doi:10.1002/2017GL072946

Y

Yamanouchi, T., and K. Takata (2020), Rapid change of the Arctic climate system and its global influences - Overview of GRENE Arctic climate change research project (2011–2016), *Polar Science*, Vol. 25, <https://doi.org/10.1016/j.polar.2020.100548>

Yang, B., L. Guo, R. Guo, M. Zhao and T. Zhao (2020), A Novel Trilateration Algorithm for RSSI-Based Indoor Localization, *IEEE Sensors Journal*, Vol. 20, No. 14, pp. 8164-8172, doi: 10.1109/JSEN.2020.2980966.

Z

Zhang, W., P. A. Miller, C. Jansson, P. Samuelsson, J. Mao, and B. Smith (2018), Self-Amplifying Feedbacks Accelerate Greening and Warming of the Arctic, *Geophysical Research Letters*. Vol. 45, Iss. 14, pp. 7102-7111, <https://doi.org/10.1029/2018GL077830>

Zweng, M. T. Boyer, O. Baranova, J. Reagan, D. Seidov, and I. Smolyar (2018), An inventory of Arctic Ocean data in the World Ocean Database, *Earth Syst. Sci. Data*, 10, 677–687, <https://doi.org/10.5194/essd-10-677-2018>